Irreversible Electroporation Therapy for the Treatment of Spontaneous Tumors in Cancer Patients

Robert Evans Neal II

Dissertation submitted to the faculty of the Virginia Polytechnic Institute and State University in partial fulfillment of the requirements for the degree of

Doctor of Philosophy

In

Biomedical Engineering

Rafael V. Davalos, Committee Chair

John L Rossmeisl

Suzy V. Torti

Steven V. Akman

Christopher G. Rylander

Marissa Nichole Rylander

October 10, 2011

Blacksburg, VA

Keywords: Electropermeabilization, Heterogeneity, Treatment Planning, Tissue Ablation, Non-thermal Focal Therapy, Combined Modality Treatment, Immune System, Clinical Translation, Bioimpedance, IRE, N-TIRE, Minimally Invasive Surgery, Electrical Conductivity

Irreversible Electroporation Therapy for the Treatment of Spontaneous Tumors in Cancer Patients

by

Robert Evans Neal II

ABSTRACT

Irreversible electroporation is a minimally invasive technique for the non-thermal destruction of cells in a targeted volume of tissue, using brief electric pulses, (~100 µs long) delivered through electrodes placed into or around the targeted region. These electric pulses destabilize the integrity of the cell membrane, resulting in the creation of nanoscale defects that increase a cell's permeability to exchange with its environment. When the energy of the pulses is high enough, the cell cannot recover from these effects and dies in a non-thermal manner that does not damage neighboring structures, including the extracellular matrix. IRE has been shown to spare the major vasculature, myelin sheaths, and other supporting tissues, permitting its use in proximity to these vital structures. This technique has been proposed to be harnessed as an advantageous non-thermal focal ablation technique for diseased tissues, including tumors.

IRE electric pulses may be delivered through small (ø ≈ 1 mm) needle electrodes, making treatments minimally invasive and easy to apply. There is sub-millimeter demarcation between treated and unaffected cells, which may be correlated with the electric field to which the tissue is exposed, enabling numerical predictions to facilitate treatment planning. Immediate changes in the cellular and tissue structure allow real-time monitoring of affected volumes with imaging techniques such as computed tomography, magnetic resonance imaging, electrical impedance tomography, or ultrasound. The ability to kill tumor cells has been shown to be independent of a functioning immune system, though an immune response seems to be promoted by the ablation. Treatments are unaltered by blood flow and the electric pulses may be administered quickly (~ 5 min).

Recently, safety and case studies using IRE for tumor therapy in animal and human patients have shown promising results. Apart from these new studies, previous work with

IRE has involved studies in healthy tissues and small cutaneous experimental tumors. As a result, there remain significant differences that must be considered when translating this ablation technique towards a successful and reliable therapeutic option for patients. The dissertation work presented here is designed to develop irreversible electroporation into a robust, clinically viable treatment modality for targeted regions of diseased tissue, with an emphasis on tumors. This includes examining and creating proving the efficacy for IRE therapy when presented with the many complexities that present themselves in real-world clinical patient therapies, including heterogeneous environments, large and irregular tumor geometries, and dynamic tissue properties resulting from treatment. The impact of these factors were theoretically tested using preliminary *in vitro* work and numerical modeling to determine the feasibility of IRE therapy in heterogeneous systems. The feasibility of use was validated *in vivo* with the successful treatment of human mammary carcinomas orthotopically implanted in the mammary fat pad of mice using a simple, single needle electrode design easily translatable to clinical environments.

Following preliminary theoretical and experimental work, this dissertation considers the most effective and accurate treatment planning strategies for developing optimal therapeutic outcomes. It also experimentally characterizes the dynamic changes in tissue properties that result from the effects of IRE therapy using *ex vivo* porcine renal cortical tissue and incorporates these into a revised treatment planning model. The ability to use the developments from this earlier work is empirically tested in the treatment of a large sarcoma in a canine patient that was surgically unresectable due to its proximity to critical arteries and the sciatic nerve. The tumor was a large and irregular shape, located in a heterogeneous environment. Treatment planning was performed and the therapy carried out, ultimately resulting in the patient being in complete remission for 14 months at the time of composing this work.

The work presented in this dissertation finishes by examining potential supplements to enhance IRE therapy, including the presence of an inherent tumor-specific patient immune response and the addition of adjuvant therapeutic modalities.

Acknowledgments

This section will be expanded upon final submission and acceptance of this dissertation, but for now I must give credit to all of the individuals who have made this work possible and provided me with the assistance and guidance to enable me the opportunity to defend a PhD dissertation. To begin, I would like to thank my advisor, Rafael Davalos for all the time spent helping me throughout my graduate career and entertaining the prospect of taking on a new student who happened across his lab by chance while getting to know the department, despite uncertainty of how we would manage to support my work in his lab. I also must recognize his generosity allowing me to travel and present my work, staving off small-town fever and helping to make my final 3 years of 7 in Blacksburg the best and most immersive. In addition, I must thank my advisory committee for their willingness to challenge and push me in completing my degree as well as for their insight into concepts of investigation and keeping me on track and focused.

I would also like to thank all of our collaborators and the staff at the Virginia Maryland Regional College of Veterinary Medicine for allowing us the opportunity to indulge in such rewarding work as actually implementing our work on real-world patients, providing first-hand experience in seeing the impact that we can make on a patient's life, 2-legged or 4. Among those are Dr. Robertson for all of his invaluable resources and ideas, and those in his lab including Lindsey Buracker, Chip Aardema, and Erica Davis. In addition, large thanks is due to Drs. Rossmeisl, Nicholson, Settlage, Lanz, and Maley for trusting me to collaborate with them in developing therapies for their patients and enabling me see how much really changes when one moves from a controlled experiment to real-life patients. These efforts would also not have been possible without the time and efforts of Dr. Henao-Guerrero, the radiology department, and the experimental lab service staff for helping us to put everything together on treatment days.

Among those most directly involved in the work for this dissertation, I would like to thank all of the other students in the Bioelectromechanical Systems Lab for the continuous flow of new ideas and methods to mutually increase our progress, as well as their perpetual enthusiasm and selflessness in helping to carry out experiments. Among these students, I would like to thank Dr. Garcia, Chris Arena, and Mike Sano for their committed hours and ability to always raise the bar in our lab, motivating the rest of us to match their creativity and success. In addition, thanks go out to John Caldwell, Andrea Andric, Dr. Shafiee, Erin Henslee, and everyone else that has come through the lab.

As well as those I have worked with in Blacksburg, I would like to acknowledge all of our collaborators at Wake Forest University Baptist Medical Center. In particular, Dr. Torti and her lab, where Drs. Singh and Hatcher not only directly aided in carrying out the work presented in this dissertation, but also instilled a sense of enthusiasm and encouragement for the field and work that we do. I would also like to acknowledge the contributors to the nanotech conference calls, including the physicians that sat through my presentations for providing constructive ideas into my latest work and helping to develop ways to move forward with bringing IRE to human patients.

My undergraduate professors and the Engineering Science Department should also be acknowledged for helping to craft my abilities as an engineer, and in particular Dr. Madigan for his guidance as I tried to determine my future career path and for the hours sitting as we scratched our heads trying to figure out how water can break a femur.

I would like to thank all of my friends from my time here in Blacksburg, especially the crowd from Pheasant Run for always providing a place where I can go to relax and clear my head when the pressures from work felt overwhelming. Finally, my ability to complete this dissertation would not have been possible without the unrelenting love and support from my parents and family. I must wholly acknowledge them for enabling me the opportunities that I have received and providing me with wisdom and skills to effectively pursue my dreams.

TABLE OF CONTENTS

List of Figures

List of Tables

Chapter 1: Introduction

1.1 Background and Motivation

It is the central hypothesis of the work presented in this dissertation that irreversible electroporation can effectively and reliably treat spontaneous clinical patient tumors, where individually unique, large and complex patient-specific tumors will require significant translational consideration. Electroporation is a phenomenon that uses brief (~ 100 μs) electric pulses to alter the transmembrane potential on the lipid bilayer in cell membranes. When the energy of the electric pulses surpasses a threshold, nanoscale defects arise in the cellular membrane, increasing its permeability to the transport of macromolecules, especially those with an inherently low ability to cross through the lipid bilayer under normal circumstances, such as large and hydrophilic molecules. This behavior has been exploited in various reversible electroporation based therapies as a technique to introduce genes or chemotherapeutics into targeted cells. However, if the energy from the pulses is too high, the cell is unable to recover from the effects of the pulses and dies in a non-thermal manner known as irreversible electroporation (IRE).

Irreversible electroporation has been postulated to be useful as a non-thermal focal ablation technique in the destruction of localized regions of targeted tissue. Pulse application is typically done through small needle electrodes (ø ≈ 1 mm) placed into or around the targeted region, making treatment minimally invasive and localized. The electric fields applied to induce IRE only affect the cell membrane, sparing the extracellular matrix and sensitive structures, such as myelin sheaths and major tissue vasculature, allowing for rapid lesion resolution and minimal scarring of the treated volume [4-6]. Due to immediate changes in the treated tissue's permeability, the affected regions may be monitored in real-time using techniques such as ultrasound, electric impedance tomography, computed tomography, or magnetic resonance imaging [6, 7]. There is sharp demarcation between treated and normal regions [4, 8], and it has been shown that the heterogeneous properties of certain structures, such as lactiferous ducts, may protect them from electroporation damage, permitting continued functioning [9].

Although not dependent on a functioning immune system, electroporation treatments promote an immune response [5, 10], including areas that experience reversible electroporation [10]. Treatments are related to the electric field to which the cells are exposed, which may be predicted through numerical modeling [11, 12], enabling treatment planning.

A primary application for IRE therapy is in the treatment of tumors. Previous work with irreversible electroporation has demonstrated its numerous advantages as a focal ablation technique [4-6, 13-17]. IRE in experimental cutaneous and orthotopically implanted murine tumors attained regression rates as high as 92% [18-20]. Veterinary case studies using IRE for canine patients were able to reach complete tumor regressions in complex, otherwise inoperable tumors, including a high-grade glioma with adjuvant radiation therapy [21], and a histiocytic sarcoma with adjuvant chemotherapy [22]. Further, IRE was demonstrated to work as a repeat therapy, even after evolution of the cancer resulted in chemotherapy resistance [22]. Phase 1 human safety trials achieved complete tumor remission for 46 of 69 tumors in patients unresponsive or untreatable with current standards of care, a regression rate of 66% [23, 24].

The previous studies using IRE to treat experimental and spontaneous tumors provide strong evidence supporting IREs ability to be a reliable standard of care therapy in the treatment of cancer. However, overall assessment of the therapeutic efficacy for IRE remains in its infancy and its translational development towards clinical tumor therapy is limited. In order for IRE to become a widespread and commonplace methodology for treating patients, it is vital to account for the high variability that arises in clinical therapy cases relative to experimental investigations and to understand how such differences will impact treatment outcome. Further, techniques must be developed to facilitate the implementation of IRE therapy to patient-specific clinical cases in an effective, reliable, and temporally efficient manner.

1.2 Research Goals and Approach

It is the goal of this dissertation to develop IRE cancer therapy from a theoretical and experimental endeavor into a technique readily capable of accurately treating

targeted tumors in a wide variety of applications. To accomplish this objective, the work in this dissertation focused on exploring the behavior of IRE therapies in very complex and irregular regions, accounting for treatment effects that will be encountered in clinical settings, including heterogeneities at the cellular and tissue scales, dynamic tissue properties, and the role of a functioning immune system. In addition, many tumors may be large or irregular in shape, and different techniques to finely customize treatment volumes must be created to account for this to ensure complete treatment of the targeted region while sparing as much neighboring healthy tissue as possible. All of these considerations are incorporated into treatment planning methodologies that were developed and tested on actual clinical patients, proving the ability to accurately plan and implement IRE treatments capable of attaining their clinical objectives in complex, real-world clinical cases. In an effort to expand the scope of IRE tumor treatment applications, a study was performed examining the potential therapeutic enhancement of combining electrochemotherapy principles to increase the volume of treated tissue or to target infiltrative cells beyond the tumor margin, which would be treated using IRE. Finally, this dissertation examined the potential for tumor-specific immunological enhancement to IRE therapeutic outcome that will be appreciated in many clinical cancer patients, but may not be present in experimental investigations of IRE on healthy tissue or in immunodeficient animal models.

1.3 Dissertation Overview

This dissertation systematically examines the potential to use IRE as a technique to treat cancer in the complex, uncontrolled cases common in clinical cancer therapy. It begins in Chapter 2 with a brief overview of relevant theory topics, including the underlying principles for electroporation and the electrical properties of biological tissue. In Chapter 3, a review of published work using electroporation based therapies is provided, including some of the major experimental *in vitro* and *in vivo* work, as well as progress made for the various therapies in the clinical venue.

After providing a brief review of the existing work done on electroporation, the preliminary original work performed to examine IREs potential utility in complex clinical

therapy is started in Chapter 4, using *in vitro* experiments combined with numerical modeling to determine the feasibility of using IRE in a simple simulated heterogeneous system composed of a tumor within peripheral tissue, with two needle electrodes placed at either end of the tumor. The efficacy for IRE therapy in such scenarios is determined by evaluating the degree of targeted volume exposure to the required effective electric field threshold, as determined by the *in vitro* experiments, without inducing significant thermal damage to deplete IREs non-thermal ablation advantages. The chapter concludes that it is possible for IRE therapy implemented in the setup used in the model should be able to treat a wide array of heterogeneous property systems, such as breast tumors, without inducing significant thermal damage.

The feasibility study in Chapter 4 permitted us to experimentally test its theoretical conclusions *in vivo* in Chapter 5, where we delivered IRE therapy to orthotopically implanted human mammary carcinoma tumors in the mammary fat pad of mice. The electric pulses were delivered through a custom-made single needle electrode that contained both energized surfaces, which was placed directly in the center of the tumor. Tumor response to the pulses was measured using growth measurements with calipers, bioluminescence, and histology for tissue samples collected 28 days after pulse delivery. This study was able to achieve complete regressions in 5 of 7 treated tumors, with no regressions from the control mice, and no histological evidence of thermal damage, validating the conclusions of Chapter 4 for a simple experimental scenario.

Chapters 6 and 7 focus on treatment planning for IRE therapies. Chapter 6 experimentally characterizes the dynamic tissue property response to pulsed electric fields and applies the findings to a numerical model, while Chapter 7 discusses general topics and considerations for treatment planning. Among the subjects addressed in Chapter 7 are the utility of, potential methods for, and limitations of rapid-solving techniques to calculate or estimate electric field distributions. Following this is a step-by-step explanation for a possible treatment planning algorithm that may be used in developing patient treatment protocols, following the steps using an example clinical case from a canine lipoma.

Chapter 8 tests the underlying hypothesis of this dissertation and describes the culmination of the earlier chapters in this dissertation by applying their conclusions and findings in developing and implementing a treatment protocol for a canine patient. The patient had a large, complex tumor in its hind limb, creating a very heterogeneous treatment environment that included tumor encapsulation of portions of the sciatic nerve and major femoral arteries, as well as a location adjacent to bone and muscle tissue. The primary symptoms for the patient were pain and sciatic neuropathy, and a palliative application of IRE was selected to address only the clinically symptomatic aspects of the cancer. Treatment planning was performed using the techniques described in Chapter 7, and the procedure was carried out using computed tomographic guidance. Following a strong initial response to therapy, the patient was placed on adjuvant chemotherapy and monitored until apparent chemoresistance was observed. The patient was then removed from chemotherapy and a second delivery of IRE therapy was applied to the only remaining focus of tumor volume, an originally untargeted region (not clinically symptomatic). Following the second application, complete remission was observed from the patient, currently lasting 14 months at the time of composing this dissertation. The strong therapeutic response of this patient to IRE therapy provides strong empirical evidence to support the hypothesis that IRE can be successfully used to treat cancer in clinical patients with large, complex tumors that include irregular geometries, heterogeneous environments, and the inclusion of sensitive supporting structures such as nerves and major vasculature.

This dissertation finishes by examining two potential mechanisms to enhance IRE therapy. The first, discussed in Chapter 9, investigates the ability to use irreversible electroporation enhanced pharmacotherapy (IREEP), where both the irreversible and reversible regimes of electroporation are used to expand the therapeutic volume with the addition of certain chemotherapeutic macromolecules. These macromolecules experience enhanced uptake and lower dose cytotoxicity on reversibly electroporated cells. Chapter 9 uses *in vitro* experiments on two malignant glioma cell lines to quantify this enhancement for typical IRE electric pulse parameters and incorporates these results into a numerical model that predicts treatment outcome from a basic electrode and pulse setup applied in a

canine brain. Finally, in Chapter 10, an inherent potential enhanced response to IRE therapy is investigated in the form of a promoted immune response. Immunocompetent and immunodeficient strains of mice were inoculated with a tumorigenic renal adenocarcinoma cell line to produce cutaneous tumors. The tumors were treated with IRE electric pulses delivered over the skin through plate electrodes with a conductive gel. This study finds that the immunocompetent mouse model responds better to the IRE therapy than the immunodeficient mice, and that both treatment groups respond better than sham treatment controls. Further, the investigation in Chapter 10 reinoculates the mice with the same cell line 18 days after treatment, and observes slowed or prevented tumor growth in the immunocompetent mice, with no measureable difference between primary and secondary tumor growth in the immunodeficient mice. The findings from this study suggest the presence of a systemic, tumor-specific immune response capable of identifying and killing the cancer cells at other locations in the body.

Chapter 2: Bioimpedance and Electroporation – A Review

2.1 Introduction

Electroporation based therapies rely on the use of brief electric pulses to alter the transmembrane potential and disrupt the cell membrane by creating nanoscale defects in the lipid bilayer. These effects can be reversible and used to facilitate macromolecule transport into the cell, such as genes or therapeutic chemicals, or the effects can be irreversible, killing the cell through a variety of potential mechanisms including necrosis and apoptosis. The effects from the pulses on the cell will depend on the electrochemical interactions between the cell and its environment. In this chapter, we will cover some of the theoretical aspects at the microscopic level involving the creation of the nanoscale defects as a result of altered transmembrane potential as well as at the macroscopic level where the properties and interaction of cells and tissue with their environment will affect the transmembrane potential to which the tissue is exposed, affecting how electroporation treatments will behave in biological tissues.

2.2 Scope of Review

The objective for this review is to introduce the reader to the relevant topics for electroporation based therapies, particularly the electrophysical interactions between biological tissues and their environment. It first presents the basic effects of external electric fields on materials in general, including both charged and uncharged particles. It then discusses how these effects will be altered when there is a restriction to the free flow of charges, such as the shell model of a cell, where the intra- and extracellular mediums are conductive, but separated by a cell membrane, whose lipid bilayer behaves as a dielectric to the flow of charges if one excludes the presence of gated ion channels and the dynamic behavior inherent in an adaptive material, such as a biological membrane.

After discussing how a cell behaves in the presence of an electric field under simple circumstances, the ability of the cell membrane energy to change with the creation of hydrophobic and hydrophilic pores is explained. In addition, an examination of changes in advantageous minimum energies in the presence of a transmembrane voltage is

discussed, as well as the behavior of pore formation, evolution, and resealing in the cell membrane when exposed to an electric field.

This chapter proceeds to review the basic concepts of electrical theory and how they may be applied to cells and tissue. An electrical model of a cell in suspension or tissue is described using an equivalent circuit model composed of several resistor and capacitor components. This section then describes how such an equivalent circuit model may be used to estimate cell behavior in the presence of a constant or alternating voltage, as well as how the bioimpedance characteristics of cells and tissue will change with frequency, an aspect known as dispersion. Finally, this chapter briefly details how electroporation affects the cellular tissue electrical properties, an attribute that will greatly affect treatment outcomes in electroporation based therapies, which is covered in greater detail in Chapter 6.

2.3 Theory of Electroporation

2.3.1 Behavior of Particles in Electric Fields

Different particle types can exhibit unique electrical characteristics. If a particle contains an unbalanced number of positive or negative ions, the material may have a net charge. This is the case for single ions, such as sodium (Na^+) and chlorine (Cl^-), or molecules composed of many atoms with an imbalance, such as a negatively charged protein like albumin. In addition, the net number positive and negative ions may balance out to result in an overall neutral charge. However, depending on the molecular characteristics, a molecule with a neutral net charge may exhibit polarized charges, resulting in a dipole behavior. This behavior may be seen in water molecules, where the two circulating exchanged electrons spend less time around the two hydrogen atoms they came from, resulting in an overall positive charge on this end of the molecule, and a negative charge on the water portion of the molecule. This behavior allows for the hydrogen-bonding behavior of water molecules and is also used as the basis for magnetic resonance imaging, where powerful magnets are used to align the poles of water molecules within a person's body.

Although some molecules may naturally be dipoles, many materials do not, such as the particle depicted in **Figure 2.1A**. However, if resistive or in free space, when these materials are placed in an electric field, electrons will become attracted to the positive end of the electric field and repelled by the negative end of the field. This results in an imbalance of electron location and an artificial polarization of the material, as seen in **Figure 2.1B**. This behavior has been used in various applications, such as dielectrophoresis, where a non-uniform electric field is used to polarize a material and move it towards the more focused end of the electric field [25].

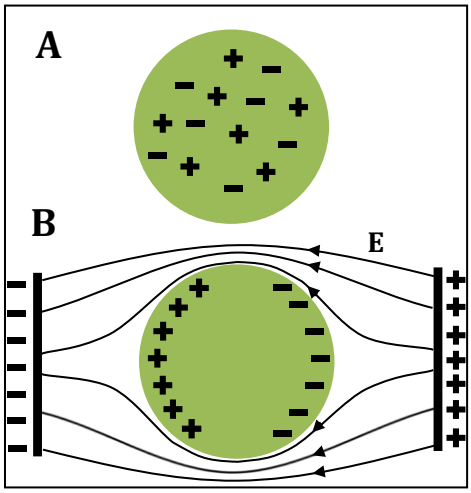

Figure 2.1: (A) Behavior of an uncharged molecule in free space without external stimuli and (B) in the presence of an external electric field.

2.3.2 Behavior of Cells in Electric Fields

2.3.2.1 Cell Biology

Cells are the smallest basic unit of life capable of performing all the basic life functions, including organization, growth and differentiation, reproduction, movement, metabolism and excretion, and responsiveness [26, 27]. They may come in a wide variety of sizes and shapes. Mammalian cells have a variety of forms and specific functions for maintaining homeostasis and the life of the living organism which they comprise [28]. In order to accomplish these tasks, cells contain various organelles, including the nucleus to hold their DNA, mitochondrion for ATP synthesis, and a cytoplasm that contains a vast amount of intracellular structural components, proteins, RNA, and ions [27]. Cell survival relies on the ability of a cell to isolate itself from its environment, creating an

enclosed collection of all cellular constituents required to perform the tasks necessary to live.

The cellular plasma membrane acts as a gatekeeper to the cell's interior environment. The cell membrane allows cell survival by selectively isolating its contents from the external environment, regulating exchange of essential substances between the cell's contents and its external environment, and performing the task of communicating with other cells [29].

The primary component of most cell membranes is the phospholipid bilayer. These materials have been shown to autoarrange from a mixture of phospholipids in water in where the hydrophilic phosphate-based heads form hydrogen bonds with the water. The hydrophobic lipid tails avoid the water and arrange to face each other, forming the double layer that shields the tails while allowing the heads to bond with the cytoplasm as well as the extracellular fluid [29]. This arrangement prevents lipid exposure to the water molecules, creating a tight seal that restricts the free movement of water and other molecules across the membrane, effectively isolating the cell from its external environment. The cell membrane also contains various proteins and cholesterol that support cell homeostasis by allowing for membrane flexibility and carrying out various tasks in relation to the cellular environment, such as ion and material exchange or communication via receptors. The matrix of phospholipids, proteins, and cholesterol for the cell membrane is known as the fluid-mosaic model [29].

2.3.2.2 Behavior of Lipid Bilayer in an Electric Field

The fluid mosaic model of phospholipid bilayers that makes up cell membranes allow cells to exhibit semipermeable properties. The channel and gate proteins give cell membranes selective permeability to regulate the exchange between the intracellular and extracellular environments of various components, including ions. This allows the cell to maintain electrical potential gradients between these two environments, creating a potential difference across the membrane. Most mammalian cells have a small transmembrane potential of roughly 70 mV, where the external environment contains slightly more positive charge than the intracellular environment [30]. This potential

gradient is maintained by proteins in the membrane. The phospholipid bilayer of cell membranes therefore results in complex electrical properties, which may be electrically modeled by a resistor and capacitor in parallel. The capacitor represents the membrane's properties as a dielectric, where charges are capable of being built up on either side, but cannot cross, while the resistor represents the ability for some ion exchange due to occasional leakiness of the membrane or protein-facilitated ion exchange.

The unique electrical characteristics of mammalian cell membranes allow one to visualize the cell as a high conductivity intracellular solution surrounded by a dielectric separating it from an external environment of another high conductivity solution (**Figure 2.2A**). When this system is placed in the presence of a constant or low frequency (≤10 kHz) external electric field, the membrane's capacitor behavior induces a polarization of the cell, similar to that of homogeneous materials, where ions move in response to the polarity of the electric field [1]. This results in the movement of negative ions, such as chlorine (Cl^-), towards the positive side of the electric field, while positive ions, such as sodium and potassium (Na^+ and K^+) are driven towards the negative side of the electric field. Within the cell, these ions are constrained by the dielectric cell membrane, resulting in an accumulation of the charged ions at each end. In contrast, the extracellular ions accumulate on the alternate corresponding charge of the cell. This process results in oppositely charged ions accumulating at either side of the cell membrane, resulting in an electric potential gradient across the membrane, as can be seen in **Figure 2.2B**.

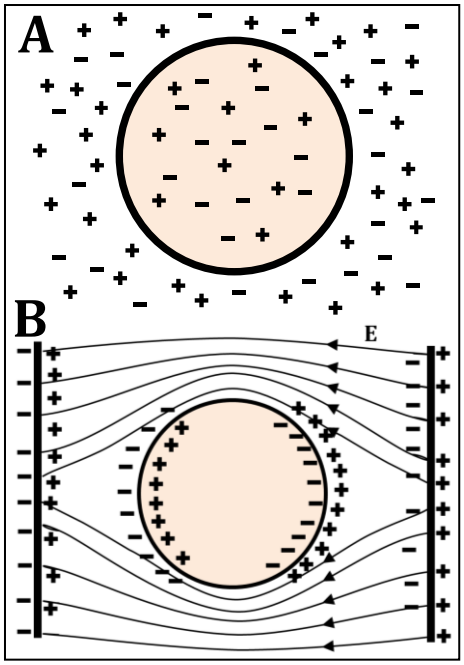

Figure 2.2: (A) Behavior of electrolytes for a cell in an isotonic aqueous environment without outside stimuli, and (B) in the presence of a constant or low frequency external electric field. Adapted from [1].

For the square wave electric pulses typically used in IRE, the waveform of the pulses used and their length (~ 100 μs) allows the scenario of the membrane capacitance behaving as an open circuit to be considered. It is important to note that because very little current flows through the cell for these pulses, charges are able to build up at the cell membrane, for continuous exposure to a pulse (DC conditions), this charge buildup changes the native transmembrane potential of the cell according to the equation:

$$V_m = \lambda \cdot r \cdot E \cdot \cos(\theta) \cdot (1 - e^{-t/\tau}) \tag{2.1}$$

$$\tau = r \cdot c_m(\frac{1}{\sigma_i} + \frac{1}{2\sigma_e}) \tag{2.2}$$

where λ is the shape factor of the cell, r is the cell radius, E is the external electric field to which the cell is exposed, and θ is the angle of the membrane relative to the direction of the electric field. τ is the membrane relaxation time, a function of the cell radius, membrane capacitance, c_m, and the intracellular, σ_i, and extracellular conductivities, σ_e.

For a spherical cell in suspension, the shape factor roughly equals 1.5, and the conditions reduce the equation to:

$$V_m = \lambda \cdot r \cdot E \cdot \cos(\theta) \cdot [1 + \left(\frac{f}{f_s}\right)^2]^{-0.5} \quad (2.3)$$

where f_s is the frequency for where beta dielectric dispersion occurs. Because the length of typical electroporation pulses are much longer than the membrane charging time, the transient term $(f/f_s)^2$ may be ignored, resulting in an approximate steady state solution for transmembrane potential assuming a constant applied electric field.

2.3.3 Pore Dynamics

2.3.3.1 Pore Energy

The transient aqueous pore hypothesis for lipid bilayer pores behavior assumes the existence of two types of pores, hydrophobic and hydrophilic [2, 3, 31, 32]. Hydrophobic pores are openings where the hydrophobic lipid tails of the bilayer are exposed to the pore opening, as may be seen in **Figure 2.3A**, and are formed as a result of thermal fluctuations of the membrane. Conversely, hydrophilic pores have the hydrophilic phosphate heads move into the gap of the pore, as seen in **Figure 2.3B**. The hydrophilic pores allow passage of other hydrophilic molecules, such as ions.

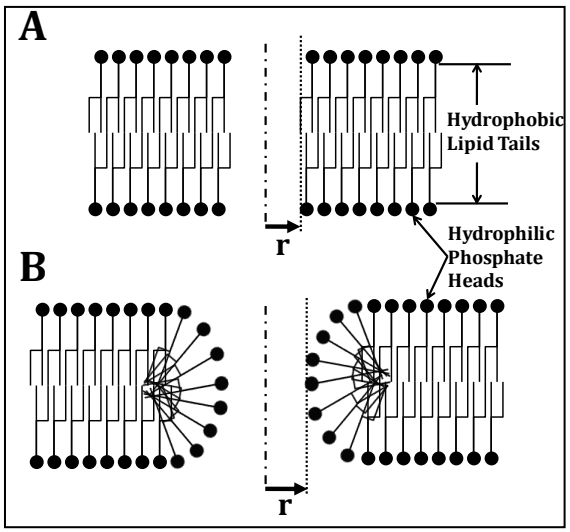

Figure 2.3: Phospholipid bilayer typical of cellular membranes with (A) hydrophobic and (B) hydrophilic pores. Adapted from [2].

The study of pore behavior relies on the assumption of a relationship between pore radius, r, and its energy, E [3]. This relationship may be calculated by the energy functions for the hydrophobic, u(r), and hydrophilic, w(r), pores. Neglecting any transmembrane potential, these functions may be approximated by the following equations:

$$u(r) \approx E_* \left(\frac{r}{r_*}\right)^2 \tag{2.4}$$

$$w(r) = 2\pi\gamma r - \pi\sigma r^2 + \left(\frac{C}{r}\right)^4 \tag{2.5}$$

where E_* and r_* represent the pore energy and radius local maximums, respectively, γ represents the edge energy per unit length of a pore, σ is the energy per unit area of an intact membrane, and a constant C which is chosen for the third term of equation (2.5) to match values measured in [2] to represent the steric repulsion between the heads lining the pores [33]. Values taken from the literature for these equations have been measured experimentally where $r_* = 0.5$ nm [2], $E_* = 45$ kT [2], $\gamma = 1.8 \times 10^{-11}$ J/m [2, 34], $\sigma = 10^{-3}$ J/m^2 [2], and $C = 9.67 \times 10^{-15}$ J$^{1/4}$·m [3]. **Figure 2.4** was adapted from [2, 3, 31] and shows the energy functions for these two pore types. From these two overlapping functions, it can be seen that there are two maxima energy radii at r_* and r_d, with an energy minimum at r_m. It may be assumed that a pore of any given radius will take the structure that has the lowest pore energy, which is the lower value of u(r) and w(r), and will be denoted as E(r).

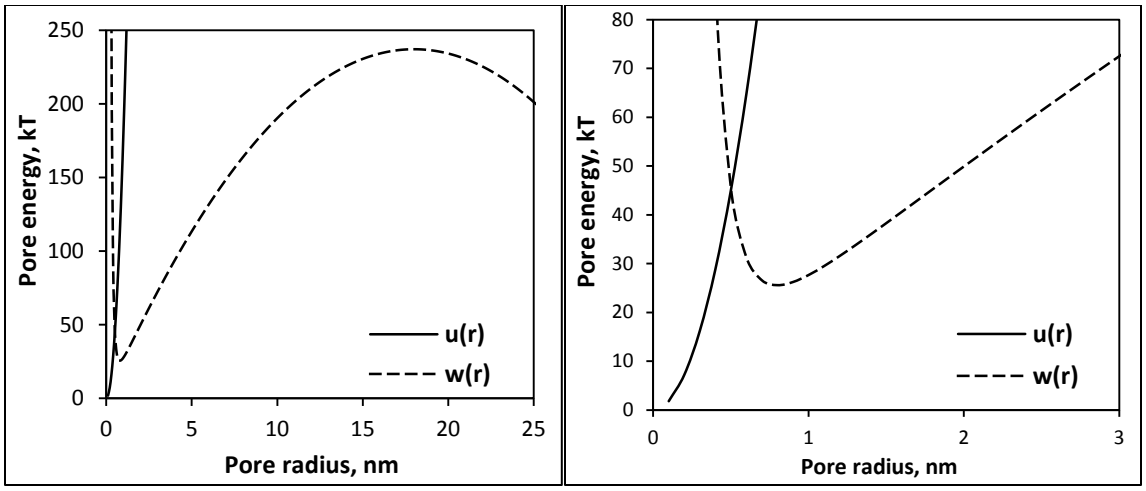

Figure 2.4: Plots of pore energies v. radius for hydrophobic, u(r), and hydrophilic, w(r), pores. Plot (B) shows a zoomed at the transition region. Adapted from [3].

When the transmembrane potential is considered with pore energy, φ(r,t), the pore energy may be calculated by:

$$\varphi(r,t) = E(r) - \pi a_p V_m(t)^2 r^2 \tag{2.6}$$

$$a_p = \frac{1}{2h}(\kappa_w - \kappa_m)\epsilon_0 \tag{2.7}$$

where the second term of equation (2.6) is the capacitive contribution, $V_m(t)$ is the transmembrane potential as it varies with time, h is the membrane thickness, κ_w and κ_m are the dielectric constants of water and the membrane, respectively, and ϵ_0 is the permittivity of a vacuum. Nominal values for these variables in the literature are a_p = 6.9×10^{-2} F·m^{-2} [3].

By accounting for transmembrane potential (TMP), it can be seen that the pore energy will decrease with the square of increasing TMP and pore radii. From **Figure 2.5**, based on [3], it can be seen that for very low voltages (V_m < 0.1 V), this term does not significantly alter the *E(r)* curve. However, as the TMP approaches 0.35 to 0.5 V, the local maximum and minimum radii values (r_d and r_m) integrate and disappear. This allows advantageous pore energies for larger radii hydrophilic pores to form.

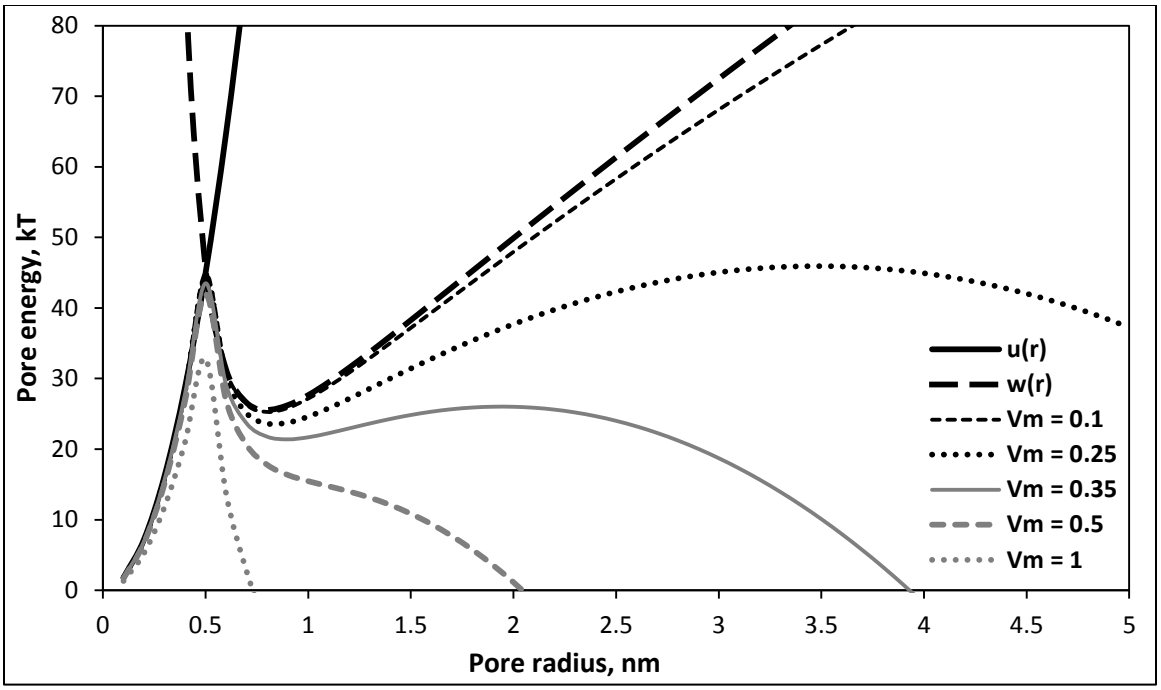

Figure 2.5: Plot of pore energy v. radius for various transmembrane voltages. u(r) and w(r) represent hydrophobic and hydrophilic pores, respectively.

2.3.3.2 Pore Creation

In the literature, it is theorized that pore formation occurs through a two-step process [2, 34-36]. In the first step, all pores are created as hydrophobic pores at a rate determined by their energy. In [3], it is described how the source density for the rate of creation and destruction for these pores with radii between r and $r+dr$ may be calculated according to the equation

$$\mathrm{S}(r) = v_c \cdot h \cdot \frac{U_r}{k \cdot T} \cdot e^{-\frac{U}{k \cdot T}} - v_d \cdot n \cdot H(r_* - r) \tag{2.8}$$

Where

$$U(r,t) = u(r) - \pi \cdot a_p \cdot {V_m}^2 \cdot r^2 \tag{2.9}$$

where the first term is the rate of pore creation, while the second term indicates the rate of pore destruction. In this equation, v_c is the "attempt rate density" [37] ($s^{-1} \cdot m^{-3}$), k is

Boltzmann's constant, T is the temperature, v_d is the frequency of lipid fluctuations, n is the number of pores, and $H(r)$ is the Heavyside's step function to account for the fact that only hydrophobic pores of radius between 0 and the maximum energy radius are destroyed.

These pores are quickly destroyed by lipid fluctuations. However, if hydrophobic pores of radius greater than or equal to the maximum energy radius are created, they will spontaneously convert into longer surviving hydrophilic pores. In this way, it is believed that most hydrophilic pores are created within a small bandwidth of radii slightly above the maximum energy radius, r_*, and then immediately expand to the minimum energy radius, r_m. The change in density of total pores is considered in [3, 38], where the rate of creation of pores with initial radius of r_m is solved for according to

$$\frac{dN}{dt} = \alpha \cdot e^{\left(\frac{V_m}{V_{ep}}\right)^2} \cdot \left(1 - \frac{N}{N_{eq}(V_m)}\right) \tag{2.10}$$

where N is the pore density, V_{ep} is the characteristic voltage of electroporation, α is the creation rate coefficient, and N_{eq} is the equilibrium pore density for a given V_m solved for as

$$N_{eq}(V_m) = N_0 \cdot e^{q \cdot \left(\frac{V_m}{V_{ep}}\right)^2} \tag{2.11}$$

where N_0 is the equilibrium pore density for $V_m = 0$ and $q = (r_m/r_*)^2$. From these equations, the density of pores and their rate of change may be determined.

2.3.3.3 Pore Evolution

Upon creation of the pores described in Section 2.3.3.2, with radii equal to r_m, the pores quickly change size in order to minimize the total energy of the lipid bilayer, W. In [39], it is described that the rate of change of pore radii can be determined by the gradient flow of the bilayer energy

$$\frac{dr_i}{dt} = -\frac{D}{k \cdot T} \cdot \frac{\partial W}{\partial r_i} \tag{2.12}$$

where N is the total number of pores of given radius r_i, and i has integer values from 1 to N. By examining the bilayer energy from equation (2.12), one can determine the total membrane energy and examine how the number of pores at a given radius, r_i, will change with respect to time.

2.3.3.4 Pore Resealing

Upon cessation of an electric pulse, electrolyte flows through any open pores in the cell membrane rapidly depletes the transmembrane potential of the cell. This causes the pores to return to their minimum energy radii r_m, where their configuration returns to that of hydrophobic pores which are then destroyed by the lipid fluctuations according to the second term in equation (2.8), causing the pore density changing rate of equation (2.10) to become negative and decrease the total number of induced pores with a time constant of roughly 3 seconds [2]. As discussed in [39], very large pores with radii much larger than the minimum pore energy radii r_m will not reseal by this mechanism due to the incorporation of other processes such as a change in cell volume [40], the requirement for active exocytotic rebuilding of the membrane [41], or membrane inability to recover from the pores for a variety of reasons such as membrane rupture [35] or loss of homeostasis.

2.3.4 Applications to Electroporation Therapies

Although values vary, previous reports exist for reversible electroporation (RE) occurring at transmembrane potentials of 0.2 to 0.5 V [3] and IRE typically occurs from a transmembrane potential on the order of 1 V [42]. The equation for V_m shows that different cell types of various sizes and shapes may have distinct susceptibilities to IRE treatment. In addition to the electric field, the induction of IRE from electrical pulses has been shown to be dependent on several other factors, including pulse repetition rate, pulse shape and length, number of pulses, and cell or tissue type [11, 17, 43, 44].

2.4 Principles of Bioimpedance

2.4.1 Basic Electrical Concepts

The interaction of biological samples with external sources of electricity may often be broken into behavior that is related to two basic electrical components, resistances and capacitances, that may be arranged and interact in multiple ways. The basic unit of electromagnetic interaction is charge, Q, which has an elementary particle value of ±1.602E-19 coulombs (C) for protons (positive charge) and electrons (negative charge). The total charge of an element is equal to the elementary value multiplied by the number of charges that exist. The relative value of total charge at one location relative to another may be regarded as an electric potential, or voltage (V). Opposite charges have an attractive force while common charges repel, both with a force defined by Coulomb's law. For two point charges, this force is defined by a magnitude proportional to their total charges and inversely related to the square of their separation, r^2, according to the equation

$$F = \frac{Q_1 Q_2}{4\pi r^2 \varepsilon_0} \tag{2.13}$$

where ε_0 is the permittivity of free space, a concept that will be later described in this section. When considering the cumulative force from many charges distributed in a volume, it becomes useful to define an electric field, *E*, a vector to represent the force per unit charge on a charge at any given point. In this way, one may calculate the overall electric field created by superposition of many charges. There exists an electromagnetic coupling where movement of charges will result in the creation of a magnetic field, and conversely, the presence of magnetic fields will induce charge movement [45].

Typical materials and tissues are often electrically defined by their ability to promote or restrict the flow of charges and are known as conductors and insulators, accordingly. The movement of electric charges is referred to as current, *I*, and is defined in amperes (A), or total flow of charge per second ($Q \cdot s^{-1}$).

Facilitated current flow in conductors will have an inherent opposition known as resistance, *R*. For an ideal resistor, its resistance is defined according to Ohm's Law as the electric potential divided by the current flow, with units of ohms (Ω). Resistance is a function of a material's resistivity, ρ, its inherent ability to restrict the flow of charge, as well as the geometry of the electrical setup, defined as a cell constant, K, which is equal to the surface area divided by length of a typical electrical setup of a conductor experiencing an electric potential across its length. The inverse of a material's resistivity is its conductivity, σ, a property that describes the material's ability to transport charge, and is used extensively throughout this dissertation due to its relation to electric fields and Joule heating, two major concepts in electroporation based therapies. Conductivity is an inherent property of a material, so in physical applications multiplying this property by the cell constant to account for the geometry results in a conductance, G. The flow of current through a conductor is known as the conductance current, and is equal to the conductance multiplied by the voltage.

The ability for a material to prohibit the flow of charges will enable it to store or trap charges when experiencing a potential drop on its ends. This ability to store charge is known as capacitance, C, given in units of Farads (F). Capacity is dependent on the geometry of the electrical setup, as with resistance (surface area divided by length), as well as the material's inherent ability to store charge, a property known as permittivity, often defined as a relative permittivity, $\varepsilon=\varepsilon_r \cdot \varepsilon_0$, compared to the permittivity of free space, $\varepsilon_0 = 8.85 \cdot 10^{-12}$ F/m. For a constant applied voltage, the charge will be stored and no net current will occur. However, a change in the applied voltage, such as with an alternating current, will cause the charge on the capacitor to change with the frequency, which will induce a net flow of current equal to the material's capacitance multiplied by the rate of change of the voltage, known as a displacement current.

When one considers a system with a dielectric (insulator) and resistor (conductor) in parallel, the total current becomes a function of the geometry of the setup, the material properties, and the signal frequency according to the equation

$$I(t) = V(t) \cdot \frac{SA}{L} \cdot (\sigma + j\omega\varepsilon) \tag{2.14}$$

where j is √-1, and ω is the radial frequency of the signal $(2 \cdot \pi \cdot f)$. The inherent property of a material's opposition to charge flow that considers both conductance and displacement currents is known as the material's impedance, solved as

$$Z = \frac{1}{G} + \frac{1}{j \cdot \omega \cdot C} \tag{2.15}$$

when the material considered is biological, this property is known as bioimpedance [45].

2.4.2 Tissue Behavior without Electroporation

2.4.2.1 Equivalent Circuit Model of a Cell

When analyzing the electrical properties of a cell in suspension or tissue, an equivalent circuit model can be constructed to represent the primary constituents. The extracellular and intracellular fluid may be regarded as solutions containing ionic electrolytes, giving them properties of charge carrying resistances. These solutions are separated by a lipid bilayer cell membrane, which may be regarded as a dielectric capacitance. The membrane is selectively permeable to certain ionic species, giving it a very small membrane conductance which may be considered to be in parallel with the capacitance. This equivalent circuit may be seen in **Figure 2.6**. Treating the membrane as a capacitor and resistor in parallel is known as a Debye-type system [45, 46]. A frequency dependent admittance may be determined as the inverse of the impedance, which may be solved according to the equation:

$$Y = G + j\omega C \tag{2.16}$$

where G is the conductive component, j is the imaginary number, √-1, ω is the radial frequency, 2 π *f*, and C is the capacitive component. G and C are based on the geometry of the measurement taken and are equal to:

$$G = K \cdot \sigma \tag{2.17}$$

$$C = K \cdot \varepsilon_0 \varepsilon_r \tag{2.18}$$

where K is the geometric scaling cell constant, σ is the conductivity (inverse of the resistivity, of units S/m), ε_0 is the permittivity of free space (8.85 x 10^{-12} F/m^2), and ε_r is the relative permittivity of the dielectric. As described in section 2.4.1.1, when the geometry of the cell is an isolated sample connected by two plates completely covering opposite ends of the sample, the cell constant may be calculated as the surface area of the sample divided by its length (SA/L).

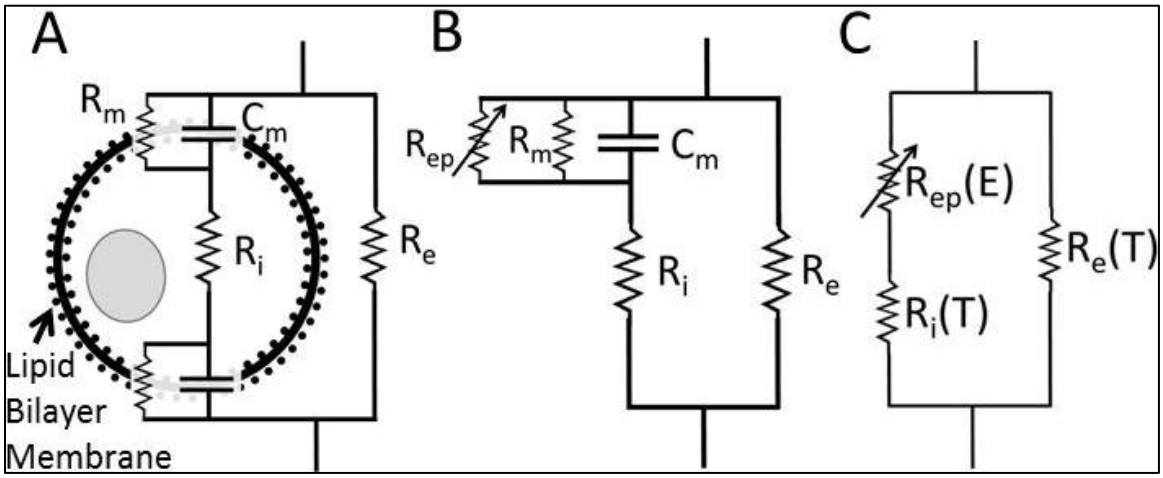

Figure 2.6. Equivalent circuit diagrams. (a) Basic circuit model of a cell. (b) Circuit model including parallel electroporation resistor. (c) Equivalent circuit when membrane ignoring capacitance (low frequency) and membrane resistance (R_m approaches infinity).

Although currents do not directly flow through capacitances, they can conduct displacement currents at high frequencies, where the rate of change of voltage produces a displacement current equal to:

$$I = C\frac{dV}{dt} \tag{2.19}$$

where I is the current, t is time, and V is voltage. From this equation, it can be seen that when the rate of voltage change is high, the displacement current through a capacitor becomes larger. According to equation (2.19), it can be seen that at high frequencies, this

capacitive component of the admittance will dominate, and it behaves as a short circuit to the current flowing through it. Alternately, at low frequencies, the capacitive term becomes small and the conductive component of the circuit dominates the flow of current.

When these equations are applied to the equivalent circuit model of a cell in suspension, at high frequencies the displacement currents through the capacitive component of the cell membrane will be large and it will behave as a short circuit. Therefore, the equivalent resistance for the circuit becomes:

$$R_{eq} = \frac{R_e R_i}{R_e + R_i} \tag{2.20}$$

However, as the frequency approaches 0 Hz, the capacitor will not allow significant admittance and behave as an open circuit. Therefore, to go through the cell, all current must flow through the relatively high resistance membrane. This causes most of the current to flow around the cell in suspension or through the interstitial space in tissue, and the equivalent resistance to the flow of charge will equal:

$$R_{eq} = \frac{R_e \cdot (R_i + R_m)}{R_e + (R_i + R_m)} \approx R_e \tag{2.21}$$

2.4.2.2 Frequency Dependent Properties - Dispersion

The above mentioned behaviors will hold and may be simply calculated for materials with constant properties. However, most materials, especially biological tissues, exhibit electrical properties that are frequency dependent, a variation known as dispersion [46]. For most biological tissues, there are three major processes involved, resulting in three independent dispersions [47, 48]. Although these dispersions will occur over independent frequency ranges and vary between tissues, they may be roughly lumped together. The first, known as α dispersion, occurs at frequencies below 10 kHz, is generally regarded to be caused by diffusion processes of ionic species and the counterion polarization along cell membranes, resulting in a sharp decline in permittivity.

Increasing the frequency into the MHz range, β dispersion is experienced, which is associated with interfacial polarization of cell membranes and their interaction with the intra- and extra- cellular electrolyte charges, essentially resulting in a short circuit across the Debye-type membrane capacitor. Further contributions for the β dispersion may be attributed to polarization of proteins and other organic macromolecules. At frequencies reaching the GHz range, polarization of small molecules and water content in the tissue result in γ dispersion.

Dispersions in Debye-type resistor and capacitor elements in parallel may approximate the relaxations for biological tissues. Due to the complex nature of biological materials and their differences from ideal resistors and capacitors, especially the varying width for each dispersion frequency range, an empirical equation known as the Cole-Cole response may be used to represent the dielectric properties and dispersions [46] according to the equations

$$\varepsilon_r{}^* = \varepsilon_\infty + \frac{(\varepsilon_1 - \varepsilon_\infty)}{[1 - (j \cdot \omega \cdot \tau)^\alpha]} - j \cdot \frac{\sigma_0}{\omega \cdot \varepsilon_0} \tag{2.22}$$

$$\sigma^* = \sigma_\infty + \frac{(\sigma_0 - \sigma_\infty)}{[1 - (j \cdot \omega \cdot \tau)^\alpha]} \tag{2.23}$$

where ε_∞ and σ_∞ are the permittivity and conductivity at a frequency well above the frequency, while ε_1 and σ_0 are the permittivity and conductivity at frequencies well below the dispersion, τ is the time constant ($1/(R \cdot C)$), and α is an arbitrary parameter that varies depending on the material, that expands the expansion as α becomes smaller.

2.4.3 Electroporation Effects on Cell and Tissue Properties

It has been shown that increasing the transmembrane potential lowers the required energy for the creation of nano-scale hydrophilic pores [3]. Though the values vary, this is believed to occur for transmembrane potentials between 0.2 and 1 V [10, 49]. These nano-scale defects in the cell membrane locally eliminate its selective permeability, allowing the flow of water and ions through the pores, therefore locally removing its

dielectric properties. This acts as a local short circuit at the defect in the membrane. As the number and size of the pores increase, this dielectric breakdown will also increase, and the membrane's resistance to current flow will decrease, thus increasing the effective conductivity of a cell in suspension or in tissue. It has been shown that the size and number of pores may be related to the strength of the transmembrane potential [39]. The inclusion of electroporation's effects may therefore be modeled as a variable resistor dependent on the transmembrane potential, $R_{ep}(V_m)$, put in parallel with the cell membrane, as seen in **Figure 2.6B**. The equivalent resistance to current flow therefore becomes

$$R_{eq} = \frac{R_e \cdot (R_i + \frac{R_m R_{ep}}{R_m + R_{ep}})}{R_e + (R_i + \frac{R_m R_{ep}}{R_m + R_{ep}})} \tag{2.24}$$

When the transmembrane potential is low, $R_{ep}(V_m)$ is very high, and the equivalent resistance approaches R_e, as shown in equation (2.21). However, as the transmembrane potential increases at a given point, $R_{ep}(V_m)$ approaches zero, and the membrane behaves as a short circuit, allowing the equation to reduce to that shown is equation (2.21). Because the shape and size of the cell will not dramatically change in the presence of an electric field, the decrease in resistance may be correlated with an increase in the electric field. This allows one to model the variable resistor and determine the effective conductivity of a cell in suspension or in tissue as a function of the electric field to which it is exposed σ(E). The behavior of a single cell in suspension or tissue may be scaled up to represent an entire system of cells in tissue using an identical equivalent circuit [50]. Therefore, the macroscopic electrical behavior of tissue where the number of electroporated cells and degree of electroporation (number and size of the pores) may be modeled as a system in which the bulk conductivity is dependent on the variable resistance component.

Chapter 3: Previous Work with Electroporation

3.1 Introduction

The ability to use electric fields and electric pulses to manipulate cells has been understood in very basic form since as early as the 18th century. However, discerning an explanation for the ability of a pulsed electric field to kill a cell in a non-thermal manner by manipulating the transmembrane potential took up until as late as the 1960's. Since then, the ability to produce electroporation without killing the cell has been discovered. Electroporation has subsequently been harnessed in therapeutics using a variety of pulse protocols to act by various remedial mechanisms both alone and in congruence with adjuvant macromolecules. In this chapter, some of the early work with electroporation is described, followed by explanations of some of the more common methods currently being used or investigated to utilize electroporation therapeutically. Descriptions of the previous work with electroporation based therapies include work from the early experimental in vitro, ex vivo, and in vivo phases of development through to preclinical and clinical use of therapeutic electroporation applications.

3.2 Background

3.2.1 Conventional Ablation Techniques

The focus of this dissertation work is to develop IRE into a better described, reliable therapy for the treatment of local disease through focal non-thermal destruction of the cells. Although some applications of electroporation, such as electrogenetherapy, target more systemic purposes, such as muscle-derived insulin production for Type I diabetes, the common objective of most electroporation based therapies is to treat a targeted volume of tissue. In this section, a brief description of conventional ablation techniques is provided.

Most focal ablation techniques rely on the use of thermal energy to destroy cells. Apart from cryoablation, the most commonly used thermal therapies, including radiofrequency ablation (RF), microwave hyperthermia, laser interstitial thermal therapy

(LITT), and high intensity focused ultrasound (HIFU) involve heating the tissue. Although their method of delivering thermal energy to the tissue varies, there is a commonality in the mechanisms and objectives of these techniques. For most thermal therapies, the desired temperature range is 50-100°C [51], a range high enough to induce cytotoxicity within minutes (50-52°C) [52] to nearly instantly (60-100°C) [53]. For percutaneous delivery methods, the heating will be greatest near the probe where the energy density is highest. The elevated tissue temperatures cause coagulative necrosis of the affected tissue.

In radiofrequency ablation, a single or array of electrodes are inserted into the targeted region of an anesthetized patient. A continuous radiofrequency signal of alternating current between 460 and 550 kHz is delivered into the tissue, using resistive Joule heating from ionic agitation to elevate the tissue to a temperature of around 100°C for a period of 10-15 minutes [54]. Oftentimes, only a single-pole energized probe is inserted into the tissue, while a patch connected to ground is attached to the skin. An additional electrically based thermal therapy is one that uses microwave hyperthermia, which delivers energy through an inserted probe and operates at the 27 MHz to 2.45 GHz range and heats the tissue by friction as polar molecules attempt to align with the magnetic field [51]. In addition to using the microwave energy to heat the tissue to the point of coagulative necrosis, microwave hyperthermia can also achieve therapeutic effects by elevating the temperature of the tissue to 43-45°C for an extended period of time, often on the order of hours [55]. The frequency of microwave used will alter its depth of penetration into the tissue [51].

Thermal therapies can operate on the deposition of energy from other sources than electricity, including light and sonic vibration. In LITT, thin optical fibers are inserted through needles inserted into the targeted region of tissue. The fibers transmit intense light into the tissue, which is absorbed and converted to heat [51]. As with microwave hyperthermia, the frequency of light waves used in the laser will alter the heating penetration characteristics of the therapy in the tissue [51]. A final thermal therapy in clinical practice uses ultrasound energy, delivered either through a probe inserted into the diseased tissue, or using HIFU, where ultrasound waves are delivered across the skin and

focused at a targeted location to achieve their tissue heating effects, permitting noninvasive therapy delivery.

Unfortunately, high temperature thermal ablation techniques can present complications including inconsistencies between the predicted and true cell death regions [56], thermal dissipative properties (the blood perfusion "heat sink" effect) of vascularized tissue [51], charring at the electrode interface [57], required treatment depth of at least a 1 cm to prevent skin injury [58, 59], and the production of significant scar tissue [60], reducing accurate follow-up.

In addition to thermal ablation techniques that rely on increased temperature to achieve cell death in the targeted region, there is also a thermal therapy that cools the tissue known as cryoablation, which kills the cells through a variety of processes, including the formation of ice crystals within cells which disrupts membrane integrity, vascular occlusion, and induction of apoptosis [61]. Cryoablation involves the placement of a single or array of hollow needle probes with typical diameters of 2.4-3 mm [60, 62] placed into the targeted region while the patient is under local anesthesia. The probes are then actively cooled through techniques such as the circulation of argon gas to achieve probe temperatures of -160°C [63]. The low temperature probe creates an ice ball starting at the probe that rapidly grows to engulf the tumor, which is then either actively or passively cooled [63]. Typical cryoablation procedures undergo a series of freeze and thaw cycles, with treatment times taking approximately 30-40 minutes [62]. As with hyperthermic techniques, there are several limitations to cryoablation therapy including inconsistency between the visualized ice ball and cell death regions [63], vascular "cold sink" effects, and the production of scar tissue [60].

An ablation technique that is beginning to be investigated uses high energy pulsed ultrasound waves delivered across the skin to kill cells by causing cavitation to shear the cells in a technique called histotripsy [64, 65]. The goal for histotripsy is to achieve cell death from the ultrasound without inducing thermal damage to the tissue, as with HIFU.

3.2.2 Early Use of Electroporation[1]

It is difficult to discern when IRE was first observed. The literature suggests that the initial studies could have been as early as the 18th century [66-70]. However, it was not until 1967 that Sale and Hamilton demonstrated the non-thermal lethal effect of high electrical fields on organisms [14, 71-73]. They concluded that the damage to the cell membrane occurs when the trans-membrane voltages of around 1 V are reached. This result (threshold) is based on the theoretical potential of an insulating sphere in a conducting medium in an analysis that has become a classic in the field of electroporation [14, 71-73].

For decades, IRE has been studied extensively within *in vitro* cellular systems, in particular the food industry for sterilization and preprocessing of food [74, 75]. IRE has also been considered an effective means to destroy both gram positive and gram negative bacteria and amoebae with regards to water decontamination for biofouling control [76-79].

Another context in which IRE has been studied is in the delayed cell damage in high-voltage accidents [80, 81] and the post-electric-shock arrhythmias during defibrillation [82]. Lee *et al.* showed that electrical injury is attributed to thermal damage as well as IRE in superposition [80, 81]. It had also been observed in medical applications involving thermal ablation using electrical fields, that the electrosurgical tools also induce electroporation and that coagulation may be due to electrofusion of the membranes [83].

IRE is currently being studied as part of a family of non-thermal methods to ablate tissue with electrical pulses, which includes electrochemotherapy (ECT) [84-89] and supra-poration [89-92]**.** ECT is a relatively new minimally invasive tissue ablation technique that employs reversible electroporation pulses to facilitate the penetration of small amounts of non-permeant or low-permeant drugs, such as bleomycin or cisplatin,

[1] This section reprinted with permission from NOVA Science Publishers, Inc. from: Non-thermal irreversible electroporation for tissue ablation, in Electroporation in Laboratory and Clinical Investigations, Enrico P. Spugnini and A. Baldi, Editors. 2010, Nova Science: Hauppauge, NY. Authors: Garcia, P.A., R.E. Neal II, and R.V. Davalos.

into cells. A major advantage of ECT is that it selectively kills only the dividing tumor cells. In tissue ablation, ECT is a safe and highly efficient method to introduce non-permeable cancer drugs into malignant cells and is currently used to treat cutaneous and subcutaneous tumors in humans [84, 86, 89, 93-95]. This method does; however, require the combination of chemical agents with an electric field, which IRE does not.

Supra-poration is achieved by means of nanosecond electrical pulses in the tens of nanoseconds range and field strengths of 40-80 kV/cm [89-91]. In supra-poration, cell death is not a consequence of the irreversible cell membrane permeabilization as in IRE, but the probable result of Ca^{2+} ions released inside the cells [89, 91]. R. Nuccitelli *et al.* [96] described antitumor effects in mice using this technique.

3.3 Electrogenetherapy (EGT)

When the energy regime employed in electroporation therapies is sub-lethal, exploitation of the cell's increased permeability may be used therapeutically to facilitate increased macromolecule transport to introduce drugs into the cell's interior. Electroporation has been used to facilitate the delivery of genetic material into cells, including DNA and RNA, which is known as electrogene transfer. When therapeutic genetic materials are introduced into cells to target a disease, it is known as electrogenetherapy (EGT). Optimization of pulsing protocols shows that the greatest transfection efficiency with low mortality occurs when a brief initial pulse to initiate pore formation, similar to IRE and ECT, is followed by a series of lower amplitude, longer pulses to electrophoretically drive the movement of genetic material into the cell. Using electric pulses to move large genetic material into cells is a technique whose application has become widespread *in vitro*. In addition, its potential implications *in vivo* present several advantages. These include the avoidance of viral vectors, high transfection efficiency with functionally permanent long-term expressions of the genetic material, and precise and predictable transfection. When targeted at cells with a long lifetime, such as muscle cells, very long-term expression increases are possible. Envisioned applications of EGT include the required genetic instructions for the creation of proteins that are deficient in the propagation of various diseases, the production of cytokines and antigens

for the treatment of tumors and cancer cells, as well as a cheap, stable alternative to vaccine production that will not expire and require cold shipment [97, 98].

3.3.1 In Vitro

The initial reports in 1982 using electroporation-mediated biophysical transport used electric pulses to achieve in vitro transfection of DNA [99, 100]. This technique rapidly became one of the most widely used methods for introducing DNA into bacteria, animal and plant cells, and yeast [101]. There a currently a wide variety of applications for EGT in studying the effects of genes and gene therapy by studying the effects on cell gene expression and phenotypic effects [102].

3.3.2 Ex Vivo and In Vivo

Electrogenetherapy experiments have been performed on animals ranging from mice to primates [103-105]. The applications for these experiments include treating anemia, autoimmune diseases, myocarditis, dystrophin, motor neuron diseases, liver injury, diabetes, muscle injury, arthritis, and cancer [103]. In treating autoimmune diseases such as Type I diabetes, diabetic mice treated with intramuscular EGT for the insulin gene survived up to 10 weeks, while controls survived only 3 weeks [106]. Some immune suppressing EGT has been attempted for autoimmune diseases such as the use of IL-10 gene to reduce the production of inflammatory cytokines that damage the heart via myocarditis. Intramuscular EGT for the IL-10 gene was found to increase IL-10 expression and inhibit the expression of inflammatory molecules, increasing the 14 and 21 day survival rates for mice by 50 and 40%, respectively [107]. One concern for using such immune-suppressing gene therapies is the potential overexpression of the genes resulting in a compromised immune system, leading to increased chances of infection and other severe diseases such as malignancy. In targeting motor neuron degeneration, *in vivo* studies showed a therapeutic effect equal to that attained with adenovirus, demonstrating the power of EGT as a non-viral vector for gene therapy [108]. It is also worth mentioning that EGT based tumor therapies are being tested for small interfering RNA molecules that will silence the expression of oncogenes, where *in vivo* experiments have

shown the ability of electroporation-mediated transfection of these RNA molecules to silence genes of solid tumors in mice [109].

The treatment of cancer with EGT has been performed predominately using IL-12 plasmid [110]. Interestingly, intramuscular EGT increases gene expression by 2-3 orders of magnitude [111], while intratumoral EGT may increase gene expression by 50-100 times [112]. The mechanism of action of IL-12 is not fully elucidated, but it is known to promote an increase in tumor infiltration of T cells, which leads to cytolytic behavior, and inhibit angiogenesis, which causes a reduction in microvascular density. The first investigation of electrogenetherapy for cancer used intratumoral injection of IL-12 in mice followed by the application of ten, 375 V/cm pulses with durations of 50 ms [113]. The targeted hepatocellular carcinoma was significantly inhibited along with a noticeable reduction in growth of distant, non-treated tumors. Since this initial study, IL-12 EGT has been performed successfully in other experimental tumor models, such as renal [114], colon [114] and breast cancer [115]. Additionally, preclinical studies have been performed on canine mast cell tumors treated with IL-12 EGT [116] and equine sarcoid treated by a combination of ECT with cisplatin and EGT with IL-12 [117]. All results provided evidence a good antitumor effect.

3.3.3 Clinical

The primary obstacles to be considered and overcome when translating the preclinical findings into the clinical setting include developing a strategy to avoid the generation of an immune response which may neutralize the therapeutic efficacy, being able to reliably control the level of gene expression in a large animal system, and controlling the duration for expression of the genes. These key marks were met in 2008, when a Phase I trial of IL-12 based EGT was performed in patients with metastatic melanoma [118]. This dose escalation study utilized plasmid concentrations of 0.1 to 1.6 mg/ml and 6, 1300 V/cm pulses with durations of 100 μs. According to the Response Evaluation Criteria in Solid Tumors (RECIST), two of 19 patients with non-targeted distant lesions showed complete regression of all metastases, and eight other patients

showed disease stabilization. This exciting result proved safety and efficacy of IL-12 mediated EGT, which will pave the way for future studies.

3.4 Electrochemotherapy (ECT)

After showing the ability to introduce DNA into a cell's interior with electric pulses, other nonpermeant molecules were attempted and shown to be able to enter the cell better with the assistance of electroporation. Of particular interest for electroporation-enhanced cellular uptake was that of chemotherapeutic agents. This technique, primarily focused at targeting cancer cells with improved chemotherapy response, has been used *in vitro* and *in vivo* [119-121].

3.4.1 In Vitro

There have been a variety of in vitro investigations to determine optimum drugs and pulse parameters for use in ECT [10, 122-127]. It was found that many chemotherapy molecules that were more permeant achieved minimal cytotoxic enhancement from electroporation [125]. Conversely, chemotherapy drugs that were less permeant, such as large and hydrophilic drugs, for example platinates and bleomycin, were found to attain improved cytotoxicity [124]. This was especially true for bleomycin, a drug with very high intrinsic toxicity, requiring only several hundred molecules to enter a cell to kill it. However, it is a very large molecule, with a molecular weight of roughly 1,400 daltons, and is hydrophilic, making it very difficult to enter the semi-permeable cell membrane. In fact, the conventional method for bleomycin entry into the cytosol is through receptor-mediated endocytosis [128]. However, it was found that combining bleomycin with electroporation pulses resulted in improved dosing toxicity by as many as 5 orders of magnitude [124, 127]. This discovery has led to a field of medicine for tumor treatment known as electrochemotherapy, where drugs are delivered either intravenously or intratumorally, followed by electric pulses delivered through electrodes in the targeted location [10, 44, 129]. In addition to in vitro and in vivo applications of reversible electroporation for intracellular transport of nonpermeant molecules, the ability to permeabilize the stratum corneum of the skin has led to the development of elecroporation-facilitated transdermal drug delivery for water soluble molecules [130].

3.4.2 In Vivo and Ex Vivo

Electrochemotherapy has undergone an array of pre-clinical experimental and spontaneous tumor studies [131]. In experimental implanted tumors, studies were carried out for various cancer types on mice, rats, hamsters, and rabbits. The drug under investigation was first allowed to perfuse through the circulatory system and/or diffuse throughout the tumor tissue. Following the time for effective drug transport, which is on the order of 10 minutes depending on the route of administration, electrodes were placed near or within the tumor either percutaneously or subcutaneously, and a series of pulses were applied. The typical pulsing protocol used was 8 pulses, each 100 μs long, at a rate of 1 pulse per second with a voltage-to-distance ratio of 1300 V/cm. The pulsing parameters used were found to have no antitumor effectiveness on their own and cause no adverse systemic effects. These studies establish that drug doses below those needed for antitumor effectiveness alone were able to produce complete regressions in nearly 80% of the subjects treated when the pulses were added. The drugs were administered via intravenous or intratumoral injection at doses low enough to prevent any observable systemic effects [131, 132].

In addition to experimental tumors, veterinary patients presenting spontaneous tumors were also treated with ECT to determine its therapeutic efficacy in human and animal patients [131, 132]. Patients studied include canines, felines, and equines, with the first study conducted in 1997 on 12 feline patients using intravenous bleomycin on large soft tissue sarcomas that had relapsed after conventional treatment [133]. Following this study, others were carried out that successfully treated the patients using ECT with intratumoral cisplatin and bleomycin [131].

3.4.3 Clinical

The first clinical trials using ECT were performed in 1991 [134], which used intravenous injection of bleomycin followed by electric pulses for patients with permeation nodules of head and neck squamous carcinomas. Over the following decade, the technique was applied for a broad range of superficial tumor varieties, using either bleomycin or cisplatinum injected either intratumorally or intravenously over a single or

multiple treatment sessions. These trials included more permeation nodules of head and neck squamous carcinomas and salivary breast adenocarcinoma, where antitumor response was observed with high patient tolerance of the therapy [135-137]; basal cell carcinomas where 99% of the nodules treated remained in complete regression 3 years after treatment [138]; oral cavity squamous cell carcinomas where half of the 10 tumors treated less than or equal 4 cm in diameter achieved complete regressions at 40 weeks [139]; a case study on bladder transitional cell carcinoma metastases, where 14 of 17 metastases on the skull completely disappeared and the remaining 3 contained no living cells [140]; and malignant melanomas using cisplatinum instead of bleomycin on malignant melanomas, where the addition of electroporation was found to induce a greater response index in the largest nodules relative to cisplatinum therapy alone [141]. These trials and several others carried out later were followed by a prospective non-randomized multi-institutional ESOPE (European Standard Operating Procedures of Electrochemotherapy) study [142]. Treatment response was characterized according to tumor type, drug used, route of drug administration, and type of electrode used. This study found objective and complete response rates of 85 and 74%, respectively, regardless of tumor histology, drug or route of administration. Overall, the clinical studies present encouraging results for ECTs ability to treat superficial tumors in patients.

3.5 Nanosecond Pulsed Electric Fields

In addition to conventional electroporation based therapies that use pulses with durations on the order of microseconds to target the plasma membrane, nanosecond order pulses of amplitudes about an order of magnitude higher than IRE, ECT, and EGT protocols have been shown to have an intracellular effect [91, 143]. Briefly, the charging time constant of the plasma membrane is determined by the geometric and dielectric properties of the different cellular regions. Typically the charging time is ~1 μs [144], and the time to reach steady state is approximately three times this value [145]. While the plasma membrane is charging, intracellular organelles and the nucleus are also exposed to electric fields. Additionally, due to their smaller size, these intracellular structures typically charge faster than the plasma membrane but require greater electric fields strengths to induce a critical TMP for pore formation. As opposed to IRE, ECT, and

EGT, the electronics required to generate nsPEFs are not commercially available [145], and their design and production requires expertise in electrical engineering. Despite this challenge, it has been shown that nsPEFs offer certain advantages over conventional electroporation protocols. For example, nsPEFs reduce the potential for muscle contractions during treatment [146] and reduce the dependence of electroporation on cell size [143, 147], resulting in more homogenous outcomes in heterogeneous systems.

3.5.1 Preclinical – In Vitro and In Vivo

In the treatment of cancer, nsPEFs have been found to result in the destruction of tumor cells both *in vitro* and for *in vivo* tumor models [148-150]. Pulse effects have been linked to cell necrosis and apoptosis [151, 152]. Other *in vivo* studies have focused on melanomas and other superficial tumor models which can readily be accessed with electrodes. One study, which used 300 pulses at 40 kV/cm each lasting 300 ns, showed complete tumor remission in the 17 nude mice treated. The pulses were found to increase plasma membrane permeability to very small molecules as well as cause an increase in intracellular calcium, promote DNA fragmentation, and disrupt the tumor's blood supply. Additional preclinical studies in another melanoma model to optimize treatment protocols found that using a single treatment of 2000 pulses, each 100 ns long at an electric field of 30 kV/cm and a rate of 5-7 pulses per second was the optimal protocol and was able to eliminate 17 melanomas in 4 mice without raising skin temperature above 40°C [153]. Studies have also been conducted on *in vivo* tumor models for a variety of other cancerous cell lines, including pancreatic cancer, where responses were seen in 4 of 6 treated tumors, with 3 complete responses [148].

3.5.2 Clinical

In addition to preclinical experimental determinations on the effects of nanosecond pulsed electric fields, a human subject treated his own basal cell carcinoma and observed a complete pathologic response [148].

3.6 Irreversible Electroporation

3.6.1 In Vitro

As discussed in Section 3.3, IRE has been studied and used *in vitro* for a variety of applications, such as sterilization. The first studies to examine IRE with the objective of treating cancer cells examined the effects of electric pulse parameters and the cell death mechanisms [154, 155]. In addition to these studies, *in vitro* experiments have continued to be performed to examine how potential IRE electric field thresholds may vary for different cell lines and applications and how these thresholds will change with different pulsing and physical conditions, as well as continued work examining what cell death mechanisms may play a role in IRE therapy [155, 156].

3.6.2 Ex Vivo and In Vivo

After being shown to be a theoretically feasible non-thermal focal ablation technique in 2005 by Davalos, *et al*. [157], the first *in vivo* study with to investigate this objective was carried out by Edd, *et al*. [158]. This study placed two plate electrodes on opposite sides of a rat liver and delivered a 20 ms long square wave pulse with a voltage-to-distance ratio of 1000 V/cm. Animals were sacrificed 3 hours after pulsing, and the tissue was perfusion fixed. Numerical simulations calibrated the lesion IRE thresholds to range between 300 and 500 V/cm, and histological examination showed cellular-scale resolution between treated and unaffected cells, with nearly indistinguishable cell borders in the treated areas. The large vessel architecture remained intact. It also showed endothelial necrosis and congestion in the treated region, subjecting any surviving cells in the treatment region to be subject to ischemia.

The vascular effects of the pulses were further explored by Maor, *et al*. [159-161]. These studies investigated the ability to use IRE for tumor ablation in close proximity to vasculature, a limitation of thermal focal ablation techniques. It used plate electrodes to apply 10, 100 µs long pulses of 3800 V/cm in one second to exposed rat carotid arteries. Rats were sacrificed and the tissue fixed at several timepoints up to 28 days after the

procedure. Overall the treated vessels showed preserved endothelial cells of the internal lamina, with a progressive decrease in vascular smooth muscle cells in the tunica media.

Investigation of the immune system's interaction with IRE was carried out for healthy tissue and tumors [5, 6, 15, 16]. In these studies, cutaneous implanted murine tumors and healthy tissue were exposed and pulsed using plate electrodes. For the tumor study [15], tissue samples were collected for immunohistochemistry and it was found that T-lymphocyte levels were highest prior to treatment, and rapidly declined within the first 6 hours after pulsing. The authors conclude that the mechanism of necrosis occurs independent of the immune system and may therefore be a suitable treatment option for immunocompromised patients. In addition, immune responses over longer time points were investigated in large animal models. In [6], porcine livers were subjected to IRE pulses. By 24 hours, there was an increase in inflammatory cells and signs of drainage by the regional lymph nodes. These findings were consistent with observations from lesions produced in canine prostates [5]. In [16], porcine liver tissue 24 hours after treatment showed that the ablated regions contained calcium deposition, were positive for the BCL-2 apoptosis marker, and showed sinusoids congested with neutrophils and eosinophils. The study performed in canine patients also showed great potential for the application of IRE in the treatment of benign prostatic hyperplasia [5].

Studies experimentally investigating the ability for IRE to effectively treat tumors have been carried using implanted tumors in a murine model [162-164]. In the first study by Al-Sakere *et al*. [162], a murine sarcoma cell line was used to grow cutaneous tumors in mice. TUNEL staining showed increased DNA double strand breaks suggesting apoptosis. Additionally, observed vascular occlusion may indicate additional hypoxia-induced tumor cell death. Tumors subjected to a protocol of 80 pulses of 2500 V/cm, each 100 μs long and separated by 3.3 seconds, showed complete regression in 12 of 13 cases. In a second study performed by Neal *et al*. [164], MDA-MB-231 human mammary carcinoma cells were grown into tumors othotopically within the mammary fat pad of mice. A total of 100 pulses ranging between 1300 and 1100 V were delivered through a single, bipolar electrode, each lasting 100 μs and separated by 3 seconds. Complete regression was achieved in 5 of 7 experimental tumors. In a third study by Guo *et al*.

[163], the N1-S1 rap hepatoma cell line was used to induce tumors in the left medial lobe of the liver in Sprague-Dawley rats. They were treated using eight 2500 V square wave pulses, each 100 μs long at a rate of 1 pulse every 100 ms. They found significant tumor volume reductions within 7-15 days post-therapy using MRI and histology.

3.6.3 Pre-Clinical and Clinical

There have been several pre-clinical trials on animal patients, two of which may be found in [165, 166]. One patient had a non-resectable forebrain malignant glioma [166]. This 12-year old canine presented with rapidly progressive neurological deterioration due to the growth of his tumor. IRE was performed at the time of biopsy for the patient based on treatment parameters derived from treatment planning numerical models and preliminary data on IRE in normal brain [167, 168].The IRE ablation procedure resulted in nearly complete resolution of focal neurological dysfunction within one week of the procedure. An MRI scan of the brain, performed 48 hours after the IRE, demonstrated a 75% reduction in tumor mass. The canine patient subsequently received adjunctive fractionated whole-brain radiotherapy for 4 weeks following N-TIRE therapy (50 Gy, delivered in 20 fractions of 2.5 Gy each). The patient was in complete remission 4 months after IRE therapy, based on serial MRI and neurologic examinations. An additional canine patient (6-year old, spayed female Labrador Retriever) has been reported on in [165]. The patient presented a large soft tissue sarcoma (high grade histiocytic sarcoma) on the inner aspect of the thigh and groin, as outlined in Section 8.2.1. The tumor was causing sciatic neuropathy, and compartmental syndrome-associated pain. Its proximity to vital nerves and vasculature made it unresectable and thermal therapies would have also damaged these vital structures. IRE was performed with 3 electrode insertions, and a 52% reduction in tumor volume was observed within 8 days, as well as improved mobility and no further need for pain medicine. The great response resulted in the use of systemic chemotherapy (four cycles of CCNU, 65 mg/m^2 every 21 days), until the tumor developed resistance to the chemotherapy. A second application of IRE to an originally untargeted region of the tumor was performed to eliminate the remainder of the tumor. Findings from this study include the ability for IRE to remain effective to cancer cells that have developed resistance to chemotherapy as well

as muscle cell sparing at the tumor boundary as observed by serial biopsies taken at the margin. Electrophysiological evaluation revealed small decreases in the amplitudes of the distal compound muscle action potentials, which returned to pre-IRE values 2 weeks after treatment. By four months post-diagnosis, the cancer was considered in remission, and remains in complete remission based on follow-up examinations currently 12 months after the original diagnosis.

In addition to the promising pre-clinical case studies using IRE to treat more delicate and complex varieties of tumors, there are several early stage human trials that have been conducted. These include a phase 1 safety trial on various localized tumors with incurable malignancies [169, 170]. One interesting result was the nearly complete absence of post-ablation pain. Biopsies one month after surgery showed preservation of tissue structure with coagulative necrosis of the cells. For the lung, it was proven safe, but pneumothorax was almost inevitable. The primary aim of the study was to determine the safety of IRE therapy at various organs in the body for patients' refractory to alternative therapies. However, complete tumor ablation verified by CT was achieved in 46 of the 69 tumors, a success rate of 66%, with most failures occurring in renal and lung tumors [169]. A separate report from this study discusses patient anesthesia considerations, including the need for general anesthesia, a neuromuscular blockade, careful patient positioning for CT-guided therapies, and the use of an ECG synchronizing system to prevent arrhythmias [170]. Overall, this safety study showed the ability to use IRE safely in treating a variety of tumors located throughout the body.

3.7 Conclusion

Effective therapy for localized disease, such as tumors, can be treated through a variety of focal techniques. There is a variety of focal ablation techniques that rely on thermal energy to kill cells in a targeted region. Advances in new techniques based on the non-thermal delivery of electric pulses, namely ECT, IRE and supra-poration, have inherent advantages and disadvantages for tissue ablation. It is likely that each will find appropriate uses in modern medicine, separately or in combination.

Chapter 4: Feasibility of Irreversible Electroporation in Heterogeneous Systems[2]

4.1 Introduction

The previous chapter described how numerical modeling can be used to predict treatment outcomes by simulating electric field and temperature distributions in tissue for a given treatment protocol. In addition, it briefly mentioned how these distributions are dependent on the conductivity distribution of the tissue, adding substantial complexity to planning treatments in heterogeneous tissues. **Here, we theoretically test our hypothesis that the advantages from IREs unique non-thermal mechanism to induce cell death may prove IRE to be an effective surgical modality for the treatment of certain breast carcinomas and other heterogeneous tissues.** The aim of this chapter is to investigate if it is possible to treat a tumor in a heterogeneous environment where the entirety of the tumor is treated by IRE without inducing significant thermal damage that may mitigate the benefits of IRE therapy, such as the ability to perform the therapy near sensitive nerves and major vasculature. The chapter carries out this investigation by theoretically examining treatments in a heterogeneous environment represented by a mammary tumor embedded within the breast using a theoretical IRE threshold determined from in vitro experiments.

4.2 Background

The National Cancer Institute estimates that 12% of women born today will be diagnosed with breast cancer at some point during their lifetime, and the Centers for Disease Control and Prevention states that breast cancer is the second most common cause of cancer death in women. Typical treatment techniques include a combined approach of surgical resection via mastectomy or lumpectomy, irradiation, and adjuvant

[2] Chapter 4 is adapted and reprinted with kind permission from Springer Science+Business Media: Annals of Biomedical Engineering, The Feasibility of Irreversible Electroporation for the Treatment of Breast Cancer and Other Heterogeneous Systems. Vol. 37, 2009, pp. 2615-2625. Authors: Robert E. Neal II, Rafael V. Davalos.

chemotherapy [171]. Breast conserving therapies that use lumpectomy have shown equivalent survival relative to mastectomy [172], creating incentive for the utilization of minimally invasive focal ablation techniques such as radiofrequency ablation and cryosurgery [57, 59, 63].

Although great strides have been made in breast conserving therapy, the invasive nature of surgical resection oftentimes results in significant scarring and disfigurement, with approximately 20% of patients undergoing breast-conserving therapy unsatisfied with their final breast cosmetic outcome [173, 174]. Such cases may undergo additional reconstructive procedures to improve aesthetic outcome [171, 173, 174]. The improvement of oncoplastic techniques may help to curb this high percentage [175]. However, of greater prognostic concern is the internal scarring that results from invasive procedures. Intramammary scar tissue may form spiculated lesions that resemble various benign or malignant entities when viewed mammographically [176, 177]. This scarring complicates monitoring for residual tumors and carcinoma recurrence, often requiring additional ultrasound, clinical examination, or magnetic resonance mammography to interpret the nature of these lesions [178]. Such additional diagnostics are cumbersome, inaccessible, expensive, and often still require a biopsy to ascertain a true lesion assessment [176-178]. From this evidence, of the reduction of scarring from invasive techniques in the treatment of primary breast cancers would yield a great benefit to patient quality of life as well as monitoring for residual cancerous tissue and recurrence.

Other focal ablation techniques such as cryosurgery, laser interstitial therapy, and radiofrequency ablation have been investigated at treating these carcinomas. Unfortunately, these thermal techniques present complications including inconsistencies between the predicted or visualized heated/cooled zone and true cell death regions [63], thermal dissipative properties (the blood perfusion “heat sink” effect) of vascularized tissue, charring at the electrode interface [57], required treatment depth of at least a 1 cm to prevent skin injury [58, 59], and the production of significant scar tissue [60], reducing accurate follow-up. These challenges have prevented widespread acceptance of thermal techniques as a viable alternative to lumpectomy in breast conserving therapy. In order for IRE to be an advantageous alternative to surgical resection, it must be shown that

substantial volumes of tumor tissue may be treated by IRE before the onset of significant thermal effects and scarring.

Adapting IRE to breast carcinomas encompasses several characteristics that must be taken into account when assessing the feasibility of such a treatment and when planning optimized protocols. Among these are the diverse and dynamic physical and electrical properties of connective and fatty breast tissue, whose low water content significantly reduces the electrical conductivity and permittivity relative to glandular carcinomas [179]. As mentioned in **Section 3.4**, it has been shown that higher conductivity of tumor tissue reduces the electric field it experiences relative to the surrounding, lower conductivity tissue when the electrodes are placed surrounding the targeted region [12]. In order to understand if IRE is an attractive alternative for the treatment of breast cancer, it must be shown that treatment-relevant protocols can be developed capable of treating the entire targeted tumor region over a range of heterogeneous conductivities without inducing significant thermal damage and scarring.

4.3 Methods

4.3.1 In Vitro Electric Field Threshold Determination

We test our hypothesis by determining a baseline *in vitro* electric field threshold for IRE for MDA-MB-231 cells, a mammary epithelial adenocarcinoma cell line. To the best of our knowledge, no such *in vitro* study has been conducted on cancerous mammary epithelial cells to experimentally determine a baseline treatment to kill such cells. Cell viability was assessed using trypan blue as a determinant of cell membrane integrity.

Cells were suspended at a concentration of ~7.5x105 cells/ml in DMEM/F12 media (Mediatech, Inc, Manassas, VA), with 125 µl samples (n=12) placed into a 96-Well Electroporation Plate System (Model No. 96/100-830, Harvard Apparatus, Holliston, MA). The cells were then subjected to 80 square wave pulses lasting 100 µs at a rate of 1 pulse per second; similar parameters to those causing complete regression in 12 of 13 aggressive cutaneous tumors in an immunodeficient mouse model[1]. The applied electric field was adjusted between 700 and 2500 V/cm in order to determine the minimum field

required to induce 95% cell death. Following treatment, the cells were incubated for 10 minutes at 37°C with 5% CO_2 to permit adequate resolution of transient electroporation effects[21]. Following the incubation period, 100 µl samples of the suspensions were extracted from each well and mixed at a 10:1 dilution with PBS. Cell viability was assessed using the Vi-Cell Cell Viability Analyzer set up to count cells between 5 and 50 µm in diameter (Beckman-Coulter, Fullerton, CA).

4.3.2 Numerical Model – Representation of Breast Cancer

A three-dimensional numerical model was constructed to represent the treatment of a targeted region located within a peripheral region. The properties were selected to simulate a breast cancer tumor embedded within a fatty connective tissue matrix. An arrangement of two monopolar electrodes, one charged and one grounded, were used. This composition allows the practitioner flexibility for electrode layout when performing a procedure in order to optimize treatment of a targeted region while minimizing undesirable effects. A convective boundary condition was applied at the electrode-tissue interface to represent the heat dissipative effects of the electrode, which were considered to be infinite fins (h_f = 50 W/(m^2•K)).

It has been estimated that nearly two thirds of women presenting breast cancer will do so with the disease localized to the breast [180]. In addition, it has been predicted that by the year 2010, 50% of newly diagnosed breast cancers may be < 1 cm in diameter [181]. Therefore, the tumor dimensions chosen for the computational model in this study were a sphere 1 cm in diameter. Various conductivity ratios (σ_t/σ_p) were used while electrode placement relative to the targeted region was manipulated in order to obtain a reasonable electric field distribution at practical voltages. A schematic of the 3-dimensional model with the electrodes, tumor, and surrounding fatty tissue may be seen in **Figure 4.1**.

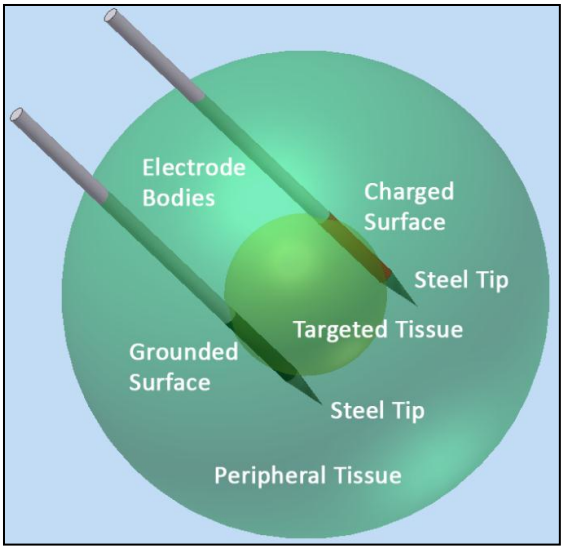

Figure 4.1: Schematic of the 3-dimensional model. The targeted tissue can be seen as a small sphere within a larger outer sphere of peripheral tissue. The charged surfaces of the electrodes have been placed primarily within the targeted tissue near the periphery.

Tissue properties were taken from the literature and may be found in **Table 4.1**. Due to the large variation found within breast carcinoma and the surrounding tissue [179], and the role of conductivity on electric field distribution [12] and thermal effects, each tissue's conductivity was varied between 0.025 and 0.25 S/m, incorporating a range of conductivities that may be found in typical breast tumors as well as the surrounding fatty and connective tissues [179, 182].

Table 4.1: Tissue Properties for Numerical Model

Property	Symbol	Units	Tissue	Value	Reference
Heat Capacity	c_p	J/(kg•K)	Tumor Peripheral	3,700 3,550	[183] [184]
Density	ρ	Kg/m^3	Tumor Peripheral	1,044 928	[185] [185]
Thermal Conductivity	k	W/(m•K)	Tumor Peripheral	.564 .499	[186] [186]
Electrical Conductivity	σ	S/m	Tumor Peripheral	0.025-0.25 0.25-0.025	[179] [179]
Blood perfusion • thermal conductivity	$w_b c_b$	$W/(m^3•K)$	Tumor Peripheral	48,000 2,400	[187] [187]
Metabolic Heat Production	q'''	W/m^3	Tumor Peripheral	65,400 700	[188, 189] [188]
Initial Temperature	T_0	K	Both	310	-

The targeted region was placed within an 8 cm diameter peripheral sphere region. This external boundary was found to be large enough not to influence model outcome, and was set as electrically insulating. The electrodes were separated by a 0.8 cm gap, with placement near opposite boundaries of the targeted volume. The electrodes' diameters were chosen to be 1 mm, a size smaller than that of typical cryoablation and radiofrequency probes [57, 63], with 3 mm long steel tips connected by an insulating material.

This model was solved for the electric field distribution and thermal effects for this setup using the techniques described in **Chapter 6** without considering electroporation-based conductivity changes. The conductivities of the targeted, σ_t, and peripheral breast tissue, σ_p, were varied with a tumor/peripheral conductivity ratio (σ_t/σ_p) between 0.1 and 10. It should be noted that the electric field distribution will not change for different absolute tissue conductivities for a given conductivity ratio. Therefore, the object of interest for treatment prediction in heterogeneous tissues is the ratio of conductivity between the two volumes. The IRE treated and thermally damaged volumes were analyzed for nine of these ratios.

4.4 Results

4.4.1 In Vitro Experiments

After performing experiments, it was found that 1000 V/cm was a suitable electric field threshold to estimate IRE induced cell death. As seen in **Figure 4.2**, there is a clear decrease in cell viability corresponding to the higher electric fields. Viability continues to decrease and asymptotically approach 0% for electric fields well beyond this baseline threshold estimate. Therefore, it may be assumed that all cells experiencing electric fields $\geq$1000 V/cm may be considered to be killed by IRE. Taking the shape factor, λ, to be 1.5, the value for spherical cells, and assuming a cell diameter of 12μm, the applied electric field of 1000 V/cm corresponds to a transmembrane voltage of V_m= 1.8 V. This potential is well above the 1 V found to typically induce IRE [42], supporting the use of this electric field as a conservative estimate to that which would be required for treatment protocol designs *in vivo.*

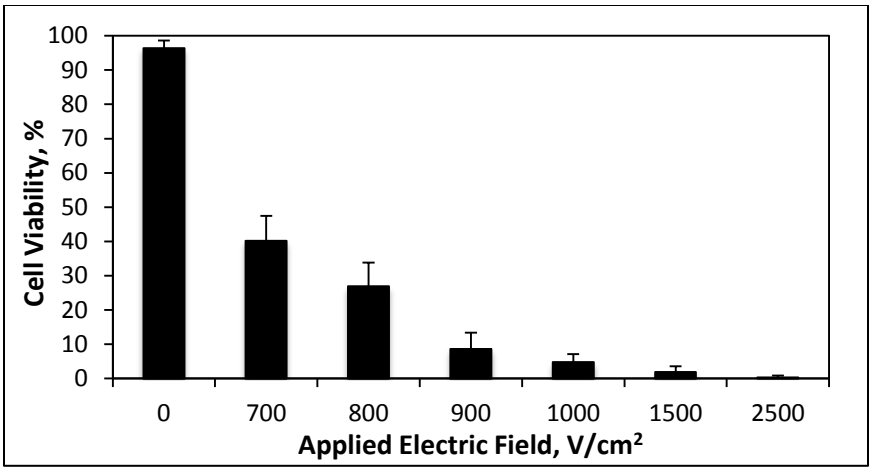

Figure 4.2: *In vitro* results (n = **12**) of MDA-MB-231 cell viability v. applied electric field. 5% viability was observed at 1000 V/cm.

4.4.2 Numerical Model Representation of Breast Cancer

The computational model was solved to determine the minimum applied voltage necessary to fully expose the tumor volume to the electric field determined from the *in vitro* experiments to induce IRE. This was repeated for conductivity ratios (σ_t/σ_p) between 0.1 and 10 to assess the presence of a threshold for the conductivity ratio where IRE loses its efficacy and to see if the effective range corresponds to physiologically relevant tissue properties.

After simulating various scenarios for electrode geometry and placement around the tumor, it was determined that placing the electrodes within the targeted tissue near its boundary yielded the best results for conductivity ratios (σ_t/σ_p) of ≥ 1, which are more physiologically relevant to breast carcinomas and many other *in situ* pathologies, while maintaining reasonable results for conductivity ratios < 1. It was ultimately determined that placing the electrodes within 0.5 mm of the tissue margin at opposing sides yielded the best results for the range of ratios studied. The exposed surfaces of the electrodes were 5.75mm excluding the steel tip, which was found to be adequate for treating the entire targeted volume.

Outputs from the model with conductivity ratios (σ_t/σ_p) of 0.1, 1, and 10 for an applied voltage of 4.2 kV may be seen in **Figure 4.3**. This applied voltage was found to be large enough to treat the entire targeted region (solid black outline) when the conductivity ratio was 1, providing a qualitative comparison for the electric field and

temperature distribution response to changing conductivity ratios for a constant applied voltage. The electric field distribution seen in **Figure 4.3A-F** is constant during the entirety of the 100 µs pulse; then rapidly decays to zero. The temperature of the tissues increases during the application of the pulse, and then spreads throughout the tumor and peripheral tissue via conduction. The temperature distribution at the end of the first second may be seen in **Figure 4.3G-I**, where the greatest thermal effects are observed to occur immediately at the charged and grounded surfaces and the steel tips. Other contours are depicted of electric fields that have previously shown to lead to irreversible (650 V/cm) and reversible (360 V/cm) electroporation from *in vivo* studies on rabbit livers

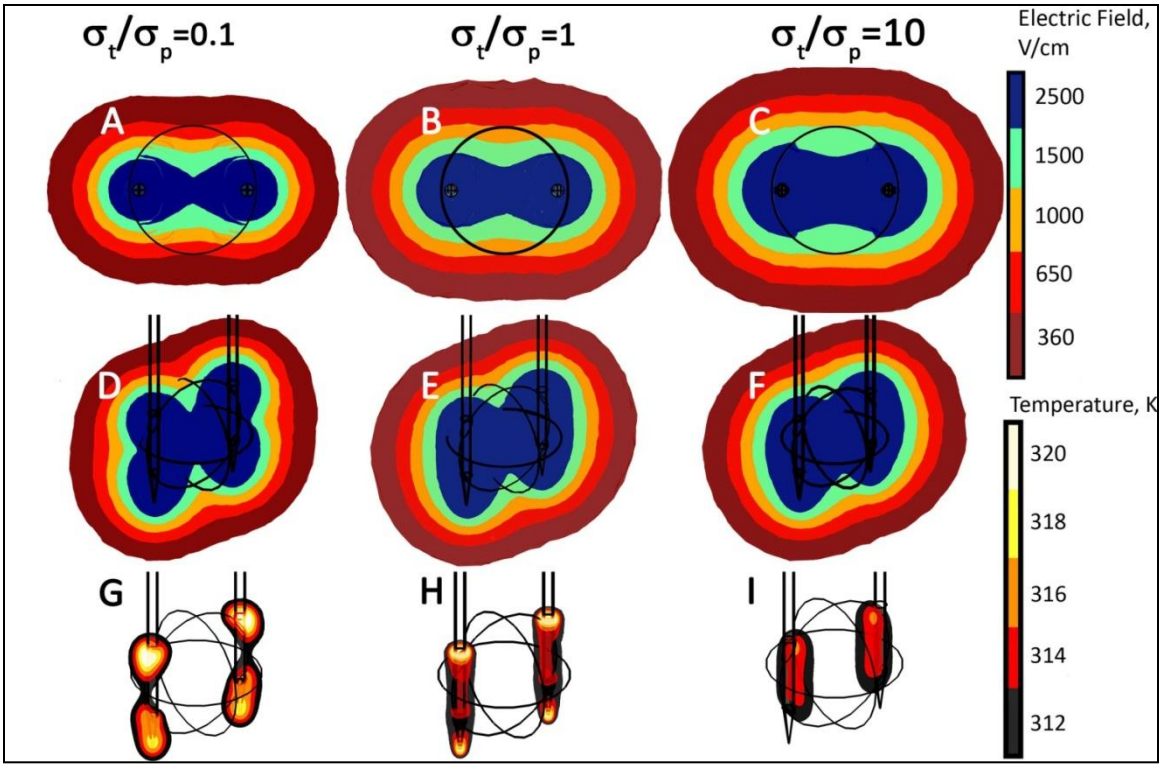

[17].

Figure 4.3: Numerical model outputs with same voltage. The outputs with a 4.2 kV applied voltage for conductivity ratios (σ_t/σ_p) of 0.1 (A,D,G), 1 (B,E,F), and 10 (C,F,I); showing electric field (A-F) during the pulse and temperature (G-I) distributions 1 second after the first pulse. The higher conductivity ratios show progressively more area treated by IRE with less thermal effects. Targeted tissue boundary may be seen as the solid black line.

Outputs from the model with conductivity ratios (σ_t/σ_p) of 0.1, 1, and 10 and applied voltages of 6.85, 4.20, and 2.95 kV, respectively, may be seen in **Figure 4.4**. These applied voltages were found to be capable of exposing the entire targeted region

(solid black outline) to an electric field of 1000 V/cm. From this, treatment-relevant distributions of the electric field may be seen for the three conductivity ratios when the required voltage is applied. In addition, more treatment-relevant temperature increases after the initial second of treatment are depicted in **Figure 4.4G-I**, where the higher required voltage of lower conductivity ratio (σ_t/σ_p) systems are seen to contribute to significantly more thermal effects.

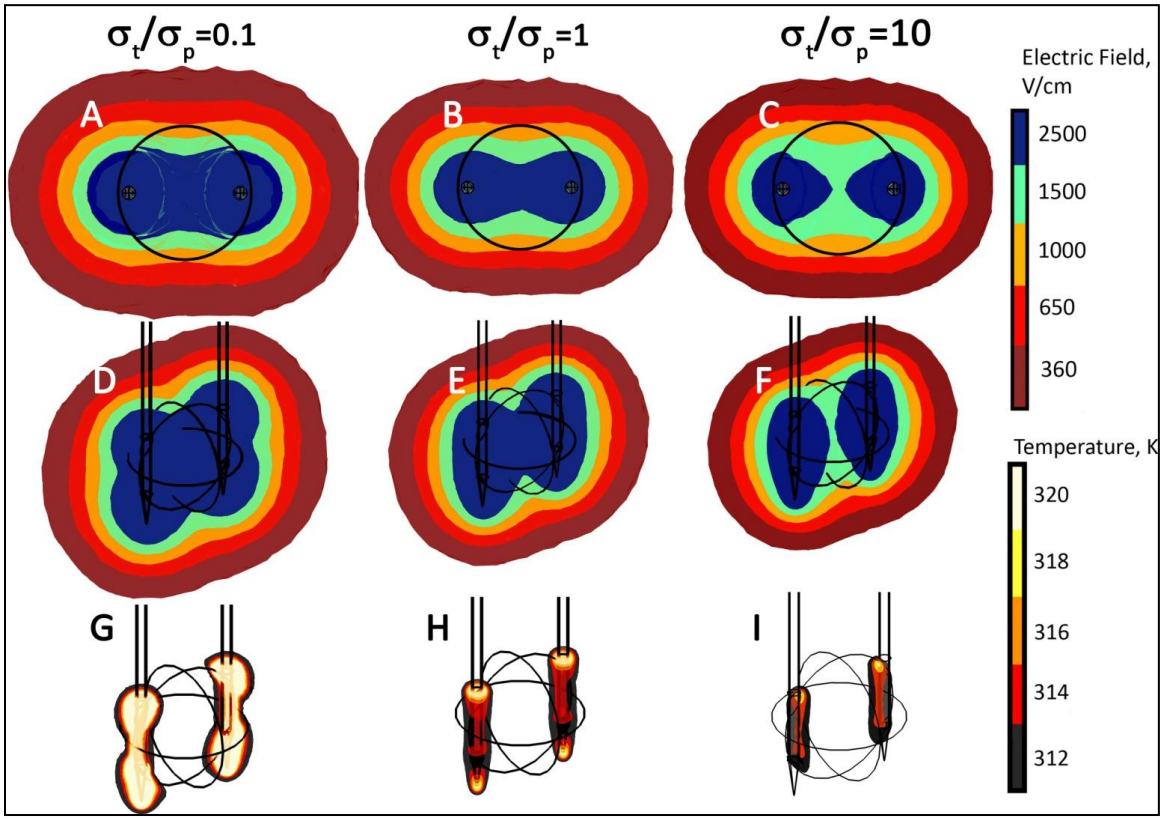

Figure 4.4: Numerical model output with applied required voltage for complete lesion ablation for conductivity ratios (σt/σp) of 0.1 (A,D,G) (6.85 kV), 1 (B,E,F) (4.20 kV), and 10 (C,F,I) (2.95 kV); showing electric field (A-F) during the pulse and temperature (G-I) distributions 1 second after the application of the first pulse. The higher applied voltage for σt/σp = 0.1 shows significantly more thermal effects than for homogeneous tissue and conductivity ratios, σt/σp, > 1. Targeted tissue boundary may be seen as the solid black line.

From these results, several effects of the varied conductivity ratios can be observed. For targeted regions that are more conductive than their surrounding tissue ($\sigma_t/\sigma_p > 1$), a common scenario for many cancers, the dramatically lower voltage allows for complete exposure of the targeted region without exposing the tissues to large volumes of higher electric fields, such as 2500 V/cm. This leads to significantly lower temperature increases, which primarily occur within the tumor. For $\sigma_t/\sigma_p < 1$, the less

conductive targeted region requires much higher voltages to treat the targeted region with 1000 V/cm, leading to larger volumes of tissue experiencing high electric fields of 2500 V/cm. These higher electric field regions coincide with much higher thermal effects, much of which preside outside of the targeted boundary in accordance to the joule heating behavior with more conductive tissues.

4.4.3 Effects of Heterogeneous Conductivity

The numerical model was solved for tissue conductivity ratios (σ_t/σ_p) between 0.1 and 10 to understand how variation in this ratio changes the required voltage to treat the entire targeted volume and the behavior of the thermal effects. A plot of the required voltage for each conductivity ratio may be found in **Figure 4.5A**. From here, it may be seen that for the electrode geometry used, higher conductivity ratios lead to significantly lower applied voltages, decreasing from 6.85 kV to 2.95 kV.

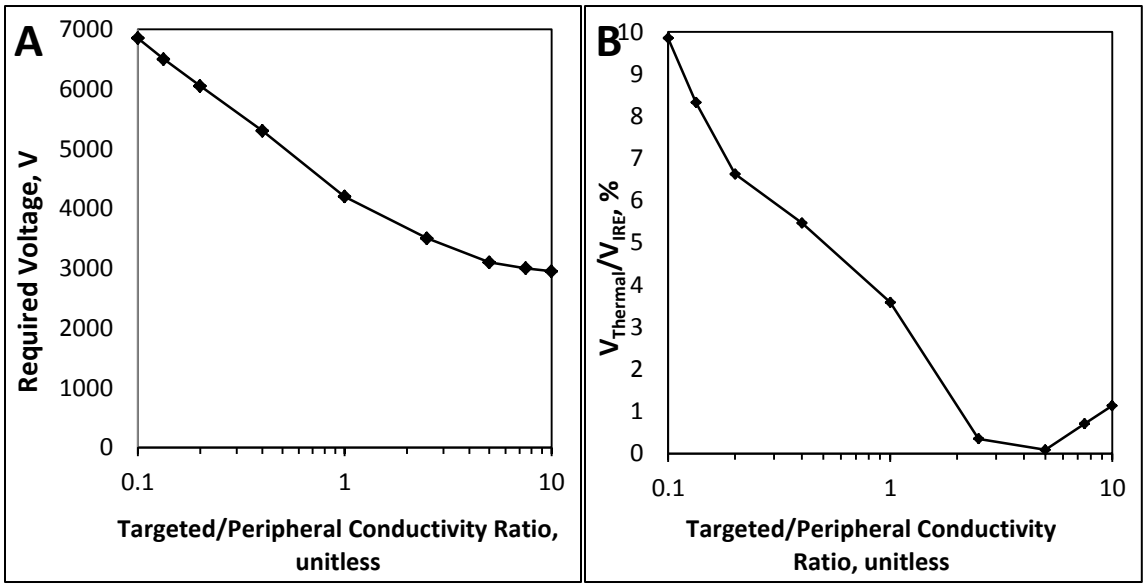

Figure 4.5: Required voltage and thermal volume consequences. (A) Voltage necessary for complete tumor IRE. (B) Ratio of tissue experiencing thermal damage to tissue treated with IRE for a range of conductivity ratios (σ_t/σ_p). The lowest voltages were observed where the tumor is more conductive than the peripheral tissue. This led to less than 5% IRE v. thermal damage for all conductivity ratios above 0.5.

The t_{43} thermal dose values for the modeled 80 pulse treatment were evaluated throughout both tissues to determine what volume ($V_{Thermal}$) experienced a thermal dose of 5400 seconds. This was a dose sufficient to thermally kill murine mammary carcinoma cells [190, 191]. In addition, the total volume experiencing an electric field of at least

1000 V/cm (V_{IRE}) was evaluated for both tissues. The ratio of $V_{Thermal}$ to V_{IRE} was computed for each conductivity ratio (σ_t/σ_p) in order to compare these volumes, which may be found in **Figure 4.5B**. From this figure, it can be seen that less than 5% of the volume experiencing IRE would be subjected to thermal effects for all $\sigma_t/\sigma_p > 0.5$. **Figure 4.5B** shows a nonlinear trend due to the layered variables described by the figure. One such reason for the non-linearity is that, in addition to changing conductivity ratios, the required voltage was adjusted in order to expose the entire targeted volume to electric fields of 1000 V/cm. Furthermore, the different volumes of the two tissue types studied (targeted and peripheral) and the prevalence of thermal effects in the more conductive regions may also affect the behavior of the trend shown in **Figure 4.5B**.

It is important to note that the analysis conducted in **Figure 4.5B** compared thermal damage to irreversible electroporation and was conducted to understand what volumes of tissue may be killed through the IRE mechanism alone. This means that the thermal dose technique used to estimate volumes experiencing thermal damage may assess regions that do not experience protein denaturation or permanent scarring, which typically occurs when tissue reaches temperatures between 50 and 60°C [192], and are the key concerns for treatment complications and follow-up monitoring. Accounting only for thermal scarring would decrease the thermal to IRE volume ratios ($V_{thermal}/V_{IRE}$) beyond those investigated here to further improve the efficacy of IRE treatment.

4.5 Evaluation and Considerations for Irreversible Electroporation in Heterogeneous Systems

These results present supporting evidence for the feasibility of using IRE for the treatment of breast cancer. The *in vitro* experiments showed a conservative electric field threshold to achieve cell death through IRE. Because it has been shown that reversibly electroporated pores re-seal in the range of nanoseconds to ~ 100 seconds [35], it may be assumed that the ten-minute incubation period prevented trypan blue from entering any cells that survived the procedure. It is important to note that there are significant differences in the conditions between *in vitro* and *in vivo* responses to pulsed electric fields. If it is found *in vivo* that mammary carcinomas experience IRE at an electric field

other than 1000 V/cm, the effects from the heterogeneous tissue conditions on electric field and thermal behavior will remain unaltered. What will change is the required voltage to obtain the electric field capable of treating the entire targeted region. For *in vivo* situations, the cells have different geometries and arrangements that may play a significant role in altering their transmembrane potential [43]. In addition, the interaction of neighboring cells and the extracellular matrix as well as longer-term responses to the electric pulses, such as inflammatory and immune responses, may also play a role in lesion creation and resolution. These effects tend to create larger IRE lesions at lower electric fields than in the *in vitro* experiments shown here [17]. The *in vitro* experiments conducted in this study were done to obtain a conservative baseline estimate of the electric field necessary for IRE treatment of breast carcinomas in order to demonstrate the feasibility of such a procedure using numerical models. For future *in vivo* experiments and clinical applications, timing the electric pulses with a patient's cardiac rhythm will prevent arrhythmia associated with high electric fields in close proximity to the heart [6].

The conductivity ratio (σ_t/σ_p) manipulations presented some interesting results regarding internally placed electrodes relative to electrodes placed surrounding the targeted region. Previous studies into heterogeneous effects on electric field distribution show that a region of higher conductivity placed between electrodes will experience reduced electric fields [12]. However, it was found that for the electrode dimensions used, by placing the electrodes within the targeted region, the required voltage for complete lesion ablation was actually lower for heterogeneous tissues when the targeted region was more conductive than the surrounding tissue. This provides very strong evidence for the ability of IRE treatments to overcome heterogeneous tissue issues present in many cancers. The measurements conducted by [179, 182] for infiltrating ductal and lobular breast carcinomas showed possible conductivity ratios from 0.68 to 23 between breast tumors and their surrounding tissue structures, with more common values between 1 and 5. These ratios occurred for tumor conductivities ranging from 0.268 to 0.58 S/m and surrounding structure conductivities between 0.0245 and 0.407 S/m [179, 182]. It should be noted that although the electric field distribution will not change with absolute tissue conductivities for a given conductivity ratio, the thermal effects will

change proportionally to the different absolute conductivities, which may affect the amount of thermal damage done. The physiological conductivities in the literature are similar to the values used in the model, so it is possible to apply the study's findings to clinical settings.

The implications of this work also provide evidence for the need to account for and determine tissue conductivities prior to treatment in order to accurately predict lesion margins, and thus treatment outcome. This may be done by first delivering a low energy pulse, measuring the current induced, and calculating the conductivity. This process may be repeated for as many different tissues as desired by changing electrode placement and exposed region, potentially using ultrasound guidance.

The numerical model physical setup used in this study was adjusted to optimize treatment protocols until the desired treatment volume was achieved with IRE while minimizing thermal damage. The optimization was done for a range of heterogeneous electrical conductivities as a means to determine a range of conductivity ratios between the targeted and peripheral tissue (σ_t/σ_p) where IRE is most effective. The results for the range of conductivity ratios studied may be applied to many various heterogeneous tissue scenarios, such as high conductivity tumors within low conductivity tissue, as with typical breast carcinomas, lower conductivity tumors within more conductive surrounding tissue, which may be the case in some brain and spinal carcinomas, or for situations where the conductivity within the targeted region may be manipulated, such as injecting saline prior to treatment. The results of this study found that IRE may be a viable focal ablation technique for the treatment of breast cancer without inducing significant scarring, while presenting non-thermal characteristics and the benefits of minimally invasive procedures.

A key aspect of the effects from heterogeneous tissues to consider from this study is the distinct redistribution of the electric field in response to the conductivity ratios (σ_t/σ_p) greater than or less than 1. The limiting margin is defined here as the final border of the targeted region to experience IRE-relevant electric fields when the applied voltage was insufficient to produce complete tumor IRE. This margin may change by changing

electrode placement within the targeted region (more central or closer to the perimeter). The geometry used where the electrodes were placed within and beside the targeted region boundaries was selected for ease of guidance during application as well as because this geometry was found to yield tumor ablation at practical voltages. For many electrode arrangements, when the peripheral tissue is more than or as conductive as the inner tissue (conductivity ratio $\leq$ 1), the limiting margin is the border between the electrodes. However, when the peripheral tissue is less conductive than the targeted region (conductivity ratio > 1), the limiting margins were more likely to be the regions closest to each electrode. These effects hold great implications for electrode design and use in the treatment of various heterogeneous tissues.

For heterogeneous tissues with a conductivity ratio, $\sigma_t/\sigma_p < 1$, the required voltage and thermal effects may be reduced by increasing the diameter of the electrodes relative to the diameter of the targeted region [17]. The targeted region/electrode diameter ratio (d_t/d_e) used in this study was 1/10, which was derived from typical primary tumor characteristics and currently used minimally invasive surgical devices. Also, the electric field may be more accurately aimed at the limiting margin by reducing the separation between the electrodes, moving each closer to the center of the targeted tissue.

The heterogeneous effects also bring the regions of healthy tissue killed by IRE into consideration when designing IRE protocols. This study focused on treating to the boundary of the targeted region. In conventional breast conserving therapies and other surgical resection treatments, a margin of healthy tissue of approximately 0.5 cm beyond the targeted region is often removed to increase the certainty of removing all cancerous cells related to the tumor [173]. For IRE treatments of cancer, killing a similar margin beyond the targeted region would likely be desirable.

To further reduce the required voltage for all scenarios investigated, electrodes can first be initially placed immediately within the perimeter of opposite borders of the targeted region. Pulses would be applied at a lower voltage that may not treat the entire targeted region**.** Following this, the electrodes would be re-inserted, with their location rotated 90° relative to the center of the targeted region. Alternatively, four electrodes

could be placed in the arrangement simultaneously. Such a technique does require additional electrode insertions, increasing invasiveness of the procedure and promoting the chances for inaccurate electrode placement, and thus treatment region. However, because tumor location and electrode placement may be accurately visualized using ultrasound guidance [16], multiple insertions should not significantly increase error in electrode placement. The application of such a technique is ultimately dependent on the scenario and should be evaluated for use on a case-by-case basis.

Although this analysis was conducted for a simple arrangement of two single-pole needle electrodes, more complex electrodes and arrangements may be used to customize the shape of the electric field distribution to more efficiently treat the targeted region while sparing the peripheral tissue. This principle may be applied when accounting for tissue heterogeneities as well as for planning and targeting treatments of irregularly shaped tumors. For such situations, ultrasound guidance can ensure accurate electrode placement prior to treatment. By adjusting electrode type, size, shape, placement, and arrangement in response to heterogeneous conductivities and irregular tumor geometries, it is possible to increase the accuracy of the desired electric field relative to the treatment, and thus decrease the required voltage and thermal effects, improving the practicality and efficacy of treatment.

A final aspect to note of the electrodes is the effect of the sharpened tip required for tissue penetration. The use of surgical steel makes this portion of the electrode highly conductive, producing thermal effects and altering the electric field, redistributing it distally. However, for some scenarios where only a very narrow electrode is required or the tissue is very soft, such as the brain, an electrode may be used without the sharpened steel tip to obtain a more uniform electric field distribution.

This study focused on interpreting the behavior of electric field and temperature distributions when planning IRE treatments on tissues with bulk heterogeneities, such as the scenario involving the unique conductive properties of mammary tumors within a fatty connective tissue matrix. To further expand upon this study as treatment planning protocols become more refined, it may be desirable to account for the multiple tissues

interacting at a finer scale. For instance, different breast tumors, such as infiltrating ductal and infiltrating lobular carcinomas, can occur in many unique locations relative to the connective, glandular, and adipose tissues that compose the majority of breast tissue, each with unique electrical and physical characteristics [182]. In addition, in some cases it may be appropriate to further refine the heterogeneities considered down to the level of distinct cell geometries and organization within the extracellular matrix. At such scales, distinct electrical behaviors for the interaction between cells and their surrounding interstitial matrix have been shown [193].

The thermal effects produced by treatments investigated with conductivity ratios (σ_t/σ_p) > 0.5 may be considered negligible, since the volume of tissue experiencing thermal damage is less than 5% of the volume treated by IRE, a relatively small value. This allows for the ablation of significant portions of targeted tissue without inducing thermal damage. Furthermore, these effects were studied in order to delineate the mechanism of cell death between IRE and thermal damage, which is likely to occur at temperatures below those that induce thermal scarring. Additional investigation comparing IRE ablation to thermal scarring would likely show even larger amounts of tissue capable of being treated by IRE for a given amount of thermal damage. It should be noted that the greatest temperatures occur at the electrode-tissue interface, where IRE treatment is strongest, ensuring that any scarring will occur in an area of tissue that has received sufficient treatment, decreasing any negative impact on monitoring treatment outcome. Finally, the thermal effects may be reduced even more with the use of an internally cooled electrode.

A significant portion of the volume treated by IRE occurs outside of the targeted region. However, this is consistent with typical breast conserving therapies, where a margin is produced beyond the primary tumor to ensure complete treatment. This volume may be further increased using higher voltages as well as re-inserting the electrodes with a different arrangement. The rapid lesion resolution exhibited by IRE procedures suggests that all healthy cells killed by the IRE procedure will be replaced with an in-growth of new healthy cells and tissue, further reducing scarring and aesthetic effects.

4.6 Conclusions

This study has investigated various aspects related to the application of irreversible electroporation to the treatment of breast carcinomas and other applications involving heterogeneous tissue systems. This was completed with regard to ensuring therapy for the entire targeted region from physiologically and anatomically relevant treatment parameters. *In vitro* experiments determined a conservative electric field estimate to induce IRE on mammary adenocarcinoma cells, which was then adapted into a numerical treatment prediction model. The model simulated procedures using two monopolar electrodes, showing numerous unique treatment characteristics and implications of heterogeneous tissue. It was found that IRE is capable of fully treating targeted heterogeneous volumes of tissue without inducing thermal effects significant enough to cause substantial thermal damage, decreasing the likelihood of significant scarring and allowing for improved treatment outcome and recurrence monitoring while minimizing aesthetic effects. It was shown that this is possible for a range of conductivity ratios (σ_t/σ_p) between the two tissue types, showing the applicability of IRE treatments for a range of such heterogeneous tissue scenarios common in clinical settings. Rapid lesion resolution would allow for healthy cells to repopulate the originally afflicted area and treatment margins. These factors, in combination with the additional benefits exhibited by the non-thermal and minimally invasive nature of IRE, provide strong evidence in support of IRE as an advantageous treatment modality for breast cancer and other localized pathologies containing heterogeneous tissue, where distinct tissue and tumor properties may alter treatment parameters and outcome.

Chapter 5: Experimental Evaluation of Irreversible Electroporation Tumor Therapy in Heterogeneous Systems[3]

5.1 Introduction

The previous chapter explored the feasibility to apply irreversible electroporation (IRE) as a therapeutic technique for the ablation of undesirable tissues in heterogeneous environments, where the conductivity distribution in the tissue will alter treatment effects. It concluded that, with proper electrode placement and appropriate pulse parameters, it should be possible to treat an entire targeted tumor with a range of distinct electrical properties from its external environment without inducing prohibitory thermal damage. In this chapter, we validate this possibility by treating tumors in a heterogeneous environment using a murine model. The same cell line examined *in vitro* in Chapter 4 (MDA-MB-231 human mammary carcinoma) was used to orthotopically grow tumors within the mammary fat pad of mice, where the low water content fat and connective tissue in this environment should create a heterogeneous situation consisting of a higher conductivity tumor embedded within a low conductivity peripheral tissue. We delivered the electroporation pulses using an electrode that contained both energized surfaces on a single needle, a design that should easily translate to the clinical setting. Our results presented here support the hypothesis that IRE is a suitable candidate for minimally invasive treatment of breast tumors.

5.2 Background

Current clinical therapy for breast cancer includes a combined approach of surgical resection via mastectomy or lumpectomy, irradiation, and adjuvant chemotherapy [194]. Although great strides have been made in breast conserving therapy, the invasiveness of surgical resection often results in significant scarring and disfigurement [173, 194].

[3] Chapter 5 is adapted and reprinted with kind permission from Springer Science+Business Media: Breast Cancer Research and Treatmtent, Treatment of breast cancer through the application of irreversible electroporation using a novel minimally invasive single needle electrode. Vol. 123, 2009, pp. 295-30. Authors: Robert E. Neal II, Ravi Singh, Heather C. Hatcher, Nancy D. Kock, Suzy V. Torti, and Rafael V. Davalos.

Intramammary scar tissue may form spiculated lesions that resemble various benign or malignant entities when viewed mammographically [176]. This scarring complicates monitoring for residual tumors and cancer recurrence, often requiring ultrasound, clinical examination, and/or magnetic resonance mammography, which may be inaccessible and expensive, and often a biopsy is still required to determine the true nature of these lesions [176, 178].

Because breast conserving therapies that use lumpectomy have shown equivalent success relative to mastectomy [172], there is an incentive for minimally invasive focal ablation techniques that can reduce scarring and improve healing after treatment. The various advantageous characteristics of IREs non-thermal ablation mechanism, as discussed in **Chapter 2,** make it a promising technique to treat breast cancer without the risk of damage to sensitive structures such as nerves or major blood vessels, while minimizing outcome obscuring scar tissue formation.

We hypothesize that thorough tumor ablation may be achieved by IRE-sufficient electric fields distributed by an electrode capable of clinical application. For IRE to be an advantageous alternative to surgical resection, it must be shown that tumors can be treated by IRE with minimal effects to the surrounding healthy tissue. Early *in vivo* investigations using IRE to treat tumors were able to get regression rates as high as 92% using plate electrodes placed on either side of the exposed cutaneous tumor. Translating IRE to the clinical setting as an improved focal ablation technique requires the design and efficacy validation of an optimized, clinically relevant electrode to minimize invasiveness and facilitate simple treatment implementation. For breast carcinomas, treatment may be facilitated through a small single needle electrode, similar to ones used in taking a biopsy, which may be easily placed under ultrasound guidance.

5.3 Methods and Materials

5.3.1 Electrode Design

Prior to treating the tumors, different electrode styles were considered to select an appropriate compromise between treatment effectiveness and procedural robustness.

Multiple electrodes would enlarge the electric field throughout the tumor, but would increase placement complexity, increasing chances for human error and physical damage from electrode penetration. Procedural practicality was vital to developing translational treatment protocols, and thus a single needle bipolar electrode design was used. The electrode prototype developed uses an insulating body for penetration into deep tissues with the tip containing two electrically conductive surfaces separated by an additional insulating layer. These conductive surfaces are the anode and cathode to deliver the energy of the IRE pulses. This design was chosen because it is capable of treating the tumors without requiring excessive invasiveness or complex electrode arrangements and placement. The dimensions of the needle used in the experiments are shown in **Figure 5.1A**. The electrode lengths were selected to fit all 4 layers of the electrode within an 8 mm long tumor. The diameters were selected to achieve a sufficient electric field distribution while keeping the 1.5 mm largest layer narrower than the 1.7 mm of typical probes used in cryoablation [62].

5.3.2 Numerical Model of Electric Field

Two three-dimensional finite element numerical models were created (COMSOL, Stockholm, Sweden) to gain an understanding of the behavior of the electric field distribution when 1300 V was applied to one charged surface and the other was set to ground, as was done in the animal studies. The models used the dimensions of the needle, shown in **Figure 5.1A**, and the dimensions of the treated tumors. The electrical properties of the tissue were chosen to simulate a conductive breast tumor (σ_t = 0.25 S/m [179]) within a layer of fatty peripheral tissue (σ_p = 0.02 S/m [179]). The first model simulates the treatments done on the animals, where the system was placed over an anisotropic layer of muscle ($\sigma_{m,\ perpendicular}$ = 0.055 S/m and $\sigma_{m,\ parallel}$ = 0.8 S/m [195]), a schematic of this setup may be seen in **Figure 5.1B**. The second model used a large outer domain of peripheral tissue to understand the electric field distribution if the protocols were performed deep within a human breast.

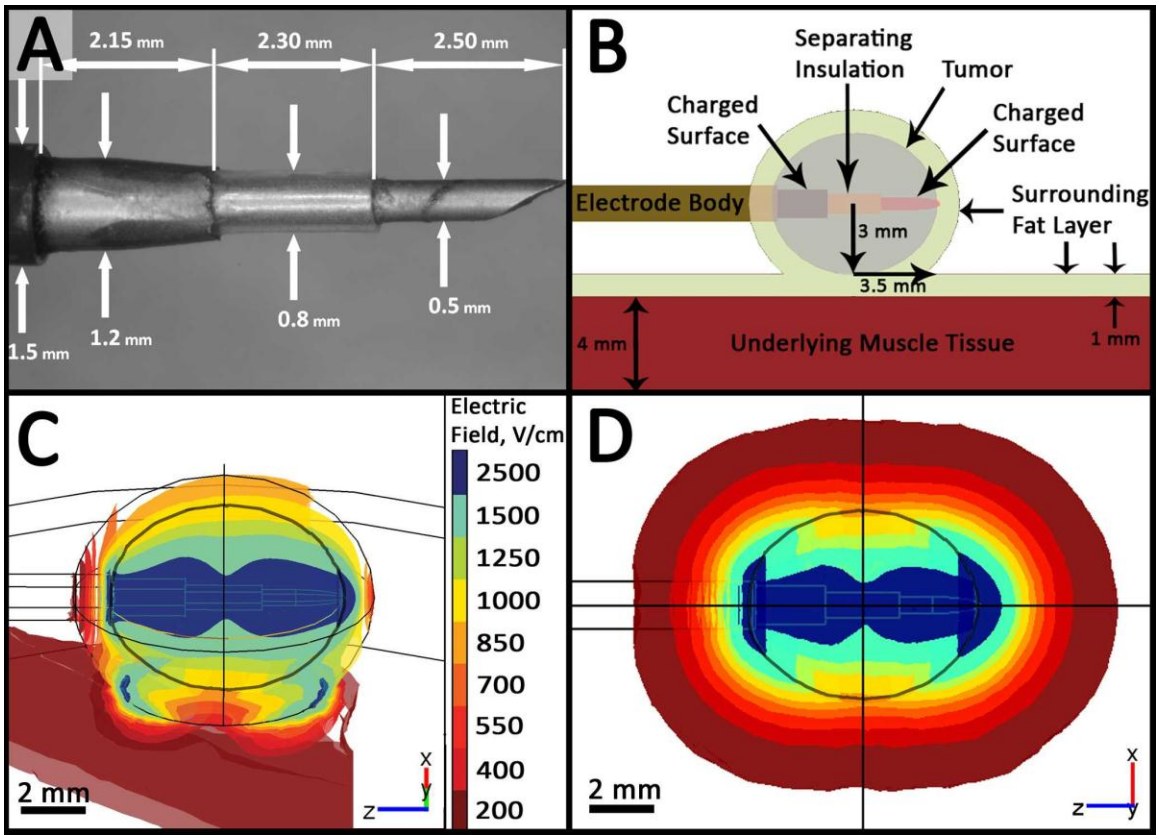

Figure 5.1: Electrode design and numerical treatment models: a Electrode and dimensions used for treatments b Schematic of model setup showing the electrode inserted into the tumor surrounded by fat and sitting on top of a layer of muscle, similar to the experiments performed c Numerical models of electric field output from experiments, where each layer corresponds to electric isofield contours. The tumor is entirely within 1000 V/cm contour, suggesting a reasonable threshold to apply to treatment planning d The electric field if same procedure were applied deep within human breast tissue.

5.3.3 Animal Studies

5.3.3.1 Tumor Inoculation

Female Nu/Nu mice (Crl:NU-Foxn1^{Nu}) were purchased from Charles River Laboratories (Wilmington, MA). Mice were housed in individually ventilated cages in groups of five under specific pathogen free conditions, and were allowed access to food and water ad libitum. Mice were approximately 6 months old at the time of tumor implantation.

For tumor implantation, luciferase expressing human breast carcinoma cells, MDA-MB231-luc(D3-H1) (Caliper Life Sciences, Hopkinton, MA), were grown to log phase in 15 cm tissue culture dishes (Corning Costar, Lowell, MA) in MEM supplemented with

10% fetal bovine serum, penicillin/streptomycin, and L-glutamine (all from Invitrogen, Carlsbad, CA). Cells were grown from frozen stocks prepared after 3 passages of the initial cell shipment from Caliper (formerly Xenogen), and were amplified for 3 passages prior to use for tumor implantation. Cells were treated with trypsin (Invitrogen) then washed in phosphate buffered saline (PBS) (Invitrogen). Tumor cells were resuspended at a concentration of $2x10^7$ cells/ml in an ice cold mixture of 50% Matrigel (BD Biosciences, San Jose, CA)/50% PBS, and 100 µl of the suspension was injected into the fourth inguinal mammary fat pad of 11 mice.

Tumor growth was measured over time using calipers. Volumes of the tumors were calculated according to the equation: $(l \times w^2)/2$. Tumors were treated when the two largest perpendicular diameters reached 5-8 mm, since it was predicted that in the near future, 50% of newly diagnosed breast cancers will be < 1 cm [2]. The experiment was conducted using a total of 11 mice divided into two groups, treated on separate days. In the first group of three mice, two were treated by IRE and the third served as a control. In this group, tumor growth was measured over time using calipers alone until the time of sacrifice. In the second group, five mice were treated with IRE and three served as controls. Tumor growth was measured by calipers and by bioluminescent imaging, as described below. At the time of sacrifice, the tumor site for this group was excised and prepared for histology as described below.

5.3.3.2 Tumor Treatment

To perform the treatment, the mice were anesthetized by isofluorane inhalation (mixed with oxygen and administered to animals at 3% for induction and 1-2% for maintenance). The skin over the tumor was disinfected by scrubbing with an iodine surgical scrub and then rinsed with 70% isopropyl alcohol. After preparation of the surgical site, a small (approximately 5 mm) incision was made to allow for visualization of the tumor and easy placement of the electrode. Next, the electrode was inserted into the tumor, parallel to the mouse's body, through the incision and advanced into the center of the tumor. Seven tumor-bearing mice were treated with 100 pulses, each 100 µs long, in 3 second intervals. After 25 pulses, the poles of the electrode were reversed and a further 25

pulses were administered. This process was repeated until 100 pulses were reached. Initially, the applied voltage was set at 1300 V. Due to changes in tissue conductivity that occurred during treatment, the voltage was reduced in 100 V increments at the first sign of electrical arcing between the anode and cathode of the electrode. The minimum voltage reached was 1100 V. Following treatment, the incision was closed using 5-0 nylon sutures (Ethicon, Cornelia, GA) and mice were injected subcutaneously with ketoprofren (5mg/kg). Sutures were removed five days later. Control mice (n=4) were treated in a similar manner, without any applied voltage. All mice were followed for 4 weeks following treatment, at which point the study was ended.

Tumor growth was monitored both by calipers and by bioluminescent imaging for 30 days. For imaging analysis, mice were injected intraperitoneally with 75 mg/kg D-Luciferin (Xenogen, Alameda, CA) in PBS. Bioluminescence images of anesthetized mice (isofluorane inhalation) were acquired by using the IVIS Lumina II Imaging System (Xenogen) 5-10 min after injection. Exposure settings were determined using the Auto feature of the instrument. Analysis was performed with LivingImage software (Xenogen) by quantifying photon flux (measured in photons/sec/cm^2/steradian). Images were set at the indicated pseudocolor scale to show relative bioluminescent changes over time.

5.3.4 Histology

The tumors and adjacent tissue were completely excised and preserved in 10% neutral buffered formalin for at least 24 hours. After trimming, the tissues were embedded in paraffin and processed routinely for histology, cut at 4-6 μm and stained with hematoxycilin and eosin. Images were taken using a Zeiss Axioplan 2 microscope (Carl Zeiss MicroImaging, Inc., Thornwood, NY) and a digital camera at 10X magnification. Digital images were imported into Adobe Photoshop, but were left unmodified save for cropping and digitally zooming to emphasize specific regions.

5.4 Results

All mice tolerated the treatment well. Following treatment mice were monitored for signs of pain or distress as indicated by: changes in posture (hunched or sleeping

appearance), piloerection, dehydration, changes in behavior (increased timidity or aggression; isolation), changes in activity (reflex withdrawal, biting at the treated area), and changes in locomotion (unsteady gait, lameness). After recovering from anesthesia, no signs of pain were noted for the duration of the study. Growth and regression of the tumors was determined as a relative value to their initial volume by dividing their volume, V, by their volume at the time of treatment, V_0. The relative growth curves of all tumors may be found in **Figure 5.2**, where the relative volumes of the individual tumors are shown versus time.

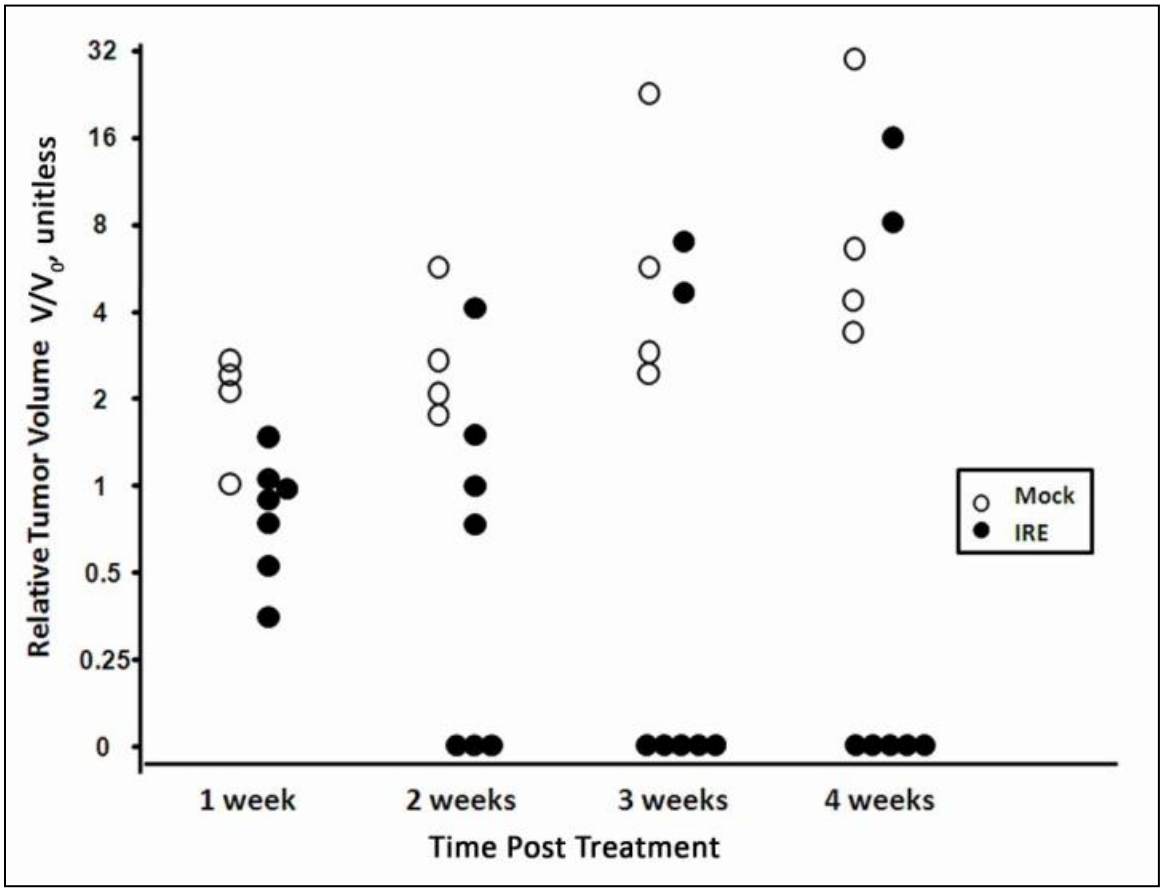

Figure 5.2: Tumor growth curves: The growth of individual tumors over time is presented relative to the volume measured immediately prior to treatment. Closed circles represent tumors in mice that received IRE treatment while open circles represent the tumors in mice receiving only a mock treatment. Continued growth can be seen in all control tumors and two of the treatment tumors while all other treated tumors regressed

The bioluminescent images seen in **Figure 5.3** are from the second experimental trial and show that the fully regressed physical tumors contained no sign of viable cancerous cells at 4 weeks post-treatment. The tumors from the treatment group that did

not regress showed continued growth, though no evidence of tumor metastasis was observed.

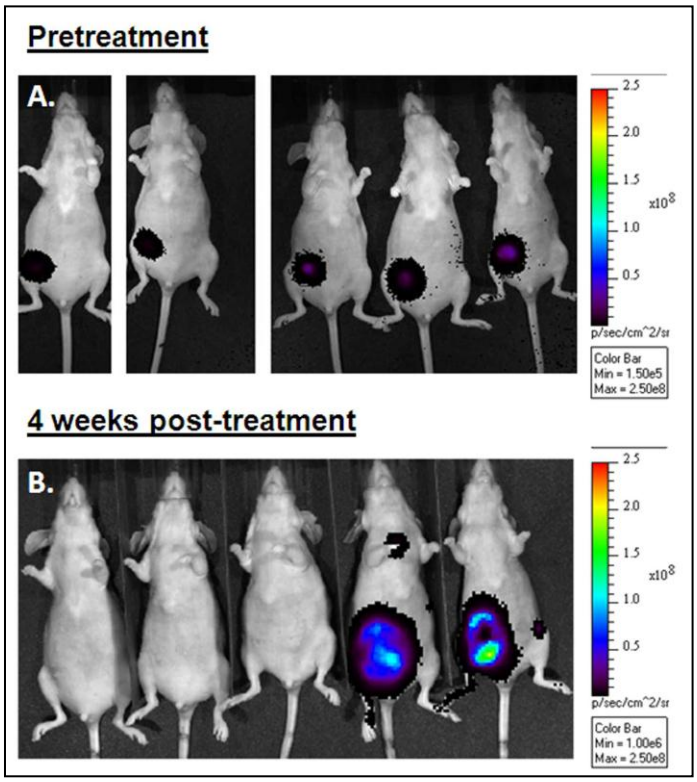

Figure 5.3: Bioluminescence of IRE treated tumors: The five mice of the second IRE treatment group with bioluminescence from the tagged cancerous cells from the tumors may be seen in location and density. The time the images were taken were at **a** 1 hour prior to treatment, where all mice have tumors of approximately the same size, and **b** 4 weeks post-treatment, where it can be seen that there is no trace of cancerous cells in the first 3 mice, while the two that did not regress continued to grow and spread

Histological examination of the tissue taken from the site of tumor implantation was done in a blinded fashion by a board certified anatomic veterinary pathologist (NDK). Three control tumors and five IRE-treated tumors, three of which regressed, were examined. As shown in **Figure 5.4**, the tumors from the control group had central necrotic cores surrounded by sheets of viable tumor cells, among which many mitoses were noted. Thick bands of plasma cells, and fewer lymphocytes, were present along the outer margins, interpreted as host reaction to the tumor (**Figure 5.4A**). The two IRE-treated tumors that did not regress had a similar appearance (not shown). For the three tumors that regressed after treatment, the neoplastic cells were absent (**Figure 5.4B**), apart from a few remaining cells, mostly degenerate, present in one of the three cases (**Figure 5.4C**). Mitoses were not noted in this lesion and the interpretation was that the

tumor was near the final stage of regression. Reactive fibroplasia and neovascularazation, with lymphoplasmacytic infiltration were present in the dermis and subcutis along the margins of the lesions.

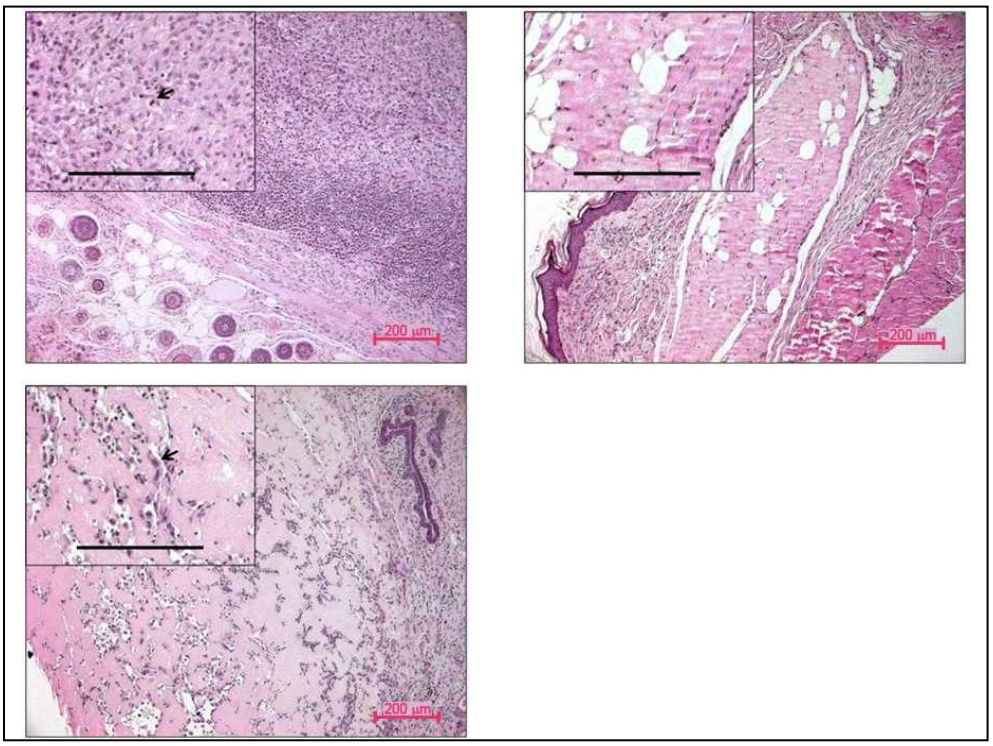

Figure 5.4: Histology of the mammary fat pad of tumor bearing mice 30 days following IRE treatment. a Mock treatment showing densely packed, viable cancer cells in the subcutis and dense inflammatory cell infiltrate along the margin. Insert: Higher magnification of the neoplastic cells with mitoses visible (arrow). b IRE treatment showing tumor regression with only remaining stromal cells, homogeneous eosinophilic material and adipose tissue (clear cells). Insert: Higher magnification of the central IRE-treated region. c IRE treatment showing near-complete tumor regression. Insert: Higher magnification of the few atypical cells (arrow) remaining. All images were taken at 10X magnification. Inserts are digital zooms (40X total magnification) taken from the corresponding low power field. Scale bars represent 200 µm.

By compiling the data from the tumor growth as measured by calipers, bioluminescent imaging of tagged cancer cells from the tumor, and histological examination, it may be determined that tumor regression occurred for 5 out of the 7 treated tumors (both treated tumors from the first group, and 3 out of 5 from the second group). All control tumors showed continued growth over the experimental period. Analysis of the tumor growth from caliper measurements (continued growth against regression) was performed using Pearson's test with JMP software (JMP, Cary, NC), where it was found that treatment is statistically significant in regressing the tumors ($p = 0.0221$).

The numerical models of electric field distribution may be seen in **Figures 5.1C** and **5.1D**, where each color represents an electric isofield contour, and the volume within each respective color is at least that electric field. The black borders represent the physical domains in the models, including the tumor and all peripheral tissues. The distribution from the treatment around the average tumor dimensions may be seen in **Figure 5.1C**, where it appears that the tumor was entirely covered by an electric field of approximately 1000 V/cm. This suggests that this electric field may be treated as the minimum threshold required to induce IRE in these tumors *in vivo*. This finding is consistent with previous *in vitro* experiments that used a similar protocol on the same cell line while in suspension and determined the electric field threshold to be 1000 V/cm [156]. The second numerical model output of **Figure 5.1D** shows how the electric field distribution would change in a clinical setting, where the tumor would likely be located within the breast. The results indicate that in deep tumors, the applied voltage should be slightly increased relative to that used in the mouse model to ensure complete treatment of a similarly sized tumor.

5.5 Discussion

Typical surgical resection procedures remove a 0.5 cm margin around the tumor to ensure removal of any potentially infiltrative cells beyond the tumor borders [173]. Such a technique would likely be employed in IRE ablation therapies as well by expanding the electric field so that the IRE threshold found to be 1000 V/cm from the numerical model in **Figure 5.1C** reaches 0.5 cm beyond the tumor. Conventional focal ablation therapies, such as radiofrequency (RF) ablation and cryosurgery, rely on thermal energy [57, 59, 63], which present complications including inconsistencies between the predicted or visualized heated/cooled zone and true cell death regions [60, 63] and trouble with thermal dissipative properties (the blood perfusion “heat sink” or “cold sink” effect) of vascularized tissue [57, 196]. Additionally, hyperthermic techniques such as RF ablation can induce charring at the electrode interface [57], require minimum treatment depth of at least 1 cm to prevent skin injury [59], and produce significant scar tissue [60], reducing accurate follow-up. IREs benefits, including rapid lesion creation and resolution, as well as minimal scarring [5, 6], means that larger treatment regions

including a margin would likely have fewer negatives than conventional surgical and ablative therapies.

Expanding and shaping the electric field to treat larger tumors and margins beyond the tumor may be done using several techniques to ensure complete treatment of the targeted area while minimizing effects on healthy tissue. One method includes using customized electrode geometries, something easily done with the electrode design used. For reasonably simple geometries, such as spheres and ellipsoids, the layer diameters and lengths of the electrode could be altered. For instance, longer and further separated cathodes and anodes will axially extend the treatment margins, while shortening them will produce a more spherical distribution. The diameters may be made larger to increase treatment volume, or narrower to reduce invasiveness or improve insertion for stiffer tumors that thicker needles may have trouble penetrating.

For very large or highly irregular lesion geometries that cannot reasonably be treated with a single insertion of the electrode, multiple insertions of electrodes allow treatment volume to be more effectively shaped, as is often done with thermal focal ablation therapies [59, 62]. When applying combinations of treatments, each pulse application will have its own electric field distribution and thus region of IRE cell death, which may be superimposed. In this way, each portion of the tumor may be independently treated until the entire mass has been ablated. The electrodes used for such an approach may be very small or of a complex geometry to keep invasiveness low. This versatility can facilitate the treatment of many different cancers located throughout the body while minimizing secondary effects from physical invasiveness. Additional analysis of electrode selection and treatment planning to shape lesions may be found in [156, 197, 198]. Furthermore, electric pulse parameters may be adjusted to treat different volumes. Because IRE lesions follow the electric field strength, larger volumes may be simply treated by increasing the applied voltage.

Most previous *in vivo* investigations of IRE used healthy tissue, and do not account for the potential differences in IRE related to the structure and organization of cancerous tissue [4, 5]. Previously published studies using IRE to treat tumors used plate

electrodes placed on the tumor to deliver IRE pulses [18]. This required that the entire tumor be physically exposed to allow for electrode placement. We present the first investigation to treat solid tumors with a clinically relevant electrode.

Understanding why two tumors continued to grow provides insight into improving upon the findings of this initial study. Both tumors that did not regress were the widest, one of which being the largest (9.7 x 8.1 mm); suggesting that the size or shape of the tumor may have exceeded the treatment region for the protocol used. This is supported by the bioluminescent image of the largest tumor taken 3 days after treatment (not shown), showing no living cancer cells near where the electrode was placed, but some remained at the outer edges of the tumor, where the electric field would be the weakest. In the image 4 weeks after treatment (**Figure 5.3B**), the largest tumor is the one furthest to the right, and the greatest concentrations of cancer cells are in these same regions, suggesting that the surviving cells were responsible for the continued growth of the tumor. To prevent this in future studies and treatments, a maximum treatment region should be found for a given protocol, such as through numerical modeling, and the treatment region should be adjusted as previously discussed for targeted volumes larger than this maximum.

In addition to preventing the errors that may have led to the 2 tumors that did not regress, the findings of this study can be improved in future studies and treatments. This experiment used a standardized electrode geometry and protocol, which did not allow for variations in tumor size or shape. In clinical settings, the electrode dimensions and protocol used may be adjusted according to treatment demands. Furthermore, tumor response was obtained in immunodepressed mice without the combinatorial approach typical of breast conserving therapies. Additional treatment modalities, such as electrochemotherapy [10], will selectively kill cancer cells in the reversible range of electroporation (~250 V/cm). This as well as an immune response, which is promoted by electroporation [5, 10], will improve the effectiveness and reliability of these treatments by killing cancer cells which may otherwise survive IRE alone.

5.6 Conclusion

The study presented here used IRE electric pulses delivered by a novel, clinically applicable IRE single needle electrode design to treat human mammary carcinomas orthotopically implanted into the murine fat pad of mice. The pulses were able to achieve complete regression in 71% of the tumors, relative to 0% regressions in the controls. These findings suggest that IRE could be an advantageous alternative to surgical resection for breast conserving therapy. In addition, they provide further support for the ability of IRE to be an effective treatment in the treatment of localized disease in the heterogeneous environments typical of clinical patient tumors.

Chapter 6: Experimental Characterization and Numerical Modeling of Tissue Electrical Conductivity[4]

6.1 Introduction

Irreversible electroporation (IRE) is a new technique to kill cells in targeted tissue, such as tumors, through a non-thermal mechanism using electric pulses to irrecoverably disrupt the cell membrane. Treatment effects relate to the tissue electric field distribution, which can be predicted with numerical modeling for therapy planning. Pulse effects will change the cell and tissue properties through thermal and electroporation-based processes. This investigation characterized these changes by measuring the electrical conductivity and temperature of *ex vivo* renal porcine tissue within a single pulse and for a 200 pulse protocol. These changes are incorporated into an equivalent circuit model for cells and tissue with a variable electroporation based resistance, providing a potential method to estimate conductivity as a function of electric field and pulse length for other tissues. Finally, a numerical model using a human kidney volumetric mesh evaluated how treatment predictions vary when electroporation and temperature based electrical conductivity changes are incorporated. We conclude that significant changes in predicted outcomes will occur when the experimental results are applied to the numerical model, where the direction and degree of change varies with the electric field considered.

6.2 Background

IRE in experimental cutaneous and orthotopically implanted murine tumors attained regression rates as high as 92% [18, 19]. Case studies using IRE in canine patients achieved complete tumor regressions in complex tumors, including a high-grade glioma with adjuvant radiotherapy [21], and a histiocytic sarcoma with adjuvant chemotherapy [22]. Further, IRE was demonstrated to work as a repeat therapy, even after cancer

[4] This chapter presents an adaptation from a manuscript that is currently under review for publication. Upon acceptance of the final publication, this chapter will be an adaptation reprinted with permission from IEEE: IEEE Transactions on Biomedical Engineering, Experimental Characterization and Numerical Modeling of Tissue Electrical Conductivity during Pulsed Electric Fields for Irreversible Electroporation Treatment Planning. Authors: Robert Neal II, Paulo Garcia, John Robertson, and Rafael Davalos

plasticity led to chemoresistance [22]. Human safety trials achieved complete tumor remission in 46 of 69 tumors unresponsive or untreatable with current techniques [23, 24].

Successful implementation of electroporation (EP) therapies requires accurate prediction of affected volumes through treatment planning [22, 199]. The outcome of EP therapies are related to the electric field distribution [17], which is dependent on the physical characteristics of the tissue, electrode configuration, pulse parameters, and the impedance distribution of the tissue(s) [9, 12, 156]. Therefore, it is vital to properly understand the spatiotemporal properties of the tissue when using finite element modeling to predict EP treatment volumes. Electric pulses will cause Joule heating due to tissue resistance, increasing the electrical conductivity by 1 to 3 $\%°C^{-1}$ [195]. In addition, cell membrane pore formation permits improved electrolyte mobility through the cell, increasing bulk tissue conductivity [200].

Several studies examine impedance characteristics of cells and tissues undergoing EP. Cima and Mir observed increases in current for electric fields as low as 125 V/cm in potato tuber [201]. Davalos, *et al.* suggested that tissue properties change during electroporation, and examined the feasibility of using the bioimpedance changes in electroporated tissues to provide real-time imaging of the affected areas using electrical impedance tomography [202]. Sel, *et al*. [203] and Pavselj, *et al.* [204] found a range of increases in mammalian tissue conductivity and used a sigmoid function to predict $\sigma(E)$ in a numerical model using estimated and experimental parameters. Ivorra and Rubinsky [205] found larger intrapulse conductivity increases at the higher of two electric fields in rat liver as well as a transient increase in conductivity after pulsing, consistent with a similar study on mice tumors [206].

Investigations of IRE have examined the role of temperature on conductivity [12, 197, 207]. EP conductivity increases will amplify thermal effects, compounding conductivity changes, providing incentive to consider both effects simultaneously. Garcia, *et al.* [208], modeled the coupled conductivity effect on treatment volume in brain tissue using experimental temperature data and an assumed EP increase in conductivity. There is a wide range of EP-based changes in conductivity observed in the

aforementioned studies. Unfortunately, there remains a large scarcity of systematically characterized tissue property changes in response to the pulsed electric fields for EP therapies. Considering the broad range of tissue and organs targeted in EP therapies, it is vital to develop a method to estimate these tissue property changes for treatment planning in any tissue type, certainly until a satisfactory body of experimental data can be accrued to provide the appropriate values.

We hypothesize that systematically characterizing tissue property response to single and multiple pulse protocols will provide a basis to develop numerical models that account for these changes, as well as provide evidence for a system to estimate tissue property changes based on the behavior of an equivalent circuit model. Here, we expand our preliminary study in [209] and present the results from an experimental investigation characterizing intrapulse and multiple pulse effects on the electrical conductivity of *ex vivo* porcine renal tissue subjected to typical IRE electric pulses.

Our experimental data is fit to an asymmetrical sigmoid equation for conductivity as a function of pulse length, as well as minimum and maximum tissue conductivity, corresponding to nominal and complete EP. We then present a common equivalent circuit model to describe cell and tissue behavior undergoing EP. We discuss how it may provide a means to estimate conductivity as a function of electric field for other tissues and organs based on our experimental results, the derived equation, and the β-dispersion frequency behavior at the capacitive component of the cell membrane. Finally, we explore the significance of accounting for EP and temperature-based conductivity changes on treatment outcome predictions using numerical simulations. The model shows that accounting for both effects produced the most significant changes in volume and shape of the predicted treatment outcome versus with a constant electrical conductivity model.

6.3 Methods

6.3.1 Experimental Characterization of Tissue Properties

6.3.1.1 Experimental Setup

Kidneys were collected from female purpose-bred swine within 15 minutes of humane euthanasia from an unrelated study. Tissue samples were collected from the renal cortex, a relatively homogeneous tissue of mostly nephron tubule segments, making electric field distributions and bulk conductivity changes in response to the electric pulses more reliable to quantify and characterize.

Tissues were sectioned to produce flat, cylindrical core samples approximately 5 mm thick and 8 mm in diameter. Sample dimensions were measured using calipers, and then samples were placed between two plate electrodes, each with a 0.7 mm diameter hole in their center for insertion of a thermal probe. Tissue temperatures were measured using the Luxtron® m3300 Biomedical Lab Kit Fluoroptic® Thermometer with the STB thermal probe (±0.2˚C at a recording rate of 4 Hz) (LumaSense™ Technologies, Santa Clara, CA USA).

Square wave electric pulses were delivered using the ECM830 pulse generator while intrapulse voltage was measured using the Enhancer 3000 Monitoring System (Harvard Apparatus, Cambridge, MA) connected to a two-channel TDS1002B oscilloscope (Tektronix, Beaverton, OR). A low impedance (0.1 Ω) voltage divider was placed in series with the pulsing circuit, and an INA128 operational amplifier (Texas Instruments, Dallas, Texas) was used to amplify the voltage drop across the resistor before sending the signal to the oscilloscope, where the current is calculated using Ohm's law. The low impedance resistor will introduce minimal resistance to the overall pulse circuit. A schematic of the experimental setup to capture the pulses may be seen in **Figure 6.1**.

Two electric pulse protocols were investigated. The first used a set of 10 pulses, each 500 µs long, where only the first captured pulse was evaluated for intrapulse behavior. The second used a 200 pulse protocol, each 100 µs long, at a rate of 1 pulse

per second. Every 4th pulse was captured to determine how pulse effects will change when a large number of pulses are applied. A new sample was used for each trial.

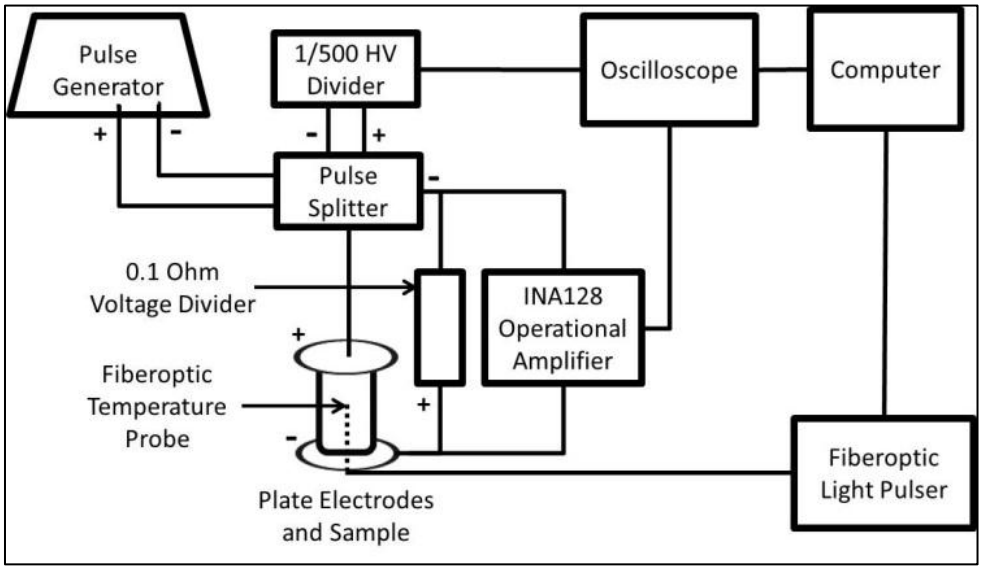

Figure 6.1: Schematic of experimental apparatus

6.3.1.2 Conductivity Calculation and Measurement

Pulses were captured by the oscilloscope and written to a .mat file with the *tmtool* toolbox using custom code developed in Matlab (Mathworks, Natick, MA). The electrical conductivity of the tissue samples were calculated from the current and voltage data. The 1 μs collection rate data was smoothed using 25 and 10 point moving averages for the current and voltage signals, respectively. Due to the relatively long duration of the pulses (100 and 500 μs), the initial transient behavior of tissue impedance was not used. Impedance was considered solely a function of the resistance in accordance with Ohm's law, where the resistance, R(t) is equal to the measured voltage, V(t), divided by the measured current, i(t). Resistance is a function of tissue properties and the physical geometry, so results were scaled according to the cell constant, *K*, equal to the surface area divided by the sample thickness. From this, the tissue specific conductivity can be solved according to the following:

$$\rho(t) = R(t) \cdot K = R(t) \cdot \frac{SA}{L} = \frac{V(t) \cdot SA}{i(t) \cdot L} = \frac{1}{\sigma(t)} \tag{6.1}$$

where $\rho(t)$ is the electrical resistivity, $\sigma(t)$ is the electrical conductivity, L is the tissue thickness, and SA is the surface area of the tissue. Tissue conductivity was calculated for all single pulse and multiple pulse trials to determine conductivity as a function of electric field and pulse length.

6.3.2 Equivalent Circuit Model

Common analogs for the bioimpedance behavior of a cell use an equivalent circuit model that considers the extra- and intracellular fluids to be resistances, (R_e and R_i, respectively), while the cell membrane is considered a dielectric capacitance, C_m, in parallel with a high membrane resistance, R_m (~14.3 TΩ) **(Figure 6.2A)**. Combining EP and thermal effects provides tissue conductivity as a function of electric field and temperature, $\sigma(E,T)$. We used our experimentally derived conductivity as a function of electric field, pulse length, and published thermal effects in a revised equivalent circuit model (**Figure 6.2B**) that includes a variable resistance, $R_{ep}(E)$, in parallel at the cell membrane to explain the macroscopic behavior of tissue undergoing EP.

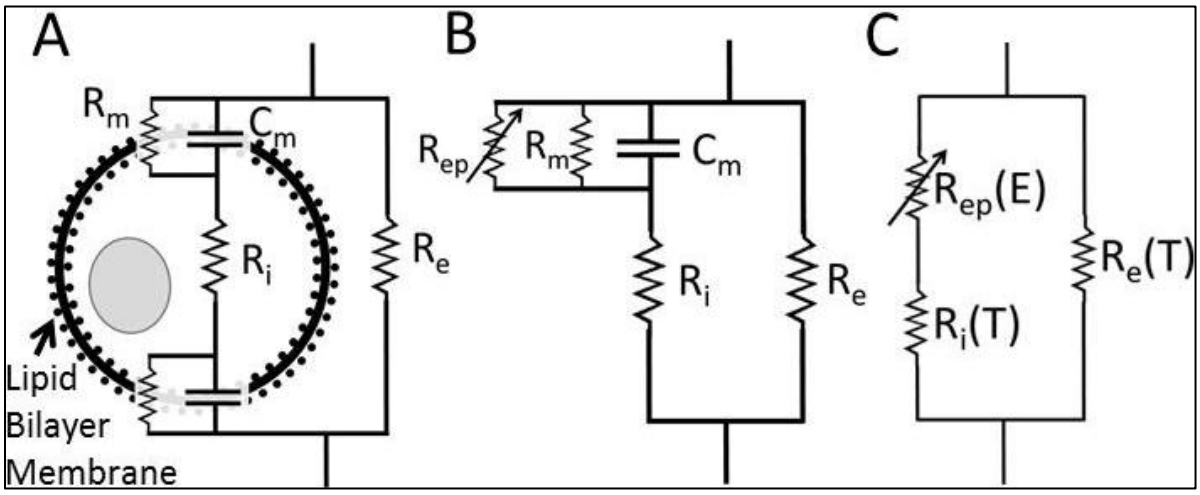

Figure 6.2: Equivalent circuit diagrams. (a) Basic circuit model of a cell. (b) Circuit model including parallel electroporation resistance. (c) Equivalent circuit when membrane ignoring capacitance (low frequency) and membrane resistance (R_m approaches infinity).

Solving the overall equivalent circuit in **Figure 6.2B** gives impedance, Z_t, the equation

$$Z_t = \frac{R_e \cdot (R_i + \frac{R_m R_{ep}}{R_m + R_{ep}})}{R_e + (R_i + \frac{R_m R_{ep}}{R_m + R_{ep}})} + \frac{1}{j \cdot \omega \cdot c_m} \tag{6.2}$$

where j is √-1 and ω is the frequency of the signal. However, the large membrane resistance can be neglected. Considering a low frequency to represent the 50 to 100 µs square wave pulses of typical EP procedures, C_m behaves as an open circuit. This gives the equivalent circuit in **Figure 6.2C**, where the equivalent resistance, R_t, can be solved according to

$$R_t(E,T) = \frac{\left[R_{ep}(E) + R_i(T)\right] \cdot R_e(T)}{R_{ep}(E) + R_i(T) + R_e(T)} \tag{6.3}$$

Here, R_i and R_e account for temperature-based conductivity changes, while $R_{ep}(E)$ is considered solely a function of electric field. Isolating $R_{ep}(E)$ gives it the equation:

$$R_{ep}(E) = \frac{-[R_i(T) \cdot \left(R_e(T) - R_t(E,T)\right) - R_t(E,T) \cdot R_e(T)]}{R_e(T) \cdot R_t(E,T)} \tag{6.4}$$

If one considers a low electric field, R_{ep} behaves as an open circuit, resulting in no intracellular pathway for current and leaving only the extracellular medium for current flow. Therefore, the equivalent resistance of the circuit at 0 V/cm is equal to the extracellular resistance contribution alone.

Although it varies with the number of pores created on a cell membrane, membrane resistance to current flow rapidly decreases after reaching sufficient EP across the membrane [210]. Therefore, R_{ep} approaches zero at complete EP, and the R_T becomes a function only of the intra- and extracellular resistances. The behavior of a single cell may be scaled up to an identical equivalent circuit to represent a system of cells in tissue [50, 193]. Our experimental results were used to derive values for model parameters.

6.3.3 Numerical Model – Simulation within Kidney

Numerical models are a useful tool for predicting EP protocol outcomes, including electric field and temperature distributions. A finite element model was created using Comsol Multiphysics v.3.5a (Stockholm, Sweden) to demonstrate the impact on the electric field distribution from EP and temperature changes to tissue conductivity. The physical setup used a 3-D volumetric mesh by reconstructing the kidney from a voluntarily donated human computed tomographic (CT) scan with Mimics 14.0 and meshing with 3-matic 5.1 software (Materialise, Leuven, Belgium).

The electrode arrangement consisted of two electrodes, each 1 mm in diameter placed into the center of the kidney. The electrodes were separated by 1 cm, and had exposed lengths of 1 cm, which were connected to 5 cm long insulated needles. The array was positioned with the tips 2.0 cm into the tissue, allowing approximately 0.75 cm separation between the renal medulla and the distal end of the electrodes, as well as 1.25 cm separation between the proximal end of the electrodes and the kidney boundary. This arrangement was selected to minimize the effects that the unique and heterogeneous properties of renal medulla and boundary would cause to the predicted electric field distribution. The numerical model physical setup can be found in the results section.

The electric field distribution in the numerical model is generated by solving the governing equation:

$$\nabla \cdot (\sigma \nabla \Phi) = 0 \tag{6.5}$$

where σ is the electrical conductivity of the tissue and Φ is the electric potential. In the body kidneys are covered with a layer of connective tissue and surrounded by a layer of fat, both of which will have very low conductivities of approximately 0.03 and 0.012 S/m, respectively [204, 211]. Therefore, the kidney boundary was considered electrically insulating. The anode was energized at 2000 V, and the cathode set to ground.

The increase in conductivity from EP occurs within the first few microseconds of the electric pulse [205]. Because typical EP pulses are 50 to 200 μs in duration, one may consider the conductivity distribution during the electric pulse to have incorporated all EP-based conductivity changes.

In this numerical study, we consider all memory effects observed for multiple pulse EP procedures to be related to the increase in temperature. The dependence of conductivity on temperature, σ(T), may be calculated as:

$$\sigma(T) = \sigma_0[1 + \alpha(T - T_0)] \tag{6.6}$$

where α is the temperature coefficient and σ_0 is the equivalent conductivity at the ambient temperature, which was used as the baseline for σ(E) function, since the E = 0 V/cm from this function was taken from the literature at 36°C [212].

The numerical model accounts for temperature dependent conductivity effects by calculating temperature using a modified Pennes' Bioheat Equation:

$$\nabla \cdot (k\nabla T) + w_b c_b (T_a - T) + q''' + \frac{\sigma|\nabla\Phi|^2 \cdot d}{\tau} = \rho c_p \frac{\partial T}{\partial t} \tag{6.7}$$

where k is the thermal conductivity of the tissue, T is the temperature, c_b and c_p are the blood and tissue heat capacity, respectively, T_a is the arterial temperature, ρ is the tissue density, q''' is the metabolic heat generation, $\sigma|\nabla\Phi|^2$ is the Joule heating term, and w_b is the blood perfusion rate, which was consistent with values reported in [213]. To reduce the calculation costs of the numerical model and prevent complex time-stepping algorithms, the Joule heating term was scaled according to the pulse duration, d, divided by the period between the pulses, τ, effectively averaging the heating over the entire intra- and interpulse duration.

The entire domain was considered to have an initial physiologic temperature of 37°C. The tissue thermal boundary was considered to represent a layer of fluid surrounding the organ, and was modeled as a heat flux boundary condition,

$$q'' = h(T - T_0) \tag{6.8}$$

where q'' is the heat transferred per unit area, h is the heat flux coefficient, and T_0 is a reference temperature, taken to be 37°C. The heat flux coefficient was derived for using

$h = \frac{k}{\vec{n} \cdot d}$, where $\vec{n}$ is the unit normal vector to the boundary and d is the distance to the reference temperature. The thickness of the fat and peritoneal fluid surrounding the kidney was averaged within the CT, and approximated to be a constant 0.5 cm thick in the model. The thermal conductivity was set to that of blood (0.47 W/(m·K)), giving the kidney boundary an effective heat flux coefficient of 94 W/(m^2·K). Tissue properties may be found in **Table 6.1**, where the baseline conductivity value σ(0) was taken from the literature for *in vivo* feline renal tissue.

The numerical model simulated electric field and temperature distributions within a single pulse as well as for a typical IRE procedure of 100 pulses, each 100 μs long and separated by 1 second. This was performed for 4 conditions, including a constant conductivity, one that depends only on temperature, σ(T), one that accounts for EP conductivity change, σ(E), and one that considers both effects, σ(E,T).

Table 6.1: Tissue Properties in Numerical Model

Property	Symbol	Value	Reference
Heat Capacity, J/(kg·K)	cp	3,890	[214]
Thermal Conductivity, W/(m·K)	k	0.547	[187, 215]
Density, kg/m3	ρ	1080	[187]
Initial Electrical Conductivity, S/m	σ0	0.15	[212]
Conductivity-Temperature Coefficient, %°C-1	α	1.7	[195, 216]
Blood Perfusion Term, W/(m3·K)	wb·cb	43,062	[187, 217]
Metabolic Heat Production, W/m3	q'''	23,889	[187]

6.4 Results

6.4.1 Characterization of Tissue Properties

6.4.1.1 Single Pulse Experiments

All experiments were completed within 2 hours of tissue collection. Numerical simulations of the plates with holes showed that < 1% of the tissue volume experienced an electric field 1.25% below the field produced by complete plates. Conductivities were measured at a resolution of 100 V/cm from 200 to 1000 V/cm, as well as at 1500 and

2000 V/cm. The moving average voltage and current data was found to be good averages during the majority of the pulse duration considered in this study, where representative waveforms can be found in [209]. A plot of the averaged conductivity behavior versus time for certain electric fields is presented in **Figure 6.3**. The median standard deviation for all data was 0.128 (range = 0.0338 to 0.205). Due to limitations in the measurement system, 200 V/cm was the lowest electric field that conductivity was measured. Therefore, the relative increase in conductivity was calculated based on a nominal conductivity of 0.15 S/m, a value for feline in vivo renal cortical tissue from the literature at 36°C, scaled to 22°C [212].

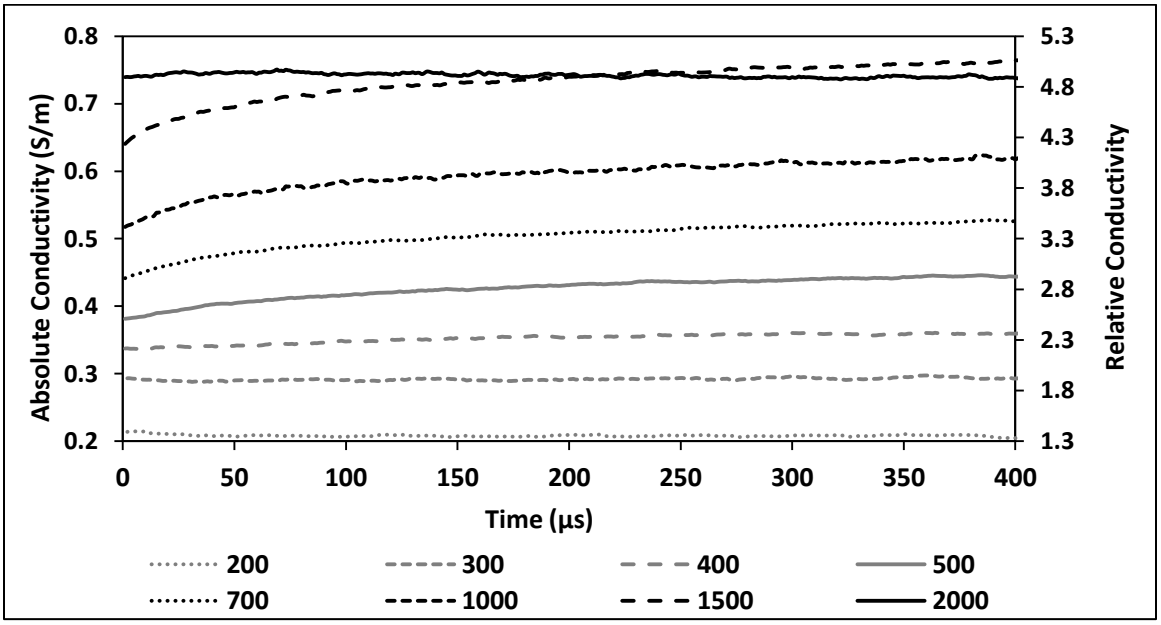

Figure 6.3: Intrapulse electrical conductivity versus time from pulse settling for varying electric fields at 24 ± 2°C (**n ≥ 6** per electric field). The legend represents electric field in V/cm.

Analysis of the intrapulse conductivities (**Figure 6.3**) revealed that as the electric field increases, the initial electrical conductivity further increases over the baseline value. For electric fields from 500 to 1500 V/cm, the conductivity is observed to continue increasing throughout the length of the pulse. A plateau electrical conductivity appears at the 2000 V/cm electric field, where no further intrapulse conductivity increase occurs. Because conductivity as a function of electric field changes during the pulse, data were averaged for conductivity at the initial pulse settling (5 µs) as well as at 50, 100, 200 and

400 µs following pulse onset. The resulting curves at these time points may be seen in **Figure 6.3**.

An appropriate fit of the experimental data for conductivity as a function of electric field, σ(E) has been performed using a modified asymmetrical Gompertz curve, calculated as follows:

$$\sigma(E) = \sigma_0 + (\sigma_{max} - \sigma_0) \cdot \exp[-A \cdot \exp(-B \cdot E)] \quad (6.9)$$

where σ_0 is the conductivity without electroporation and σ_{max} is the maximum possible conductivity when the cells are thoroughly permeabilized. *E* is the electric field in V/cm exposed to the tissue, and *A* and *B* are constants to determine the displacement and growth rate of the curve, respectively. Wolfram Mathematica (Wolfram Research, Champaign, IL) was used with the *FindFit* function to optimize the *A* and *B* parameters using least-squares regression to match the *σ(E)* data in **Figure 6.4**. The baseline σ_0 was always set to 0.15 S/m. An overlay of the optimized curves with the data may be found in **Figure 6.4**, and the best fit parameters are presented in **Table 6.2**. The *A* and *B* coefficients versus time in µs may be fit according to $A = -5x10^{-6} \cdot t^2 + 0.004 \cdot t + 2.8026$ ($R^2 = 0.9656$) and $B = -7x10^{-9} \cdot t^2 + 5x10^{-6} \cdot t + 0.002$ ($R^2 = 0.9766$). From these polynomials, Gompertz function coefficients can be calculated for any pulse length between 5 and 400 µs.

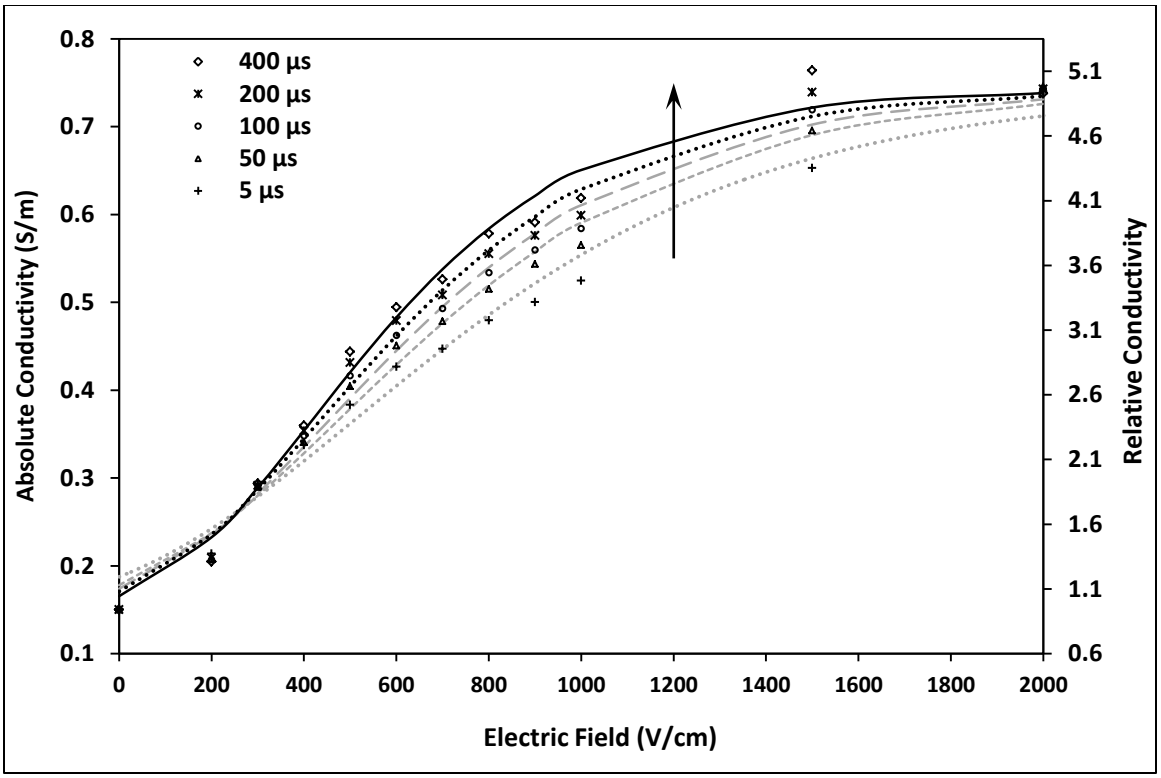

Figure 6.4: Average electrical conductivity versus electric field at various intrapulse time points and σ(E) function fits (dashed lines) at 24±2°C (**n ≥ 6** per electric field).

Table 6.2: Gompertz Function Coefficients to Fit σ(E,t)

Time t, µs	σ_{max}	A	B	R^2
5	0.740	2.75976	0.001974	0.9911
50	0.746	3.05271	0.00233	0.9944
100	0.744	3.21166	0.002543	0.9950
200	0.743	3.34856	0.002751	0.9947
400	0.738	3.64458	0.003071	0.9937

Joule heating's possible role in the intrapulse conductivity increases observed for the 500 to 1500 V/cm electric field pulses was examined. Analytical and numerical techniques representing a single 2000 V/cm (500 µs) pulse resulted in maximum temperature increases of 3.81 and 3.55°C, respectively, leading to predicted electrical conductivity increases of 6.5 and 5.7% using a 1.7 %°C^{-1} temperature coefficient (**Table 6.1**). This predicted increase is lower than the 20% intrapulse conductivity observed for the 1500 V/cm pulses. Therefore, the conductivity increase observed for 500 to 1500

V/cm electric fields during the pulse likely results from some process beyond temperature-based conductivity increase, such as continued membrane pore formation or expansion.

6.4.1.2 Multiple Pulse Effects

The existence of a "memory effect" from electroporation protocols has been observed [205]. In addition, the accumulation of many pulses will cause greater increases in temperature, and may play a more significant role on electrical conductivity than for a single pulse. Cumulative conductivity and thermal effects were evaluated for a complete 200 pulse protocol, with each pulse 100 μs long delivered at a rate of 1 pulse per second. The conductivity of each captured pulse was averaged between 80 and 82.5 μs after pulse onset. The relative conductivities and measured temperatures are displayed in **Figure 6.5**. A maximum increase in conductivity of 10 to 12% occurred for 1100 and 1600 V/cm trials, respectively, despite a higher increase in temperature for 1600 V/cm. There was no appreciable conductivity change at 600 V/cm. It is possible that the observed increases in relative conductivity are a cumulative result of an electroporation memory effect that exists for the irreversible realm of EP, but is not present at the lower 600 V/cm realm. However, if one were to assume the increase in electrical conductivity was solely a result of temperature increase, it would result in a temperature coefficient of 0.988±0.187 $\%°C^{-1}$ V/cm; a value near typical temperature coefficients of 1 to 3 $\%°C^{-1}$ [195].

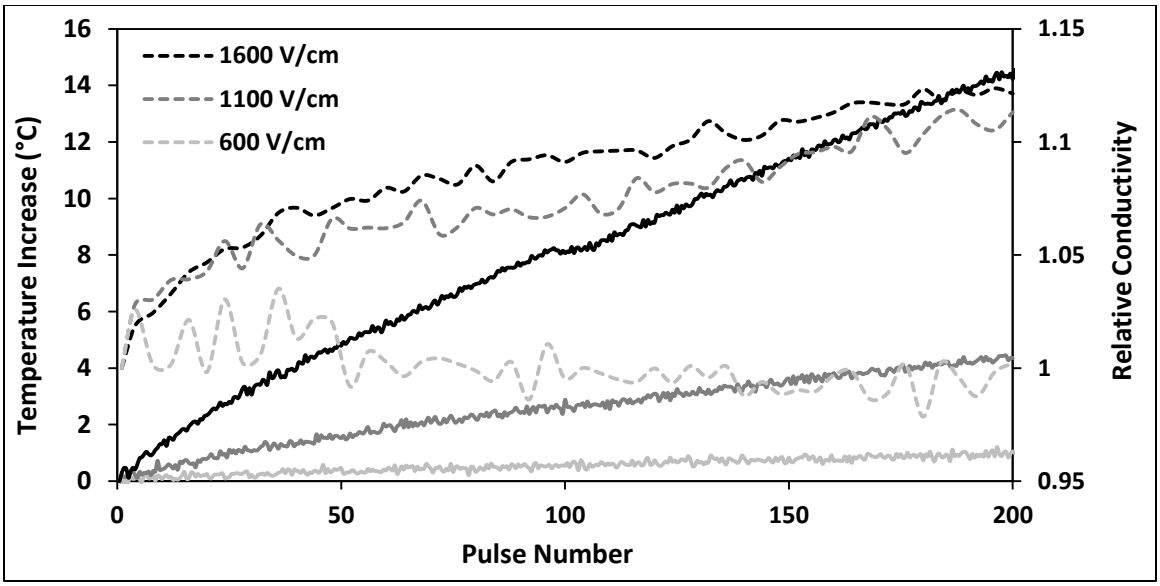

Figure 6.5: Experimental temperature rise (solid lines, **n ≥ 6**) and relative conductivity (dashed lines, **n ≥ 6**) versus pulse number for experimental multiple pulse IRE protocols.

6.4.2 Revised Circuit Model

Tissue conductivity as a function of electric field, $\sigma_t(E)$ measured in this study from the single and multiple pulse trials can be used with published $\sigma(T)$ values to calculate the equivalent circuit resistance, $R_t(E,T)$ with the inclusion of the cell constant, K.

$$R_t(E,T) = \frac{\rho_t(E,T)}{K} = \frac{1}{\sigma_t(E,T)\cdot K}$$
$$= [[\sigma_0 + (\sigma_{max} - \sigma_0)\cdot \exp(-A\cdot \exp(-B\cdot E))]\big(1+\alpha(T-T_0)\big)\cdot K]^{-1} \quad (6.10)$$

where T_0 is the ambient temperature at which σ_0 and σ_{max} were measured. If one assumes a spherical cell with a 25 μm diameter, the cell constant becomes roughly 20 μm. If one assumed all cumulative increases in conductivity observed from our multiple pulse experiments resulted from temperature increase, we obtain an average α of 1%°C^{-1}. Using the $\sigma(E)$ function for a 100 μs pulse, the equation has been solved for resistances at 22, 37, and 50°C (**Figure 6.6**).

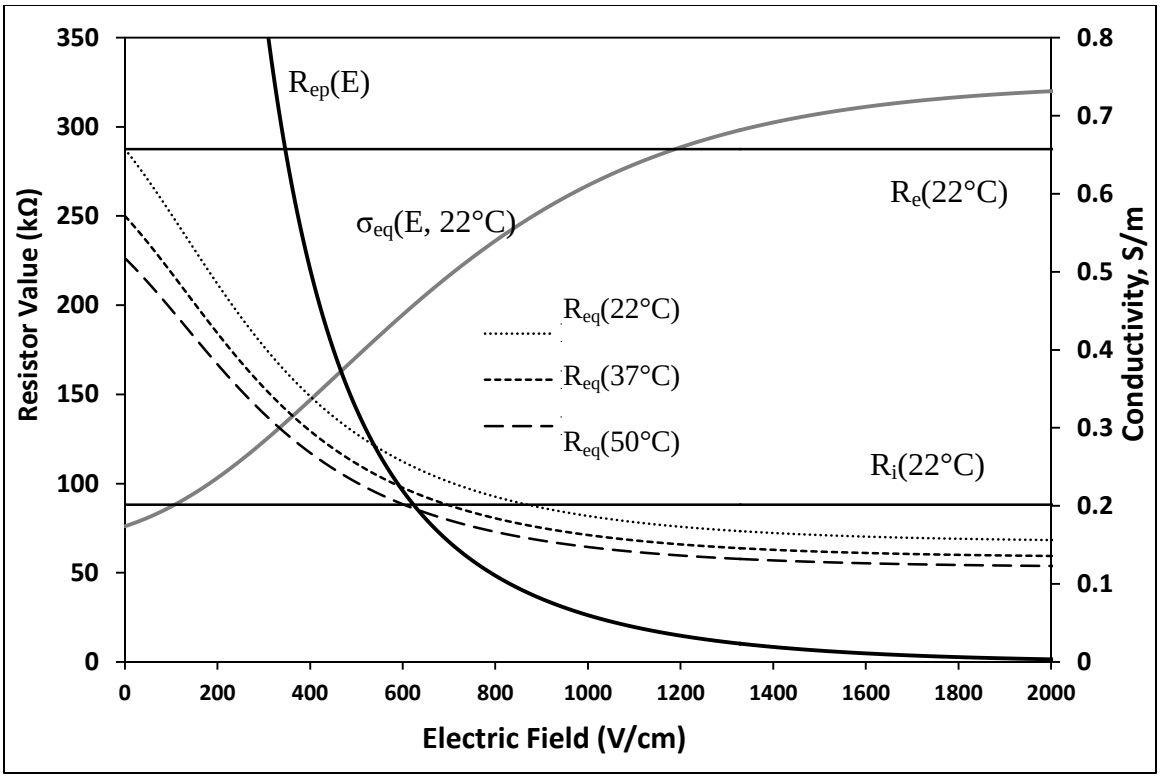

Figure 6.6. Conductivity and equivalent resistance versus electric field at multiple temperatures.

Further examination of the equivalent circuit in **Figure 6.2B** shows two possibilities to bypass the cell membrane's role in bulk tissue conductivity. As mentioned, sufficient electroporation of the cell membrane at high enough electric fields will cause the EP-based resistance to become negligible. However, it is also possible to short-circuit the capacitive component of the cell membrane by approaching a sufficiently high AC frequency. In the MHz frequency range, interfacial polarization of the lipid bilayer occurs in a realm known as β dispersion, where the reactance of the membrane capacitance behaves as a short circuit to membrane resistance [218]. This also makes tissue conductivity a function only of the intra- and extracellular resistances in parallel, meaning this dispersion range should exhibit the same increased conductivity observed when the EP variable resistance is short-circuited.

The two methods to bypass the cell membrane introduces the possibility to use frequency-dependent bioimpedance to estimate σ_0 and σ_{max} values for the $\sigma(E)$ function when developing treatment planning models for other tissues. Such a method would be

done using values from the literature for the desired tissue's conductivity at very low (σ_0) and β dispersion relevant (σ_{max}) frequencies.

6.4.3 Numerical Model

The numerical model was solved to understand the relative impact of the factors considered in this study that could influence EP-based therapy. Analysis of the temperatures for a pulsed model and one averaged found that temperatures and predicted degree of thermal damage follow similar patterns, with the averaging technique producing slightly lower thermal effects (data not shown). The greatest discrepancy occurs at the tissue-electrode interface, and decreases rapidly away from this location, which is more representative of what most tissue will experience. The averaged method solved 31 times faster. Due to the similarity in solutions, and the calculation savings, we performed our analyses using the averaging technique.

The first simulation examined the effect of considering pulse lengths from **Figure 6.4**. The volume of tissue exposed to electric fields from reversible EP realms (200 V/cm) to the EP plateau observed in the experimental results (2000 V/cm), are presented in **Figure 6.7**. It can be seen that adding any $\sigma(E)$ plays a greater role in affected volume than pulse length. Only the $\sigma(E)$ for a 100 µs pulse was used in the remaining analyses.

From our multiple pulse trials, it is possible to develop a σ(n) equation to describe increase in tissue conductivity as a function of the number of pulses, considering previously reported memory effects for multiple pulse protocols. However, the reasonable relationship between the increases in conductivity and temperature for the multiple pulse protocols led us to consider all long-term effects on conductivity to be related to the temperature rise in the tissue for our models.

Analysis of EP-based and temperature effects on treatment outcome for a 100 pulse treatment was performed. The electric field distribution and final conductivity maps may be seen in **Figure 6.8**. Here, it is clear that the electric field distribution increases and alters its shape more significantly when EP is taken into account versus the nominal and thermal-only distributions. The largest electrical conductivities were in the combined

scenario, *σ(E,T)*, where the original increases in conductivity from led to increased Joule heating and greater thermal-induced increases in conductivity.

Tissue exposures were calculated for 100 pulses with thermal effects (**Figure 6.7**). Percent change versus the σ_0 model is presented in **Table 6.2**. 43°C is a common threshold for prolonged exposure thermal damage [219], while 50°C is begins rapid thermal damage [219]. The σ_0 model never reached either temperature, while *σ(T)* had 0.0271 cm^3 exposed to 43°C. The *σ(E)* and σ(E,T) models had 1.17 and 1.63 (43°C) as well as 0.144 and 0.371 (50°C) cm^3 exposure volumes for 43 and 50°C, respectively. Volumes at 500 V/cm (a typical IRE threshold [8]) increased as more effects were modeled.

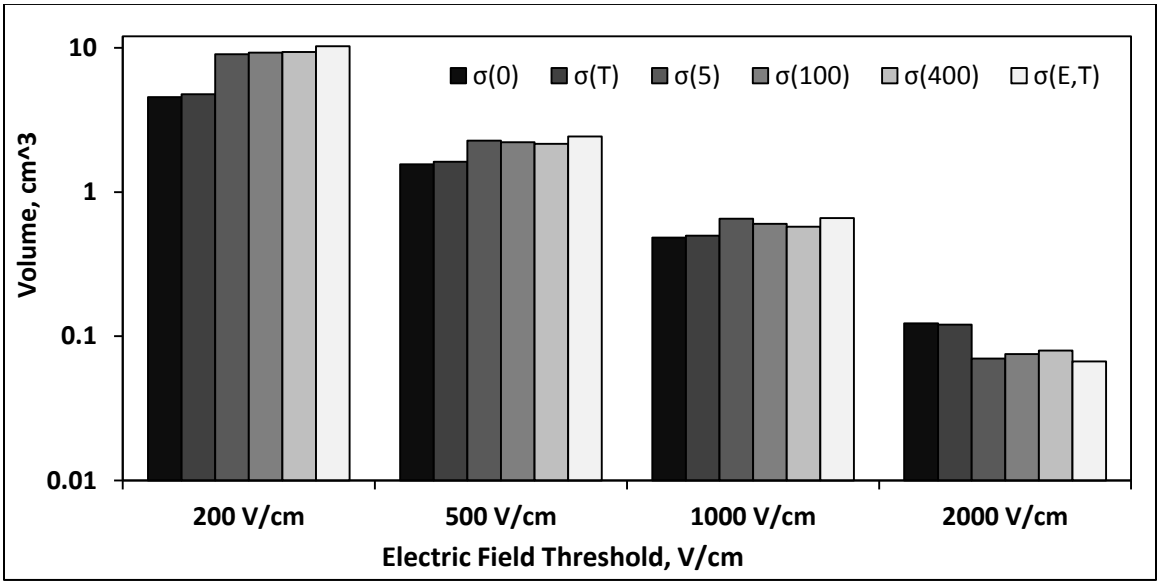

Figure 6.7: Volume of exposure versus electric field threshold for conductivity functions based at different time points, σ(0, 5, 100, and 400 μs) and a 100 pulse treatment using 100 μs long pulses at 1 pulse per second incorporating thermal, σ(T), and combined effects, σ(E,T).

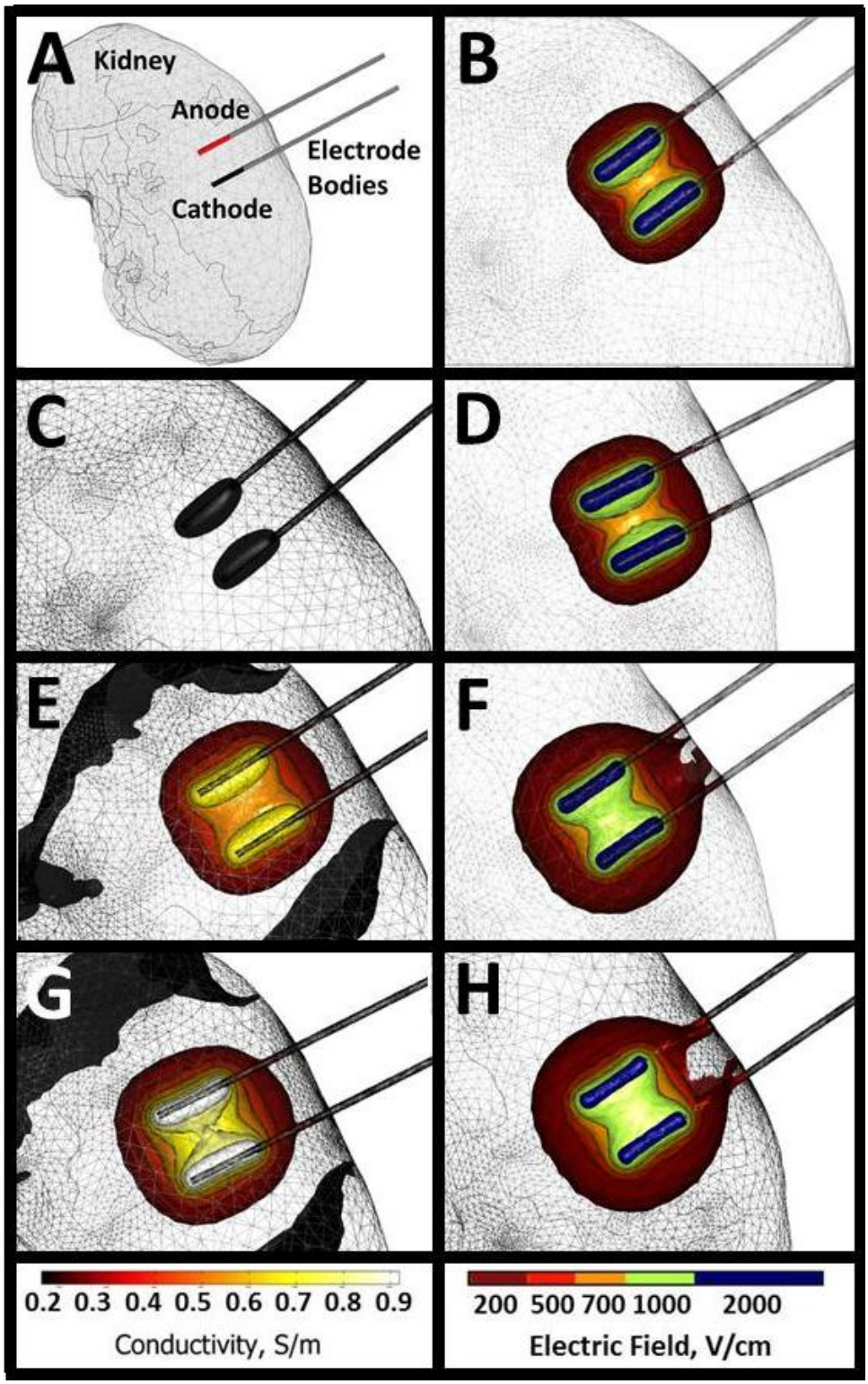

Figure 6.8: (A) Numerical model setup. (B,D,F,H) Electric field and (C,E,G) electrical conductivity distributions for the numerical model for (B) σ_0; (C,D) $\sigma(T)$; (E,F) $\sigma(E)$; and (G,H) $\sigma(E,T)$ numerical simulation scenarios.

Table 6.3: Percent Volume Change v. Nominal σ_0 Model with σ(100 µs)

Model	200 V/cm	500 V/cm	1000 V/cm	2000 V/cm
σ(T)	4.812	4.156	3.270	-2.112
σ(E)	103.2	42.78	24.67	-38.95
σ(E,T)	125.5	55.85	36.56	-45.48

6.5 Discussion

This investigation explored the role of EP-dependent tissue properties to better understand tissue response and improve the accuracy of numerical treatment planning. *Ex vivo* tissue was used to reduce the number of animals expended for testing by utilizing tissues from animals euthanized for unrelated studies. There are two processes that affect post-mortem conductivity. The first results from a rapid redistribution of blood volume, which may be similar to the temporary vascular occlusion effects that occur due to electroporation [4, 220]. The second occurs over several hours due to cellular changes [195]. Electrical conductivity in bovine kidney showed similar values at 1.5 and 5.2 hours post-mortem [221]. Feline kidney conductivity *ex vivo* and *in vivo* was similar at 10 kHz relative to the conductivity changes in this study [222]. Where all experiments were performed within 2 hours post-mortem, the findings should provide a suitable representation of *in vivo* kidney behavior in response to the electric pulses. Isolated explanted tissues also enabled characterization of uniform samples, permitting accurate translation of the voltage and current data into conductivity without any interfering macroscopic anatomical structures.

It should be noted that the *σ(E)* curve and relative conductivity values used a baseline conductivity *σ(0)* from the literature for *in vivo* feline renal tissue, which has a higher cellular fat content than porcine tissue, likely making the tissue more resistive. However, this region of the curve is at the lowest realm of the EP effects (0 to 200 V/cm), where changes to numerical models will be the least, and the value seems to fall reasonably in line with our data trend.

Another assumption in our study is that the resulting conductivity and electric field distribution of interest in the numerical models is based on the behavior observed within

the pulse, ignoring spikes at the beginning and end of the pulses. This is because the spike temporal space is small relative to the length of the pulse. Previous investigations have shown predicted electric field distribution within the pulse correlates with lesion dimensions [17], suggesting that IREs effects are related to the intrapulse electric field. It should be noted that this does not eliminate the need to understand interpulse conductivity distributions in heterogeneous systems.

We used *ex vivo* core samples of renal cortical tissue to eliminate variability caused by macroscopic heterogeneities, such as the outer kidney fascia, collecting system, and ureter; all of which were also neglected in the current numerical model. Actual treatments will contain such large-scale heterogeneities, especially in tumor therapy, where tumors tend to have distinct electrical properties relative to their environment [195]. Furthermore, although we consider the renal cortical tissue to be relatively homogeneous for this study, there are significant microscopic heterogeneities present in this and all other tissues, such as microvasculature, glomeruli, nephron tubules, all of which will have distinct electrical properties and differences in response to the pulsed electric fields. As imaging improves to better observe these macro- and micro-heterogeneities prior to treatment, and numerical simulations can account for their presence, treatment planning should include their presence to obtain the most representative conditions for predicting treatment effects.

In addition to different initial tissue properties, large deviations in relative conductivity change have been reported for different tissues at the macro- and micro-levels [204]. This can be explained by accounting for concepts such as the packed density of cells relative to extracellular components. Tightly packed cells will reduce the path for current to flow, leading to large extracellular resistance. Upon cell electroporation, membrane resistance decreases, resulting in a larger increase in relative conductivity compared to tissue with sparsely packed cells. Further work examining the effects of electric pulses on electrical conductivity in other tissues is needed. The most accurate treatment planning models would combine inherent tissue property heterogeneities and their unique response to pulsed electric fields.

This study examined the possibility to use an equivalent circuit model to correlate the conductivity plateau from substantial cell membrane electroporation with the increase in conductivity due to short-circuiting the capacitive component of the cell membrane at β dispersion frequencies. Values in the literature for kidney conductivity in the MHz range approach approximately 0.6 S/m at 10 MHz up to 0.77 S/m at 500 MHz [223, 224]. These values are in good agreement with the maximum conductivity of 0.74 S/m found in this study at 2000 V/cm during a single pulse. An additional preliminary correlation can be drawn from published literature to support our hypothesis. In [205], rat liver experiments show a conductivity increase of approximately 3.8x from their nominal σ_0. Comparatively, work on *in vivo* cat liver tissue [195] shows an increase of 4.2x at 50 MHz. This similarity is further supported by the fact that our study showed conductivity continued to increase up to 2000 V/cm. Because the 3.8x increase was observed at 1500 V/cm, it is likely that at 2000 V/cm, the relative change in liver conductivity would increase, further approaching the 4.2x.

Despite the very different phenomenon causing increased conductivity, there appears to be a strong correlation between the effects on bulk tissue conductivity from EP pulsed electric fields and β dispersion frequencies. This provides promising support for the ability to use the equivalent circuit characteristics to attain a reasonable approximation for tissue change in conductivity during EP. Such a technique for estimating these effects is highly desirable due to the varied nature of tissue property response to EP, and the relative scarcity of data characterizing these effects explicitly using EP. Such a method could provide reasonable values for numerical simulation treatment planning until sufficient experimental data exists in the literature. Further, if future work continues to support this correlation, it may be possible to solely use this relationship to derive appropriate $\sigma(E)$ functions for treatment planning, sparing the financial burden and cost to life that such thorough characterization requires.

We hypothesize that accounting for temperature and EP dependence of tissue conductivity will improve the accuracy of numerical models for treatment planning. Ivorra *et al.* [225] showed that a numerical model accounting for EP-induced conductivity changes improved the accuracy of the predictions in potato tuber. Here, we

present experimental characterization of the tissue electrical conductivity and describe how it changes numerical simulations. Future studies should correlate predictions from these results with *in vivo* IRE procedures.

Previous investigations mapping the change in tissue conductivity as a function of electric field included basic step functions, linear functions, and exponential functions [203, 204]. These methods assume conductivity change from a nominal value up to a maximum plateau. Here, we found that the increase in conductivity was similar in general shape to a sigmoid function, but the over-weighted increase at the initiation of EP onset (lower electric fields) made an asymmetrical Gompertz curve the most appropriate fit. This curve fits the conductivity from a baseline value up to a maximum plateau. As discussed in [210], this progressive approach for high electric fields at a given temperature likely results from the sudden increase in electrolyte mobility across the lipid membrane, locally reducing membrane capacitance and transmembrane potential. Therefore, external electric fields must be high enough to maintain adequate transmembrane potential to further increase the number of electroporated cells, membrane defects, or size of the defects.

The fact that electrical conductivity appears to reach an upper limit is likely related to the composition of adjuvant tissue structures. Once cell membranes have developed adequate aqueous pathways, the conductivity becomes a function solely of the intracellular and extracellular resistances. Biological fluids such as blood and interstitial fluid have conductivities between 0.8 and 1.9 S/m [195]. If tissue was composed entirely of fluid, this value would serve as an absolute maximum that the conductivity can reach. However, even if all of the cells become completely permeabilized, inherent resistance from support structures such as the extracellular matrix will contribute to tissue resistance. The presence of such structures therefore likely introduces the electrical conductivity plateau reached in the tissue, explaining why it is below that of pure isotonic fluids.

One important observation from our experimental results includes the apparent anomaly for the 2000 V/cm electric pulses. Although these data followed the trend of

reaching a higher electrical conductivity for the higher electric field, all trials at this field did not show the intrapulse conductivity increase observed at electric fields between 500 and 1500 V/cm. It is difficult to discriminate the exact cause for this deviation in behavior. Most previous investigations on intrapulse electric conductivity increase do not approach 2000 V/cm. One speculative explanation could be that we were reaching the upper limits of our equipment and experimental protocol. An additional possibility is that the high field caused some secondary biophysical change that prevented a further increase in conductivity, such as hydrolysis or protein denaturation at the tissue-electrode interface, where boundary effects would cause locally higher temperatures than those measured at the center of the tissue.

EP-based conductivity changes were more significant than thermal effects on electric field distribution using a conductivity temperature coefficient of 1.7 $\%°C^{-1}$. This point is further supported when one considers a correlated α value from our multiple pulse trials of ~1 $\%°C^{-1}$.

Incorporation of the $\sigma(E)$ function was found to increase the volume of tissue exposed to 200, 500, and 1000 V/cm, but decrease the volume for 2000 V/cm. This may be due the local increase in conductivity to the maximum value that occurs nearest the electrodes, as seen in **Figure 6.7**. This region of high conductivity will incur a lower voltage drop, reducing the electric field. This explanation was supported by analyzing the volume of tissue exposure for $\sigma(T)$ and $\sigma(E,T)$ models over time, where temperature continues to increase tissue electrical conductivity (data not shown). As conductivities increased due to temperature, the volume of tissue exposed to 2000 V/cm decreased, while the 200, 500, and 1000 V/cm volumes increased. This provides evidence for the importance of including thermal effects in treatment planning models..

6.6 Conclusion

This study experimentally characterized tissue impedance behavior in response to electrical pulse protocols common for EP therapies. We determined tissue conductivity as a function of electric field, temperature, and pulse duration using fresh core samples of *ex vivo* porcine renal cortex. Conductivity versus electric field was fit to an asymmetrical

sigmoidal curve for pulse lengths between 5 and 400 μs. We derived representative equations and values for an equivalent circuit model of cell electrical behavior, including an EP-based, variable resistance. We also examined the ability to use the equivalent circuit model as a means to estimate the necessary parameters for conductivity functions in other tissues, based on the β dispersion characteristics of these tissues. We used the conductivity function in a numerical model to simulate IRE therapy in a healthy kidney for scenarios that account for thermal and EP effects. The model conveyed the significance of including these factors in the predicted treatment outcome, including an increase in volume for EP and IRE relevant fields, with a decrease for very high electric fields. Using a model that accounts for these changes should improve the accuracy of numerical models in treatment planning. This should enable therapeutic IRE applications to better ensure treatment of the entire targeted region while minimizing damage to the neighboring healthy tissues, a key aspect to developing IRE into a robust, reliable therapy for the treatment of localized regions of disease.

Acknowledgment

The authors acknowledge Chris Arena, Mike Sano, and John Caldwell for their assistance with the instrumentation

Chapter 7: Treatment Planning for Clinical Irreversible Electroporation Therapy

7.1 Introduction

Simple predictions of superimposed treatment regions for complex electrode geometry protocols are difficult to visualize when managing a complex case in real-time. In order to effectively and reliably use IRE and other electroporation based therapies, it is critical for practitioners to be able to develop and implement treatment protocols capable of treating the entire targeted region while sparing the neighboring healthy tissue. Treatment planning techniques that aid or allow a practitioner to develop treatment protocols for complex clinical tumors is essential to capitalize on the great therapeutic potential for IRE and other EBTs. In this chapter, several techniques to predict electroporation treatment outcomes are discussed, including simple solutions that may be adjusted in real-time as well as numerical solutions capable of accounting for the complexities often present in clinical cases, such as dynamic tissue electrical properties and heterogeneous environments.

7.2 Background

In electroporation based therapies, ensuring adequate coverage of the targeted region while sparing undesirable tissues is vital to therapeutic success. Electrode and pulse parameters (including electrode geometry and orientation, number of pulses, pulse length, repetition rate, pulse shape, applied voltage) will have a large impact on the affected areas, with typical therapeutic geometries ellipsoidal in shape. Many tumors encountered in clinical cases can be highly irregular in shape and do not readily fit the shapes created by a single electrode setup. Such irregular targeted geometries require a complex array of electrodes and pulse parameters arranged in a specific manner to satisfy the clinical procedure objectives.

The numerical techniques presented in the previous section allow for the prediction of the electric field distribution ahead of time, along with the associated thermal effects, and permit the planning of treatments preoperatively. These simulations are capable of

modeling how the tissue properties change as a result of the procedure itself, both due to the increase in conductivity resulting from higher temperatures as well as increased ion mobility in tissue that occurs from pore formation [226]. The models can further account for fixed characteristics including pulse properties as well as electrode geometry and placement. Case studies on multiple electrode geometries and voltages for parallel plate and needle electrode have been performed in [227] where dimensional analysis is implemented on the parameters to develop curves for predicted treatment volumes and heat dissipation based on characteristic constants. In addition, discussions are included on anecdotal effects for heterogeneities, thermal effects, and evaluating thermal damage.

In addition to treating the entirety of the targeted region, there are several additional factors that must be taken into consideration. Physical access barriers, such as bones or vital organs will complicate treatment implementation by restricting viable access points for some treatments. Furthermore, identification of highly sensitive and vital structures, such as major arteries or nerves, should be considered to prioritize increased caution regarding any potential thermal damage to these tissues. These considerations must be accounted for when developing and implementing electroporation based therapy protocols. This chapter discusses some of the techniques that may be used to facilitate and assist developing treatment protocols by allowing treatment planning prior to administration of the therapy and adjustment based on any deviations from the initial plans or other unforeseen challenges to following through with the initial plan. Finally, it uses an example treatment plan to introduce and discuss a step-by-step process that may be used in treatment planning when developing treatment protocols.

7.3 Rapid Solution Techniques

There is extensive literature that has presented sample electric field and temperature distributions for a wide array of treatment scenarios. In [12], the authors provide normalized, tentative guidelines to practitioners for what volumes of exposure they may expect when using a typical electrode geometry in order to aid them in planning treatments. While useful, oftentimes planned treatments will encounter new variables during implementation of the procedure. This can arise from a variety of sources, such as

disease progression from the time of the scans used to develop the treatment plan or the inherent error placing electrodes in their exact prescribed locations and orientations relative to the body and targeted tissues. Therefore, it is desirable to enable practitioners to adjust their protocols ‘on the fly’ in order to account for any such variations. Furthermore, although sample images and tables of predicted lesions will give some perspective to a clinician for anticipated therapeutic volumes, it is important to enable them to visualize and intuitively understand how treatment volumes will be affected by changing electrode geometries or applied voltages.

Although predicted treatment volumes can developed and examined using numerical methods, typical clinicians will not be versed in using finite element modeling software. In addition, such methods often require considerable time and computational power, making it difficult to quickly adjust protocols to sufficiently ensure complete treatment of the targeted region. These factors promote the need to rapidly calculate and show predicted lesion dimensions that may be adjusted and provide feedback in real-time.

It has been shown that treatment volumes may be superimposed when using more than two electrodes [43]. The complex and difficult to spatially recognize treatment patterns that will occur when using multiple electrodes further promote the need for a clinician to be able to adjust treatment protocols in real-time. In this section, an introduction to rapid solution techniques is provided as well as a discussion on their utility and inherent limitations.

7.3.1 Analytical Equations

Analytical equations provide closed form solutions to mathematical problems that can be solved exactly and quickly in relatively simple cases, making them a great technique to allow a practitioner to adjust their treatment protocol and solve for the electric field distribution in real-time. There have been several studies comparing the use of analytical and numerical solutions when evaluating the electric field distribution from a given electrode array and voltage [228-230]. Here, the techniques described in [231]

and expanded in [229] are explained and compared to numerical simulations for two electrode geometries and applied voltages.

The analytical solution described here assumes two needle electrodes and solves for the electric potential and field assuming the needles to be infinite cylinders, an assumption that holds when electrode diameters are much smaller than their length. It also assumes a homogeneous conductivity of the tissue that the electrodes are in. The basic equation for the electric potential at any point in the tissue (x,y) plane is the solution to Laplace's equation:

$$\nabla^2 \Phi(x, y) = 0 \tag{7.1}$$

where Φ is the electric potential. For convenience, the system is converted to the imaginary plane where $z = x + iy$. Due to superposition, the total electric potential at a given point is the sum of the potentials generated by each electrode, which is calculated by

$$\Phi(z) = \sum_{n=1}^{N} \Phi_n(z) \tag{7.2}$$

where

$$\Phi_n(z) = C_n \cdot \ln\left(\frac{a}{z - z_n}\right) + \sum_{k=1}^{\infty} A_{nk}\left(\frac{a}{z - z_n}\right)^k \tag{7.3}$$

$$z_n = r_n \cdot e^{i(n-1)\theta} \tag{7.4}$$

where $\Phi_n(z)$ is the electric potential generated by the nth electrode, C_n is a coefficient based on the voltage and geometry of the electrode setup, a is the electrode radius, r_n is the distance to the nth electrode from the origin, and θ is the angular separation between two adjacent electrodes. It has been shown in [229, 230] that including 1st order and higher corrections result in marginal change to the solution relative to the leading order

term when $r_n >> a$. Therefore, this term will be ignored. Further, we will only consider the electric potential and field between two electrodes, located at z_1 and z_2. For a potential drop of V_0 between the two electrodes, we set electrode 1 to be energized at $+V_0/2$ and electrode 2 energized at $-V_0/2$. Solving for the coefficient C of these electrodes gives:

$$C_1 = -C_2 = \frac{V_0}{2 \cdot ln\left(\frac{b}{a}\right)} \tag{7.5}$$

where *b* is the separation distance between the electrodes. Using these coefficients, the leading order electric potential becomes:

$$\Phi^0(z) = \frac{V_0}{2 \cdot ln\left(\frac{b}{a}\right)} \cdot \ln\left(\frac{z - z_2}{z - z_1}\right) \tag{7.6}$$

which can be differentiated to provide the leading term electric field at any given point, z.

$$E^0(z) = \frac{V_0}{2 \cdot ln\left(\frac{b}{a}\right)} \cdot \left(\frac{1}{z - z_1} + \frac{1}{z - z_2}\right) \tag{7.7}$$

This equation has been incorporated into a simple table to provide solutions for two electroporation scenarios. The first one positions 1 mm diameter electrodes at (±0.0075, 0) (units in meters), with 2250 V applied (1500 V/cm voltage-to-distance ratio), while the second places 2 mm diameter electrodes at (0.0025, -0.01) and (-0.0075, 0.02), using an applied voltage of 3000 V (948 V/cm voltage-to-distance ratio).

Numerical simulations using exactly the same electrode geometries and applied voltages were created for comparison to the analytical simulations using Comsol Multiphysics (Comsol, Stockholm, Sweden). The resulting predicted electric field distributions may be found in **Figure 7.1**, where similar shapes are notable. In addition, plots of electric field along the x- and y-axes for all models were created and may be seen in **Figure 7.2**, where it can be seen that the analytical and numerical solutions match best

in regions between the electrodes, and have greater differences as one moves away from the electrodes.

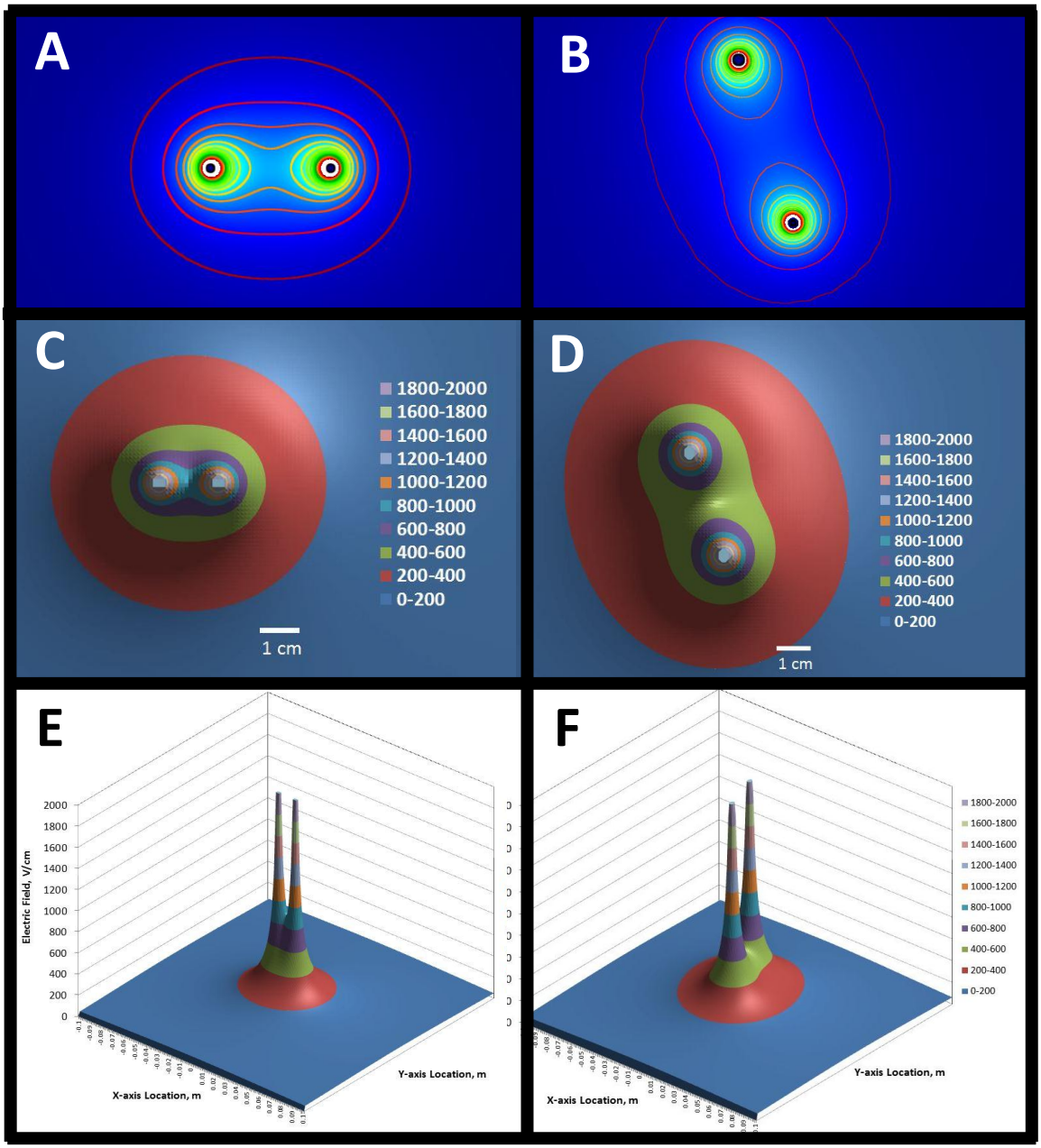

Figure 7.1: Electric field distributions for (A,B) numerical and (C-F) analytical solutions for (A,C.D) simple case of electrodes 1 mm electrodes located at (±0.0075, 0) with 2250 V applied; and (B,E,F) more complicated case of electrodes located at (0.0025, -0.01) and (-0.0075, 0.02), using an applied voltage of 3000 V. (A-D) provide overhead view into plate of electrodes, while (E,F) provides a 3-dimensional spatial depiction of electric field. * Contour separations in A, B are identical to those in C-F.

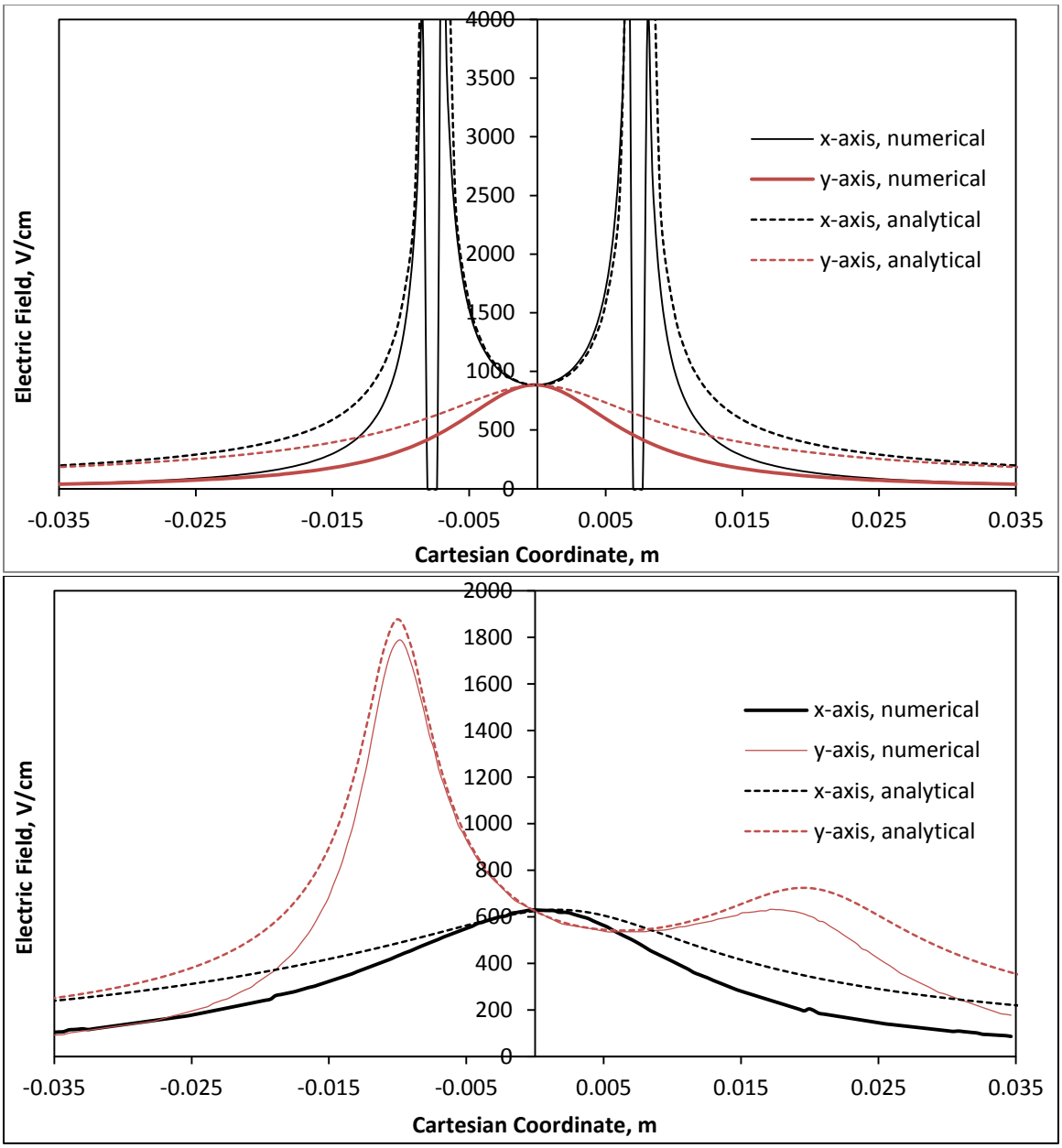

Figure 7.2: Electric field of numerical and analytical models along x- (black) and y-axes (red) for (A) simple case of electrodes 1 mm electrodes located at (±0.0075, 0) with 2250 V applied and (B) more complicated case of electrodes located at (0.0025, -0.01) and (-0.0075, 0.02), using an applied voltage of 3000 V.

7.3.2 Cassini Oval Approximations of Numerical Solutions

From the above results, one can conclude that a pure analytical solver will give reasonably accurate predictions of electric field, especially in the regions between the electrodes. However, such an analytical solution can still be difficult to solve and plot predicted lesion areas for the electrodes if one were to move the voltage or electrode

position in real-time. In an effort to further reduce calculation and display time, we present an additional technique to solve for electric field distributions based on calibrating an equation that mimics the shape and behavior of potential fields. This is shown here using an adaptation of the cassini oval equation.

7.3.2.1 Basic Shape

The cassini oval is a plane curve that derives its set of values based on the distance of any given point, *a*, from the fixed location of two foci, q_1 and q_2, located at (x_1, y_1) and (x_2, y_2). The equation is similar to that of an ellipse, except that it is based on the product of distances from the foci, rather than the sum. This makes the equation for such an oval

$$[(x_1 - a)^2 + (y_1 - a)^2] \cdot [(x_2 - a)^2 + (y_2 - a)^2] = b^4 \tag{7.8}$$

where b^4 is a scaling factor to determine the value at any given point. For incorporation of this equation into rapidly solving for a shape to mimic the electric field distribution, it is possible to simplify the equation by rotating the cartesian axes to where the x-axis falls between y_1 and y_2 and make the origin equidistant from x_1 and x_2, i.e. $x = (x_1 + x_2)/2$, making the foci located at $(\pm x, 0)$. From here, the equation can be converted to its polar form

$$r^4 - 2 \cdot a^2 \cdot r^2 \cdot \cos(2\theta) = b^4 - a^4 \tag{7.9}$$

by solving this equation in terms of r as a function of θ, it is possible to create a plane curve with a geometry scaled to the *b* term, which may be deemed as a gain denominator. The scaling term may then be derived as a function of the pulse and tissue parameters, such as separation distance, applied voltage, and electric field threshold. This has been performed to calibrate the basic cassini equation to numerical models of the same setup.

7.3.2.2 Initial Calibration Algorithm:

The Cassini oval creates a reasonable visualization that mimics the shape of numerical results for the distribution of the electric field. However, in order to understand which values or levels correspond to a desired electric field of interest, a calibration

involving the b^4 term was necessary to develop the relationship between the analytical Cassini oval and the numerical results. This was done through an empirical backwards calibration process defined as follows:

1. A reference contour was selected to correlate the analytical and numerical solutions. This was chosen to be when b/a=1, forming a lemniscate of Bernoulli (the point where the two ellipses first connect, forming "∞"); where a is the separation distance between the two foci.
2. A reference electric field threshold of 650 V/cm was selected to calibrate the numerical simulations with the shapes produced by the cassini oval.
3. Numerical models were developed to mimic the x-y output from the Cassini oval for scenarios where a = ± 0.25, 0.5, 0.75, 1.0, 1.25, 1.5, 1.75, 2.0, 2.25, and *2.5* cm. The tissue properties used are consistent with ones found in the literature for liver (σ=0.286 S/m, ρ=1050 kg/m^3, k=0.512 W/(m•K), and c_p=3600 J/(kg•K))[195]. All models were solved with varying voltage on the energized electrode until the 650 V/cm contour resulted in the shape of a lemniscate of Bernoulli.
4. The determined voltage was placed into the Cassini oval excel worksheet for the same electrode geometry and the "gain denominator" was adjusted until the shape from the cassini oval matched that from the numerical solution. A plot of all corresponding voltages (numerical model) and gain denominators (cassini curve) may be found in **Figure 7.3**.

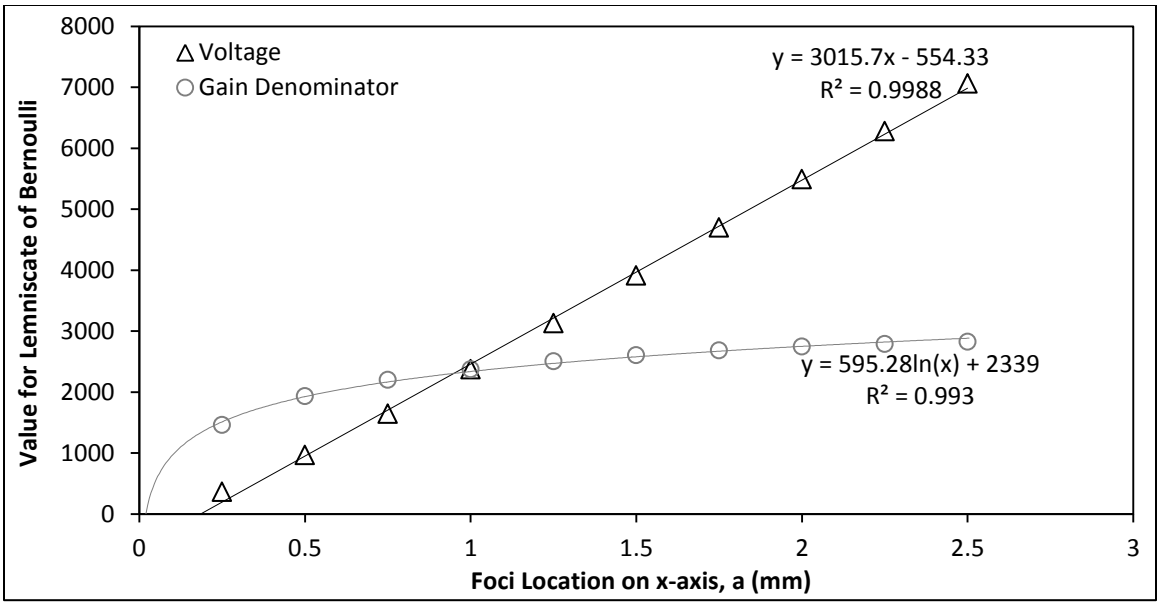

Figure 7.3: Plot of required voltage (numerical model) and gain denominator (cassini approximation) to achieve lemniscate of Bernoulli for given electrode distance from the origin.

5. The determined gain denominators for all values of *a* were collected and a calibration plot was made and fitted with a logarithmic trendline of:

$$\text{Gain Denominator} = 595.28 \bullet \ln(a) + 2339;\ R^2 = 0.993 \qquad (7.10)$$

6. The calibration function was incorporated into the Cassini Oval excel spreadsheet, where it became possible to output an approximated electric field contour of 650 V/cm for any electrode separation distance, $\pm a$, and applied voltage, V.
7. The calibration function was scaled to adjust for variable desired electric field contours. This allowed the cassini approximation to solve for any electric field when given a separation distance and voltage.

The resulting excel worksheet incorporates all the steps above to yield a single, calibrated Cassini Oval output that analytically predicts the electric field distribution; providing a quick and simple solution for the prediction of IRE treatment regions that may be adjusted in real-time. When provided with inputs including the electrode location as a distance, $\pm a$, from the origin along the x-axis, the applied voltage, and the desired electric field, the spreadsheet will calculate and present a set of values to visualize the

approximated shape of the electric field contour. A set of several comparisons between the calibrated cassini ovals and numerical predictions may be found in **Figure 7.4**.

It should be considered that the cassini approximation was calibrated for an electric field contour of 650 V/cm. Due to linearity of the electric field, other contours should still yield reasonable results that mimic the overall shape of the electric field. It is important to note that because the calibrations were performed using the lemniscate of Bernoulli as a reference point, the cassini oval best matches the numerical simulation at electric field strengths near this point, and tends to overestimate the lesion for higher electric fields, which are more relevant to therapeutic tissue ablation. However, as discussed in Chapter 6, incorporating changing conductivity due to temperature and electroporation effects will produce larger lesions than those for static conductivity, so the error between the calibrated cassini curves and true lesions will not be as significant. This is demonstrated in **Figure 7.5**, where the 1 cm separation, 2000 V scenario is repeated with a basic $\sigma(E)$ dynamic conductivity equation. Overall, the cassini curve approximation yields reasonable predictions for electric field contours, and may be solved very rapidly, providing real-time treatment region estimates that may be used during treatment planning or analysis.

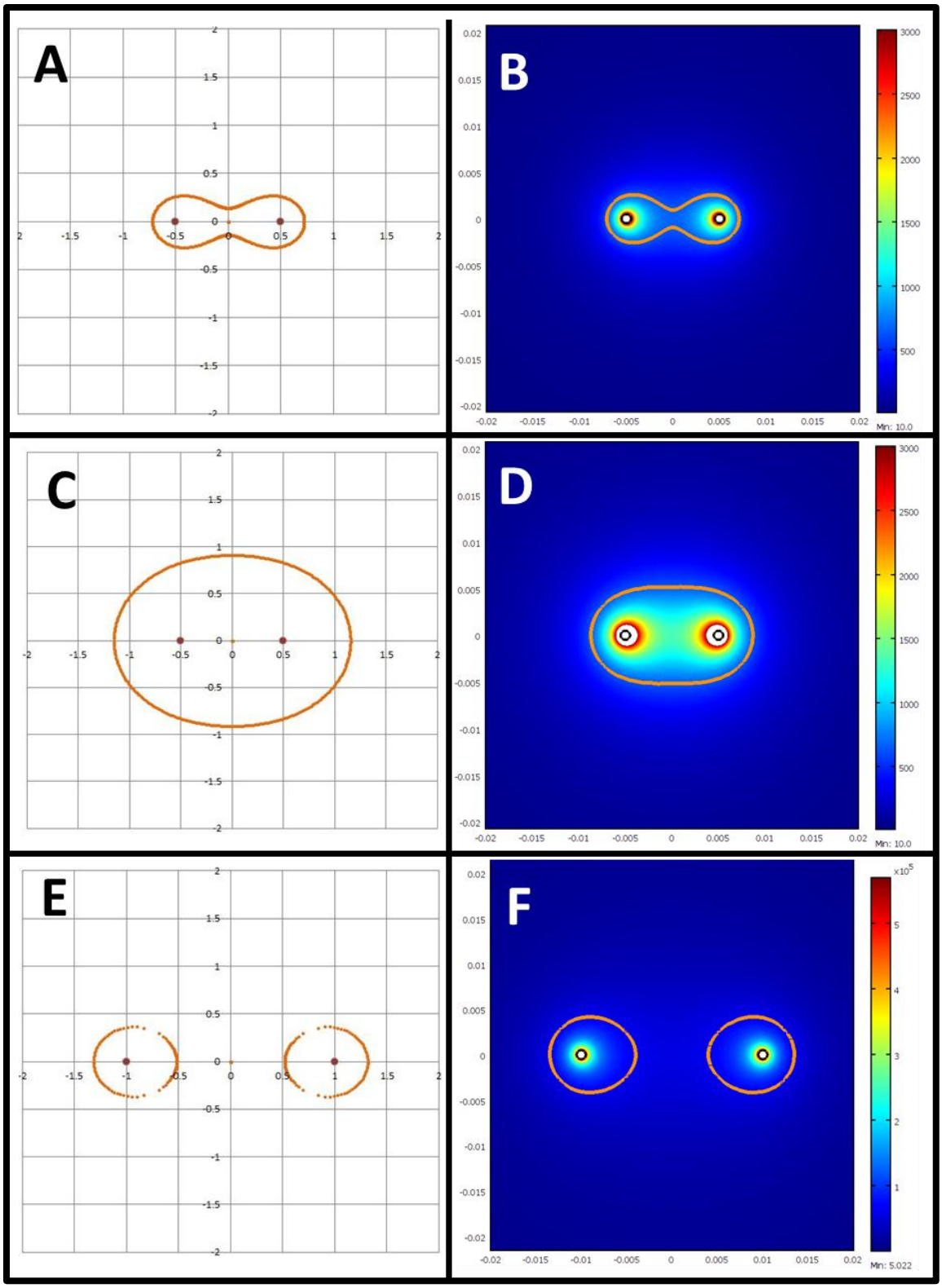

Figure7.4: Sample comparisons between (A, C, E) cassini curve and (B, D, F) numerical simulations for 650 V/cm electric field contour for (A, B) 1 cm separation, 1000 V, (C, D) 1 cm separation, 2000 V, and (E, F) 2 cm separation, 2000 V.

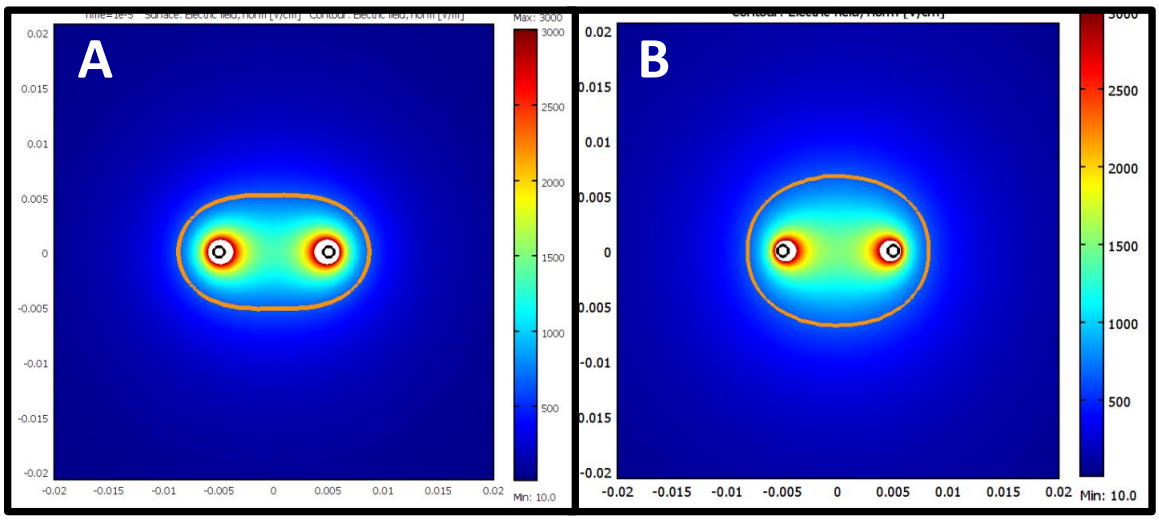

Figure 7.5: Comparison of 1 cm separation, 2000 V case from **Figure 7.4C, 7.4D** above when using (A) static and (B) dynamic conductivities. From here, a clear enlargement of the 650 V/cm contour is present.

7.3.2.3 Incorporation of Complexities

Although the cassini approximation results in reasonable shapes to mimic the results from numerical models of the electric field distribution, there are several differences between the cassini curve and real world situations using needles to deliver electric pulses. Some of these can be accounted for by further manipulations of the gain denominator, *b*, in the equation. This has been performed for several representative situations.

1. Single Needle Electrode

The cassini approximation was designed for two parallel, infinitely long cylindrical electrodes. However, at times it may be appropriate to use a single needle electrode that contains both energized surfaces, such as the one used in Chapter 5. The cassini oval may be adjusted to account for this new orientation of energized surfaces. Adapting the cassini curve to mimic numerical results presents some challenges because the distribution is now resulting from the two exposed cylinder lengths, rather than two distinct loci of points. To account for this, calibrations were performed for electric field contours by manipulating the separation distance ($\pm a$) and gain denominator. This was performed for a single needle electrode of diameter = 1.65 mm, with a 7 mm exposed tip, 8 mm of insulating separation, and 7.5 mm exposed proximal end. The resulting empirical matches were fit to the equations:

$$a = 7 \cdot 10^{-9} \cdot E^3 - 2 \cdot 10^{-5} \cdot E^2 + 0.015 \cdot E + 6.162;\ \mathrm{R2} = 0.981 \qquad (7.11)$$

$$GD = 1.0121 \cdot E + 1920;\ \mathrm{R}^2 = 0.993 \qquad (7.12)$$

where E is the electric field magnitude contour desired. These two equations may then be used to calibrate the cassini ovals into a satisfactory shape to mimic the electric field contours. It should be noted that this process would need to be repeated if the dimensions of the single needle electrode were changed.

2. Exposure Length

The original calibrations for matching the cassini curve to numerical simulations were performed using two dimensional models, simulating cylindrical electrodes of infinite length. This assumption is reasonable for very long electrodes, but progressively breaks down as the exposure length of the electrode is reduced. This effect is demonstrated in **Figure 7.6**.

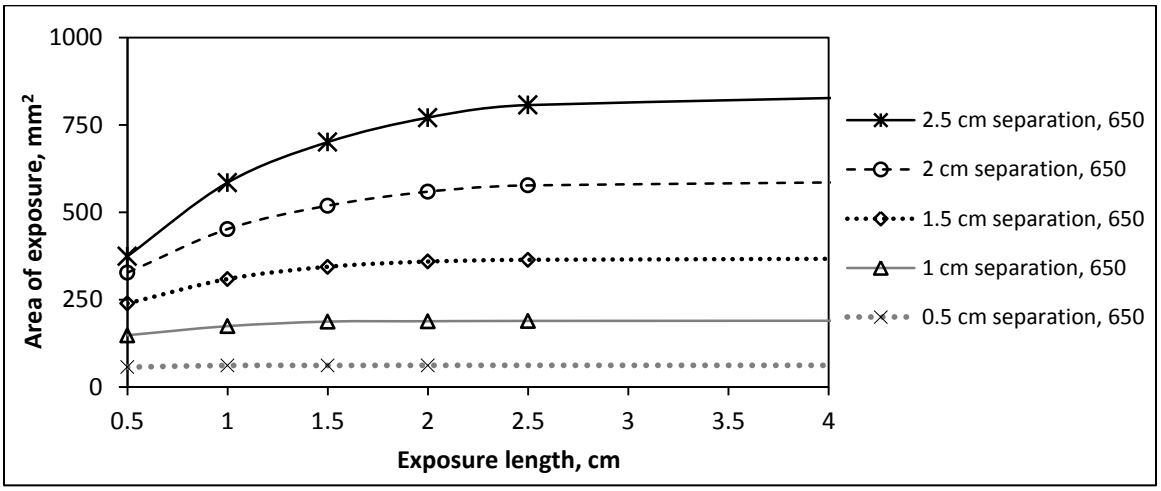

Figure 7.6: Numerically determined area of exposure to 650 V/cm versus electrode exposure length at various separation distances. Areas were taken at the midpoint along the length of the electrodes. Voltages were adjusted to maintain electrode voltage to separation distance ratio of 2500 V/cm.

Electric field contour areas were shown to be directly proportional to exposure length, *L* (cm) and inversely proportional to separation, *S* (cm). One way to account for the additional variable of exposure length is to add a multiplier that goes from 0 to 1 as the exposure length approaches infinity. This multiplier was solved for each separation between 0.5 and 2.5 cm according to the equation:

$$E(L,S) = E(\infty,S) \times \frac{L^m}{S^n} \tag{7.13}$$

where *m* and *n* variables to be solved for, where *m* adjusts the shape and *n* adjusts the size. The *m* and *n* values were adjusted until the cassini approximation produced a curve that matched the numerical solution at exposure lengths from 0.5 to 2.5 cm in 0.5 cm increments and for separation distances between 0.5 and 2.5 cm in 0.5 cm increments.

After tuning the curves, it was determined that *m* changed with each separation and *n* could be reasonably estimated as 0.5 for all S > 1 cm. For S = 1 cm, the *n* term was unable to manipulate the size of the curve. Additionally, for S < 1 cm, *n* was negative. Because *n* does not change predicted dimensions for S = 1 cm, and needed to be negative for S < 1 cm, a different function was required for these cases. The $1/S^n$ term was eliminated for S ≤ 1 cm. and replaced with a *p*(S) term. The resulting equations for the two situations may be found in **Table 7.1**. The way that these equations would be applied to the cassini curve numerical approximations is described in **Table 7.2**.

Table 7.1: Calibration Functions to Account for Electrode Exposure Length

Case	Function	Name
S > 1	$3D(L,S) = 2D \times \frac{L^{(0.17\times S-0.045)}}{S^{0.5}}$	$3D_1$
S ≤ 1	$3D(L,S) = L^{(0.17\times S-0.045)} \times (-0.15 \times S + 1.02)$	$3D_2$

Table 7.2: Applying Calibration Functions to Cassini Approximation

Case:	Function:	Exposure criteria:
S ≤ 1 cm	$3D_2$	L ≤ 2.5 cm
1 < S < 1.5 cm	$3D_1$	L < 2 cm
S > 1.5 cm	$3D_1$	L < 3 cm

7.3.3 Limitations of Analytical Approximations

Although analytical solutions for electric field distribution and strength contours provide a rapid means of predicting treatment outcome that may be adjusted in real-time, there are several limitations to such techniques that must be accounted for when considering the possibility of using such techniques in treatment planning. The first is the

assumption of homogeneous tissue conductivity. As it was shown in Chapter 4, heterogeneous environments will significantly alter predicted electric field and temperature distributions. Although the analytical solution and cassini calibration curves could be adjusted to account for such environments, the prohibitive amount of complexity and wide variety of conductivity distributions that will be encountered essentially eliminate the justification to do so. In addition, as described in Chapter 6, tissue properties will change with electroporation and thermal effects, modifying the electrical conductivity and field distributions, changing predicted treatment outcomes.

The analytical solution is contingent upon the assumption that the length of the electrode is much longer than its diameter. As the electrode length is reduced relative to its diameter, errors will be encountered, similar to those discussed in Section 7.3.2.3. An issue to consider when using the calibrated cassini curves is that the equation is based on the product of a particular location's distance from two foci, q_1 and q_2. These foci are infinitely small points, and the difference between a point and an electrode with a finite diameter will introduce errors as the separation distance between the electrodes is reduced. This was may be somewhat accounted for by re-calibrating the curves to numerical simulations and developing two calibration functions, one for small electrode separations and one for large separations.

An additional limitation to using analytical calculations and calibrated curves of electric field distributions is again related to the finite length of the electrodes. Both methods described above are designed to solve for the electric field distribution at the midpoint along the electrode length. However, this distribution will change with a decrease in electric field near the tips of the electrodes. It is possible for this to be accounted for by performing additional calibrations and adding scaling terms to the cassini approximation. The above techniques also do not provide a method for determining the depth of the electric field distribution along the length of the electrode.

Both discussed approaches to predicting the electric field distribution are only solved for two needle electrodes, and roughly for a single needle electrode. In treating large and irregularly shaped tumors, the optimal electrode arrangement and pulse

parameters may be very complex and cannot adequately be planned for using simple approximations of the electric field distribution, even when superposition of electric fields for parallel electrodes is included. Finally, the analytical and approximation techniques solve only for electric field distribution and do not consider thermal effects. Although solving for temperatures and potential thermal damage may be performed once the electric field distribution is determined, typical methods for evaluating tissue heating would only work within a single pulse, and incorporating the cooling that would occur during the interpulse pulses would become too difficult to rapidly provide predictions of thermal damage for practitioners. Despite these limitations, there is still significant utility in being able to rapidly solve for predicted treatment regions using the techniques described here, particularly for simple shaped and smaller tumors. However, for large and difficult cases, it becomes attractive to plan treatments using more robust numerical solution techniques that can account for all of the heterogeneities, three-dimensional effects, and complex electrode arrangements.

7.4 Numerical Solution Techniques

Numerical modeling provides a useful tool in vigorously predicting treatment outcomes while accounting for effects such as tissue heterogeneities, temperature changes, three dimensional treatment situations, and dynamic tissue properties. An in depth description of numerical models that account for these effects may be found in Chapter 6, and may be seen applied in the treatment of a canine patient in Chapter 8.

7.5 Treatment Planning Process – Example in a Canine Lipoma[5]

A canine patient with a 360 cm^3 spontaneous tumor in the left thigh recently treated with IRE demonstrates the complexity and numerous steps required for a comprehensive treatment plan in all electroporation based therapies. The following figures represent the treatment planning steps from a treatment plan developed and successfully implemented in a canine patient. The system can be broken into the stages as follows:

[5] Section 7.5 is adapted and reprinted with permission from Elsevier: Physical Medicine and Rehabilitation: Principles and Applications, Physics-stimulated and intelligent therapies, 2011. Electroporation Therapy. Authors: Christopher B. Arena, Robert E. Neal II, and Rafael V. Davalos.

7.5.1 Acquire images

The first step to developing a comprehensive treatment plan for a patient is to acquire a sense of the clinical case. Any array of medical images (CT, MRI, PET, US) may be used to develop an understanding of the targeted region geometry. Estimations based on palpation may also be used for superficial tumors or in areas where advanced imaging techniques are inaccessible. **Figure 7.7A** and **7.7B** shows three-dimensional reconstructions of the example patient's tumor which were created from CT scans using TeraRecon (TeraRecon, Inc, Foster City, CA).

7.5.2 Trace regions of interest

Based on the scans, identification and isolation of the targeted region should be performed. Depending on the type of tumor and its location in the patient, this may be readily evaluated from the scans themselves, or performed by coordinating clinical examination with the scans of the patient. Isolation may be done manually using image analysis software or using a computer program capable of detecting anomalies or specific tissue regions of interest. In the example case here, the patient had a fatty lipoma in the leg, which provided strong contrast of a hypoattenuating region in the CT scans compared to the neighboring muscle and bone tissue. The targeted region can be seen isolated in **Figure 7.7C**.

7.5.3 Visualize and reconstruct 3D geometry

Traced regions of interest can be compiled and interpolated between the image slices to create a 3D geometry that the practitioner can use to gain an understanding of the basic shape of the mass and/or its location relative to other tissues. This also allows one to identify physical constraints, such as vital structures (nerves, brain, and blood vessels), access orientation preferences (from head, from rear, supine, prone patient positioning), and physical barriers (bones and sensitive structures). These are used to guide what electrode placements and orientations are possible as well as any need to avoid specific regions.

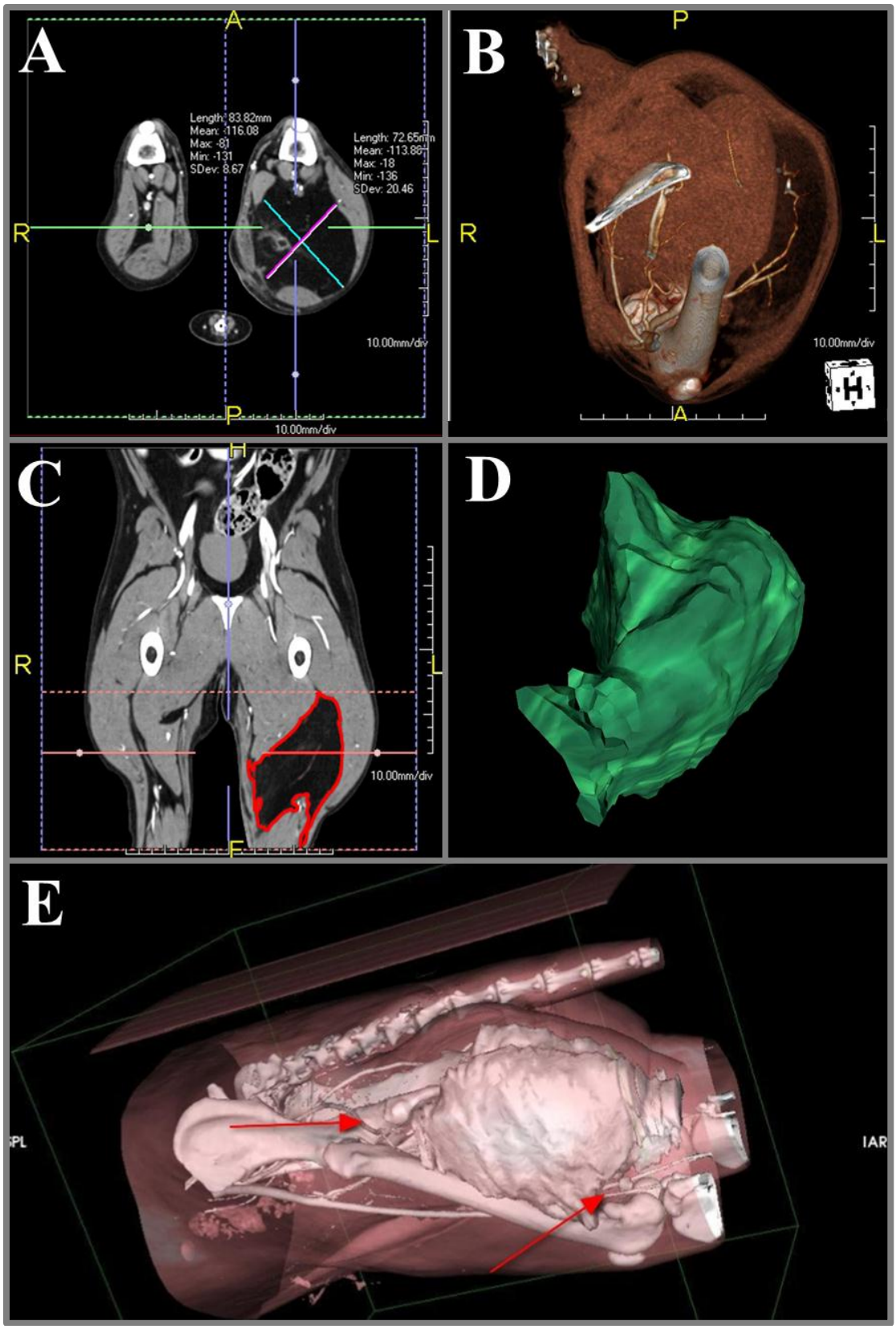
A
Length: 83.82mm
Mean: -116.08
Max: -81
Min: -131
SDev: 8.67
Length: 72.65mm
Mean: -113.86
Max: -18
Min: -136
SDev: 20.46
10.00mm/div
10.00mm/div
B
10.00mm/div
C
10.00mm/div
D
E

Figure 7.7: Assessment of Clinical Case for Treatment Planning. **(A)** Computed tomographic scan with dimensions used to initially assess presence of tumor. (B) Three dimensional reconstruction of patient using TeraRecon from a series of axial CT images, which then allows sagittal and coronal slice views. (C) Trace of targeted region, a compilation of which can be used to create (D) a three dimensional representation of targeted region of interest. This reconstruction may be maneuvered to assess its general shape and allow determination of optimally efficient electrode insertion approaches. (E) This reconstructed geometry may be assessed relative to the rest of the patient's body, permitting assessment of physical constraints such as bones preventing electrode insertion, relative location of sensitive structures (arrows point to major vasculature and nerves), and orientation of the lesion relative to the body, allowing for the evaluation of optimal electrode insertion approaches. For example, in this figure, the long axis of the tumor is roughly parallel to the length leg and femur, so a user may consider reducing the number of electrodes and insertions used by orienting the electrodes along this axis, or if such approach angles are not feasible, more electrodes may be inserted perpendicular to the top of the leg (since the femur prevents access from the bottom of the leg).

7.5.4 Import geometry into finite element modeling software

The three dimensional reconstructed targeted volume may be converted into a volumetric mesh that can be used to numerically evaluate predicted treatment outcomes using finite element software. In addition, various traced neighboring regions such as muscle, fat, and bone may be imported, with their unique tissue properties accounted for, creating a heterogeneous environment and to provide reference points in the resulting treatment plan. Furthermore, rather than importing various selected regions, a three dimensional map of all the voxels from the scan may be imported and treated as independent elements with discrete properties.

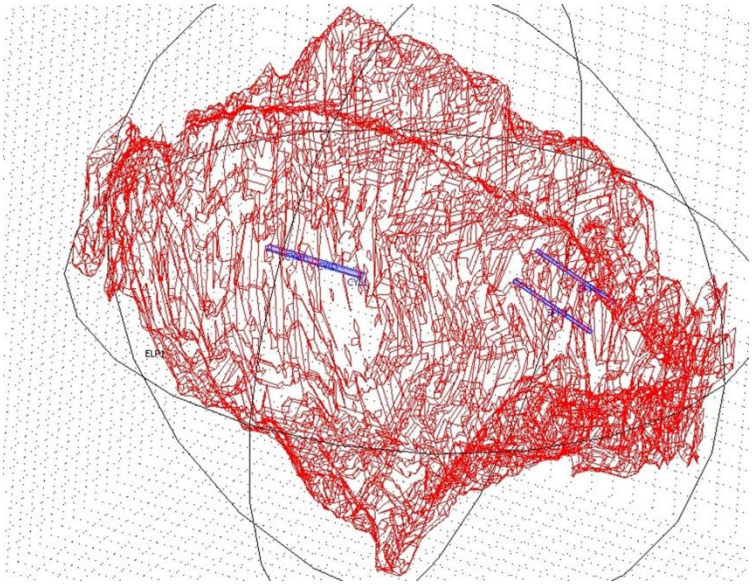

Figure 7.8: Imported geometry. The geometry may be converted to a surface or a solid and imported into numerical modeling software. Here, the geometric representation of the targeted region is depicted in red, while representations of typical electrode styles and sizes are shown at two locations in blue. The number, orientation, and location of these electrodes may be manipulated with results from the numerical solutions to develop an optimum placement scheme to satisfy the treatment objectives.

7.5.5 Assign model properties

Model properties that may be considered in the numerical simulation include all physical and thermal properties, as well as electrical properties. These properties can be selected by several methods. On method involves designating regions from the images as a specific tissue type and using corresponding values from the literature. If adequate treatment time is permissible or prior to the actual treatment day, electrodes may be inserted into any regions of interest and a low voltage pulse applied to facilitate retroactive calculation of the tissue conductivity. Finally, depending on the type of scan used to evaluate the patient, it may be possible to deduce tissue properties directly from the voxel value. An example of a possible way to do this would be to use the radiodensity of each tissue or voxel from a CT to derive water content according to the equation:

$$HU = \frac{\mu_X - \mu_{water}}{\mu_{water} - \mu_{air}} \cdot 1000 \tag{7.14}$$

where *HU* is the image attenuation relative to distilled water, and μ_X, μ_{water}, and μ_{air} are the linear attenuation coefficients of that point in the tissue, water, and air, respectively. It may be possible that a tissue's HU value can serve as a representation of its relative water content, with larger absolute value HU's containing less water. The HU and conductivity of several tissue types may be seen in **Table 7.3**.

Table 7.3: Normalized CT Attenuation and Electrical Conductivity of Various Tissues

Substance	HU	Conductivity, S/m [195]
Air	-1000	0
Fat	-120	0.025
Water	0	-
Muscle	+40	0.5
Bone	>+400	.0025

If water were to be considered physiological saline, then its conductivity would be approximately 1.9 S/m, an effective maximum conductivity for biological tissues. **Table 7.3** provides strong supporting evidence that the smaller the absolute value of a voxels HU, the higher the electrical conductivity.

7.5.6 Place electrodes in model

Any number of electrodes would be placed into or around the targeted region of the volumetric mesh in the finite element modeling software. Their number, location, orientation, and size could all be adjusted independently. **Figure 7.8** depicts 2 electrodes placed within the targeted mass.

7.5.7 Solve for electric field distribution and thermal effects

The electric field distribution and thermal effects would be solved for in the numerical model according to the methods described throughout this dissertation, particularly Chapters 4 and 6. The electric field and temperature distribution would be correlated with experimental data on electric field thresholds for reversible electroporation, irreversible electroporation, and thermal damage to superimpose and integrate predicted volumes of affected regions, including regions of treated and untreated tissue, as well as regions experiencing thermal damage.

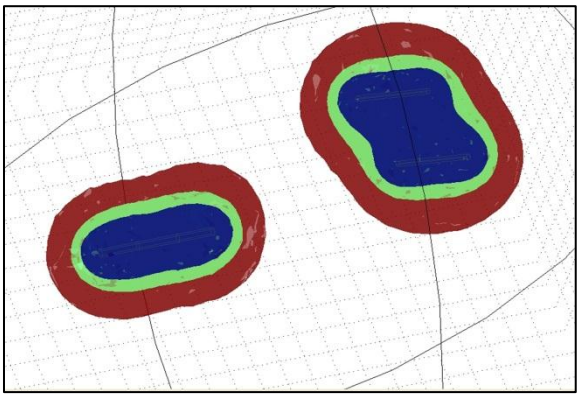

Figure 7.9: Numerically calculated electric field distributions. Here, the electrodes depicted in **Figure 7.8** are energized. The color maps are representative electric field isocontours that may be used in determining predicted IRE treatment regions (green), reversible regions (red), or safety margins (beyond red) based on electric field threshold data.

7.5.8 Evaluate success of outcome

Treating the desired regions while preventing unacceptable effects on sensitive regions determines whether the electrode setup and pulsing protocol used appropriately meets the clinical treatment demands. Preoperatively, this could be assessed qualitatively or quantitatively with a fitness function on the numerically calculated electric field distribution and reconstructed geometry. Evaluating the effectiveness of a treatment

protocol may be done using a fitness function where the quality of a protocol Ψ, may be evaluated according to the equation

$$\begin{aligned}\Psi(ET, EP, \Phi, \dots) \\ &= A \cdot [IRE]_D + B \cdot [REB]_D - C \cdot [Therm]_D - E \cdot [IRE]_U \\ &- F \cdot [REB]_U - G \cdot [Therm]_U\end{aligned} \tag{7.15}$$

where *D* is the targeted volume as a percentage, *U* is the undesired volume as an absolute value, and A, B, C, E, F, and G are coefficients to provide scaling factors for the priorities in clinical outcome. For instance, it is likely that A and B will be much greater than the other coefficients since ensuring complete treatment of the targeted volume is the most important priority, and G would be larger than C since thermal damage to healthy tissue would be worse than to targeted tissue. In addition, B and F may be neglected in purely IRE treatments. In addition, *ET* represents the electrode type and geometry (e.g., single/dual/hybrid, diameter, length), *EP* describes a specific case for electrode positioning (e.g., location and orientation in 3D space), Φ is the applied voltage

7.5.9 Adjust and iterate steps 5-8 until a suitable solution is developed

If the predicted treatment plans success is deemed unsatisfactory, the planning process may be iteratively repeated until a suitable treatment protocol is determined.

7.5.10 Program the generator system to deliver the predetermined pulsing protocol

Following development of the final treatment protocol, all pulse parameters would be input into the pulse generator. The practitioner would then place the electrodes according to the prescribed protocol and apply the pulses through the electrodes. The resulting treatment protocol for the example canine patient may be found in **Figure 7.10**.

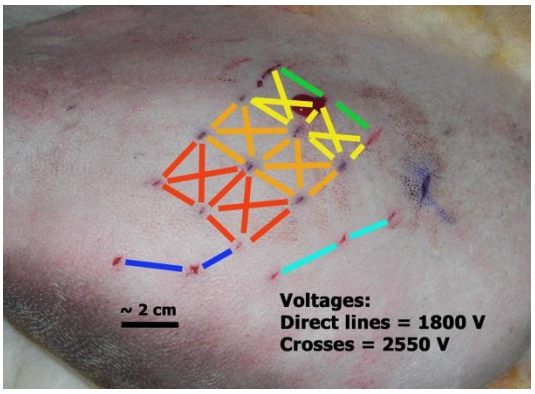

Figure 7.10: Actual utilized treatment protocol. Here, the final protocol used to treat the patient is shown. There is no crossover from the cyan pulsing regions due to the presence of the sciatic nerve running parallel to those pulsing paths, and the pre-clinical experimental objectives of the study wanted to ensure no risk to this critical structure.

7.6 Conclusions

In this chapter several methods for predicting treatment outcomes are discussed. In Section 7.3, the potential for rapidly solving for electric field distributions or contours is explored. Such techniques would permit practitioners to plan and adjust treatment protocols in real-time. However, examination of the limitations for such techniques provides incentive for utilizing numerical simulations to more accurately predict treatment effects. Finally, this chapter provides an outlined algorithm that may be used for performing patient-specific treatment plans, using an actual canine patient clinical case to demonstrate how such an algorithm would be applied.

Chapter 8: Irreversible Electroporation for Patient Tumor Therapy[6]

8.1 Introduction

The previous work in this dissertation has been aimed at determining the efficacy and developing the techniques to design and implement procedures using irreversible electroporation to treat in true clinical environments, where tumors will often be large, irregular shaped, and in complex heterogeneous environments. Other previous IRE work focused on characterizing the effects of IRE pulses on healthy tissue and treating small experimental and spontaneous tumors, while clinical IRE therapy remains in its infancy. In this chapter, we examine a case study where the knowledge gained from the previous work was applied to test our underlying hypothesis that IRE treatments can be designed and implemented to successfully treat soft tissue malignancies, including large and complex tumors, a crucial step for effective and reliable translation of the technology into routine clinical use. Here, we report our treatment of a focal histiocytic sarcoma of the coxofemoral joint in a canine patient. Follow-up examinations demonstrated prolonged relief of cancer-associated pain, preservation of pelvic limb function, and complete tumor regression by 6 months after initial treatment. At the time of composing this dissertation, repeated follow-up continues to show no signs of cancer in the patient for a complete regression period of 14 months.

8.2 Methods and Results

8.2.1 Patient Description

The patient was a 7-year-old, spayed female Labrador Retriever with a 5 year history of degenerative coxofemoral joint disease, resulting in bilateral pelvic limb lameness. Preceding referral, the left pelvic limb lameness had progressed to the point of frequent non-weight bearing lameness, refractory to medical management (Video1 on-

[6] Chapter 8 is adapted and reprinted with permission. © 2008 American Society of Clinical Oncology. All rights reserved. Neal 2nd, R. E., et al: J Clin Oncol. Successful Treatment of a Large Soft Tissue Sarcoma With Irreversible Electroporation. Vol. 29 (13), 2011: e372-e377

line). Examination revealed postural reaction deficits associated with sciatic neuropathy and an extensive periarticular mass involving the left coxofemoral and proximal thigh. Biopsies of the mass were cytomorphologically and immunohistochemically (positive immunoreactvity to CD1, CD11c, CD18 and MHC II) consistent with histiocytic sarcoma. No evidence of metastatic disease was detected on full body radiographic and CT examinations. Significant bilateral coxofemoral degenerative joint disease made the patient a poor candidate for current standard-of-care hemipelvectomy with hindlimb amputation.

8.2.2 Treatment Planning

CT scans of the pelvis and hindlimbs were used to visualize the targeted region (**Figure 8.1A-C**). The tumor partially surrounded the femur and was directly adjacent to the sciatic nerve and femoral and circumferential arteries. The targeted region on each slice was traced using open-source image analysis software (Osirix, Geneva, Switzerland) and compiled to create a 3D representation of the pre-operative tumor with a volume of 136cm^3 (**Figure 8.1D**).

For protocol planning, the 3D reconstruction of the targeted tumor was imported into Comsol Multiphysics FEM software (Comsol, Stockholm, Sweden), to determine electric field distributions for various electrode orientations and pulse parameters. Because electric field strength is the primary determinant of treatment outcome [17], the numerical models were solved according to methods described in [8, 232], for the predicted ablation regions. Two electrode styles were examined: dual-probes of two needle electrodes, each 1mm in diameter, 1cm long, and separated by 1cm; and a single probe containing two charged surfaces within a single needle of diameter 1.65mm, with distal and proximal conducting surfaces of 0.70 and 0.75cm long, respectively, each separated by a 0.80cm long insulation area; dimensions smaller than those for radiofrequency and cryo-ablation[57, 63]. The predicted treatment regions were arranged to appropriately fulfill the treatment objectives. The therapeutic intent was palliative to mitigate clinical signs of pain and lameness while ensuring functional limb sparing through preservation of the adjacent sciatic nerve and femoral artery. Considering this

with the physical treatment constraints resulted in a 3-stage electrode insertion process. The electrode orientation and predicted treatment regions within the tumor may be found in **Figures 8.1E** and **8.1F**, respectively.

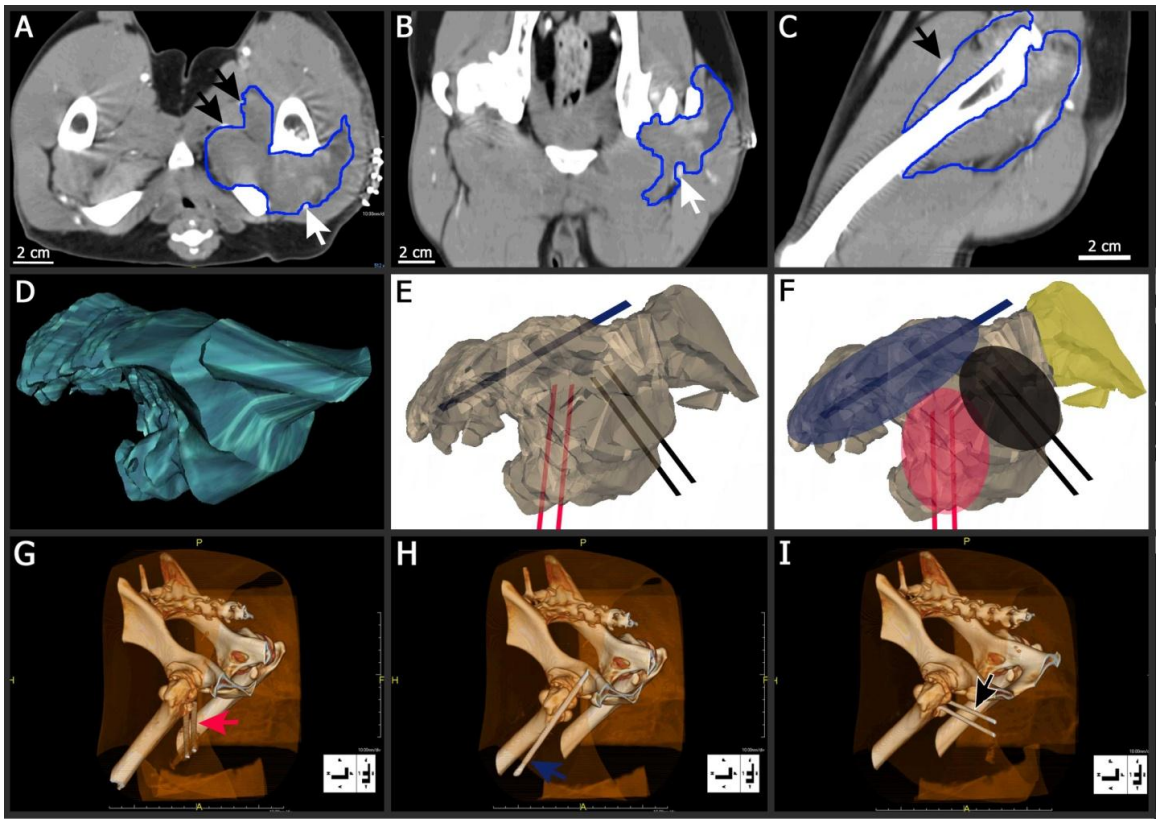

Figure 8.1: Initial Treatment. (A) Axial, (B) coronal, and (C) sagittal computed tomography slices of the patient prior to treatment. The lesion has been outlined in blue. (D) 3D reconstruction of the tumor, with (E) the proposed electrode placements, and (F) their resulting theoretical ablation regions. The region highlighted in yellow was determined to be asymptomatic and therefore was not targeted for the initial treatment. (G-I) TeraRecon 3D reconstructions of CT images for the (G) first, two-needle electrode, (H) second, single-needle electrode, and (I) third, two-needle electrode insertions immediately prior to pulse application. Black arrows indicate the location of the sciatic nerve. White arrows indicate the deep and circumferential femoral arteries.

8.2.3 Treatment Implementation

The patient was premedicated with intravenous midazolam and oxymorphone, and general anesthesia was induced with intravenous propofol and maintained with isoflurane in 100% oxygen. Intra-operative temperature monitoring at the electrode showed a maximum change of 2.43°C, with temperatures returning to baseline within 3 minutes (**Figure 8.2**). Electromyography and motor nerve conduction studies of the left sciatic nerve were performed using standard procedures with a commercial electrodiagnostic

system (**Figure 8.3A** and **8.3C**) (Nicolet Viking IV, Madison WI, USA). Immediately before treatment, atracurium was administered intravenously (0.4 mg/kg) for neuromuscular blockade, and an epidural of preservative free morphine and bupivicaine administered. Following application of the paralytic, the electrodes were inserted according to the treatment plan and their placement was assessed using CT. **Figures 8.1G-I** show the actual electrode placements for each insertion used during the surgical procedure.

After confirming electrode location, the pulses were applied according to **Table 8.1** using the Nanoknife® pulse generator system (Angiodynamics, Queensbury, NY). After the pulsing at the deepest insertion, the electrodes were withdrawn enough to prevent overlap of IRE regions prior to administering the next set of pulses. This was repeated until the anticipated IRE region reached the superficial margin of the tumor. This withdrawal technique reduces the number of insertions and may help to kill any cancerous cells on the electrode, reducing potential seeding of these cells along the needle tracks.

Table 8.1: Physical and Pulse Parameters for Treatment

Pulse Application Set	Insertion	Electrode Style	Separation, cm	Depth, cm	Voltage, V	Repetition Rate, pulses/sec
1/1	1	Dual Probe	1	6.5	1000	90
1/2	1	Dual Probe	1	5	1250	90
1/3	2	Single Probe	0.8	11	1000	90
1/4	2	Single Probe	0.8	8	1200	90
1/5	2	Single Probe	0.8	6	800	90
1/6	3	Dual Probe	1	1.4	1500	90
1/7	3	Dual Probe	1	0.9	1000	90
2/1	4	Dual Probe	1.5	4.1	1150	ECG
2/2	5	Dual Probe	1.5	4.1	1150	ECG

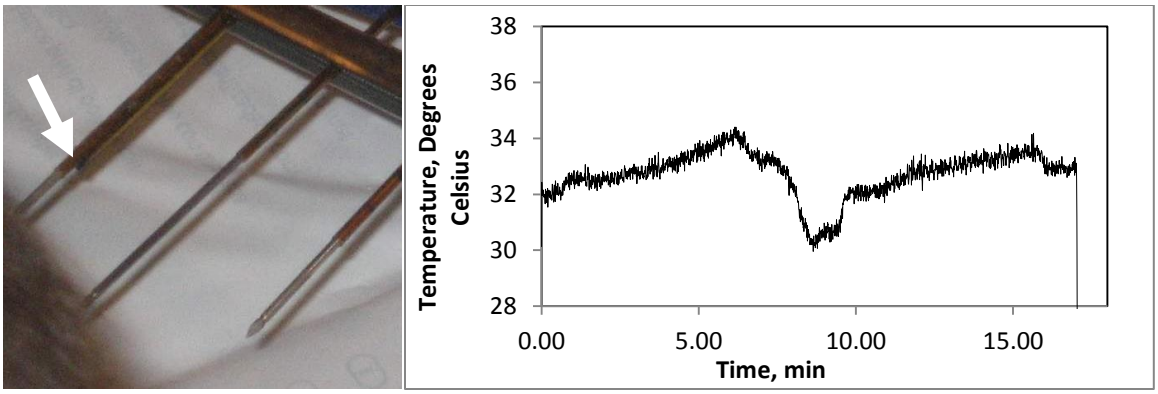

Figure 8.2: Temperature measurement during 2 sets of electroporation pulses. (A) Image of temperature probe (white arrow) relative to electrode. (B) Temperature measurement during pulse sets 2/1 and 2/2 from second treatment.

8.2.4 Clinical Results and Follow Up

Following IRE therapy, the left sciatic nerve was electrophysiologically re-evaluated, which revealed small decreases in the amplitudes of the distal compound muscle action potentials compared to pre-IRE values, suggestive of mild conduction block (**Figure 8.3B-C**). The patient was hospitalized for 24 hours following IRE and maintained on parenteral oxymorphone. The acute post-IRE electrophysiologic changes observed were subclinical, as the degree of lameness and sciatic nerve dysfunction clinically observed 24 hours after IRE remained unchanged from pre-treatment. Percutaneous biopsies 24 hours after the IRE revealed marked coagulative necrosis of the tumor, and the dog was discharged to the owners to continue medical therapy with deracoxib, tramadol, and fish oil supplements.

Clinical and CT recheck examinations were performed 8 days after IRE. Clinically, the owner reported improvement in the lameness to the extent where the dog no longer had episodes of non-weight bearing, and the owner discontinued the administration of tramadol 4 days after the IRE therapy. The CT study showed a tumor volume of 65cm^3, a reduction of 52% from pre-IRE treatment. Although the CT demonstrated a significant volumetric improvement in the tumor targeted with IRE, enlarged and abnormally enhancing intrapelvic lymph nodes and enlargement of a focus of tumor in the proximal region of the femur outside of the IRE treatment area were visualized. Metastases were cytologically confirmed as the cause of the observed

intrapelvic lymphadenopathy. Thus, a chemotherapeutic regimen of 1-(2-chloroethyl)-3-cyclohexyl-l-nitrosurea (CCNU; 65 mg/m^2 PO every 21 days) was prescribed.

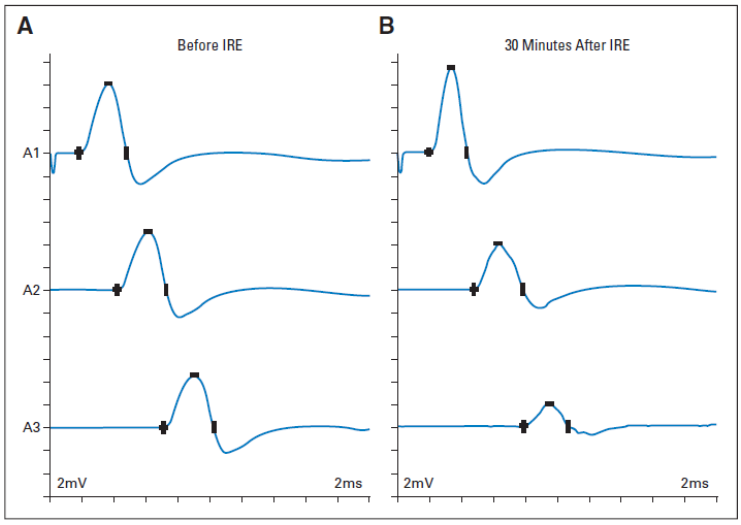

Figure 8.3: Nerve conduction study of the left sciatic nerve showing minimal effects of the IRE treatment in vicinity of the nerve.

Table 8.2: Motor Conduction Study of Left Sciatic Nerve

Evaluation	Left Sciatic Tibial Nerve	Latency (ms)	Amplitude (mV)	Segment	Latency Difference (ms)	Distance (mm)	Conduction Velocity (m/s)
Before IRE	Hock (A1)	1.8	6.1	Interosseous muscle—hock	1.8	30	17
	Stifle (A2)	4.2	5.1	Hock—stifle	2.4	150	63
	Hip (A3)	7.1	4.6	Stifle—hip	2.9	185	64
				Hock—hip	5.3	335	63
30 minutes after IRE	Hock (A1)	1.9	7.6	Interosseous muscle—hock	1.9	30	16
	Stifle (A2)	4.6	4.1	Hock—stifle	2.7	150	56
	Hip (A3)	8.0	2.2	Stifle—hip	3.4	185	54
				Hock—hip	6.1	335	55
2 weeks after IRE	Hock (A1)	1.7	7.4	Interosseous muscle—hock	1.7	30	18
	Stifle (A2)	4.0	5.3	Hock—stifle	2.3	150	65
	Hip (A3)	6.9	4.8	Stifle—hip	2.9	185	64
				Hock—hip	5.2	335	64

Abbreviation: IRE, irreversible electroporation.

The temporal relationships of applied treatments on gross measurable disease are summarized in **Figure 8.4**. By 2 weeks post-IRE, the degree of lameness improved to where the dog was capable of daily activities such as controlled leash walks, negotiation of stairs, and swimming, with the severity of gait deficit in the left pelvic limb indistinguishable from that of the right. The left sciatic nerve was electrophysiologically re-evalauted, with results returning to pre-treatment values (**Figure 8.3C**). All previously prescribed analgesic medications were discontinued by 2 months post-IRE. By 13 weeks post-IRE, the entire targeted volume of tumor and previously observed lymph node metastases were completely eliminated.

8.2.5 Irreversible Electroporation to Eradicate Tumor

A 4 month recheck visualized a new focus of tumor on CT and ultrasound examinations in a region outside of the previous IRE treatment field in the medial aspect of the left coxofemoral region (**Figures 8.4A-C**), which suggested development of chemoresistance to CCNU. Because the relapsed tumor was focal, a second IRE session was selected to treat this remaining region. The treatment planning process was repeated. The pre-operative tumor volume was 36cm^3. A parallel 3-needle electrode array was chosen for treating the shape of the targeted region. The electrodes were separated by 1.5 cm, with exposure lengths of 2.5 cm at the center electrode and 1.5 cm on the sides. Electrode placement was facilitated under ultrasound guidance (**Figure 8.4D**). The pulses were applied using the same parameters as the first treatment (**Table 8.1**), with the center energized and one side being grounded at a time, for a total of 2 pulse sets. Pulse rate was synchronized to the cardiac rhythm of the patient using the Accusync system (Accusync, Milford, CT), with pulses administered 500µs after the R-peak wave.

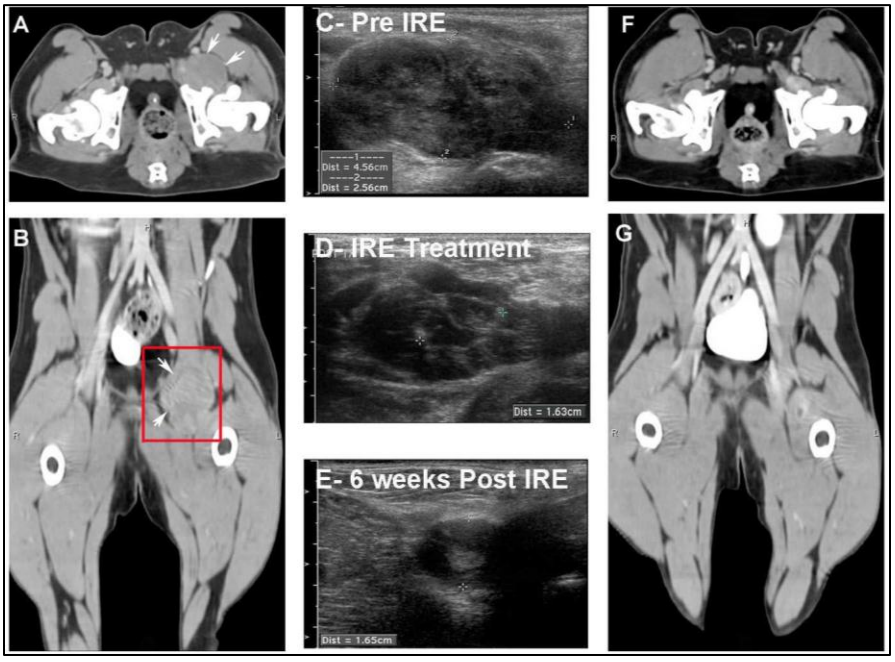

Figure 8.4: Axial (A) and dorsal planar (B) computed tomographic images obtained 121 days after initial IRE treatment showing tumor relapse in previously left inguinal area (white arrows). The area outlined in red (B) represents the field from which serial sonographic images of histiocytic sarcoma obtained prior to (C), during (D), and following (E) the second IRE treatment. The tumor appears as a lobular intramuscular mass lesion (C) with mixed echotexture. Intralesional IRE electrodes tips are visible as hyperechoic punctuate spots within the mass (D) during IRE therapy. Post IRE tumor regression is associated with hypoechoic treated regions, as well as a progressive decrease in tumor dimensions (D and E). All images obtained with 14MHz linear transducer. Computed tomographic images (F and G) obtained 6 months post-diagnosis demonstrating complete regression of the tumor.

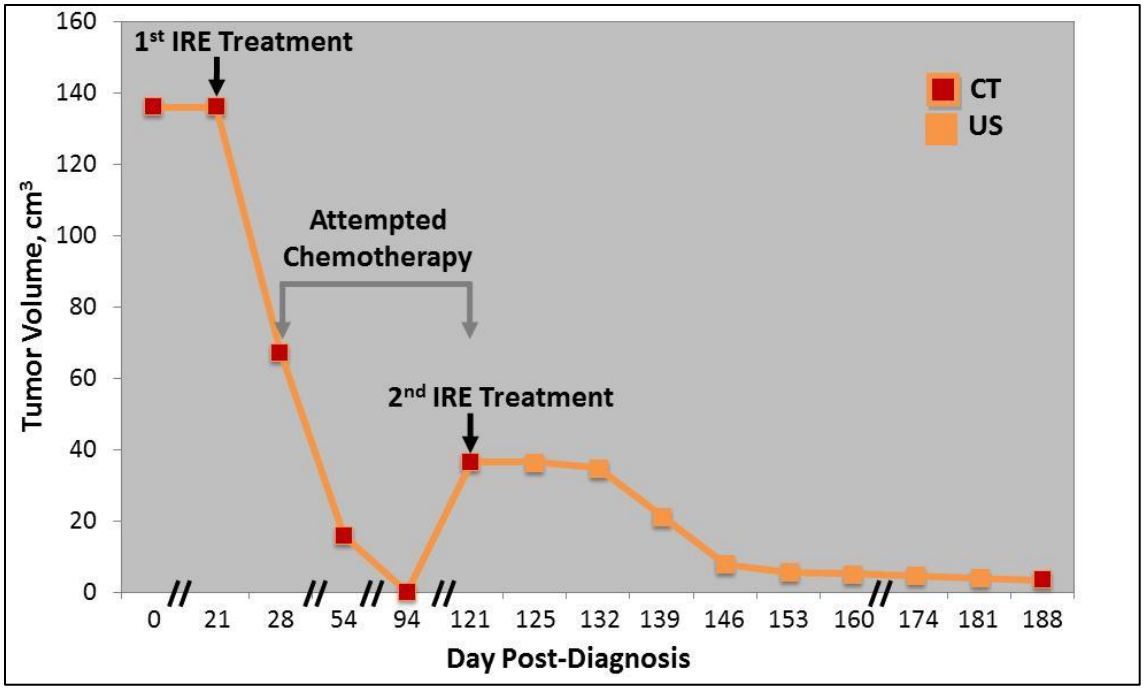

Figure 8.5: Treatment effects on tumor volume over time. Black time points indicate tumor volumes measured from CT scans; tumor volumes obtained from ultrasonographic images from time points indicated in gray.

It was found that both IRE treatments resulted in temporally progressive coagulative tumor necrosis in the acute periods of 24-48 hours post-therapy. **Figures 8.6A-F** illustrate the progression of tumor necrosis over 48 hours following the second IRE treatment, while the majority of skeletal muscle at the margin of the tumor remains viable (**Figures 8.6A-C**). In addition, the IRE treatment resulted in marked influx of mixed inflammatory infiltrate into the treatment region, which was comprised of neutrophils, macrophages, and lymphocytes (**Figures 8.6D** and **8.6G-I**). The majority of infiltrating lymphocytes were CD3+ (**Figures 8.6G** and **8.6I**).

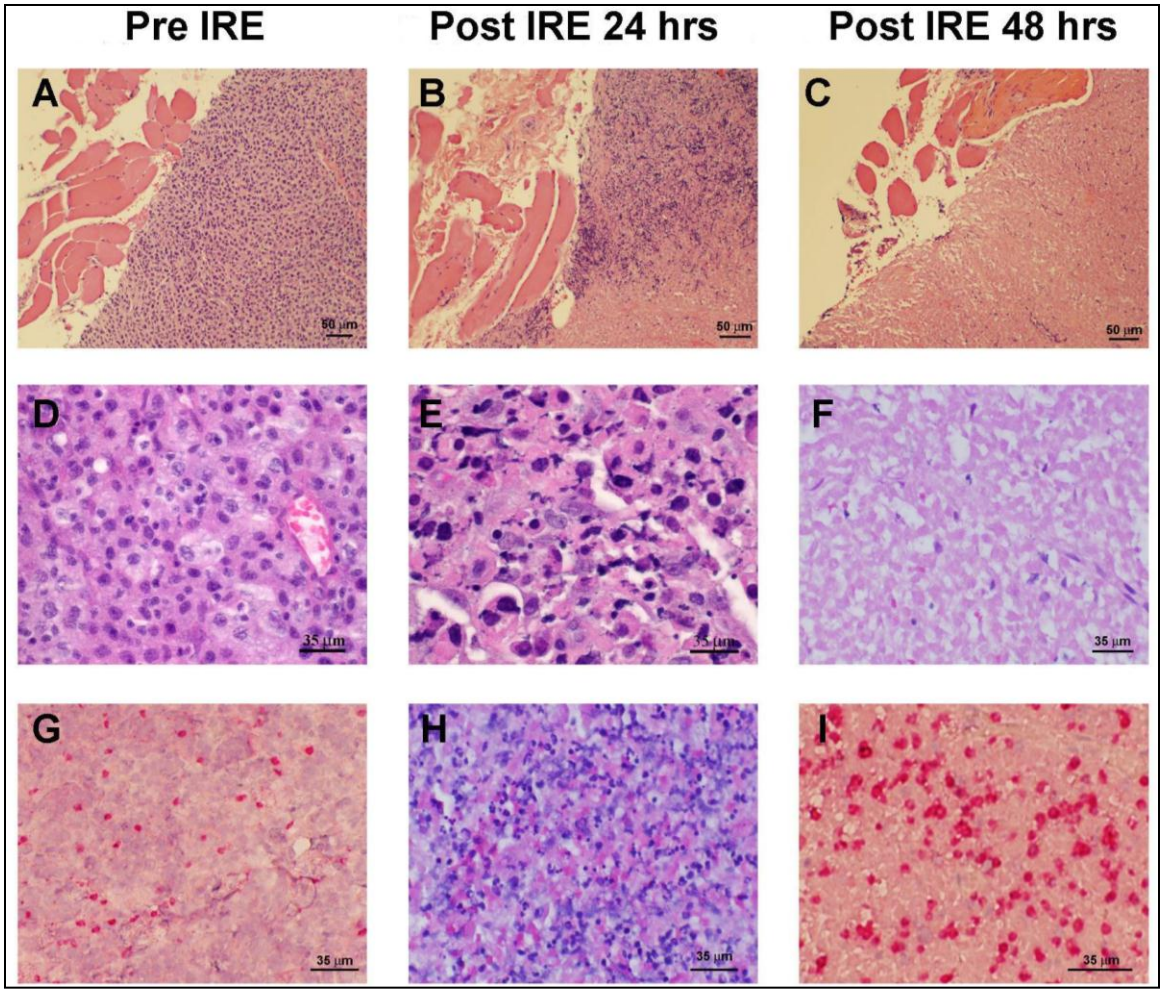

Figure 8.6: Serial biopsies of the tumor associated with second IRE treatment demonstrating progressive tumor necrosis, sparing of skeletal muscle at the tumor margin, and treatment associated imflammatory cell infiltrate. Panels A-F and H, hematoxylin and eosin stain. Panels G and I, CD3 immunohistochemistry with fast red counterstain.

Although complete tumor necrosis was observed within 48 hours of IRE treatments, volumetric regression of tumor occurred for several weeks following IRE therapy (**Figure 8.5**), as necrotic tissue was resorbed by the immune system and local tissue healing and remodeling occurred. At the 6 month recheck examination, the patient was in complete remission based on her clinical and CT examinations (Video 2 available on-line). The dog displayed mild, bilaterally symmetric pelvic limb lameness consistent with the degenerative coxfemoral joint disease, but was able to perform daily low impact exercises (walking, swimming) without exacerbation of the lameness, was receiving no adjunctive analgesic or anti-inflammatory medications, and had no evidence of the tumor on the CT scan (**Figures 8.4F-G**). A focus of hyperattenuating and contrast enhancing

muscle tissue was present at the margin of the second IRE treatment site on the CT scan, but this was confirmed by biopsy to be muscle fibrosis.

8.3 Discussion

Considering that treatment of spontaneous solid tumors with IRE is still in its infancy, this study provides novel and encouraging results regarding the future role of IRE in clinical oncology. We demonstrated the ability to plan and implement IRE therapy for a large and irregular tumor in a minimally invasive fashion. The original tumor was over 136cm^3 in volume and was located in a heterogeneous setting that encompassed bone, muscle, fascia, major arteries, and the sciatic nerve. Imaging and reconstruction technology enabled design and implementation of a treatment plan capable of attaining our clinical objectives without causing detrimental effects. The successful ablation of the tumor in proximity to the sciatic nerve resulted in alleviation of pain as well as improved mobility and quality of life.

As the facilitation of IRE expands its scope to increasingly complex clinical settings, it is vital to develop therapies easily administered by practitioners that can provide predictable outcomes. This is especially important for the utilization of IRE in settings where neighboring structures make surgical resection and other focal ablation techniques impractical or dangerous, or where traditional therapies are possible, but would negatively impact the patient due to significant concurrent disease, as in this case. Although prescribed electrode placement was determined prior to treatment, real-time guidance of electrodes and adaptability of the treatment plan was important to account for the imprecise nature inherent in executing placements. Additionally, typical IRE-affected and sub-lethal margins should be well-defined in advance to allow a treatment to safely achieve its specific aims.

Although tumors of dendritic origin, such as the histiocytic sarcoma of this patient, are rare in dogs and humans, they are being recognized with greater frequency in both species[233, 234], and surgical resection is the primary therapy used[233, 235]. In dogs, histiocytic sarcoma is a biologically aggressive neoplasm where the prognosis is considered grave, with studies reporting variable but universally poor median survivals

ranging from 3-6 months with treatment[234, 235]. Given the biological behavior of canine histiocytic sarcoma, we believe therapeutic clinical outcome we report is excellent for several reasons. Principally, we were able to achieve complete remission 6 months after diagnosis with multimodality IRE and chemotherapy, while simultaneously improving patient and owner quality of life. Secondly, we completely ablated relapsed and suspected chemoresistant tumor using IRE alone with minimal collateral damage to healthy tissues. This demonstrates the potential for IRE as both a primary therapeutic modality or when faced with neoplasms refractory to other therapy. Our real time *in vivo* temperature monitoring data (not shown) also illustrates that the desired therapeutic effect occurs via non-thermal mechanisms, as opposed to using theoretical modeling[11, 18, 236].

The serial biopsies performed on this patient demonstrated relative sparing of the skeletal muscle at the tumor margins and the generation of a significant post-treatment immune response. The muscle sparing suggests pre-operative treatment plans are able to be practically executed at the submillmeter resolution of IRE reported in healthy tissue[4]. Although IRE has been demonstrated to effectively ablate tumors independent of an associated immune response[15], we observed significant infiltrate of T-lymphocytes into the tumor. These data raise important questions that deserve attention in future studies, such as the possibility of inherent differences in IRE selectivity to neoplastic versus healthy tissues, as well as further molecular characterization of tumor infiltrating lymphocytes to identify any association between IRE and the induction or modulation of host immunosurveillance and adaptive immunity.

8.4 Conclusions

This investigation used irreversible electroporation (IRE) to achieve complete remission and improved quality of life in a canine patient with a large and complex tumor in a heterogeneous environment. An initial treatment resulted in improved clinical signs of cancer-associated pain without adverse effects and allowed functional limb sparing. A strong tumor response to IRE with adjuvant chemotherapy was later observed. After developing chemoresistance, new tumor growth was treated with a second application of

IRE, which resulted in complete remission 6-months after the initial treatment. Post-operative biopsies showed complete tumor necrosis with sparing of adjacent muscle. These findings demonstrate the feasibility and efficacy of IRE as an attractive, minimally-invasive, primary ablative therapy for the treatment of soft-tissue malignancies.

Chapter 9: Irreversible Electroporation in Combined Therapeutic Modalities[7]

9.1 Introduction

The American Cancer Society (ACS) estimates that there will be 26,020 new cases of brain and central nervous system malignancies in 2010 [237]. Current methods to treat these tumors include radiation therapy, surgical resection, various chemotherapeutic regimens, or a combination of these modalities [238]. Despite the availability of these techniques and advances in modern medicine, only 7 months have been added to the mean survival rate of patients with malignant gliomas (MGs) in the past 70 years [239].One reason for poor survival is that glioma cells infiltrate up to 2 cm beyond the margin of visible tumor [240], making them hard to detect and treat. Further, treatment of MGs is limited by insufficient delivery of chemotherapy drugs due to the blood-brain-barrier and an inherent resistance of glioma cells to conventional drug therapies [241, 242].

IRE therapy has effectively treated experimental tumors in mice as well as spontaneous tumors in patients [18-22, 243]. The effects of the electric pulses are dependent on the electric field to which the cells are exposed, which is highest beside the electrodes and rapidly decreases away from the electrodes. Large treatment volumes therefore require larger applied voltages or additional electrodes to attain complete lesion exposure to the IRE electric field threshold, which will begin to introduce significant thermal effects and thermal damage due to Joule heating, reducing the benefits of IRE therapy. Although IRE therapies have shown some selectivity in killing cancer cells while sparing neighboring healthy myocytes [22], the effects are typically regarded as non-selective. Where the overall ineffectiveness in current MG therapies is believed to

[7] This chapter presents results from a manuscript currently under review. Upon acceptance of the manuscript for publication, this chapter will be an adaptation reprinted with permission from Elsevier: Bioelectrochemistry, Irreversible Electroporation Enhanced Pharmacotherapy (IREEP): Feasibility Study in the Treatment of Gliomas. Authors: RE Neal II, JH Rossmeisl Jr, V D'Alfonzo, JL Robertson, PA Garcia, S Elankumaran, RV Davalos.

result from infiltrative neoplastic cells beyond the macroscopic margin of the tumor, it is desirable to kill these cancer cells while sparing the healthy brain tissue. It was shown that injections of bleomycin, a common ECT chemotherapeutic, directly into the brain is relatively well tolerated by patients, even at doses higher than those commonly used in ECT [244]. IREs ability to reliably kill all cells within large volumes of tissue and ECTs ability to selectively target rapidly dividing, neoplastic cells make it attractive to combine the promising non-thermal ablation aspects of IRE to kill the main tumor volume, using the lower, reversible realm of electroporation to target infiltrative cancer cells beyond the margin of visible tumor.

Reversible electroporation is a technique that relies on a lower energy regime of electric pulses, permitting cell recovery to enhance cellular uptake of relatively impermeable macromolecules, such as certain chemotherapy drugs (electrochemotherapy, ECT) and DNA (electrogenetherapy) [10, 85]. Facilitated drug delivery significantly increases the local cytotoxicity of certain chemotherapeutic drugs, and has successfully been used to treat melanomas, basal cell carcinomas, and other superficial tumors [85].

We hypothesize that combining the enhanced macromolecule transport from reversible electroporation with the focal ablation of IRE as the primary therapy will enhance the therapeutic outcome beyond that of either modality alone. In such a combined-modality therapy we designate as irreversible electroporation enhanced pharmacotherapy (IREEP), IRE would treat the tumor, and the larger reversible electroporation region would allow for ECT beyond the tumor's margins. If the drug used in ECT selectively kills rapidly dividing neoplastic cells, it becomes possible to use low drug doses locally kill infiltrative cancer cells beyond the tumor margin. In addition, there is evidence that electroporation disrupts the blood brain barrier [245, 246], permitting increased diffusion of systemic chemotherapeutics into the targeted region.

This concept was originally suggested in [207]. However, to assess the feasibility of combining IRE with ECT treatment modalities, it must be determined if significant realms of ECT enhanced cytotoxicity are attainable when subjecting cells to IRE pulse

parameters. *In vitro* studies have shown that increases in pulse number may decrease the electric field threshold required to induce IRE [155]. Accordingly, previous investigations have found unique pulse parameters to be the most effective for each electroporation therapeutic modality, both *in vitro* and *in vivo*. ECT therapies typically employ a total of 8 pulses, each 100 µs to 1 ms long, at a repetition rate of 1 Hz or 5 kHz for maximum chemotherapeutic uptake without killing the cells [247]. Alternatively, an *in vivo* investigation of IRE on cutaneous mouse tumors found that using a total of 80 pulses, each 100 µs long, at a repetition rate of 1 pulse every 3 seconds was the most effective at regressing the tumors [18]. Therefore, to clarify the feasibility of a combined modality approach it must be determined if IRE's unique pulse parameters, such as the higher number of pulses, still contain a realm of lower electric fields that enables increased chemotherapeutic cytotoxicity while allowing cell survival from the pulses alone.

This study analyzes enhancing the outcome of IRE therapies to target infiltrative cells beyond a tumor margin by adding chemotherapeutic drugs prior to pulse delivery, as is done for ECT therapies. This was performed by characterizing the enhanced uptake and cytotoxicity from bleomycin and carboplatin *in vitro* on canine J3T and human U-87 malignant glioma cell lines when subjected to pulse parameters used in IRE therapies. Combined effects were evaluated using metabolic spectrophotography, luminescent cell viability assays, Hoechst 33342 apoptosis staining, and transmission electron microscopy. Optimized electric pulse parameters and drug doses determined to enhance cytotoxicity were incorporated into a comprehensive numerical model using a 3D volumetric domain mesh from computed tomographic scans of a canine brain. This model was used to predict the region of ablation from IRE as well as the margins for enhanced chemotherapeutic cytotoxicity. This study found that combining chemotherapeutics with typical IRE protocols should result in increased treatment margins, with cancer cell toxicity beyond the IRE focal tumor ablation volume.

9.2 Experimental Evaluation and Theoretical Simulation

9.2.1 Methods

9.2.1.1 In Vitro Characterization of Cellular Response

Both the canine J3T and human U-87 malignant glioma (MG) cell lines were cultured in 75 cm^2 flasks in RPMI 1640 medium (Cellgro, Mediatech, Manassas, VA, USA) with supplemental 10% fetal bovine serum (Atlanta Biologicals, Lawrenceville, GA, USA) and 5% Anti-Biotic/Mycotic Solution (Cellgro) in a 5% CO2 chamber at 37°C. The canine glioma cell line J3T was a kind gift from the laboratory of Dr. E. Subbiah, Virginia Tech, Blacksburg, VA, USA. The U-87 cell line was obtained from ATCC (Rockville, MD).

Cells used for experimental purposes were detached using trypsin-EDTA (0.05% trypsin-0.5 mM EDTA; Cellgro), and collected by centrifugation at 250 *g* for 10 minutes. Cells were then washed three times in a 75/25 DEP buffer and RPMI media blend, resuspended in the media, and transferred to a hemocytometer for quantification (Cellometer, Nexelcom, Lawrence, MA, USA). Cell viability was determined using the Trypan blue method, and only suspensions with > 95% viability were used for experimental purposes.

Chemotherapeutic Agent Growth Inhibition

A baseline dose-dependent level of chemotherapeutic effectiveness for the cell lines was determined. The native chemotherapeutic drugs bleomycin (Hospira, Lake Forest, IL, USA) and carboplatin (Sigma, St. Louis, MO, USA) were received as lyophilized solids, and reconstituted in RPMI 1640 media (Cellgro). The cytotoxic effects of bleomycin and carboplatin against J3T and U-87 cells were measured by preparing serial two-fold dilutions of each chemotherapeutic agent in 96-well plates in triplicate, and then adding 2 x 10^3 J3T or U-87 cells to each well to achieve a final well volume of 100 µl. The initial bleomycin concentration used was 20 µg/ml and 100 µg/ml for carboplatin. Following 48 hours of culture in a 5% CO_2 chamber at 37°C, the wells were decanted and cells stained with 0.5% crystal violet in 20% methanol for 5 minutes at room temperature.

The plates were washed 8 times with tap water and dried at room temperature. The crystal violet was dissolved with 100 µl of 50% ethanol in 0.1M sodium phosphate, and the absorbance measured at 570 nm with a spectrophotometer (Spectramax 250, Molecular Devices, Sunnyvale, CA, USA). The growth of the treated cells was expressed as the percentage of absorbance value in relation to that of untreated controls, and the dose of each drug that resulted in 50% growth inhibition was subsequently determined.

Chemotherapeutic Agent Preparation for IREEP

Based on results of the growth inhibition assays, six concentrations of bleomycin (0, 1 pg/ml, 100 pg/ml, 10 ng/ml, 1 µg/ml, and 100 µg/ml) and seven concentrations of carboplatin (1 mg/ml in addition to the same six concentrations for bleomycin) were evaluated. For each drug, concentration, and cell line, mixtures of 2 x 10^6 cells/ml and each drug at the appropriate concentration were placed into 6 individual, 4 mm gap electroporation cuvettes (BTX Cuvette Plus 640, Harvard Apparatus, Holliston, MA) and incubated at room temperature for 10 minutes prior to IRE pulsing as described below. An aliquot of 1640 RPMI media was used as a substitute for drug solutions for samples that received IRE treatment alone.

In vitro Irreversible Electroporation Optimization

Understanding the effects of the various pulse parameters employed in IRE therapies is vital to maximizing the effective IRE volume and minimizing the thermal damage from a given applied voltage. Here, an effective *in vitro* IRE electric field threshold for the glioma cell lines was determined as well as examination of the impact from the number of pulses. Aliquots (200 µl) of glioma cell suspensions containing 2 x 10^6 cells/ml for were placed into commercial 4 mm gap electroporation cuvettes, with self-contained aluminum plate electrodes arranged in parallel (BTX Cuvette Plus 640, Harvard Apparatus, Holliston, MA). A BTX generator (ECM 830, Harvard Apparatus, Holliston, MA, USA) was used to generate and deliver rectangular 50 µs DC pulses. To optimize the pulse parameters evaluated in the final IREEP experiments, cells were subjected to variable applied electric field strengths (0, 200, 400, 600, 800, and 1600 V/cm) and pulse numbers (0-100, in increments of 10). Pulse parameter optimization was

determined by examining dose-response curves of cell viability versus electric field and pulse number for each cell line, using the luminescent cell viability assay described below. All treatments were performed in triplicate.

Luminescent Cell Viability Assay

Five minutes following completion of delivery of electrical pulses at each field strength and for each glioma cell line after IRE alone or IREEP, cell suspensions were diluted to a concentration of 1 x 10^4 cells/ml, and three 100 µl aliquots from each cuvette were plated into a 96-well tissue culture plates, and the plates were incubated for 24 hours at 37°C. Following equilibration to room temperature for 30 minutes, a luminescent cell viability assay was performed (Cell Titer Glo, Promega, Madison, WI, USA) according to the manufacturer's instructions. For the assay, 100 µl of assay reagent was added to each well, the plate agitated on an orbital shaker for 2 minutes, and the plate incubated at room temperature for 10 minutes, followed by luminescence recording (LMax Luminometer, Molecular Devices, Sunnyvale, CA, USA). Wells filled with 100 µl RPMI 1640 media alone were used to obtain background luminescence.

Hoechst 33342 Staining

Aliquots of J3T and U-87 cells diluted to a concentration of 1 x 10^4 cells/ml subjected to all treatments were stained with a 10 µM final concentration of Hoechst 33342 stain and allowed to incubate for 1 hour at 37°C prior to examination via fluorescent microscopy (Leica DMRXA, Germany), with excitation centered at 360 nm and emission longer than 425 nm. Morphologically, glioma cells with homogenously stained nuclei were considered viable whereas apoptotic cells demonstrated condensed or fragmented and intensely stained nuclei. The percentage of apoptotic cells was determined from three independent quantifications, each counting at least 500 cells per treatment group, using a digital thresholding algorithm and image analysis software (NIS-Elements AR, Nikon, Japan) that labeled positively staining nuclei from the background and digital photomicrographs obtained with a 40X objective.

Transmission Electron Microscopy

Cells were detached, washed, suspended in PBS, and concentrated by centrifugation at 250 *g* for 10 minutes. Cells were then fixed in 2.5% glutaraldehyde, post-fixed in 1% osmium tetroxide, dehydrated in ethanol, and embedded in plastic using standard procedures. Thin sections (50 nm) were obtained with an ultramicrotome, treated with lead citrate and uranyl acetate, and examined using a transmission electron microscope (Zeiss EMC-10 CA, Carl Zeiss SMT, Inc., Peabody, MA, USA).

Statistical Analysis

For pulse parameter optimization analyses, one-way ANOVA was used. The results of IREEP experiments were subjected to two-way ANOVA. For all statistical analyses, the effects of treatment were compared to untreated controls, and α was set at 0.05. A commercial software package was used to perform all statistical analyses (SAS Version 9.1, Cary, NC, USA).

9.2.1.2 Numerical Model – Simulation within Brain

Treatment outcomes can be correlated to the electric field distribution, which can be predicted using numerical modeling [248, 249]. This provides a useful tool for understanding predicted treatment outcomes. We harnessed this to determine how treatment outcomes would be affected by incorporating the reversible electroporation enhancements when simulating a typical treatment using Comsol Multiphysics 3.5a finite element modeling software (Comsol, Stockholm, Sweden). The effective IRE and ECT electric field thresholds found from the *in vitro* experiments were employed to calculate predicted treatment volumes for both therapeutic regimes. The physical setup of the model is depicted in the results section, where Mimics software (Materialise, Leuven, Belgium) was used to generate a domain mesh based on the geometry of a canine brain taken from MRI scans. The model simulates two single-pole electrodes, each 1 mm in diameter, separated by 0.5 cm with a 0.5 cm exposed tip and the rest of the length simulated as electrical insulation. Both electrode tips are placed 0.5 cm into the brain, so the entire exposed regions are exposed to the brain. The electric field distribution is calculated by solving the governing equation:

$$\nabla \cdot (\sigma \nabla \phi) = 0 \tag{8.1}$$

where σ is the electric conductivity of the tissue and φ is the electric potential. Due to the low conductivity of bone, the boundary of the brain was considered to be a skull, which was treated as electrical insulation. The electrode portions inserted into the brain were considered conductive, with one of the electrodes considered to be energized at V_0, while the other was set to ground.

Electroporation-induced changes were considered in the model. It was shown in Neal et al. (Kidney paper reference), submitted, that the dependence of tissue electrical conductivity on electric field may be modeled using an asymmetrical sigmoid Gompertz function. The conductivity function, σ(E), was solved according to the equation:

$$\sigma(E) = \left[\sigma_0 + (\sigma_{max} - \sigma_0) \cdot e^{-B \cdot e^{-C \cdot E}}\right] \tag{8.2}$$

where σ_0 and σ_{max} are the minimum and plateau conductivities within a single pulse. The baseline electrical conductivity of grey matter, σ_0 = 0.2849 S/m, was applied to this function using curve parameters fit to a 50 μs long pulse from (Neal et al). It was shown in (Neal et al) that when applying an equivalent circuit model, shorting membrane resistance with complete electroporation gives a σ_{max} that matches the electrical conductivity measured at the frequency of β dispersion, where the lipid bilayer's capacitive behavior becomes short-circuited [218]. Therefore, the σ_{max} selected for our model was 0.7791 S/m, the conductivity of grey matter at 500 MHz, taken from the literature [250].

The numerical model simulated the electric field distribution within the tissue for the electrode setup solved for V_0 in 500 V increments between 500 and 2500 V. The predicted volumes of IRE and ECT affected tissue were then integrated to determine how each region grows with applied voltage.

9.2.2 Results

9.2.2.1 Cellular Response Characterization

Irreversible Electroporation Pulse Parameter Optimization

To investigate the effects of the applied electric field on glioma cytotoxicity, we applied a total of 90 pulses, each 50 µs long over the range of the experimental electrical fields, as we have previously shown the efficacy of this combination for the *in vivo* IRE ablation of normal and neoplastic brain tissue [8]. We found no significant differences between the two cell lines (**Figure 9.1A**) with respect to the mean applied electric field ED50 (J3T, 619±18 V/cm; U-87, 599±13 V/cm) or ED90 (J3T, 739±16 V/cm; U-87, 756±22 V/cm). Based on the electric field ED90 results, 800 V/cm was chosen as the electric field at which to test pulse number optimization (**Figure 9.1B**). No difference between the two cell lines was observed for the mean pulse number ED50, which was 43.7±1 pulses for the J3T and 43.5±2 pulses for the U-87 glioma cells (**Figure 9.1B**). The mean pulse number ED90 was significantly ($p = 0.0004$; **Figure 9.1B**) higher in U-87 glioma cells (73.9±8 pulses) compared to the J3T (66.7±7 pulses). For the remaining IREEP experiments, J3T glioma preparations were electroporated with 80 total pulses, and U-87 glioma cells with 90 total pulses.

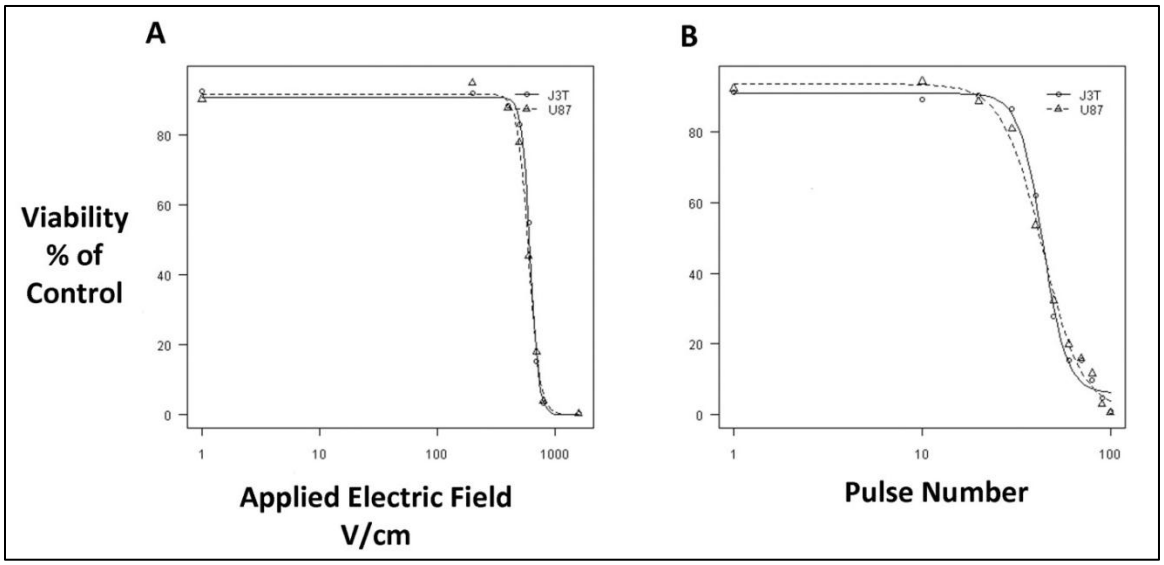

Figure 9.1: *In vitro* pulse parameter results. Dose-response curves for J3T and U-87 cell viability as a function of (A) applied electric field for 90, 50 µs pulses, and (B) number of pulses using 50 µs pulses at 800 V/cm.

Chemotherapeutic Agent Growth Inhibition

Chemotherapeutic response curves may be found in **Figure 9.2**. For bleomycin, the mean ED50 were 136±11 ng/ml and 345±52 µg/ml for the J3T and U-87 lines, respectively. The mean ED50 for carboplatin were 687±102 ng/ml for the J3T and 459±87 µg/ml for the U-87; both of which were significantly higher ($p < 0.0001$) than those for bleomycin in both glioma cell lines.

Irreversible Electroporation Enhanced Pharmacotherapy Induced Glioma Cytotoxicity

For the J3T, IREEP induced glioma cytotoxicities were significantly and markedly greater (all $p < 0.01$) than IRE or drug therapy alone over the entire dose ranges tested for both bleomycin and carboplatin (**Figures 9.2A** and **9.2B**) at electric field strengths of 200, 400, and 600 V/cm. For both bleomycin and carboplatin, there was also a significant (all $p < 0.02$) and negative association between cell viability and increasing drug dosage for applied electrical field strengths in the range of 200 to 600 V/cm (**Figure 9.2A** and **9.2B**). At higher electrical field strengths (800 V/cm and 1600V/cm), significant ($p < 0.04$) but mild increases in tumoricidal effect of IREEP were noted only for doses of bleomycin or carboplatin $\geq$ 1 µg/ml (**Figure 9.2A** and **9.2B**).

In the U-87 glioma, at electrical field strengths of 200 to 600 V/cm the most significant ($p < 0.01$) and marked cytotoxic effects of bleomycin IREEP were observed only at the highest drug concentrations (1 mg/ml) tested (**Figure 9.2C**). At electrical filed strengths at or above 800 V/cm, there were mild cytotoxic effects of bleomycin IREEP at drug concentrations $\geq$ 100 pg/ml ($p < 0.03$; **Figure 9.2C**). There was an overall more modest cytotoxic enhancing effect for carboplatin IREEP on the U-87 glioma, which was most evident at higher carboplatin doses (**Figure 9.2D**). Compared to carboplatin alone, there was essentially no enhancement of U-87 glioma cytotoxicity using carboplatin IREEP delivered at 200 V/cm, although at progressively higher field strengths, significantly ($p < 0.02$) enhanced U-87 cytotoxicity was observed with successively lower carboplatin doses (**Figure 9.2D**).

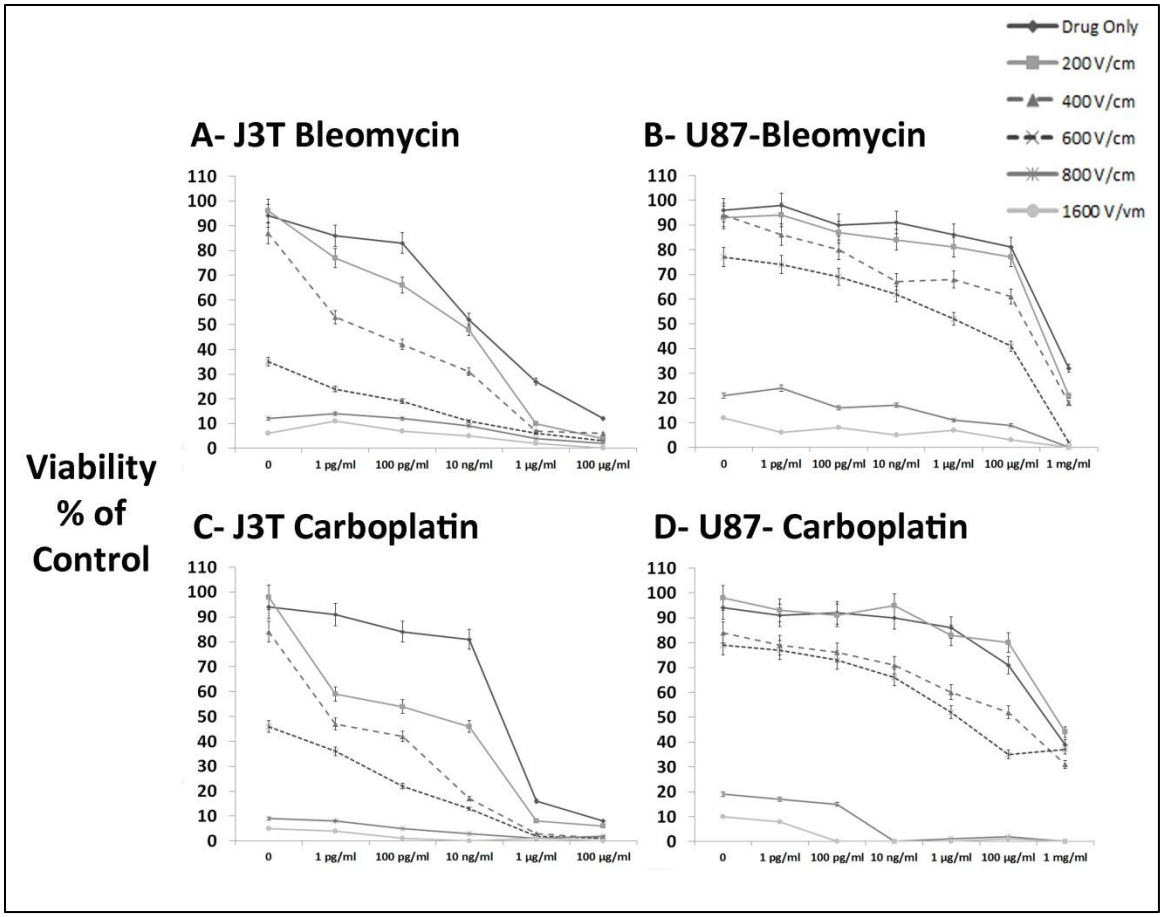

Figure 9.2: IRE and bleomycin or carpboplatin IREEP induced cytotoxicity in J3T (A and B) and U-87MG (C and D) glioma.

IRE and IREEP Induced Apoptosis of Glioma Cells

Evidence of glioma apoptosis was observed in response to all treatments. Morphologically, apoptotic J3T and U-87 glioma cells displayed cellular shrinkage, loss and fragmentation of cytoplasmic processes, formation of cytoplasmic apoptotic bodies, and chromatin condensation (**Figure 9.3**). Qualitatively, positive associations between the percentage of apoptotic J3T and U-87 glioma cells and the applied electric field were observed (**Figure 9.4**). Quantitatively, the enhancing effects of IREEP on J3T and U-87 apoptosis were most pronounced at higher drug concentrations, and at increasingly higher applied electrical fields at and above 400 V/cm.

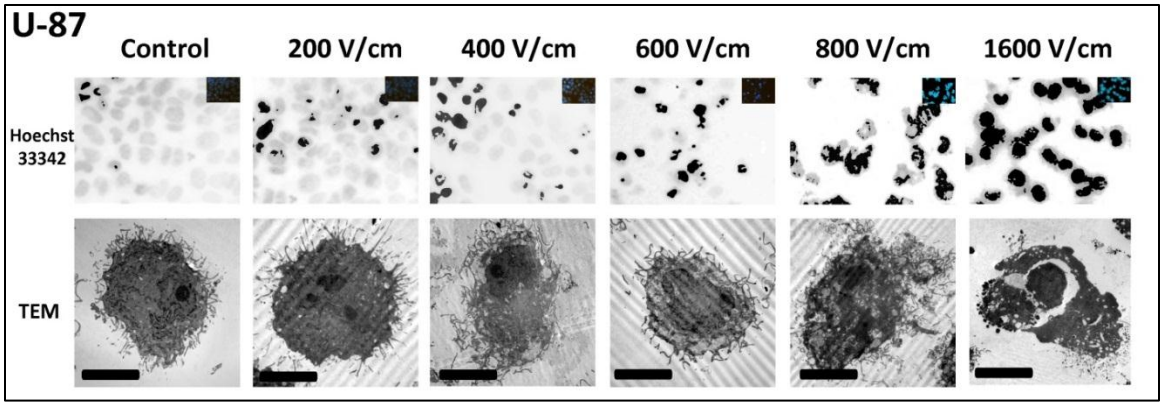

Figure 9.3: Apoptosis in U-87 glioma induced by IRE. The top panels demonstrate thresholding used to quantify apoptotic cells in Hoechst 33342 preparations (inset), and the bottom panels illustrate single cell glioma ultrastructural morphology in response to the applied electric field (TEM - transmission electron microscopy, bar = 2 µm in all panels).

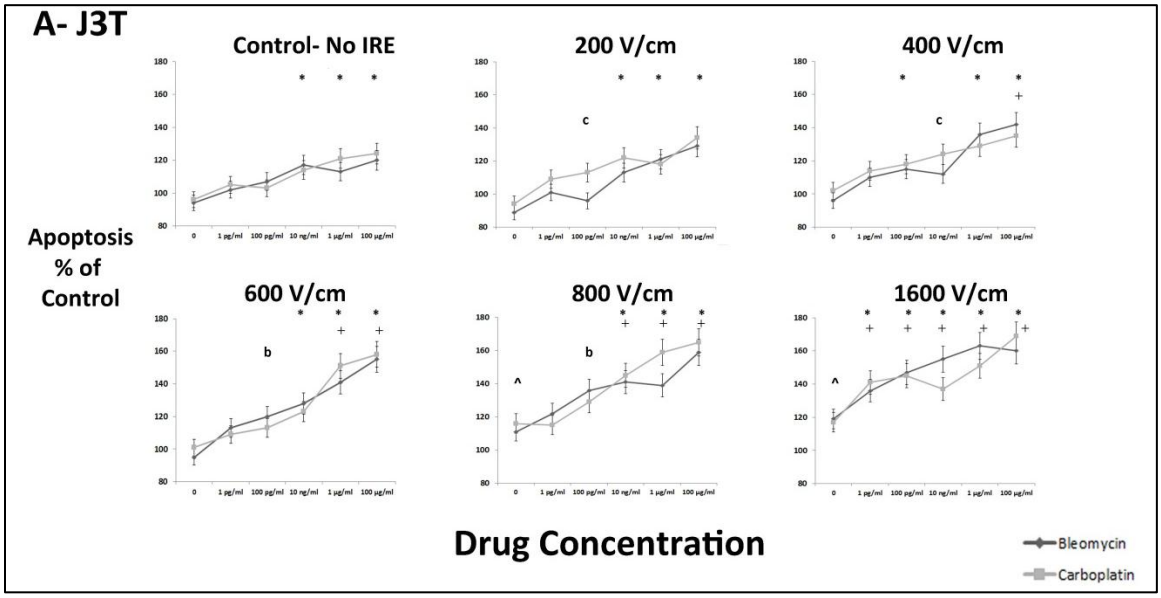

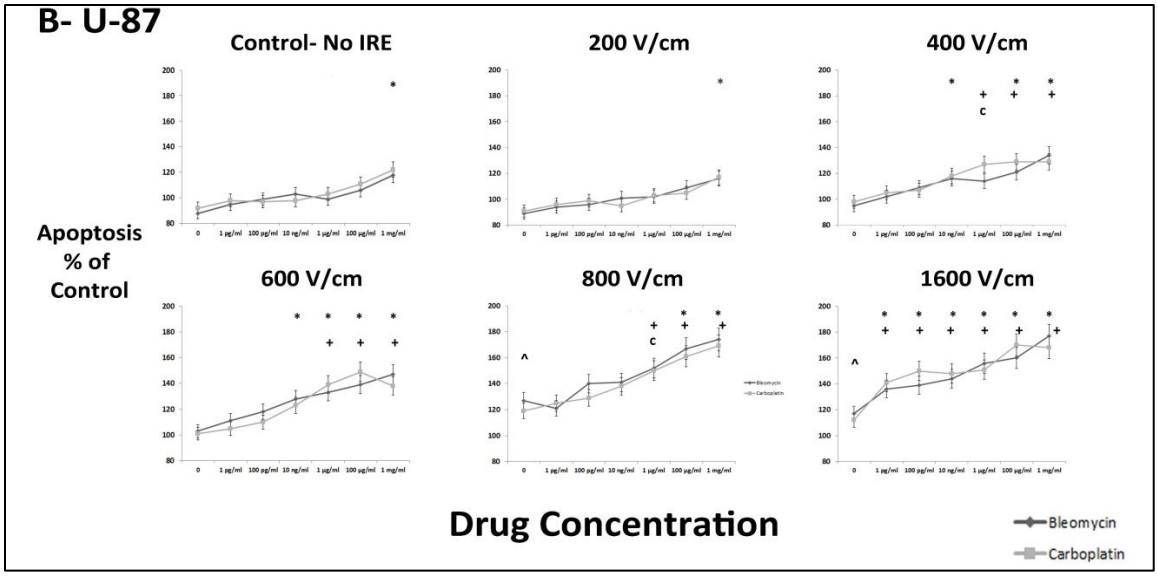

Figure 9.4: IRE and IREEP induced apoptosis in J3T (A) and U-87MG (B) glioma as determined from Hoechst 33342 staining.

9.2.2.2 Numerical Models

Two sets of numerical models were solved, one that assumed a constant (static) conductivity of σ_0 = 0.2849 S/m, and one that accounted for electroporation based conductivity change, giving conductivity as a function of electric field, $\sigma(E)$ (dynamic). The dynamic conductivity function was created using the curve coefficients from Neal et al. and minimum and maximum conductivities from the literature. A plot of this conductivity curve may be found in **Figure 9.5**.

The model was solved for the electric field distribution for the setup depicted in **Figure 9.6A** and **9.6B** using voltages at the anode between 500 and 2500 V/cm in 500 V/cm increments. Based on the results from the *in vitro* experiments, the volume of tissue exposed to 400 and 800 V/cm were selected to represent the regions of tissue experiencing enhanced drug cytotoxicity and IRE, respectively. Representative distributions for the 2500 V applied voltage may be found for solutions using the static (**Figures 9.6C)** and dynamic (**Figure 9.6D)** conductivity methods.

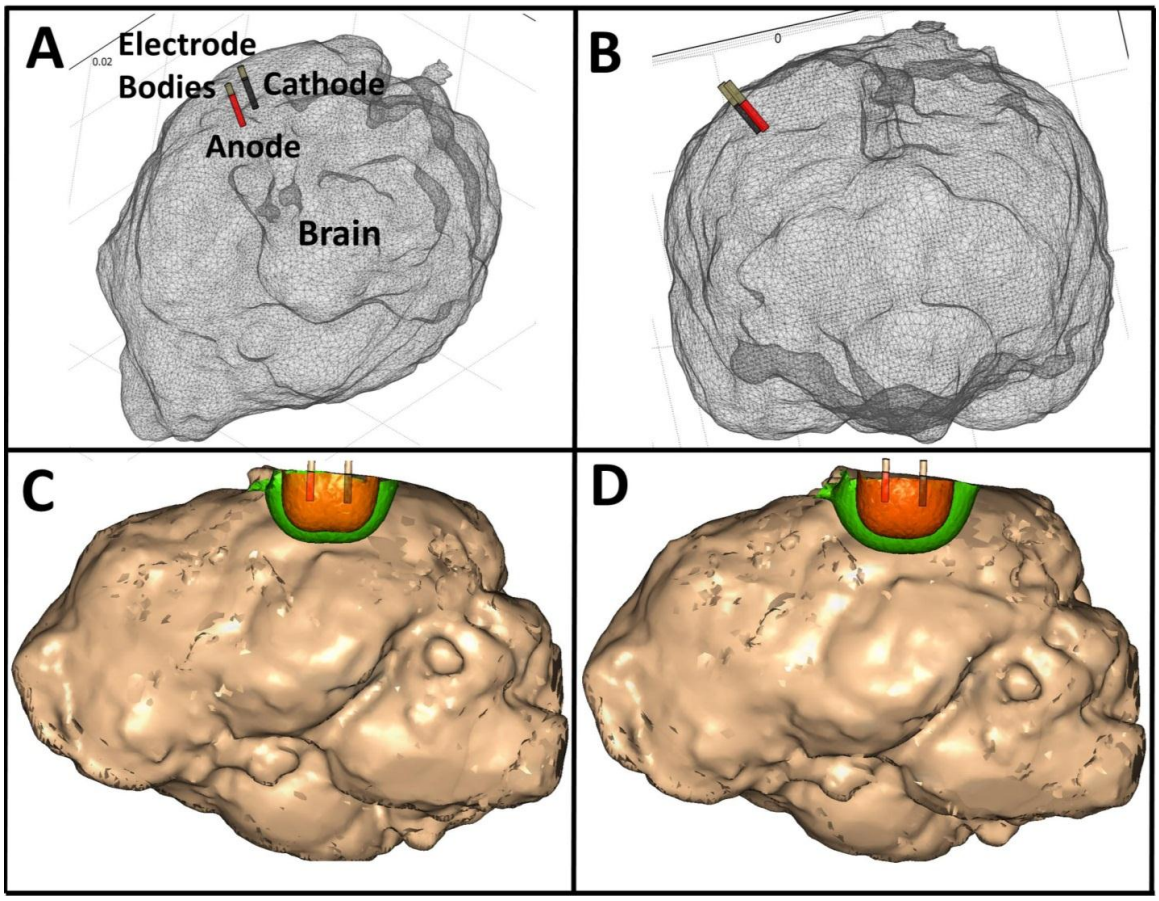

Figure 9.5: Numerical model. (A,B), model setup showing canine brain mesh from (A) above isometric and (B) front views. (C,D) model solution at 2500 V applied voltage depicting volumes experiencing IRE (orange) and ECT (green) using (C) constant and (D) dynamic conductivity techniques, side view.

Volumes of tissue experiencing electric pulse mediated increased chemotherapeutic cytotoxicity and IRE were integrated within the brain. This quantified the increased treatment volume that may be experienced by incorporating enhanced drug uptake in the lower realm of electroporation. A plot of affected volume versus applied voltage from the numerical model was created (**Figure 9.7**), where significantly increased therapeutic dimensions are observed when the 400 V/cm threshold is included in the treatment volume. Incorporation of the dynamic conductivity function resulted in higher treatment volumes for all applied voltages and thresholds, with dramatically increased 400 V/cm volumes, and less significant changes in the 800 V/cm regime. The percent increase in predicted treatment volume by including ECT at each applied voltage ranged between 104 and 220% (**Table 9.1)**.

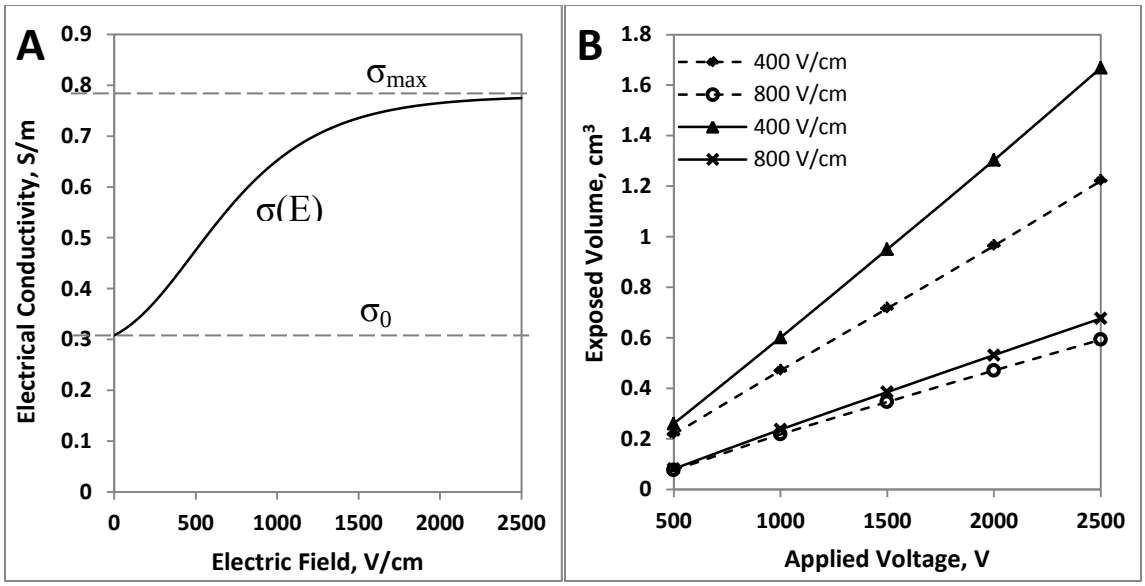

Figure 9.6: Numerical Model Results. (A) Electrical conductivity versus electric field for static, σ_0, and dynamic, $\sigma(E)$, numerical models. (B) Predicted Treatment Volumes of exposure to *in vitro* thresholds for ECT (400 V/cm) and IRE (800 V/cm) for static (σ_0 = 0.2849 S/m, dashed lines) and dynamic ($\sigma(E)$ function, solid lines) conductivities.

Table 9.1: Percent Increase in Treatment Volume when Including IREEP

Model	Voltage, V	Treatment Volume Increase, %
Static	500	186.56
	1000	116.12
	1500	106.91
	2000	104.84
	2500	106.08
Dynamic	500	220.29
	1000	153.72
	1500	146.77
	2000	145.11
	2500	146.64

9.2.3 Discussion

This study provides encouraging results regarding the potential to improve IRE focal ablation therapy for the treatment of tumors, particularly malignant gliomas, by examining increased therapeutic efficacy and predicted treatment volume when cytotoxic drugs are administered in conjunction with application of IRE-relevant electric pulses. These findings support the hypothesis that treatment volumes may be increased by utilizing the reversible regime of electroporation to facilitate enhanced drug delivery and tumor cytotoxicity, a process we refer to as IREEP. This would enable selectively

increased lesion volumes as well as larger general lesions without increasing the invasiveness of the procedure by requiring additional electrode insertions or larger applied voltages.

It can be seen in **Figure 9.6** that the increase in treatment volume from incorporating the 400 V/cm IREEP threshold reduces the required voltage for treating a targeted volume of tissue by 250% or more. As applied voltages increase to enlarge treatment volumes, so will the associated Joule heating and thermal effects. If the temperatures or time at elevated temperatures surpass thresholds for thermal damage processes to commence, several advantages of electroporation-based ablation compared to thermal therapies would be lost, such as sparing of sensitive and supportive structures [207], rapid lesion creation and resolution [5], and the near absence of post-ablation pain [24].

An important consideration for the increased, possibly selective, treatment margins induced by including the enhanced cytoxicity of the chemotherapeutic drugs in conjunction with the electric pulses is that the electric field thresholds used were derived from *in vitro* experiments. There is evidence that electroporation effect thresholds observed *in vitro* will change within *in vivo* environments. Although 800 V/cm was selected as an IRE threshold based on the cell lines used in this investigation, a study by Garcia, et al [8], found an IRE threshold of ~500 V/cm by calibrating a lesion volume produced using IRE in healthy canine brain with three-dimensional volumetric reconstructions. In addition, the time permitted for the carboplatin and bleomycin to induce apoptosis on the cells was 24 hours. Even greater efficacy of the drug may occur *in vivo*, where there will be no time restriction for these drugs to kill the cells.

This study reveals that typical IRE electric pulses previously used to produce focal ablations in brain will permit a regime of electric fields capable of enhancing chemotherapeutic efficacy without inherently killing the cells. It should be noted that a major obstruction to conventional chemotherapy in the treatment of malignant gliomas is the presence of the blood brain barrier and their relatively strong drug resistance [242]. Electroporation's permeabilizing effects increase the permeability of the vasculature, with noted edema in electroporated tissues, which has also been shown to disrupt the

blood brain barrier, improving biotransport of the drugs selectively into the targeted region [245]. An additional comparison between *in vitro* and *in vivo* environments is that an immune response has been shown to be promoted in electroporated tissues [5, 10]. Although the exact implications of an immune response have not been well characterized, it is possible that the tissue undergoing this 400-800 V/cm reversible electroporation regime may experience improved, selective, treatment outcome by the increased presence of immune cells in the affected volume.

Previous investigations employing the enhanced chemotherapy efficacy effects to treat diseased tissues such as tumors have generally avoided the irreversible, focal ablation regime of electric pulses [10]. These studies and clinical practice of ECT utilize a distinct set of pulse parameters that were found to generate the largest enhancement of drug cytotoxicity without innately killing the cells, resulting in protocols of 8 to 12 pulses. This study, among other investigations, has shown that increasing the number of pulses will dramatically alter cellular viability resulting from the electric pulses [155]. Therefore, a primary objective of this investigation was to experimentally determine the effective ECT electric field thresholds for IRE pulse protocols. There is currently a clinical trial underway using ECT as a sole therapeutic technique in the treatment of brain metastases at the Copenhagen University Hospital at Herlev. The group conducting the study has performed preclinical *in vivo* studies using ECT on brain tumors in a rat model [251], where they found a 69% regression rate. Evaluation of the safety and efficacy for bleomycin in the treatment of brain cancer without any electric pulses deemed the drug only therapy to be fairly tolerable by patients, and it is anticipated that the required dose may be reduced when including the electric pulses [244].

The presence of a substantially reduced threshold where improved drug uptake was observed permitted using a numerical model to explore the potential benefit to therapeutic outcome by combining these two methods for the destruction of cancer cells. This enhanced treatment outcome is of particular benefit for glioma therapy, since the poor prognosis for this variety of tumors is associated with their infiltrative capacity beyond the tumor margin [240]. The method for treatment presented here may be employed to use IRE to treat the observable margin of the tumor, while the ECT with

neoplastic-targeting chemotherapeutics at the lower electric field threshold would allow selective eradication of the cancer cells beyond the tumor margin.

The numerical model employed in this investigation was solved considering two conditions, a constant conductivity, and one that changes as a function of electric field. There is strong supporting evidence that the electrical conductivity of tissue changes in response to electroporation [203-206, 252]. However, these effects have been shown to vary widely depending on tissue type [204], and heterogeneous environments between tumor and healthy tissue will affect electric field distribution [156]. Because brain tissue has not yet been well characterized in this regard, it was determined to use two solutions to demonstrate how predicted treatment outcomes will change between model types. Although the curve for $\sigma(E)$ was derived from the behavior of kidney tissue exposed to electric pulses using values for σ_0 and σ_{max} for brain from the literature, it is likely that the trend will be the same, where even larger increases in volumes at 400 V/cm were observed for dynamic conductivity scenarios. Ultimately, both models showed that treatment volumes will at least double when incorporating the ECT for all applied voltages investigated in the simulated treatment setup. This effect will be even greater for numerical model simulations that place the electrodes deeper into the brain, where the electric field is able to occur in the direction along the proximal lengths of the electrodes, rather than being limited by the boundary of the brain tissue.

In addition to electroporation-based conductivity increases, it is well documented that temperature increases will also increase the conductivity of tissue (~ 1 to 3 $\%C^{-1}$) due to increased electrolyte mobility in the intra- and extracellular fluids [195]. This aspect of the numerical investigation was not included here. It was shown in [252], that the impact of this effect is less significant on the overall treatment volume relative to the electroporation-based dynamic conductivity. Future investigations of predicted enhanced treatment volume may include the combined thermal and electroporation-based effects on conductivity, $\sigma(E,T)$, to develop a stronger understanding of potential increased therapeutic volumes.

The numerical model showed an increased margin of effective treatment zone of approximately 0.5 cm for the 2500 V/cm case. Although this is not the 2 cm desired by the nature of malignant gliomas, it is still a significant increase. In addition, the rate of electric field decay away from the electrodes is related to the inverse of the distance. If it is found that the threshold is lower for *in vivo* conditions than those determined *in vitro*, the margin of enhancement will increase exponentially, providing significantly larger margins of treatment and increased therapeutic volume for a given applied voltage.

Acknowledgments

This work was supported by the Coulter Foundation and NSF CAREER Award CBET-1055913. The authors thank Kathy Lowe for her assistance with the cell morphology and histology work.

9.3 Clinical Examination – Spontaneous Tumor in a Horse Patient

The principles described in Section 9.2 have been applied in the treatment of a squamous cell carcinoma in the lip of an 11 year old neutered male thoroughbred equine patient. Here, we will briefly describe the case and its results.

9.3.1 Treatment Planning and Implementation

The patient had a squamous cell carcinoma in its lip (**Figure 9.7**) where conventional treatment would require removal through surgical resection, resulting in a large defect in the lip of the patient. The tumor presented indeterminate margins of infiltration beyond the core of visible tumor. Due to the large size of the patient relative to the tumor, it was decided that combined modality therapy would be possible without major risk for detrimental secondary systemic effects to the patient from the chemotherapeutic regimen used in the ECT realm of therapy.

Figure 9.7: Squamous cell carcinoma cancer in equine patient's lower lip. Here, the lip is elevated to show the inner portion of the lesion, which is more readily distinguished from the healthy gum.

Treatment planning was performed using Comsol Multiphysics finite element software (Comsol, Stockholm, Sweden). The lesion was modeled as using an approximate geometry of cancerous tissue with visible dimensions equal to measurements taken from the patient. This lesion was placed within a flat plate of tissue to approximate the interior of the lip. The lesion and interior were sandwiched on top and bottom by a thin layer of tissue to represent the skin and gum. Based on the geometry of the visible target, a three-electrode parallel insertion protocol was chosen to ensure maximum coverage of the cancerous region, which was inserted with the middle electrode in the center of the tumor, and the peripheral electrodes at either boundary of the target. The resulting three-dimensional mesh used in the numerical software can be seen in **Figure 9.8B**. The numerical solution for a pulse applied between two electrodes is shown in **Figure 9.8C**, where the energized center electrode is set at 2000 V and the right electrode is set to ground. Based on representative values in the literature and the desire to remain conservative in applying the therapy, electric field thresholds of 500 and 200 V/cm were selected to predict the regions of IRE and ECT, respectively, for a combined therapeutic treatment realm of IREEP within the deep blue isocontour.

The numerical simulations were used to develop a treatment protocol, and custom electrodes using hollow needles connected to syringes were constructed (**Figure 9.8A**). During implementation of treatment, the equine surgeon placed the hollow needle electrodes into the targeted lesion while simultaneously administering the chemotherapeutic agent bleomycin. After allowing 10 minutes for diffusion of the

intratumoral bleomycin injection throughout the targeted region, pulses were applied over the course of approximately 3 minutes. The electrodes were then removed and the patient was uneventfully recovered from anesthesia.

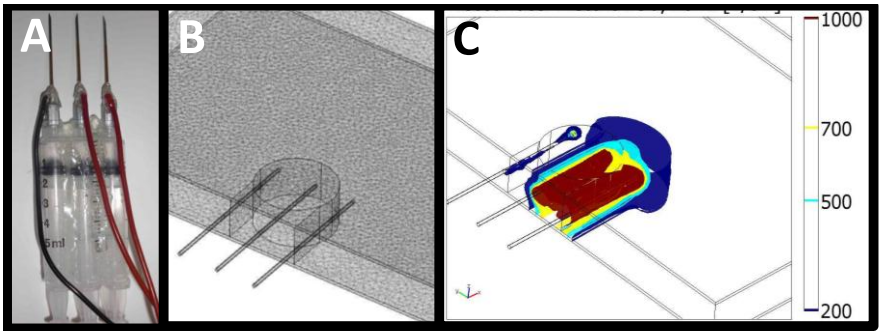

Figure 9.8: Treatment protocol design. (A) 3-needle parallel hollow electrode array for delivery of electric pulses. (B) Three dimensional volumetric mesh used to develop treatment plan, consisting of 3 electrodes inserted into center of the lesion, which is contained within the lip tissue and covered on top and bottom by skin. (C) Electric field distribution for numerical simulation using 2000 V applied pulse, predicted treatment realms for IREEP therapy for 500 V/cm for IRE and 200 V/cm for ECT.

9.3.2 Results

The patient was followed after therapy, where the treated region of lip tissue became necrotic. Images of the patient 2 and 8 weeks after therapy can be seen in **Figures 9.9A** and **9.9B**, respectively. By 8 weeks after therapy, nearly complete tumor resolution was seen, where only a small residual ulcerated lesion remained. The residual focus at the site of ulceration was removed with carbon dioxide laser and the patient recovered without requiring any further therapy for the tumor.

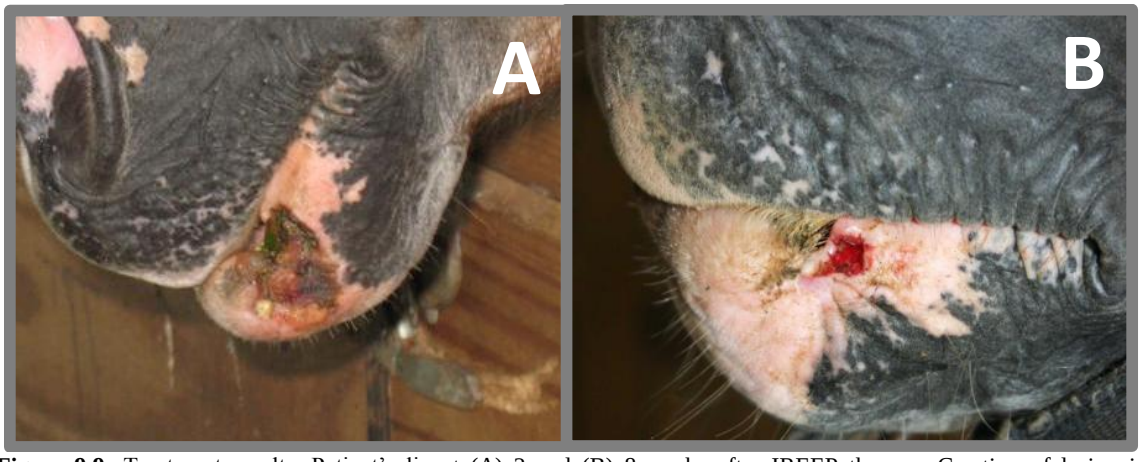

Figure 9.9: Treatment results. Patient's lip at (A) 2 and (B) 8 weeks after IREEP therapy. Creation of lesion in treatment region is clearly visible at 2 weeks post-therapy, while the small residual ulcerated cancerous focus is all that is seen to remain by 8 weeks post-treatment.

9.3.3 Discussion

Although we remain in the early, anecdotal periods of investigation for targeted IREEP, this study shows the safety and ability to design and implement IREEP protocols that can be applied in clinical patients. It further showed the ability for IREEP to treat localized diseases, and allowed a less invasive therapeutic alternative to surgical resection of the targeted region, reducing wounding, scarring, and creation of a defect in the patient's anatomy.

9.4 Conclusions

This chapter examined the potential enhancement of electroporation based therapies by combining irreversible electroporation pulses with increased cytotoxicity of chemotherapeutics below the IRE threshold. In Section 9.2, we demonstrate that bleomycin and carboplatin IREEP enhance the cytotoxic effects using IRE protocols on canine and human glioma *in vitro*. We provide evidence that IREEP cytotoxicity occurred predominantly via apoptosis, although other mechanisms may contribute. The enhanced cytotoxicity IREEP was achieved at drug concentrations several orders of magnitude below typical clinical systemic doses. In addition, we use a numerical model for predicting electric field distribution to demonstrate the potential increased treatment margins when combining modalities, where treatment volumes more than double for all scenarios investigated. These results lay the foundations for future investigations into IREEP for the *in vivo* combinatorial treatment of glioma. In Section 9.3, we report on a preliminary case study using IREEP in the treatment of a lip squamous cell carcinoma of an equine patient. Numerical simulations developed the treatment protocol, which was implemented through a custom-built hollow needle electrode array to administer bleomycin intratumorally during insertion. Following a latency period to allow for chemotherapeutic diffusion, the IREEP pulses were delivered within 3 minutes. The patient experienced regression of the targeted cancer volume to a small residual focus that was readily eliminated using laser excision. This chapter presents supporting evidence to the potential efficacy and utility of combined IREEP therapy in the treatment of tumors, especially those with targeted margins beyond the boundary of visible tumor.

Chapter 10: Immunological Enhancement of IRE Tumor Therapy[8]

10.1 Introduction

In the previous chapters of this dissertation, we have discussed external methods for targeting and killing localized regions of diseased tissues, such as tumors, using electric pulses with or without the inclusion of adjuvant macromolecules, such as drugs or DNA. However, previous work investigating the potential role that an immune response may play in IRE therapies has suggested the possibility for an enhanced therapeutic outcome when an immune response is permitted to operate on diseased tissues. As discussed in Section 10.2, multiple studies have investigated the short term immune response following treatment of cutaneously implanted murine tumors, as well as lymphatic drainage and the presence of immunocytes when IRE is used to ablate healthy tissue. Though these studies have shown evidence of an immune presence, the nature of observing immunocytes present in healthy tissue does not indicate if these immunocytes would improve patient response to IRE tumor therapy. In addition, the short-term investigations on tumors do not allow sufficient time for the immune system to mount a supplemental attack on any remaining cancer cells, actually showing a lack of role for the immune system in the immediate IRE ablation results. Further, it should be noted that previous tumor ablation studies that investigated both immunocompetent and immunocompromised mouse strains achieved the highest rate of regressions in an immunocompromised model [18]. However, the pulsing protocol used to attain the observed 92% regression rate in nude mice was not used in the immunocompetent murine model, preventing conclusive comparative efficacy.

[8] This chapter presents the work from an investigation currently in progress. Upon completion of the investigation and acceptance for publication, this chapter will be revised to reprint an adaptation of the final accepted manuscript, with appropriate reference made to the journal, article, and all contributing authors; including (in no specific order): Robert Neal II, John Rossmeisl, John Robertson, Christopher Arena, Erica Davis, Ravi Singh, Heather Hatcher, Suzy Torti, and Rafael Davalos

In addition to the studies discussed in Section 10.2, there exists anecdotal evidence that IRE promotes an immune response that enhances the therapeutic outcome. For example, Chapter 8 examined a case study treating a histiocytic sarcoma in a canine patient. The poor prognosis for this particular variety of tumor (3-6 month median survival [234, 235]) led to clinical objective of performing a conservative, palliative treatment to address the primary clinical symptoms of the patient. Therefore, the treatment protocol implemented was targeted to the symptomatic regions of the tumor, using IRE thresholds in the treatment planning process based on values taken from the literature of approximately 500-650 V/cm [8, 17]. However, within the first 8 days of treatment (before any adjuvant therapy was applied), a reduction in tumor volume of 52% was observed. The treatment plan IRE threshold values were calibrated from IRE lesions produced in healthy canine brain and rabbit liver tissue from lesions created within hours after pulsing.

The dramatically larger treatment volume observed in the canine patient implies either a secondary, slow growth realm of the treatment, as well as the possibility of an enhancement in response due to the patient's immune system infiltrating and killing additional tumor volume. Such a process may be induced by the destruction of the cells without thermal coagulation, leaking antigens recognized by antigen presenting cells that may then provoke a tumor-specific immune cascade for the body to recognize and attack additional cancer cells. Though highly speculative, the dramatically increased tumor response to IRE therapy from an immunocompetent patient relative to predictions based on immunodeficient tumor models and healthy tissue ablations resulted in the motivation to investigate the potential immunological enhancement of IRE therapies.

In this chapter, we test our hypothesis that the presence of a functioning immune system will enhance the therapeutic outcome of IRE cancer treatments. This was investigated by performing identical IRE treatments on immunodeficient (ID) athymic (nude) mice and immunocompetent (IC) balb/c mice. Tumor response to therapy was evaluated by measuring tumor growth with calipers and with histological assessment of tumor viability at the end of the study

In addition to evaluating the comparative responses between ID and IC murine tumor models, we also investigated the ability of the immune system to mount a long-lived, tumor-specific systemic response that will attack cancer cells not directly located in the IRE ablation volume. This aspect of the study was performed by re-inoculating the mice 18 days after treatment with the identical tumor induction protocol and monitoring secondary tumor growth compared to the initial tumor.

10.2 Previous Work with IRE and Immune Response

There are several investigations that assessed the reaction of the immune system to IRE pulses in healthy tissue and tumors [5, 6, 15, 16]. In [15], cutaneous tumors grown on the hind limb of mice were physically exposed and pulsed using plate electrodes. Prior to treatment as well as 2 and 6 hours after pulsing, mice were humanely euthanized and tumor tissue samples were harvested. Tissue samples were processed for immunohistochemical analysis from frozen tissue sliced into 5 μm-thick sections and stained for macrophages, CD4+ and CD8+ T-lymphocytes (effector cells of the antitumor response), and antigen-presenting and dendritic cells (CD80, CD86, CD11c). It was found from the analysis that the T-lymphocyte levels were highest before treatment, and rapidly declined within the first 2 hours, continuing to decrease by 6 hours after pulsing. The macrophage and dendritic cell stains showed no major change within the first 2 hours, but a marked decrease in the stain was observed by 6 hours after pulsing, with no observable decline at later sacrifice timepoints within 24 hours.

Although there was a decline in the number of positive stains by 6 hours after pulsing, the tumor cells were also not observed to demonstrate their compromised morphology within the first 2 hours of pulsing [18]. The authors suggest that the analysis does not show the tumor infiltrating cells leaving the tumor after the pulsing, but were killed by the pulses, and simply did not show a decrease from the immunohistochemical analysis until the 6 hour time point. Furthermore, the authors suggest that there is no new infiltration of the immune cells into the tumors due to vascular occlusion caused by disruption and disorganization of the micro-vasculature, as presented in [6, 253]. The authors conclude that because the immune cells are destroyed along with the tumor cells,

without immediate infiltration of new immune cells, IRE-induced cell death occurs independently from an immune response, suggesting that IRE may be a feasible therapeutic modality for immunocompromised patients.

In addition to the short-term study of the immune response in a murine tumor model, there have been several longer-term evaluations of the immune response to IRE pulses in healthy liver and prostate in a pig and dog model, respectively. The first large animal model to study the immune response was performed in [6]. In this study, IRE lesions were created in the livers of pigs which were then euthanized and evaluated at 1, 3, 7, and 14 days after pulsing. Within the first 24 hours, there was a small to moderate number of inflammatory cells (neutrophils and eosinophils) as well as regional lymph nodes showing mild cortical reactivity and expansion of the medullary sinuses consistent with a drainage reaction. The later timepoints showed lesion contraction and replacement with fibrous scar tissue as the lymph nodes continued to show a drainage reaction with expanded medullary sinuses expanded by eosinophils, neutrophils, lymphocytes, macrophages, and a temporally decreasing number of red blood cells. In a more detailed study on the immunohistological reaction to IRE pulses in a large animal model, lesions were created in swine, with euthanasia and tissue harvesting performed 24 hours after pulsing [16].

Tissue sections from [16] were fixed in 10% formalin and stained for analysis with Hematoxylin and Eosin, Von Kossa (for calcium deposition), and BCL-2 oncoprotein for analysis of apoptotic cell death. It was found that the ablated regions showed sinusoids congested with neutrophils and eosinophils. All ablated zones contained mineralization and were positive for the BCL-2 apoptosis marker. These findings, in conjunction with those presented in [5] of an immunologic reaction in lymph node draining in the area of ablation of canine prostates at 24 hours after pulsing, raise the possibility for a tumor specific immunological reaction to IRE that may be harnessed to augment IRE therapeutic outcome.

10.3 Methods

10.3.1 Tumor Inoculation

Two strains of female mice, ID Nu/Nu athymic nude and IC Balb/c, (Charles River Laboratories, New York, NY) were housed in individually ventilated cages in groups of five under specific pathogen free conditions. Mice were allowed access to sterilized water and feed ad libitum, and were kept in the animal facility for approximately 2 weeks, and reached an age of between 7 and 10 weeks prior to tumor implantation.

For tumor implantation, the murine renal adenocarcinoma (Renca) cell line was used (CRL-2947) (ATCC, Manassas, VA). This cell line was selected because it was derived from an adenocarcinoma that arose spontaneously in the renal cortex from the Balb/cCr strain of mice, permitting it to grow as a tumorigenic model in the IC Balb/c murine strain used in the study. Cells were cultured in RPMI 1640 media supplemented with 10% fetal bovine serum, 1% penicillin/streptomycin, and 1% sodium pyruvate (WHERE PURCHASED?). Cells were grown from frozen stocks and amplified for at least two passages prior to implantation. Once reaching approximately 80% confluency, cells were washed with phosphate buffered solution (PBS) and treated with 0.25% trypsin EDTA for detachment from culture flasks. Cells were resuspended in a 50/50 mixture of Matrigel High Concentration (BD Biosciences, San Jose, CA) and PBS at a concentration of $1x10^7$ cells/ml. Mice were anesthetized and 200 µl portions of the suspension were injected subcutaneously on the rear right flank of 30 mice total, 15 nude and 15 Balb/c. In addition, for histological analysis comparison of immune response, 6 Balb/c mice were injected with 200 µl of the Matrigel/PBS mixture alone. Four days after tumor inoculation, saphenous vein bleeding was performed to acquire baseline immune data in the presence of the tumor.

10.3.2 Tumor Treatment

Tumor growth was measured over time using calipers. Once reaching a minimum of 5 x 5 mm in top cross-sectional area and approximately 4 mm deep, tumors were treated in 10 mice from each strain. Mice were anesthetized using isofluorane inhalation

with the vaporizer set at 3% for induction of anesthesia, and 2% for maintenance during treatment. The skin over the tumor was prepped with disinfecting iodine and 70% isopropyl alcohol. Following preparation of the treatment area, 2 small metal needles of diameter = 0.3 mm with insulated bodies and exposed tips were inserted into the tumor to measure tumor impedance prior to and after pulsing as well as to measure the voltage drop during pulse delivery to ensure adequate electric field exposure to induce IRE. After measuring initial impedance using a Tenma 72-1025 LCR meter (Tenma, Hiroshima, Japan), conductive gel (4.15 S/m) (Parker Laboratories, Enumclaw, WA) was applied to opposing ends of the tumor, perpendicular to needle orientation.

A thin layer of conductive gel was applied to custom-built plate electrodes with insulated rear and perimeter regions, and the plates were placed on opposite ends of the tumor, perpendicular to needle orientation, and closed until reaching slight compression of the tumor. After determining the separation distance of the plate electrodes, electric pulses with a voltage-to-distance ratio of 1500 V/cm were delivered to the tissue, each 100 μs long, delivered at a rate of 1 pulse per second. A total of 100 pulses were delivered, reversing polarity after the first 50. Following completion of pulse delivery, impedance was measured and the needles and plates were removed from the tumor, re-oriented at 90 degrees relative to their original position, and the pulsing process was repeated, delivering a total of 200 pulses, with sets of 100 crossing perpendicular directions of the tumor.

In addition to the treatment groups, 5 mice with tumors from each strain received sham treatments, where the needles were inserted into the tumor and plates placed over the tumor, but without delivery of the electric pulses. Further, the 6 Balb/c mice inoculated with Matrigel/PBS only were treated over the remaining Matrigel plug 9 days after inoculation, an average time for tumors to reach treatable dimensions. These mice were sacrificed 18 and 34 days after pulse delivery to analyze and discriminate any innate immune response from a tumor-specific immune response.

10.3.3 Treatment Outcome Monitoring

Upon completion of the 200 pulse protocol, impedance within the tumor was measured again before removal of the needles. Topical antibiotic ointment was applied to the needle insertion wounds. Mice were then removed from anesthesia and provided 0.05 mg/kg buprenorphine analgesic diluted in 2 ml sterile saline solution. The analgesic diluted in 2 ml saline was administered for an additional 2 days after delivery of treatment.

Mice were followed after treatment and tumor measurements were taken at least three times a week and weights recorded twice weekly. Tumor volumes were calculated according to the equation for that of an ellipsoid:

$$V = \frac{4}{3} \cdot \pi \cdot a \cdot b^2 \tag{10.1}$$

where *a* is the long dimension of the tumor ellipsoid and *b* is the shorter dimension of the ellipsoid, perpendicular to the axis along *a*.

Mice were sacrificed if continued tumor growth resulted in tumors reaching 18 mm in any single dimension. For those that did not need require sacrifice due to tumor burden, mice were re-challenged with a second inoculation 18 days after treatment using the same protocol described in Section 10.3.2. The re-challenged mice were followed for an additional 16 days (34 days since initial treatment) or until any tumor reached 18 mm in any one dimension, with measurements of any observable tumor recorded.

10.3.4 Histology

When mice reached a point in the study to require sacrifice, terminal aortic bleeds were performed, followed by cervical dislocation. Samples of any present tumor tissue were excised and sectioned for processing. Tissue samples were divided into three groups for histologic analysis: representative tissues were embedded in Optimum Cutting Temperature compound (Tissue-Tek, Redding, CA) and frozen at -80°C, preserved in 10% neutral buffered formalin and embedded in paraffin, and were frozen in RNAlater media and frozen at -80°C. Frozen and formalin preserved samples were sectioned and

processed for histology using Haematoxylin and Eosin and immunohistochemistry marker $CD3^+$ to check for general B and T-cell lymphocytes.

10.4 Results

10.4.1 Initial Tumor Response

Initial inoculations produced tumors of treatable size after an average of 9.3 days for the nude mice and 9.5 days for the Balb/cs. All mice tolerated treatment followed by analgesic administration well. Due to the nature of delivering the electric pulses through the skin of the mice, initial damage to the skin resulted in scab formation, making accurate measurement of tumor size difficult. Scab formation resolved itself approximately 1 week after treatment delivery. Curves of initial tumor growth for both mouse strains may be seen in **Figure 10.1**, where an improved therapeutic response in the IC Balb/c is clearly evident.

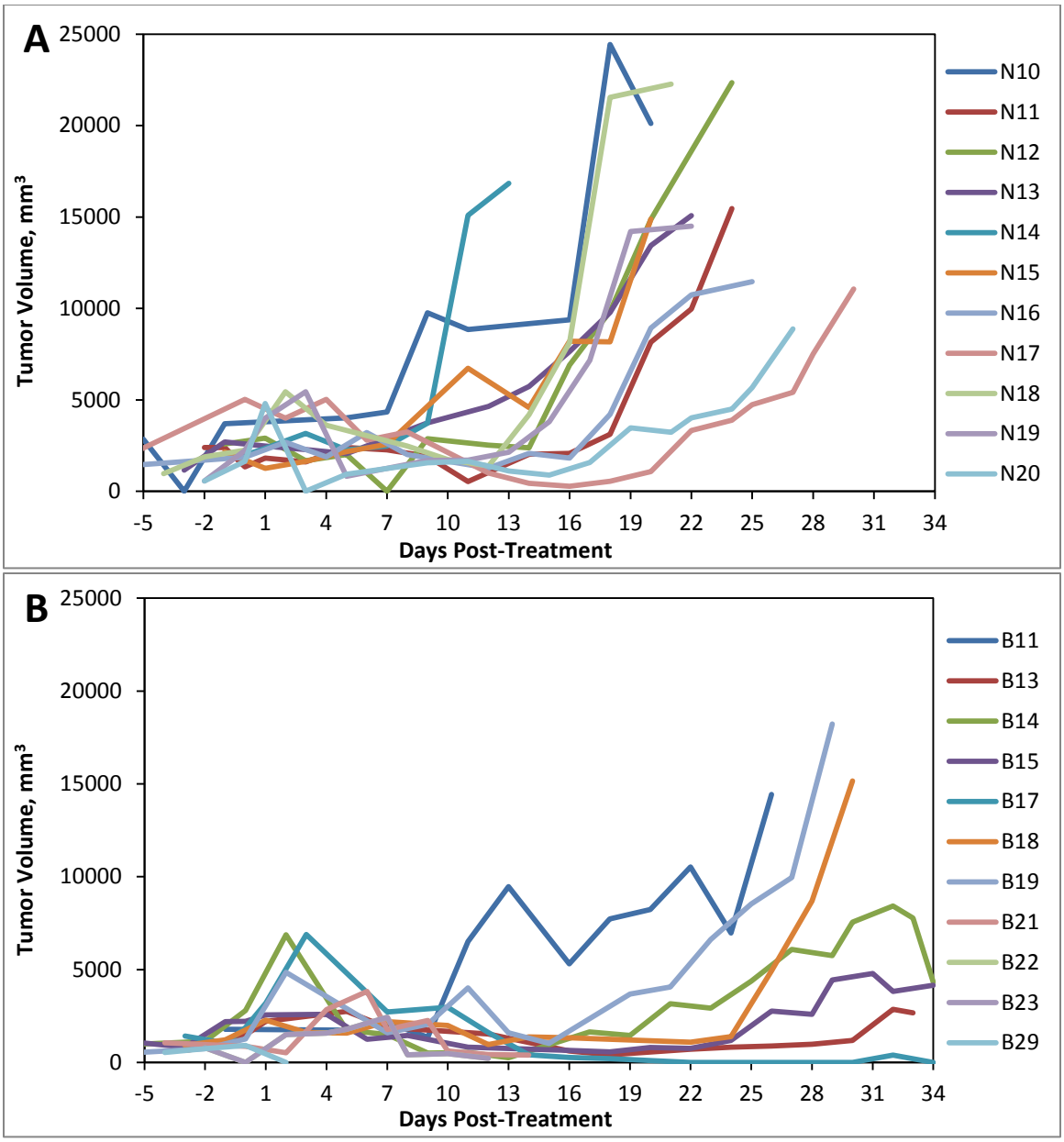

Figure 10.1: Volume curves for tumors in (A) nude and (B) balb/c mie strains. All endpoints in data are a result of sacrifice due to tumor reaching 18 mm in any single dimension.

The behavior of tumor growth for both treatment groups can be seen to be improved relative to the sham control mice, which may be seen in **Figure 10.2**. It should be noted in this figure that short-term (first 7 days) tumor volumes following treatment are smaller than those in the treatment groups due to the lack of scab formation.

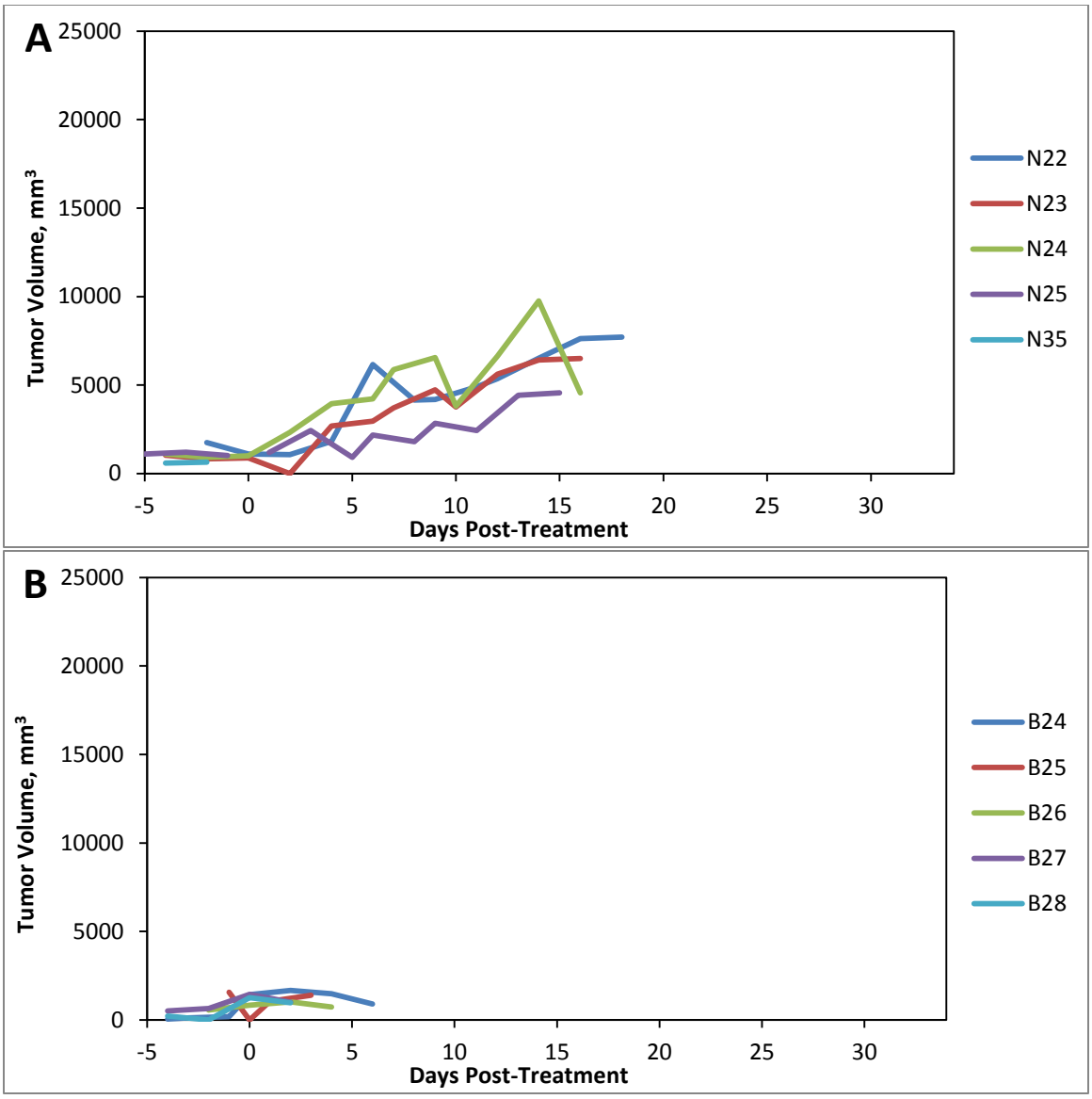

Figure 10.2: Tumor volume curves for sham-treated controls in (A) nude and (B) balb/c mice.

A Kaplain-Meier plot mapping survival of all mice from the 4 treatment groups can be found in **Figure 10.3**, where long-term survival is seen to be best among the treated IC Balb/c mice, followed by the treated ID Nude mice, IC Balb/c sham controls, and ID Nude controls, respectively.

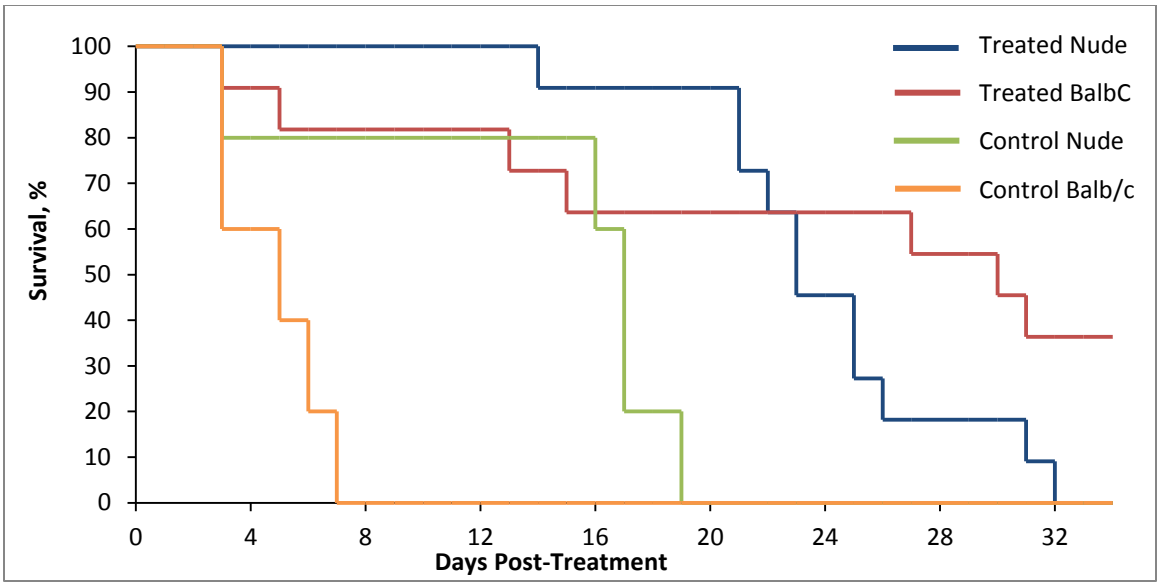

Figure 10.3: Survival plot for 4 treatment groups studied. * There remain mice to be followed in Treated BalbC and both Control Groups

10.4.2 Second Tumor Rechallenge

In addition to measuring initial tumor growth over time with calipers, mice were rechallenged with a second tumor inoculation of the same cell line 18 days after their initial treatment. These mice were followed for an additional 15-16 days after their secondary inoculation before being sacrificed for tissue collection, unless sacrificed earlier due to their primary tumor reaching 18 mm. Tumor growth curves for the initial and secondary tumor inoculations may be seen in **Figures 10.4** and **10.5**. From these figures, there appears to be no innate ability for the nude mice to prevent the second tumor from forming. However, it is clear that the second tumor inoculations in the Balb/c mice result in slower tumor growth, if there is any tumor present at all.

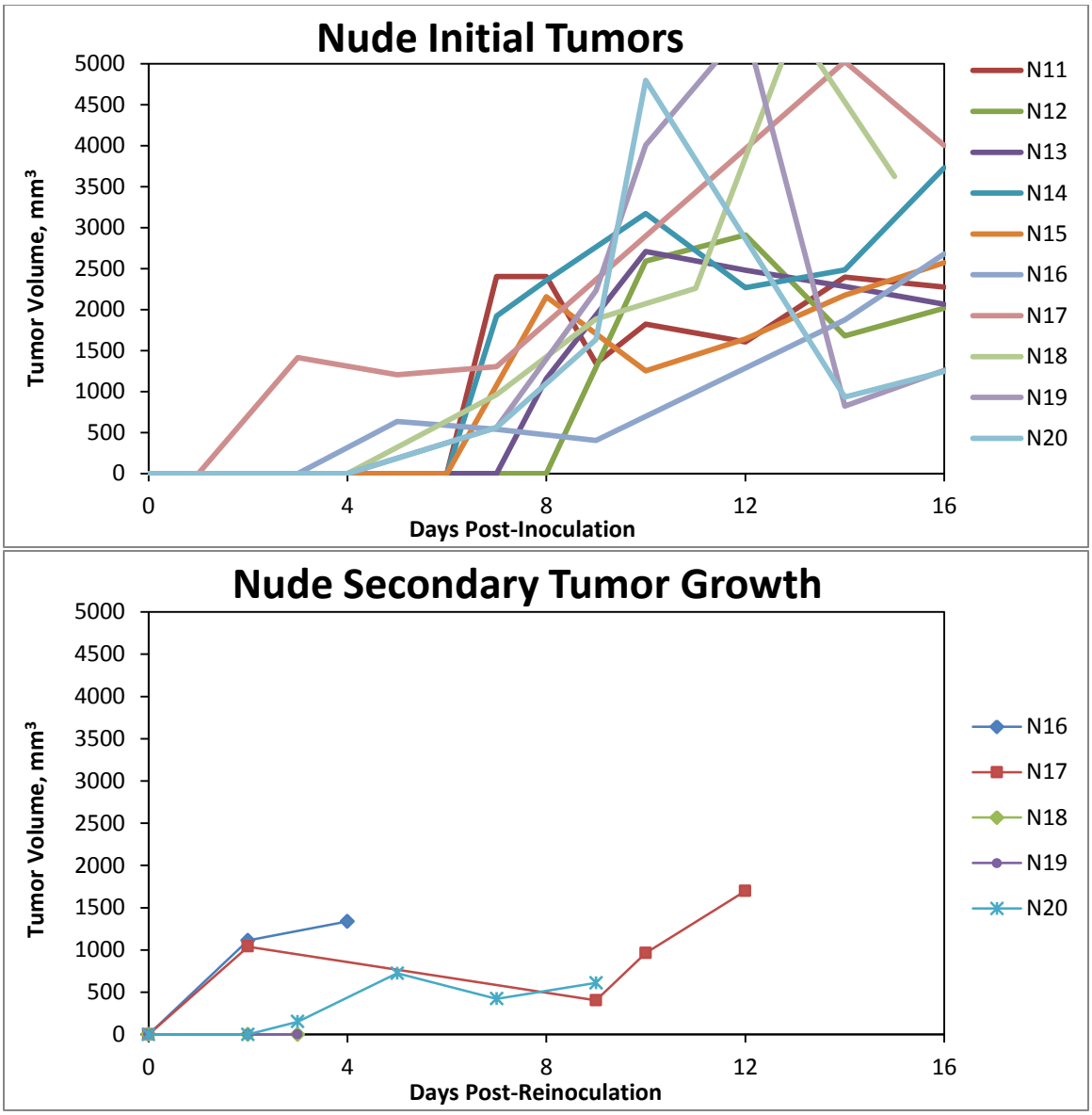

Figure 10.4: Tumor growth comparisons for immunodeficient Nude mice, where secondary tumor growth appears similar in trend to initial tumor growth.

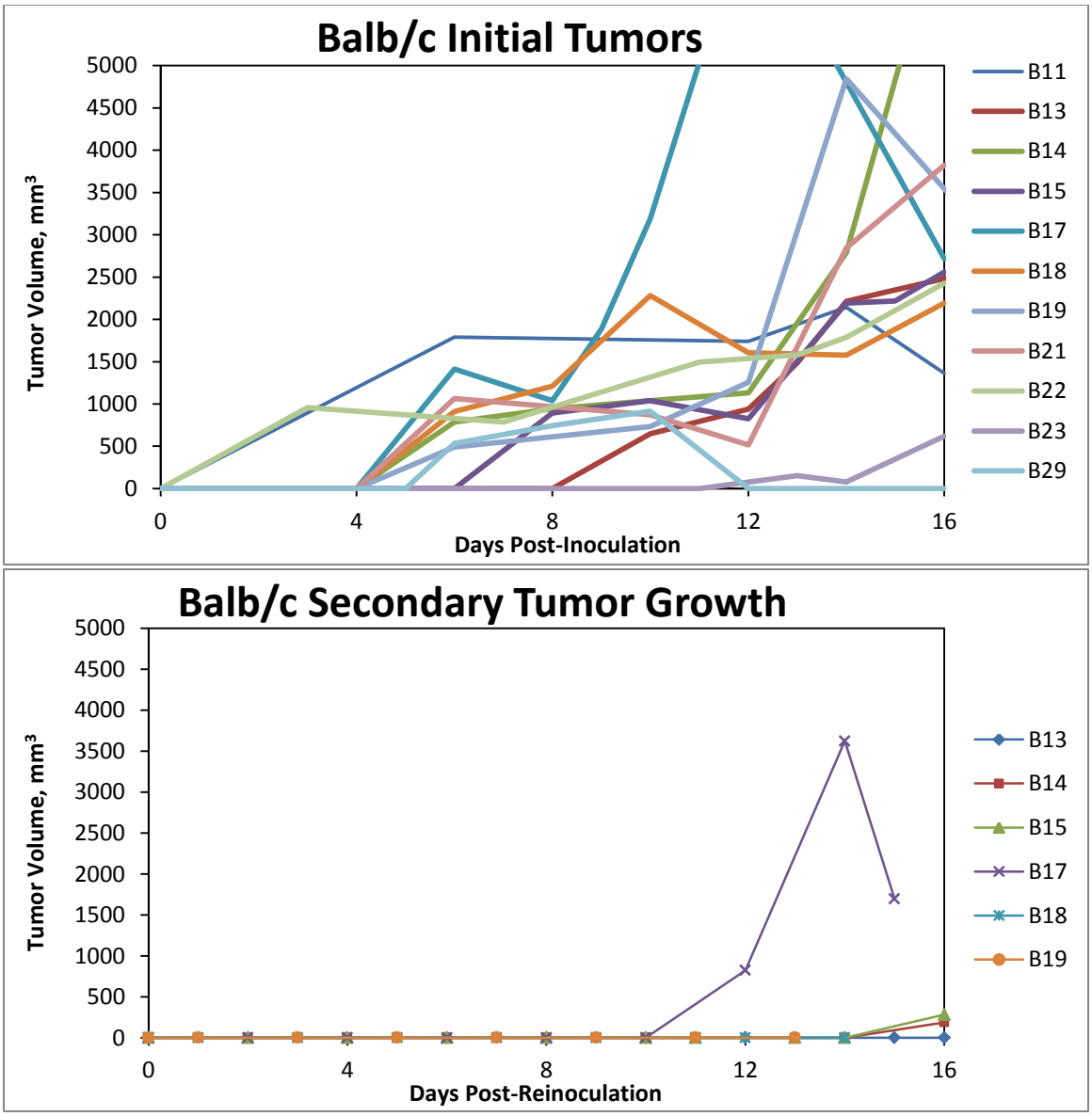

Figure 10.5:. Tumor volume comparisons for immunocompetent Balb/c mice, where an inhibition to secondary tumor growth is present compared to the initial tumors.

* In addition to plots, once all data is collected from mice, ANOVA and other tests of statistical significance will quantify changes between Balb/c and Nude mice as well as primary and secondary tumor growth. Values will be included for tumor doubling time.

10.5 Discussion

This study provides interesting evidence supporting the supplemental role that a functioning immune system may provide in response to IRE cancer therapy. The

implications that such support may provide are widespread. In the first portion of this investigation, we examined if the presence of a complete, functioning immune system would improve response to tumor treatment using IRE. It was shown in our results that this effect is evident, supporting the notions alluded to in the introduction based on the results from studies in [5, 6, 16, 22]. Preliminary *in vivo* experimental work was performed in healthy tissue, using immunodeficient animal models, or studying the short-term effects that the immune system performs in initial tissue response to IRE ablation. In addition, the first *in vivo* tumor ablation paper did not directly compare tumor response between ID and IC animal models for the protocol that attained a 92% regression rate [18]. Here, we show that the therapeutic response of an immunocompetent patient to IRE cancer therapy should be better than predictions drawn from these previous studies, due to a direct supporting role of the immune system. It should be noted, however, that previous studies, such as [15], show that a response from the immune system is not essential in attaining complete tumor regression and IRE ablation.

This investigation also presents evidence supporting the hypothesis that there is a long-lived, tumor-specific immune response capable of identifying and killing cancer cells at other locations throughout the body. Promotion of such a response provides promising prospects for IREs potential role in the treatment of late-stage, metastatic cancer. IREs utility as a focal ablation technique has shown great promise as an advantageous technique to kill localized disease, such as tumors. However, conventional sentiment has relied on a practitioner's ability to locate all targeted disease regions in order to treat the patient. The ability for an IC animal model to slow or prevent the growth of a reinoculation with cancer cells opens the possibility of using IRE to treat any observable tumors in a patient, where the tumor specific immune response may circulate through the body to identify and kill other regions of cancerous cells not detectable by modern healthcare techniques. The strength of this ability has yet to be determined and should be investigated in greater detail in future work. Although it may be found to not be a substitute for aggressive systemic cancer therapies, such as chemotherapy, combatting such a broad destructive disease as cancer, which is highly unique to each

individual patient, any adjuvant role that may be exploited from primary treatment modalities is welcome.

Follow-up on the tumor growth from second inoculations was dependent on the ability to detect the tumor over the skin. This was also the case for the primary tumor inoculations, where there is a clear difference in tumor growth curves. However, it should be noted that there were several instances where no secondary tumor was observed or measured during the 16 day secondary tumor follow-up period on the mice, but very small lobules at the reinoculation site were found after animal sacrifice and tissue collection, when the skin could be removed. Although these small lobules were undetectable during the follow-up period and recorded as no secondary tumor, the small lobules at the time of sacrifice were measured and recorded as the final secondary tumor measure, which can be seen in **Figure 10.5**. It should also be considered in **Figures 10.4A** and **10.5A** that many of the initial tumor growth curves extend over a time period that includes the days of treatment and follow-up. Most tumors met the treatment criterion when their volume exceeded approximately 600 mm^3, so data in the figure beyond this threshold should be considered post-treatment volumes.

The tumor specific immune response observed in this study may derive itself from IREs non-thermal method of causing cell death. By remaining below the temperatures that cause protein coagulation and molecular denaturation, the dead electroporated cells will maintain identifying molecules that may be used by antigen-presenting cells, such as macrophages, to activate the body's systemic immunity. In addition, IRE, as with many focal therapies, appears to promote a near-immediate inflammatory response, rapidly attracting leukocytes to the treated region, which may acquire the antigens as well as detect and kill any remaining cancer cells that survived the IRE electric pulses.

*Details on possible mechanisms will be added once the histology samples are processed.

Post-therapy injection of the analgesic diluted in 2 ml sterile saline for 3 days was essential to the treatment protocol in the immunocompetent mice. Preliminary work using a similar protocol on slightly larger tumors resulted in sudden morbidity and mortality of the IC Balb/c mice (data not shown). Although not confirmed, symptoms were consistent

with systemic inflammatory response syndrome (SIRS) or tumor lysis syndrome, both of which may be a result of suddenly ablating a large volume of cells or provoking a massive inflammatory response. The presence of this effect in the Balb/c's but not the nudes suggested the likelihood of SIRS. Therefore, it was decided to administer supplementary fluids following IRE therapy in an effort to mitigate the detrimental effects SIRS without requiring the use of immune-altering anti-inflammatories. Adding fluid administration to the protocol prevented any further immediate post-treatment morbidity or mortality of the mice.

10.6 Conclusion

This investigation studied the effects on tumor response in the presence, or absence of a functioning immune system. Identical renal adenocarcinoma cell lines were used to produce tumors in immunodeficient athymic Nu/Nu mice and the immunocompetent Balb/c mouse strain from which the cell line was derived. Tumors grew to treatable size in both mouse strains by approximately the same average day. Mice were treated with IRE by delivery of 200 electric pulses at 1500 V/cm through plate electrodes placed on opposite sides of the tumor, rotating the arrangement 90° halfway through and using conductive gel to direct the current into the targeted volume. Tumor response to therapy was observed to be better in the immunocompetent mice than the immunodeficient model, as measured by macroscopic dimensions to evaluate tumor doubling time and overall tumor growth trends. In addition, re-inoculation of the same cell line 18 days after IRE therapy was found to result in limited, if any, tumor growth in the immunocompetent mice. There no significant difference between primary and secondary inoculations in the immunodeficient mice. Histology of the collected tissues showed ***. This study provides strong supporting evidence for the enhancement or IRE therapeutic outcome in immunocompetent cancer patients, including the possibility for a systemic, tumor-specific response that may identify and kill cancer cells at untreated sites in the rest of the patient's body.

Chapter 11: Summary

11.1 Introduction

Electroporation based therapies use brief electric pulses to destabilize the cellular membrane to facilitate increased macromolecule transport or to kill the cell in a non-thermal manner. Although some applications of electroporation have been used for decades, using the irreversible realm of electroporation to kill localized regions of diseased tissue is a relatively new objective. It is the goal of this work to develop irreversible electroporation into a robust, clinically viable treatment modality for targeted regions of diseased tissue, with an emphasis on tumors.

This dissertation has focused on developing irreversible electroporation therapy to manage the many complexities that present themselves in real-world clinical patient therapies. It included theoretical and experimental investigations into the feasibility of using electroporation based therapies in heterogeneous systems, developing accurate treatment planning algorithms for implementing electroporation therapies in patients, validating IREs effectiveness in complex and irregular spontaneous tumor environments. It also examined potential supplements to enhance IRE therapy, including the presence of an inherent tumor-specific patient immune response and the addition of adjuvant therapeutic modalities.

11.2 What This Work Accomplished

In this work, we aimed to support our underlying hypothesis that irreversible electroporation is an effective focal ablation technique in treating localized disease, particularly cancer patients. We began this effort in Chapter 4 by exploring the feasibility of using IRE to treat tumors in heterogeneous environments, using breast cancer as our disease model. After determining an effective IRE threshold to kill cells *in vitro* with a standard pulsing protocol (pulse length, number of pulses, repetition rate), we created a numerical finite element model to simulate treatment of a breast tumor using two 1 mm diameter needles. This model manipulated the conductivity ratio between the tumor and peripheral tissue while quantifying the volume of tissue exposed to the effective IRE

threshold and thermal damage. This chapter concludes that when using the physical setup established in the numerical model, it is possible to treat the entirety of the targeted tissue over a wide range of conductivity ratios while keeping the extent of thermal damage to less than 5% of the total treated volume.

Chapter 5 developed on the results from Chapter 4 by treating orthotopically implanted human breast tumors in the mammary fat pad of mice. The IRE electric pulses were delivered into the tissue using a single needle electrode that contained both energized surfaces and could be readily manufactured for use in patient clinical therapies. The treatment was able to attain complete regressions in 5 of 7 treated mice based on tumor dimensions measured with calipers and further confirmed with bioluminescence and histology.

Following empirical validation for the ability to use IRE cancer therapy in clinically relevant settings, this dissertation shifted towards developing treatment planning to improve the therapeutic outcome in patients by ensuring treatment of the targeted region while sparing as much neighboring healthy tissue as possible. In Chapter 6, we experimentally characterized the changes that occur in tissue properties as a result of electroporation. These changes were incorporated into a numerical model to evaluate how treatment volume predictions would change when the dynamic tissue conductivity is accounted for. The experimental values were also applied to a revised equivalent circuit model for cells and tissue to derive representative element values and simulate how conductivity conditions would change under varying conditions and possibly other tissues.

After characterizing the dynamic conditions of tissue undergoing electroporation, we moved on to a discussion of treatment planning techniques and considerations in Chapter 7. This included a description of several rapid-solving techniques and their potential functionality in aiding a physician to develop or adjust a treatment plan in real-time, as well as a thorough description of the step-by-step process involved in developing a treatment plan that accounts for the complexities commonly present in clinical cancer cases.

The efforts in developing treatment plan algorithms described in Chapter 7 are then applied to the treatment of an actual clinical canine patient. The patient presented a 136 cm^3 histiocytic sarcoma in its hindlimb that was causing sciatic neuropathy and tumor-associated pain. The treatment planning process described in Section 7.5 was performed in consultation with the veterinary surgeon that implemented the procedure, and a three-stage electrode insertion process was selected to palliate the clinical symptoms of the patient. After observing improved clinical symptoms and a 52% reduction in tumor volume 8 days after therapy, adjuvant chemotherapy was added to attempt to eliminate the remaining tumor. The tumor continued to decrease to a small focus of cancer in an area not originally targeted by IRE therapy (not clinically significant) before developing chemoresistance. A second application of IRE to the remaining tumor, using a new treatment plan, was able to eradicate the cancer and the patient currently remains in complete remission for a total of 14 months.

After empirically validating our hypothesis that IRE can be used as an effective method to treat cancer in complex and patient-specific clinical scenarios, this thesis investigated potential enhancements to IRE therapy by the addition of macromolecule therapy to extend the range of the therapeutic region and by the body's own ability to recognize the cancer cells in a treated volume in order to mount its own supplemental attack on the cancer. The intentional augmentation of IRE therapy with the addition of chemotherapeutics followed the investigative model performed in Chapter 4, where *in vitro* experiments on two glioma cell lines were performed to examine the increased cytotoxicity of irreversible electroporation enhanced phamacotherapy. The experiments were used to derive two theoretical effective electric field thresholds, one for IRE (800 V/cm) and one for the enhanced phamacotherapy (400 V/cm), which were then applied to a numerical model where it was found that the therapeutic volume more than doubled for any given applied voltage when the modalities are combined.

Finally, this dissertation studied the innate improvement of cancer response that results from an IRE-facilitated promotion of an immune response to the ablated volume. IRE electric pulses were delivered to subcutaneous tumors in a murine model using immunocompetent and immunodeficient strains of mice. 18 days following treatment of

the first tumor, a second inoculation using the same tumorigenic cell line was administered at a different location on the body. This investigation found that a functioning immune system improved IRE treatment outcome as well as demonstrated a long-lasting, tumor-specific immune response capable of slowing or preventing the growth of a new tumor.

11.3 Future Work

The field of electroporation-based therapies remains in its infancy, especially irreversible electroporation as method for achieving non-thermal focal ablation. Although therapies such as electrochemotherapy and IRE have started to be used in clinical patients, ECT is only beginning to be used for internal tumors, and IRE is primarily being investigated for its safety and rough examination of its therapeutic efficacy. There remains significant work to be done in order for these therapies to be developed into robust, reliable therapies implemented into routine standard of care use.

One facet of work that requires continued exploration is the characterization of relevant tissue properties undergoing electroporation. In Chapter 6, this was carried out for *ex vivo* renal cortical tissue, which was used to develop a numerical model capable of accounting for these effects. However, it remains to be seen if such a numerical model more accurately predicts lesion volumes on animal tissues *in vivo*. In order to validate such efforts, *in vivo* experiments should be performed and the resulting lesions should be compared to those predicted by numerical simulations to determine what biological processes are the most relevant in predicting treatment outcomes. Effects that should be considered include electroporation and temperature dependent electric properties of the tissue, localized heterogeneities in the treatment environment from the presence of additional tissues (tumors, major blood vessels and nerves, bone, etc), as well as accounting for blood flow and metabolic heat generation.

In addition, different tissues inherently have different bioimpedance characteristics. Although Chapter 6 presents a hypothetical method for deriving these characteristics based on the equivalent circuit model and published tissue properties at β-dispersion frequencies, such a technique has yet to be tested. Future work in this field should

continue to characterize the bioimpedance properties of additional tissues and examine how these characteristics compare with those of kidney. After determining the behavior of these tissues, more complex numerical treatment simulations may be developed using the unique dynamic tissue properties for all tissues involved in a treatment environment. This is especially true for tissues with very different properties, such as low conductivity bone, adipose and connective tissue, and skin.

Moving forward with understanding the impact of tissue properties, IRE therapy has been clinically investigated for a variety of soft tissue applications, but remains relatively uninvestigated for hard tissues, such as bone. Bone's very low conductivity is likely to dramatically affect IREs utility in the treatment of hard tissue tumors, such as osteosarcomas. Some preclinical work has alluded to this being the case for tumors with localized calcifications (data not shown), where a significantly smaller treatment volume was observed relative to predictions made from treatment plans without prior knowledge of the presence of such calcifications.

Tissue electrical properties will direct the distribution of the electric field, and therefore transmembrane potential to which the targeted cells are exposed. However, different cell and tissue types, as well as different cancers, also exhibit different susceptibility to death from the IRE electric pulses. For instance, it was observed in [17] that 637 V/cm appeared to be an effective IRE electric field threshold in healthy rabbit tissue, while [168] found an IRE threshold of 500 V/cm for healthy brain tissue. Studies using IRE in healthy tissue also observed sparing of certain structures, such as nerves and major vasculature [5, 6, 22]. Further, in Chapter 4, an effective *in vitro* IRE threshold for a human mammary carcinoma cell line was found to be 1000 V/cm [156], while a similar protocol used in Chapter 9 found the threshold to be 800 V/cm in malignant glioma cell lines, providing evidence that certain cancers will be more resilient to the electric pulses than others. Finally, in [22], biopsies taken at the tumor margin definitively show complete cancer cell death while the adjacent muscle cells were able to recover from the pulses. Understanding the susceptibility to IRE-induced cell death of different tissues will be vital to developing treatments that will ensure complete ablation of the targeted volume while attempting to preserve as much of the neighboring healthy tissue as

possible. Future work should continue to investigate the effective IRE threshold on different tissues and tumor types.

Most treatment planning protocols rely on the electric field distribution to assess predicted treatment outcome. However, there is substantial evidence showing that the other electric pulse parameters will play an important role in what this "effective" IRE electric field threshold will be. The relevance of pulse length, pulse shape, number of pulses, and pulse repetition rate has been characterized in several unpublished studies performed here (data not shown) as well as in published *in vitro* and *ex vivo* investigations, [155, 254]. Future work characterizing the effects of the pulse parameters should be used to develop an understanding of total pulse energy delivered to the tissue, from which effective IRE energy thresholds would be derived based on the pulse parameters and electric field distribution, providing the IRE electric field threshold as a function of number of pulses, pulse length, pulse shape, and pulse repetition rate. In this way, treatment planning would be performed using the electric field distribution to determine the overall shape, while the energy contour considered to relate to cell death will be based on this overall pulse energy.

An additional realm for continued work developing IRE for patient cancer therapy would be the iterative development of treatment planning protocols. Current treatment plans are developed based on observations from *in vitro, ex vivo,* and *in vivo* experiments and anecdotal observations. While these investigations provide a suitable guideline for developing treatment plans for patients, it is likely that treatment outcomes will vary from predictions based on this work when implemented in clinical patients. Such a result was observed in [22], as described in Chapter 8, where the actual ablation volume and therapeutic outcome was greater than what was originally anticipated from treatment planning predictions. This is likely a result of complex interactions and changes that occur when moving from experimental work to actual patients, such as the promotion of a treatment-enhancing supplemental immune response as described in Chapter 10. Therefore, future work should emphasize comparing treatment plan outcome predictions with actual therapeutic volumes when implemented in true clinical settings. In this way, treatment planning models may be evolved to account for any discrepancy from

predictions in order to more accurately plan future treatments. Once numerical treatment plans can accurately predict treatment outcomes, efforts should be made to automate the treatment planning process as much as possible to enable rapid solving of optimum treatment protocols on a patient-by-patient basis. Such a robust and accurate treatment planning system is vital to the continued success of applying IRE therapy to patients in a reliable, standard of care manner capable of treating the millions of IRE-eligible cancer patients worldwide.

11.4 Conclusion

This dissertation provides strong supporting evidence for the utilization of irreversible electroporation non-thermal focal ablation in the treatment of complex and unique tumors commonly encountered in clinical patient cancer therapy. After theoretically determining the efficacy for IRE cancer treatment in heterogeneous systems, such as breast cancer, this work validated its findings by successfully attaining non-thermal complete regression in orthotopically implanted mammary carcinomas in the mammary fat pad of mice, simulating the macroscopically heterogeneous environment of breast cancer. This dissertation then worked to improve numerical model treatment planning by characterizing the biophysical changes that occur in tissue properties when subjected to electric pulses and outlining treatment planning algorithms that may be used to ensure complete treatment of the targeted region while sparing as much neighboring healthy tissue as possible. The underlying hypothesis was then tested by planning and implementing IRE therapy on a canine patient that had a large, complex tumor in a heterogeneous environment that included bone, muscle, nerves, and major arteries. Following a second application of electric pulses, the patient remains in complete remission, currently for a total of 14 months. Finally, this dissertation examined potential methods to enhance the outcome of IRE tumor treatments through the use of adjuvant treatment modalities in IREEP and by inherently promoting a tumor-specific immune response capable of augmenting treatment outcome in the targeted region as well as throughout the body. This investigation concludes that IRE is a useful non-thermal tissue ablation technique capable of being implemented to successfully treat clinical cancer patients, including those with complex cases or refractory to conventional therapies.

References

1. Cosman, E.R., *Electric and thermal field effects in tissue around radiofrequency electrodes.* Pain Medicine, 2005. **6**(6): p. 405-424.
2. Glaser, R.W., S.L. Leikin, L.V. Chernomordik, V.F. Pastushenko, and A.I. Sokirko, *Reversible electrical breakdown of lipid bilayers: formation and evolution of pores.* Biochim Biophys Acta, 1988. **940**(2): p. 275-87.
3. Neu, J.C. and W. Krassowska, *Asymptotic model of electroporation.* Physical Review E, 1999. **59**(3): p. 3471.
4. Edd, J.F., L. Horowitz, R.V. Davalos, L.M. Mir, and B. Rubinsky, *In Vivo Results of a New Focal Tissue Ablation Technique: Irreversible Electroporation.* IEEE Trans Biomed Eng, 2006. **53**(5): p. 1409-1415.
5. Onik, G., P. Mikus, and B. Rubinsky, *Irreversible Electroporation: Implications for Prostate Ablation.* Technol Cancer Res Treat, 2007. **6**(4): p. 295-300.
6. Rubinsky, B., G. Onik, and P. Mikus, *Irreversible Electroporation: A New Ablation Modality - Clinical Implications.* Technol Cancer Res Treat, 2007. **6**(1): p. 37-48.
7. Davalos, R.V., D.M. Otten, L.M. Mir, and B. Rubinsky, *Electrical impedance tomography for imaging tissue electroporation.* Biomedical Engineering, IEEE Transactions on, 2004. **51**(5): p. 761-767.
8. Garcia, P., J. Rossmeisl, R. Neal, T. Ellis, J. Olson, N. Henao-Guerrero, J. Robertson, and R. Davalos, *Intracranial Nonthermal Irreversible Electroporation: In Vivo Analysis.* J Membr Biol, 2010. **236**(1): p. 127-136.
9. Daniels, C. and B. Rubinsky, *Electrical Field and Temperature Model of Nonthermal Irreversible Electroporation in Heterogeneous Tissues.* J Biomech Eng, 2009. **131**(7): p. 071006.
10. Mir, L.M. and S. Orlowski, *Mechanisms of electrochemotherapy.* Adv Drug Deliv Rev, 1999. **35**: p. 107-118.
11. Davalos, R.V., L.M. Mir, and B. Rubinsky, *Tissue Ablation with Irreversible Electroporation.* Ann Biomed Eng, 2005. **33**(2): p. 223-231.
12. Edd, J.F. and R.V. Davalos, *Mathematical Modeling of Irreversible Electroporation for Treatment Planning.* Technol Cancer Res Treat, 2007. **6**(4): p. 275-286.
13. Ellis, T.L., P.A. Garcia, J.H. Rossmeisl, N. Henao-Guerrero, J. Robertson, and R.V. Davalos, *Nonthermal irreversible electroporation for intracranial surgical applications.* J Neurosurg. **0**(0): p. 1-8.
14. Maor, E., A. Ivorra, J. Leor, and B. Rubinsky, *The Effect of Irreversible Electroporation on Blood Vessels.* Technol Cancer Res Treat, 2007. **6**(4): p. 307-312.
15. Al-Sakere, B., C. Bernat, F. Andre, E. Connault, P. Opolon, R.V. Davalos, and L.M. Mir, *A Study of the Immunological Response to Tumor Ablation with Irreversible Electroporation.* Technol Cancer ResTreat, 2007. **6**(4): p. 301-305.

16. Lee, E.W., C.T. Loh, and S.T. Kee, *Imaging Guided Percutaneous Irreversible Electroporation: Ultrasound and Immunohistological Correlation.* Tech Cancer Res Treat, 2007. **6**(4): p. 287-293.
17. Miklavcic, D., D. Semrov, H. Mekid, and L.M. Mir, *A validated model of in vivo electric field distribution in tissues for electrochemotherapy and for DNA electrotransfer for gene therapy.* Biochimica et Biophysica Acta, 2000. **1523**: p. 73-83.
18. Al-Sakere, B., F. Andre, C. Bernat, E. Connault, P. Opolon, R.V. Davalos, B. Rubinsky, and L.M. Mir, *Tumor Ablation with Irreversible Electroporation.* PLoS One, 2007. **2**(11): p. e1135.
19. Neal, R.E., 2nd, R. Singh, H.C. Hatcher, N.D. Kock, S.V. Torti, and R.V. Davalos, *Treatment of breast cancer through the application of irreversible electroporation using a novel minimally invasive single needle electrode.* Breast Cancer Res Treat, 2010. **123**(1): p. 295-301.
20. Guo Y., Zhang Y., Klein R., Nijm G. M., Sahakian A. V., Omary R. A., Yang G. Y., and L.A. C., *Irreversible electroporation therapy in the liver: longitudinal efficacy studies in a rat model of hepatocellular carcinoma.* Cancer Res, 2010. **70**: p. 1555-63.
21. Garcia, P.A., T. Pancotto, J.H. Rossmeisl, Jr., N. Henao-Guerrero, N.R. Gustafson, G.B. Daniel, J.L. Robertson, T.L. Ellis, and R.V. Davalos, *Non-thermal irreversible electroporation (N-TIRE) and adjuvant fractionated radiotherapeutic multimodal therapy for intracranial malignant glioma in a canine patient.* Technol Cancer Res Treat., 2011. **10**(1): p. 73-83.
22. Neal, R.E., 2nd, J.H. Rossmeisl, Jr., P.A. Garcia, O.I. Lanz, N. Henao-Guerrero, and R.V. Davalos, *Successful Treatment of a Large Soft Tissue Sarcoma With Irreversible Electroporation.* J Clin Oncol, 2011. **14**: p. 14.
23. Thomson, K.R., W. Cheung, S.J. Ellis, D. Park, H. Kavnoudias, D. Loader-Oliver, S. Roberts, P. Evans, C. Ball, and A. Haydon, *Investigation of the Safety of Irreversible Electroporation in Humans.* Journal of vascular and interventional radiology : JVIR, 2011.
24. Ball, C., K.R. Thomson, and H. Kavnoudias, *Irreversible Electroporation: A New Challenge in "Out of Operating Theater" Anesthesia.* Anesth Analg, 2010. **110**(5): p. 1305-1309.
25. Pohl, H.A., *The motion and precipitation of suspensoids in divergent electric fields.* Journal of Applied Physics, 1951. **22**: p. 869-71.
26. Martini, F.H., *An Introduction to Anatomy and Physiology*, in *Fundamentals of Anatomy and Physiology*, S.L. Snavely, Editor. 2004, Pearson Benjamin Cummings: New York. p. 3-29.
27. Martini, F.H., *The Cellular Level of Organization*, in *Fundamentals of Anatomy and Physiology,* S.L. Snavely, Editor. 2004, Pearson Benjamin Cummings: New York. p. 66-109.
28. Saladin, K.S., *Cytology - The Study of Cells*, in *Human Anatomy*. 2008, Mcgraw-Hill: New York. p. 45-73.

29. Teresa Audersirk, Gerald Audersirk, and B.E. Byers, *Cell Membrane Structure and Function*, in *Biology: Life on Earth*. 2005, Pearson Prentice Hall: Upper Saddle River, New Jersey. p. 56-73.
30. Arthur C. Guyton and J.E. Hall, *The Body Fluid Compartments: Extracellular and Intracellular Fluids; Interstitial Fluid and Edema*, in *Textbook of Medical Physiology*, Saunders, Editor. 2006, Elselvier: Philadelphia, Pennsylvania.
31. Abidor, I.G., V.B. Arakelyan, L.V. Chernomordik, Y.A. Chizmadzhev, V.F. Pastushenko, and M.R. Tarasevich, *ELECTRIC BREAKDOWN OF BILAYER LIPID-MEMBRANES .1. MAIN EXPERIMENTAL FACTS AND THEIR QUALITATIVE DISCUSSION*. Bioelectrochemistry and Bioenergetics, 1979. **6**(1): p. 37-52.
32. Weaver, J.C., *MOLECULAR-BASIS FOR CELL-MEMBRANE ELECTROPORATION*, in *Electrical Injury: A Multidisciplinary Approach to Therapy, Prevention, and Rehabilitation*, R.C. Lee, M. CapelliSchellpfeffer, and K.M. Kelley, Editors. 1994, New York Acad Sciences: New York. p. 141-152.
33. Israelachvili, J.N., *Intermolecular and surface forces / Jacob N. Israelachvili*. 1991, London ; San Diego :: Academic Press.
34. Freeman, S.A., M.A. Wang, and J.C. Weaver, *Theory of electroporation of planar bilayer membranes: predictions of the aqueous area, change in capacitance, and pore-pore separation.* Biophysical Journal, 1994. **67**(1): p. 42-56.
35. Weaver, J.C. and Y.A. Chizmadzhev, *Theory of electroporation: A review.* Bioelectrochem Bioenerg, 1996. **41**: p. 135-160.
36. Abidor, I.G., V.B. Arakelyan, L.V. Chernomordik, Y.A. Chizmadzhev, V.F. Pastushenko, and M.P. Tarasevich, *Electric breakdown of bilayer lipid membranes: I. The main experimental facts and their qualitative discussion.* Journal of Electroanalytical Chemistry and Interfacial Electrochemistry, 1979. **104**(0): p. 37-52.
37. Weaver, J.C. and R.A. Mintzer, *Decreased bilayer stability due to transmembrane potentials.* Physics Letters A, 1981. **86**(1): p. 57-59.
38. DeBruin, K.A. and W. Krassowska, *Modeling electroporation in a single cell. I. Effects Of field strength and rest potential.* Biophys J., 1999. **77**(3): p. 1213-24.
39. Smith, K.C., J.C. Neu, and W. Krassowska, *Model of Creation and Evolution of Stable Electropores for DNA Delivery.* Biophysical Journal, 2004. **86**(5): p. 2813-2826.
40. Sandre, O., L. Moreaux, and F. Brochard-Wyart, *Dynamics of transient pores in stretched vesicles.* Proc Natl Acad Sci U S A., 1999. **96**(19): p. 10591-6.
41. McNeil, P.L. and R.A. Steinhardt, *Loss, restoration, and maintenance of plasma membrane integrity.* J Cell Biol., 1997. **137**(1): p. 1-4.
42. Weaver, J.C., *Electroporation of Biological Membranes from Multicellular to Nano Scales.* IEEE, 2003: p. 754-768.
43. Krassowska, W., G.S. Nanda, M.B. Austin, and S.B. Dev, *Viability of Cancer Cells Exposed to Pulsed Electric Fields: The Role of Pulse Charge.* Annals of Biomedical Engineering, 2003. **31**: p. 80-90.
44. Mir, L.M., *Therapeutic perspectives of in vivo cell electropermeabilization.* Bioelectrochemistry, 2000. **53**: p. 1-10.

45. Ivorra, A., *Tissue Electroporation as a Bioelectric Phenomenon: Basic Concepts*, in *Irreversible Electroporation*, B. Rubinsky, Editor. 2010, Springer Berlin Heidelberg. p. 23-61.
46. Miklavčič, D., N. Pavselj, and F.X. Hart, *Electric Properties of Tissues*, in *Wiley Encyclopedia of Biomedical Engineering*. 2006, John Wiley & Sons: New York.
47. Reilly, J.P., *Applied bioelectricity: from electrical stimulations to electropathology*. 1998: Springer.
48. Pethig, R., *Dielectric and electronic properties of biological materials / Ronald Pethig*. 1979, Chichester, [Eng.] ; New York :: Wiley.
49. Zimmermann, U., G. Pilwat, and F. Riemann, *Dielectric breakdown of cell membranes.* Biophys J., 1974. **14**(11): p. 881-99.
50. Fricke, H., *A Mathematical Treatment of the Electric Conductivity and Capacity of Disperse Systems I. The Electric Conductivity of a Suspension of Homogeneous Spheroids.* Physical Review, 1924. **24**(5): p. 575.
51. Goldberg, S.N., G.S. Gazelle, and P.R. Mueller, *Thermal ablation therapy for focal malignancy: a unified approach to underlying principles, techniques, and diagnostic imaging guidance.* AJR Am J Roentgenol., 2000. **174**(2): p. 323-31.
52. Goldberg, S.N., G.S. Gazelle, E.F. Halpern, W.J. Rittman, P.R. Mueller, and D.I. Rosenthal, *Radiofrequency tissue ablation: importance of local temperature along the electrode tip exposure in determining lesion shape and size.* Acad Radiol., 1996. **3**(3): p. 212-8.
53. Thomsen, S., *Pathologic analysis of photothermal and photomechanical effects of laser-tissue interactions.* Photochem Photobiol., 1991. **53**(6): p. 825-35.
54. Mirza, A.N., B.D. Fornage, N. Sneige, H.M. Kuerer, L.A. Newman, F.C. Ames, and S.E. Singletary, *Radiofrequency ablation of solid tumors.* Cancer J., 2001. **7**(2): p. 95-102.
55. Harrison, T.R. and E. Braunwald, *Harrison's principles of internal medicine*. 1987, New York: McGraw-Hill.
56. Chang, I., *Finite element analysis of hepatic radiofrequency ablation probes using temperature-dependent electrical conductivity.* Biomed Eng Online., 2003. **2**: p. 12.
57. Kontos, M., E. Felekouras, and I.S. Fentiman, *Radiofrequency ablation in the treatment of primary breast cancer: no surgical redundancies yet.* Int J Clin Pract, 2008. **62**(5): p. 816-820.
58. Dowlatshahi, K., D. Francescatti, and K. Bloom, *Laser therapy for small breast cancers.* Am J Surg, 2002. **184**: p. 359-363.
59. Singletary, S., B. Fornage, N. Sneige, and e. al, *Radiofrequency ablation of early-stage invasive breast tumors: an overview.* Cancer J, 2002. **8**: p. 177-180.
60. Janzen, N.K., K.T. Perry, K.-R. Han, B. Kristo, S. Raman, and e. al, *The effects of intentional cryoablation and radio frequency ablation of renal tissue involving the collecting system in a porcine model.* J Urol, 2005. **173**: p. 1368-1374.
61. Rukstalis, D.B. and A.E. Katz, *Handbook of urologic cryoablation*. 2007, Abingdon, UK; Boca Raton: Informa Healthcare ; Distributed in North and South America by Taylor & Francis.

62. Littrup, P.J., B. Jallad, P. Chandiwala-Mody, M. D'Agostini, B.A. Adam, and D. Bouwman, *Cryotherapy for Breast Cancer: A Feasibility Study without Excision.* Journal of Vascular and Interventional Radiology, 2009. **20**(10): p. 1329-1341.
63. Sabel, M.S., C.S. Kaufman, P. Whitworth, H. Change, L.H. Stocks, R. Simmons, and M. Schultz, *Cryoablation of Early-Stage Breast Cancer: Work-in-Progress Report of a Multi-Institutional Trial.* Ann Surg Oncol, 2004. **11**(5): p. 542-549.
64. Kieran, K., T.L. Hall, J.E. Parsons, J.S. Wolf, Jr., J.B. Fowlkes, C.A. Cain, and W.W. Roberts, *Refining histotripsy: defining the parameter space for the creation of nonthermal lesions with high intensity, pulsed focused ultrasound of the in vitro kidney.* J Urol., 2007. **178**(2): p. 672-6. Epub 2007 Jun 15.
65. Lake, A.M., Z. Xu, J.E. Wilkinson, C.A. Cain, and W.W. Roberts, *Renal ablation by histotripsy--does it spare the collecting system?* J Urol., 2008. **179**(3): p. 1150-4.
66. Nollet, J.A., *Recherches sur les causes particulieres des phenomenes electriques*. 1754, Paris: Chez H.L. Guering & L.F. Delatour.
67. Fuller, G.W., *Report on the investigations into the purification of the Ohio river water at Louisville Kentucky*. 1898, New York: D. Van Nostrand Company.
68. Biedermann, W., *Electrophysiology*. Vol. 2. 1898, London: Macmillan.
69. Rockwell, A.D., ed. *The medical and surgical uses of electricity: including the X-ray, Finsen light, vibratory therapeutics, and high-frequency currents*. 1903, E.B. Treat & Company: New York.
70. Frankenhaueuser, B. and L. Widen, *Anode break excitation in desheated frog nerve.* J Physiol, 1956. **131**: p. 243-247.
71. Sale, A.J. and W.A. Hamilton, *Effects of high electric fields on micro-organisms. 1. Killing of bacteria and yeasts.* Biochimica et Biophysica Acta, 1967. **148**: p. 781-788.
72. Hamilton, W.A. and A.J. Sale, *Effects of high electric fields on microorganisms. 2. Mechanism of action of the lethal effect.* Biochimica et Biophysica Acta (BBA), 1967. **163**: p. 37-43.
73. Sale, A.J. and W.A. Hamilton, *Effects of high electric fields on micro-organisms. 3. Lysis of erythrocytes and protoplasts.* Biochim Biophys Acta, 1968. **163**(1): p. 37-43.
74. Doevenspeck, H., *Influencing cells and cell walls by electrostatic impulses.* Fleishwirtshaft, 1961. **13**: p. 986-987.
75. Toepfl, S., A. Mathy, V. Heinz, and D. Knorrr, *Review: Potential of high hydrostatic pressure and pulsed electric field for energy efficient and environmentally friendly food processing.* Food Review International, 2006. **22**: p. 405-423.
76. Vernhes, M.C., A. Benichou, P. Pernin, P.A. Cabanes, and J. Teissie, *Elimination of free-living amoebae in fresh water with pulsed electric fields.* Water Res, 2002. **36**(14): p. 3429-38.
77. Joshi, R.P. and K.H. Schoenbach, *Mechanism for membrane electroporation irreversibility under high-intensity, ultrashort electrical pulse conditions.* Phys Rev E Stat Nonlin Soft Matter Phys, 2002. **66**(5 Pt 1): p. 052901.

78. Rowan, N.J., S.J. MacGregor, J.G. Anderson, R.A. Fouracre, and O. Farish, *Pulsed electric field inactivation of diarrhoeagenic Bacillus cereus through irreversible electroporation.* Lett Appl Microbiol, 2000. **31**(2): p. 110-4.
79. Schoenbach, K.H., F.E. Peterkin, R.W.I. Aldden, and S.J. Beebe, *The effect of pulsed fields on biological cells: Experiments and applications.* IEEE Trans Biomed Eng, 1997. **25**: p. 284-292.
80. Lee, R.C., *Cell Injury by Electric Forces.* Annals of the New York Academy of Sciences, 2005. **1066**: p. 85-91.
81. Lee, R.C. and M.S. Kolodney, *Electrical injury mechanisms: Electrical breakdown of cell membranes.* Plast Reconstr Surg, 1987. **80**(5): p. 672-9.
82. Jones, J.L., C.C. Proskauer, W.K. Paull, E. Lepeschkin, and R.E. Jones, *Ultrastructural injury to chick myocardial cells in vitro following "electric countershock".* Circ Res, 1980. **46**(3): p. 387-94.
83. Belov, S.V., *Effects of high-frequency current parameters on tissue coagulation.* Biomedical Engineering, 1978. **12**: p. 209-211.
84. Mir, L.M., S. Orlowski, J. Belehradek, Jr., and C. Paoletti, *Electrochemotherapy potentiation of antitumour effect of bleomycin by local electric pulses.* Eur J Cancer, 1991. **27**(1): p. 68-72.
85. Mir, L.M., *Therapeutic perspectives of in vivo cell electropermeabilization.* Bioelectrochemistry, 2001. **53**(1): p. 1-10.
86. Mir, L.M., L.F. Glass, G. Sersa, J. Teissie, C. Domenge, D. Miklavcic, M.J. Jaroszeski, S. Orlowski, D.S. Reintgen, Z. Rudolf, M. Belehradek, R. Gilbert, M.P. Rols, J. Belehradek, Jr., J.M. Bachaud, R. DeConti, B. Stabuc, M. Cemazar, P. Coninx, and R. Heller, *Effective treatment of cutaneous and subcutaneous malignant tumours by electrochemotherapy.* Br J Cancer, 1998. **77**(12): p. 2336-42.
87. Mir, L.M., J. Gehl, G. Sersa, C.G. Collins, J.R. Garbay, V. Billard, P. Geertsen, Z. Rudolf, G.C. O'Sullivan, and M. Marty, *Standard Operating Procedures of the Electrochemotherapy.* Eur J Cancer Supplements 2006. **4**(11): p. 14-25.
88. Marty, M., G. Sersa, J.R. Garbay, J. Gehl, C.G. Collins, M. Snoj, V. Billard, P.F. Geertsen, J.O. Larkin, D. Miklavcic, I. Pavlovic, S.M. Paulin-Kosir, M. Cemazar, N. Morsli, D.M. Soden, Z. Rudolf, C. Robert, G.C. O'Sullivan, and L.M. Mir, *Electrochemotherapy - an easy, highly effective and safe treatment of cutaneous and subcutaneous metastases: results of the ESOPE (European Standard Operating Procedures of Electrochemotherapy) study.* Eur J Cancer Supplements, 2006. **4**(11): p. 3-13.
89. Al-Sakere, B., F. André, C. Bernat, E. Connault, P. Opolon, R.V. Davalos, B. Rubinsky, and L.M. Mir, *Tumor Ablation with Irreversible Electroporation.* PLoS ONE, 2007. **2**(11): p. e1135:1-8.
90. Deng, J., K.H. Schoenbach, E.S. Buescher, P.S. Hair, P.M. Fox, and S.J. Beebe, *The effects of intense submicrosecond electrical pulses on cells.* Biophys J, 2003. **84**(4): p. 2709-14.
91. Beebe, S.J., J. White, P.F. Blackmore, Y. Deng, K. Somers, and K.H. Schoenbach, *Diverse effects of nanosecond pulsed electric fields on cells and tissues.* DNA Cell Biol, 2003. **22**(12): p. 785-96.

92. Gowrishankar, T.R. and J.C. Weaver, *Electrical behavior and pore accumulation in a multicellular model for conventional and supra-electroporation.* Biochem Biophys Res Commun, 2006. **349**(2): p. 643-53.
93. Belehradek, M., C. Domenge, B. Luboinski, S. Orlowski, J. Belehradek, Jr., and L.M. Mir, *Electrochemotherapy, a new antitumor treatment. First clinical phase I-II trial.* Cancer, 1993. **72**(12): p. 3694-700.
94. Gothelf, A., L.M. Mir, and J. Gehl, *Electrochemotherapy: results of cancer treatment using enhanced delivery of bleomycin by electroporation.* Cancer Treat Rev, 2003. **29**(5): p. 371-87.
95. Sersa, G., M. Cemazar, and Z. Rudolf, *Electrochemotherapy: advantages and drawbacks in treatment of cancer patients.* Cancer Therapy, 2003. **1**: p. 133-42.
96. Nuccitelli, R., U. Pliquett, X. Chen, W. Ford, R. James Swanson, S.J. Beebe, J.F. Kolb, and K.H. Schoenbach, *Nanosecond pulsed electric fields cause melanomas to self-destruct.* Biochem Biophys Res Commun, 2006. **343**(2): p. 351-60.
97. Gehl, J., *Electroporation: theory and methods, perspectives for drug delivery, gene therapy and research.* Acta Physiologica Scandinavica, 2003. **177**(4): p. 437-447.
98. Mir, L.M., P.H. Moller, F. Andre, and J. Gehl, *Electric Pulse-Mediated Gene Delivery to Various Animal Tissues*, in *Non-Viral Vectors for Gene Therapy, Second Edition: Part 2*. 2005, Elsevier Academic Press Inc: San Diego. p. 83-114.
99. Neumann, E., M. Schaefer-Ridder, Y. Wang, and P.H. Hofschneider, *Gene transfer into mouse lyoma cells by electroporation in high electric fields.* EMBO J, 1982. **1**(7): p. 841-5.
100. Wong, T.-K. and E. Neumann, *Electric field mediated gene transfer.* Biochemical and Biophysical Research Communications, 1982. **107**(2): p. 584-587.
101. Potter, H., *Electroporation in biology: methods, applications, and instrumentation.* Anal Biochem, 1988. **174**(2): p. 361-73.
102. Li, S.L., *Electroporation gene therapy: New developments in vivo and in vitro.* Current Gene Therapy, 2004. **4**(3): p. 309-316.
103. Li, S., *Electroporation gene therapy: new developments in vivo and in vitro.* Curr Gene Ther., 2004. **4**(3): p. 309-16.
104. Simon, A.J., D.R. Casimiro, A.C. Finnefrock, M.E. Davies, A. Tang, M. Chen, M. Chastain, G.S. Kath, L. Chen, and J.W. Shiver, *Enhanced in vivo transgene expression and immunogenicity from plasmid vectors following electrostimulation in rodents and primates.* Vaccine., 2008. **26**(40): p. 5202-9. Epub 2008 Apr 14.
105. Rice, J., C.H. Ottensmeier, and F.K. Stevenson, *DNA vaccines: precision tools for activating effective immunity against cancer.* Nat Rev Cancer., 2008. **8**(2): p. 108-20.
106. Martinenghi, S., G.C. De Angelis, S. Biressi, S. Amadio, F. Bifari, M.G. Roncarolo, C. Bordignon, and L. Falqui, *Human insulin production and amelioration of diabetes in mice by electrotransfer-enhanced plasmid DNA gene transfer to the skeletal muscle.* Gene Therapy, 2002. **9**(21): p. 1429-1437.
107. Yamamoto, M., Y. Kobayashi, M. Li, H. Niwa, N. Mitsuma, Y. Ito, T. Muramatsu, and G. Sobue, *In vivo gene electroporation of glial cell line-derived*

neurotrophic factor (GDNF) into skeletal muscle of SOD1 mutant mice. Neurochemical Research, 2001. **26**(11): p. 1201-1207.
108. Lesbordes, J.C., T. Bordet, G. Haase, L. Castelnau-Ptakhine, S. Rouhani, H. Gilgenkrantz, and A. Kahn, *In vivo electrotransfer of the cardiotrophin-1 gene into skeletal muscle slows down progression of motor neuron degeneration in pmn mice.* Human Molecular Genetics, 2002. **11**(14): p. 1615-1625.
109. Golzio, M., L. Mazzolini, A. Ledoux, A. Paganin, M. Izard, L. Hellaudais, A. Bieth, M.J. Pillaire, C. Cazaux, J.S. Hoffmann, B. Couderc, and J. Teissie, *In vivo gene silencing in solid tumors by targeted electrically mediated siRNA delivery.* Gene Therapy, 2007. **14**(9): p. 752-759.
110. Cemazar, M., T. Jarm, and G. Sersa, *Cancer Electrogene Therapy with Interleukin-12.* Current Gene Therapy, 2010. **10**(4): p. 300-311.
111. Hanna, E., X.J. Zhang, J. Woodlis, R. Breau, J. Suen, and S.L. Li, *Intramuscular electroporation delivery of IL-12 gene for treatment of squamous cell carcinoma located at distant site.* Cancer Gene Therapy, 2001. **8**(3): p. 151-157.
112. Li, S., X. Xia, X. Zhang, and J. Suen, *Regression of tumors by IFN-alpha electroporation gene therapy and analysis of the responsible genes by cDNA array.* Gene Therapy, 2002. **9**(6): p. 390-397.
113. Yamashita, Y., M. Shimada, H. Hasegawa, R. Minagawa, T. Rikimaru, T. Hamatsu, S. Tanaka, K. Shirabe, J. Miyazaki, and K. Sugimachi, *Electroporation-mediated interleukin-12 gene therapy for hepatocellular carcinoma in the mice model.* Cancer Research, 2001. **61**(3): p. 1005-1012.
114. Tamura, T., T. Nishi, T. Goto, H. Takeshima, S.B. Dev, Y. Ushio, and T. Sakata, *Intratumoral delivery of interleukin 12 expression plasmids with in vivo electroporation is effective for colon and renal cancer.* Human Gene Therapy, 2001. **12**(10): p. 1265-1276.
115. Shibata, M.A., Y. Ito, J. Morimoto, K. Kusakabe, R. Yoshinaka, and Y. Otsuki, *In vivo electrogene transfer of interleukin-12 inhibits tumor growth and lymph node and lung metastases in mouse mammary carcinomas.* Journal of Gene Medicine, 2006. **8**(3): p. 335-52.
116. Pavlin, D., M. Cemazar, A. Cor, G. Sersa, A. Pogacnik, and N. Tozon, *Electrogene therapy with interleukin-12 in canine mast cell tumors.* Radiology and Oncology, 2011. **45**(1): p. 31-39.
117. Tamzali, Y., B. Couderc, M.P. Rols, M. Golzio, and J. Teissie, *Equine Cutaneous Tumors Treatment by Electro-chemo-immuno-geno-therapy*, in *11th Mediterranean Conference on Medical and Biomedical Engineering and Computing 2007*, T. Jarm, P. Kramar, and A. Zupanic, Editors. 2007, Springer Berlin Heidelberg. p. 630-630.
118. Daud, A.I., R.C. DeConti, S. Andrews, P. Urbas, A.I. Riker, V.K. Sondak, P.N. Munster, D.M. Sullivan, K.E. Ugen, J.L. Messina, and R. Heller, *Phase I Trial of Interleukin-12 Plasmid Electroporation in Patients With Metastatic Melanoma.* Journal of Clinical Oncology, 2008. **26**(36): p. 5896-5903.
119. Mir, L.M., *Therapeutic perspectives of in vivo cell electropermeabilization.* Bioelectrochemistry, 2001. **53**: p. 1-10.

120. Neumann, E., M. Schaeferridder, Y. Wang, and P.H. Hofschneider, *Gene-Transfer into Mouse Lyoma Cells by Electroporation in High Electric-Fields.* Embo Journal, 1982. **1**(7): p. 841-845.
121. Orlowski, S., J. Belehradek, C. Paoletti, and L.M. Mir, *Transient Electropermeabilization of Cells in Culture - Increase of the Cyto-Toxicity of Anticancer Drugs.* Biochemical Pharmacology, 1988. **37**(24): p. 4727-4733.
122. Todorovic, V., G. Sersa, K. Flisar, and M. Cemazar, *Enhanced cytotoxicity of bleomycin and cisplatin after electroporation in murine colorectal carcinoma cells.* Radiology and Oncology, 2009. **43**(4): p. 264-273.
123. Gehl, J., T. Skovsgaard, and L.M. Mir, *Enhancement of cytotoxicity by electropermeabilization: an improved method for screening drugs.* Anticancer Drugs., 1998. **9**(4): p. 319-25.
124. Orlowski, S., J. Belehradek Jr, C. Paoletti, and L.M. Mir, *Transient electropermeabilization of cells in culture: Increase of the cytotoxicity of anticancer drugs.* Biochemical Pharmacology, 1988. **37**(24): p. 4727-4733.
125. Jaroszeski, M.J., V. Dang, C. Pottinger, J. Hickey, R. Gilbert, and R. Heller, *Toxicity of anticancer agents mediated by electroporation in vitro.* Anticancer Drugs, 2000. **11**(3): p. 201-8.
126. Mir, L.M., H. Banoun, and C. Paoletti, *Introduction of definite amounts of nonpermeant molecules into living cells after electropermeabilization: direct access to the cytosol.* Exp Cell Res, 1988. **175**(1): p. 15-25.
127. Poddevin, B., S. Orlowski, J. Belehradek, and L.M. Mir, *Very high cytotoxicity of bleomycin introduced into the cytosol of cells in culture.* Biochemical Pharmacology, 1991. **42**(Supplement 1): p. S67-S75.
128. Pron, G., N. Mahrour, S. Orlowski, O. Tounekti, B. Poddevin, J. Belehradek, Jr., and L.M. Mir, *Internalisation of the bleomycin molecules responsible for bleomycin toxicity: a receptor-mediated endocytosis mechanism.* Biochem Pharmacol, 1999. **57**(1): p. 45-56.
129. Mir, L.M., S. Orlowski, J.J. Belehradek, J. Teissie, and M.P. Rols, *Biomedical applications of electric pulses with special emphasis on antitumor electrochemotherapy.* Bioelectrochemistry and Bioenergetics, 1995. **38**: p. 203-207.
130. Weaver, J.C., T.E. Vaughan, and Y. Chizmadzhev, *Theory of electrical creation of aqueous pathways across skin transport barriers.* Advanced Drug Delivery Reviews, 1999. **35**(1): p. 21-39.
131. Cemazar, M., Y. Tamzali, G. Sersa, N. Tozon, L.M. Mir, D. Miklavcic, R. Lowe, and J. Teissie, *Electrochemotherapy in veterinary oncology.* Journal of Veterinary Internal Medicine, 2008. **22**(4): p. 826-831.
132. Sersa, G., D. Miklavcic, M. Cemazar, Z. Rudolf, G. Pucihar, and M. Snoj, *Electrochemotherapy in treatment of tumours.* European Journal of Surgical Oncology (EJSO), 2008. **34**(2): p. 232-240.
133. Mir, L.M., P. Devauchelle, F. Quintin-Colonna, F. Delisle, S. Doliger, D. Fradelizi, J. Belehradek, Jr., and S. Orlowski, *First clinical trial of cat soft-tissue sarcomas treatment by electrochemotherapy.* Br J Cancer., 1997. **76**(12): p. 1617-22.

134. Mir, L.M., M. Belehradek, C. Domenge, S. Orlowski, B. Poddevin, J. Belehradek, Jr., G. Schwaab, B. Luboinski, and C. Paoletti, *Electrochemotherapy, a new antitumor treatment: first clinical trial.* C R Acad Sci III, 1991. **313**(13): p. 613-8.
135. Belehradek, M., C. Domenge, B. Luboinski, S. Orlowski, J. Belehradek, Jr., and L.M. Mir, *Electrochemotherapy, a new antitumor treatment. First clinical phase I-II trial.* Cancer., 1993. **72**(12): p. 3694-700.
136. Domenge, C., S. Orlowski, B. Luboinski, T. De Baere, G. Schwaab, J. Belehradek, Jr., and L.M. Mir, *Antitumor electrochemotherapy: new advances in the clinical protocol.* Cancer., 1996. **77**(5): p. 956-63.
137. Mir, L.M., L.F. Glass, G. Sersa, J. Teissie, C. Domenge, D. Miklavcic, M.J. Jaroszeski, S. Orlowski, D.S. Reintgen, Z. Rudolf, M. Belehradek, R. Gilbert, M.P. Rols, J. Belehradek, J.M. Bachaud, R. DeConti, B. Stabuc, M. Cemazar, P. Coninx, and R. Heller, *Effective treatment of cutaneous and subcutaneous malignant tumours by electrochemotherapy.* British Journal of Cancer, 1998. **77**(12): p. 2336-2342.
138. Heller, R., M.J. Jaroszeski, D.S. Reintgen, C.A. Puleo, R.C. DeConti, R.A. Gilbert, and L.F. Glass, *Treatment of cutaneous and subcutaneous tumors with electrochemotherapy using intralesional bleomycin.* Cancer., 1998. **83**(1): p. 148-57.
139. Panje, W.R., M.P. Hier, G.R. Garman, E. Harrell, A. Goldman, and I. Bloch, *Electroporation therapy of head and neck cancer.* Ann Otol Rhinol Laryngol., 1998. **107**(9 Pt 1): p. 779-85.
140. Kubota, Y., L.M. Mir, T. Nakada, I. Sasagawa, H. Suzuki, and N. Aoyama, *Successful treatment of metastatic skin lesions with electrochemotherapy.* J Urol., 1998. **160**(4): p. 1426.
141. Sersa, G., B. Stabuc, M. Cemazar, B. Jancar, D. Miklavcic, and Z. Rudolf, *Electrochemotherapy with cisplatin: potentiation of local cisplatin antitumour effectiveness by application of electric pulses in cancer patients.* Eur J Cancer., 1998. **34**(8): p. 1213-8.
142. Marty, M., G. Sersa, J.R. Garbay, J. Gehl, C.G. Collins, M. Snoj, V. Billard, P.F. Geertsen, J.O. Larkin, D. Miklavcic, I. Pavlovic, S.M. Paulin-Kosir, M. Cemazar, N. Morsli, D.M. Soden, Z. Rudolf, C. Robert, G.C. O'Sullivan, and L.M. Mir, *Electrochemotherapy - An easy, highly effective and safe treatment of cutaneous and subcutaneous metastases: Results of ESOPE (European Standard Operating Procedures of Electrochemotherapy) study.* European Journal of Cancer Supplements, 2006. **4**(11): p. 3-13.
143. Esser, A.T., K.C. Smith, T.R. Gowrishankar, and J.C. Weaver, *Towards Solid Tumor Treatment by Nanosecond Pulsed Electric Fields.* Technology in Cancer Research & Treatment, 2009. **8**(4): p. 289-306.
144. Weaver, J.C., *Electroporation - a General Phenomenon for Manipulating Cells and Tissues.* Journal of Cellular Biochemistry, 1993. **51**(4): p. 426-435.
145. Kolb, J.F., S. Kono, and K.H. Schoenbach, *Nanosecond pulsed electric field generators for the study of subcellular effects.* Bioelectromagnetics, 2006. **27**(3): p. 172-187.

146. Long, G., P. Shires, D. Plescia, S. Beebe, J. Kolb, and S. Karl, *Targeted tissue ablation with nanosecond pulses.* IEEE Trans Biomed Eng, 2011.
147. Esser, A.T., K.C. Smith, T.R. Gowrishankar, and J.C. Weaver, *Towards solid tumor treatment by irreversible electroporation: intrinsic redistribution of fields and currents in tissue.* Technol Cancer Res Treat, 2007. **6**(4): p. 261-74.
148. Garon, E.B., D. Sawcer, P.T. Vernier, T. Tang, Y.H. Sun, L. Marcu, M.A. Gundersen, and H.P. Koeffler, *In vitro and in vivo evaluation and a case report of intense nanosecond pulsed electric field as a local therapy for human malignancies.* International Journal of Cancer, 2007. **121**(3): p. 675-682.
149. Beebe, S.J., W.E. Ford, W. Ren, X. Chen, and K.H. Schoenbach, *Non-ionizing radiation with nanosecond pulsed electric fields as a cancer treatment: in vitro studies.* Conf Proc IEEE Eng Med Biol Soc., 2009. **2009**: p. 6509-12.
150. Ren, W. and S.J. Beebe, *An apoptosis targeted stimulus with nanosecond pulsed electric fields (nsPEFs) in E4 squamous cell carcinoma.* Apoptosis., 2011. **16**(4): p. 382-93.
151. Nuccitelli, R., X. Chen, A.G. Pakhomov, W.H. Baldwin, S. Sheikh, J.L. Pomicter, W. Ren, C. Osgood, R.J. Swanson, J.F. Kolb, S.J. Beebe, and K.H. Schoenbach, *A new pulsed electric field therapy for melanoma disrupts the tumor's blood supply and causes complete remission without recurrence.* International Journal of Cancer, 2009. **125**(2): p. 438-445.
152. Schoenbach, K.H., B. Hargrave, R.P. Joshi, J.F. Kolb, R. Nuccitelli, C. Osgood, A. Pakhomov, M. Stacey, R.J. Swanson, J.A. White, S. Xiao, J. Zhang, S.J. Beebe, P.F. Blackmore, and E.S. Buescher, *Bioelectric effects of intense nanosecond pulses.* Ieee Transactions on Dielectrics and Electrical Insulation, 2007. **14**(5): p. 1088-1109.
153. Nuccitelli, R., K. Tran, S. Sheikh, B. Athos, M. Kreis, and P. Nuccitelli, *Optimized nanosecond pulsed electric field therapy can cause murine malignant melanomas to self-destruct with a single treatment.* International Journal of Cancer, 2010. **127**(7): p. 1727-1736.
154. Miller, L., J. Leor, and B. Rubinsky, *Cancer cells ablation with irreversible electroporation.* Technol Cancer Res Treat., 2005. **4**(6): p. 699-705.
155. Rubinsky, J., G. Onik, P. Mikus, and B. Rubinsky, *Optimal parameters for the destruction of prostate cancer using irreversible electroporation.* J Urol., 2008. **180**(6): p. 2668-74. Epub 2008 Oct 31.
156. Neal, R.E., 2nd and R.V. Davalos, *The Feasibility of Irreversible Electroporation for the Treatment of Breast Cancer and Other Heterogeneous Systems.* Ann Biomed Eng, 2009. **37**(12): p. 2615-2625.
157. Davalos, R.V., L.M. Mir, and B. Rubinsky, *Tissue ablation with irreversible electroporation.* Ann Biomed Eng, 2005. **33**(2): p. 223-31.
158. Edd, J.F., L. Horowitz, R.V. Davalos, L.M. Mir, and B. Rubinsky, *In vivo results of a new focal tissue ablation technique: irreversible electroporation.* IEEE Trans Biomed Eng, 2006. **53**(7): p. 1409-15.
159. Maor, E., A. Ivorra, J. Leor, and B. Rubinsky, *The effect of irreversible electroporation on blood vessels.* Technol Cancer Res Treat, 2007. **6**(4): p. 307-12.

160. Maor, E., A. Ivorra, J. Leor, and B. Rubinsky, *Irreversible electroporation attenuates neointimal formation after angioplasty.* Ieee Transactions on Biomedical Engineering, 2008. **55**(9): p. 2268-2274.
161. Maor, E., A. Ivorra, and B. Rubinsky, *Non Thermal Irreversible Electroporation: Novel Technology for Vascular Smooth Muscle Cells Ablation.* Plos One, 2009. **4**(3): p. -.
162. Al-Sakere, B., F. Andre, C. Bernat, E. Connault, P. Opolon, R.V. Davalos, B. Rubinsky, and L.M. Mir, *Tumor Ablation with Irreversible Electroporation.* Plos One, 2007. **2**(11): p. -.
163. Guo, Y., Y. Zhang, R. Klein, G.M. Nijm, A.V. Sahakian, R.A. Omary, G.Y. Yang, and A.C. Larson, *Irreversible Electroporation Therapy in the Liver: Longitudinal Efficacy Studies in a Rat Model of Hepatocellular Carcinoma.* Cancer Research, 2010. **70**(4): p. 1555-1563.
164. Neal, R.E., R. Singh, H.C. Hatcher, N.D. Kock, S.V. Torti, and R.V. Davalos, *Treatment of breast cancer through the application of irreversible electroporation using a novel minimally invasive single needle electrode.* Breast Cancer Research and Treatment, 2010. **123**(1): p. 295-301.
165. Neal, R.E., 2nd, J.H. Rossmeisl, Jr., P.A. Garcia, O.I. Lanz, N. Henao-Guerrero, and R.V. Davalos, *Successful Treatment of a Large Soft Tissue Sarcoma With Irreversible Electroporation.* J Clin Oncol, 2011.
166. Garcia, P.A., T. Pancotto, J.H. Rossmeisl, N. Henao-Guerrero, N.R. Gustafson, G.B. Daniel, J.L. Robertson, T.L. Ellis, and R.V. Davalos, *Non-Thermal Irreversible Electroporation (N-TIRE) and Adjuvant Fractionated Radiotherapeutic Multimodal Therapy for Intracranial Malignant Glioma in a Canine Patient.* Technology in Cancer Research & Treatment, 2011. **10**(1): p. 73-83.
167. Ellis, T.L., P.A. Garcia, J.H. Rossmeisl, N. Henao-Guerrero, J. Robertson, and R.V. Davalos, *Nonthermal irreversible electroporation for intracranial surgical applications.* J Neurosurg, 2010.
168. Garcia, P.A., J.H. Rossmeisl, R.E. Neal, T.L. Ellis, J.D. Olson, N. Henao-Guerrero, J. Robertson, and R.V. Davalos, *Intracranial Nonthermal Irreversible Electroporation: In Vivo Analysis.* Journal of Membrane Biology, 2010. **236**(1): p. 127-136.
169. Thomson, K.R., W. Cheung, S.J. Ellis, D. Park, H. Kavnoudias, D. Loader-Oliver, S. Roberts, P. Evans, C. Ball, and A. Haydon, *Investigation of the Safety of Irreversible Electroporation in Humans.* J Vasc Interv Radiol, 2011.
170. Ball, C., K.R. Thomson, and H. Kavnoudias, *Irreversible electroporation: a new challenge in "out of operating theater" anesthesia.* Anesthesia and Analgesia, 2010. **110**(5): p. 1305-9.
171. Gomez-Iturriaga, A., L. Pina, M. Cambeiro, and R. Martinez-Monge, *Early breast cancer treated with conservative surgery, adjuvant chemotherapy, and delayed accelerated partial breast irradiation with high-dose-rate brachytherapy.* Brachytherapy, 2008. **7**: p. 310-315.
172. Fisher, B., C. Redmond, R. Poisson, and e. al, *Eight-year results of a randomized clinical trial comparing total mastectomy and lumpectomy with or without*

irradiation in the treatment of breast cancer. N Engl J Med, 1989. **320**: p. 822-828.
173. Fedorcik, G.G., R. Sachs, and M.A. Goldfarb, *Oncologic and Aesthetic Results Following Breast-Conserving Therapy with 0.5 cm Margins in 100 Consecutive Patients.* Breast J, 2006. **12**(3): p. 208-211.
174. Fitzal, F., M. Mittleboeck, H. Trischler, and W. Krois, *Breast-Conserving Therapy for Centrally Located Breast Cancer.* Ann Surg, 2008. **247**(3): p. 470-476.
175. Clough, K.B., *Oncoplastic surgery allows extensive resections for conservative treatment of breast cancer.* Eur J Cancer, 2006. **4**: p. S119.
176. Franquet, T., C.D. Miguel, R. Cozcolluela, and L. Donoso, *Spiculated lesions of the breast: mammographic-pathologic correlation.* Radiographics, 1993. **13**: p. 841-852.
177. Sickles, E.A. and K.A. Herzog, *Intramammary scar tissue: a mimic of the mammographic appearance of carcinoma.* Am. J. Roentgenol., 1980. **135**(2): p. 349-352.
178. Preda, L., G. Villa, S. Rizzo, and L. Bazzi, *Magnetic resonance mammography in the evaluation of recurrence at the prior lumpectomy site after conservative surgery and radiotherapy.* Breast Cancer Res, 2006. **8**(53).
179. Surowiec, A.J., S.S. Stuchly, J.R. Barr, and A. Swarup, *Dielectric Properties of Breast Carcinoma and the Surrounding Tissues.* IEEE Transactions on Biomedical Engineering, 1988. **35**(4): p. 257-263.
180. Jemal, A., R. Tiwari, T. Murray, and e. al, *Cancer statistics 2004.* CA Cancer J Clin, 2004. **54**: p. 8-29.
181. Cady, B., *Breast cancer in the third millennium.* Breast J, 2000. **6**: p. 280-287.
182. Jossinet, J., *Variability of impedivity in normal and pathological breast tissue.* Medical and Biological Engineering and Computing, 1996. **34**(5): p. 346-350.
183. Giering, K., I. Lamprecht, O. Minet, and A. Handke, *Determination of the specific heat capacity of healthy and tumorous human tissue.* Thermochimica Acta, 1995. **251**: p. 199-205.
184. Skinner, M.G., *A theoretical comparison of energy sources - microwave, ultrasound and laser - for interstitial thermal therapy.* Physics in Medicine and Biology, 1998. **43**: p. 3535.
185. Johns, P.C. and M.J. Yaffe, *X-ray characterisation of normal and neoplastic breast tissues.* Phys Med Miol, 1987. **32**: p. 675-695.
186. Bowman, H.F., *Heat transfer and thermal dosimetry.* J Microwave Power, 1981. **16**: p. 121-133.
187. Werner, J. and M. Buse, *Temperature profiles with respect to inhomogeneity and geometry of the human body.* J Appl Physiol, 1988. **65**(30): p. 1110-1118.
188. Gautherie, M., Y. Quenneville, and C.M. Gros, *Metabolic heat production, growth rate, and prognosis of early breast carcinomas.* Biomedicine, 1975. **22**: p. 328-336.
189. Ng, E.Y.K. and N.M. Sudharsan, *An improved three-dimensional direct numerical modeling and thermal analysis of a female breast with tumor.* Proceeding of the Institution of Mechanical Engineers, 2001. **215**(H): p. 25-37.

190. Field, S.B. and C.C. Morris, *The relationship between heating time and temperature: its relevance to clinical hyperthermia.* Radiother. Oncol., 1983. **1**: p. 179-183.
191. Perez, C.A. and S.A. Sapareto, *Thermal Dose Expression in Clinical Hyperthermia and Correlation with Tumor Response/Control.* Cancer Research, 1984. **44**: p. 4818s-4825s.
192. Diller, K.R., *Advances in Heat Transfer*, in *Bioengineering Heat Transfer*, Y.I. Choi, Editor. 1992, Academic Press: Boston. p. 157-357.
193. Axel T. Esser, Kyle C. Smith, Thiravallur R. Gowrishankar, and J.C. Weaver, *Towards Solid Tumor Treatment by Irreversible Electroporation: Intrinsic Redistribution of Fields and Currents in Tissue.* Technology in Cancer Research and Treatment, 2007. **6**(4): p. 261-273.
194. Florian Fitzal, Martina Mittleboeck, Herwig Trischler, and W. Krois, *Breast-Conserving Therapy for Centrally Located Breast Cancer.* Annals of Surgery, 2008. **247**(3): p. 470-476.
195. Duck, F.A., *Physical Properties of Tissue: A Comprehensive Reference Book*. 1990, New York: Academic Press.
196. Hinshaw, J.L. and F.T. Lee Jr, *Cryoablation for Liver Cancer.* Techniques in Vascular and Interventional Radiology, 2007. **10**(1): p. 47-57.
197. Davalos, R.V. and B. Rubinsky, *Temperature considerations during irreversible electroporation.* International Journal of Heat and Mass Transfer, 2008. **51**(23-24): p. 5617-5622.
198. Garcia, P.A., R.E. Neal, and R.V. Davalos, *Non-thermal irreversible electroporation for tissue ablation*, in *Electroporation in Laboratory and Clinical Investigations*, Enrico P. Spugnini and A. Baldi, Editors. 2010, Nova Science: Hauppauge, NY.
199. Kos, B., A. Zupanic, T. Kotnik, M. Snoj, G. Sersa, and D. Miklavcic, *Robustness of Treatment Planning for Electrochemotherapy of Deep-Seated Tumors.* Journal of Membrane Biology, 2010. **236**(1): p. 147-153.
200. Lee, R.C., D. Zhang, and e. al, *Biophysical Injury Mechanisms in Electrical Shock Trauma.*, in *Ann. Rev. Biomed. Eng.*, M. L. Yarmish, K. R. Diller, and M. Toner., Editors. 2000, Annual Review Press.: Palo Alto. p. 477-509.
201. Cima, L.F. and L.M. Mir, *Macroscopic characterization of cell electroporation in biological tissue based on electrical measurements.* Applied Physics Letters, 2004. **85**(19): p. 4520-4522.
202. Davalos, R.V., B. Rubinsky, and D.M. Otten, *A feasibility study for electrical impedance tomography as a means to monitor tissue electroporation for molecular medicine.* Ieee Transactions on Biomedical Engineering, 2002. **49**(4): p. 400-403.
203. Sel, D., D. Cukjati, D. Batiuskaite, T. Slivnik, L.M. Mir, and D. Miklavcic, *Sequential finite element model of tissue electropermeabilization.* Biomedical Engineering, IEEE Transactions on, 2005. **52**(5): p. 816-827.
204. Pavselj, N., Z. Bregar, D. Cukjati, D. Batiuskaite, L.M. Mir, and D. Miklavcic, *The course of tissue permeabilization studied on a mathematical model of a*

subcutaneous tumor in small animals. Biomedical Engineering, IEEE Transactions on, 2005. **52**(8): p. 1373-1381.
205. Ivorra, A. and B. Rubinsky, *In vivo electrical impedance measurements during and after electroporation of rat liver.* Bioelectrochemistry., 2007. **70**(2): p. 287-95. Epub 2006 Oct 21.
206. Ivorra, A., B. Al-Sakere, B. Rubinsky, and L.M. Mir, *In vivo electrical conductivity measurements during and after tumor electroporation: conductivity changes reflect the treatment outcome.* Phys Med Biol., 2009. **54**(19): p. 5949-63. Epub 2009 Sep 17.
207. Davalos, R., L. Mir, and B. Rubinsky, *Tissue Ablation with Irreversible Electroporation.* Annals of Biomedical Engineering, 2005. **33**(2): p. 223-231.
208. Garcia, P.A., J.H. Rossmeisl, Jr., R.E. Neal, 2nd, T.L. Ellis, and R.V. Davalos, *A Parametric Study Delineating Irreversible Electroporation from Thermal Damage Based on a Minimally Invasive Intracranial Procedure.* Biomed Eng Online., 2011. **10**(1): p. 34.
209. Robert E. Neal II, Paulo A. Garcia, John L. Robertson, and R.V. Davalos, *Experimental Characterization of Intrapulse Tissue Conductivity Changes for Electroporation*, in *Engineering in Medicine and Biology Society 2011 Annual International Conference of the IEEE*. 2011: Boston, MA.
210. Ivorra, A., J. Villemejane, and L.M. Mir, *Electrical modeling of the influence of medium conductivity on electroporation.* Phys Chem Chem Phys., 2010. **12**(34): p. 10055-64. Epub 2010 Jun 28.
211. Kyber, J., H. Hansgen, and F. Pliquett, *Dielectric properties of biological tissue at low temperatures demonstrated on fatty tissue.* Phys Med Biol., 1992. **37**(8): p. 1675-88.
212. Stuchly, M.A., T.W. Athey, G.M. Samaras, and G.E. Taylor, *Measurement of Radio Frequency Permittivity of Biological Tissues with an Open-Ended Coaxial Line: Part II - Experimental Results.* Microwave Theory and Techniques, IEEE Transactions on, 1982. **30**(1): p. 87-92.
213. Mudaliar, A.V., B.E. Ellis, P.L. Ricketts, O.I. Lanz, C.Y. Lee, T.E. Diller, and E.P. Scott, *Noninvasive Blood Perfusion Measurements of an Isolated Rat Liver and an Anesthetized Rat Kidney.* Journal of Biomechanical Engineering, 2008. **130**(6): p. 061013.
214. Cooper, T.E. and G.J. Trezek, *Correlation of thermal properties of some human tissue with water content.* Aerosp Med., 1971. **42**(1): p. 24-7.
215. Valvano, J.W., J.R. Cochran, and K.R. Diller, *Thermal conductivity and diffusivity of biomaterials measured with self-heated thermistors.* International Journal of Thermophysics, 1985. **6**(3): p. 301-311.
216. Osswald, K., *Messung der Leitfahigkeit und Dielektrizitatkonstante biologischer Gewebe und Flussigkeiten beikurzen Wellen Hochfrequenz Tech.* Elektroakustik, 1937 **49**(40-50).
217. Middlekauff, H.R., E.U. Nitzsche, A.H. Nguyen, C.K. Hoh, and G.G. Gibbs, *Modulation of Renal Cortical Blood Flow During Static Exercise in Humans.* Circ Res, 1997. **80**(1): p. 62-68.

218. Foster, K.R. and H.P. Schwan, *Dielectric properties of tissues and biological materials: a critical review.* Crit Rev Biomed Eng., 1989. **17**(1): p. 25-104.
219. Sapareto, S.A., *Thermal Dose Determination in Cancer Therapy.* Radiation Oncology, 1984. **10**(6): p. 787-795.
220. Sersa, G., T. Jarm, T. Kotnik, A. Coer, M. Podkrajsek, M. Sentjurc, D. Miklavcic, M. Kadivec, S. Kranjc, A. Secerov, and M. Cemazar, *Vascular disrupting action of electroporation and electrochemotherapy with bleomycin in murine sarcoma.* Br J Cancer, 2008. **98**(2): p. 388-398.
221. Surowiec, A., S.S. Stuchly, and A. Swarup, *Radiofrequency dielectric properties of animal tissues as a function of time following death.* Phys Med Biol., 1985. **30**(10): p. 1131-41.
222. Surowiec, A., S.S. Stuchly, M. Keaney, and A. Swarup, *In vivo and in vitro dielectric properties of feline tissues at low radiofrequencies.* Phys Med Biol., 1986. **31**(8): p. 901-9.
223. Athey, T.W., M.A. Stuchly, and S.S. Stuchly, *Measurement of Radio Frequency Permittivity of Biological Tissues with an Open-Ended Coaxial Line: Part I.* Microwave Theory and Techniques, IEEE Transactions on, 1982. **30**(1): p. 82-86.
224. Stoy, R.D., K.R. Foster, and H.P. Schwan, *Dielectric properties of mammalian tissues from 0.1 to 100 MHz: a summary of recent data.* Phys Med Biol., 1982. **27**(4): p. 501-13.
225. Ivorra, A., L.M. Mir, and B. Rubinsky, *Electric Field Redistribution due to Conductivity Changes during Tissue Electroporation: Experiments with a Simple Vegetal Model*. 2009, Springer Berlin Heidelberg. p. 59-62.
226. Sel, D., D. Cukjati, D. Batiuskaite, T. Slivnik, L.M. Mir, and D. Miklavcic, *Sequential finite element model of tissue electropermeabilization.* IEEE Trans Biomed Eng, 2005. **52**(5): p. 816-27.
227. Edd, J.F. and R.V. Davalos, *Mathematical Modeling of irreversible Electroporation for treatment planning.* Technology in Cancer Research & Treatment, 2007. **6**(4): p. 275-286.
228. Corovic, S., M. Pavlin, and D. Miklavcic, *Analytical and numerical quantification and comparison of the local electric field in the tissue for different electrode configurations.* BioMedical Engineering OnLine, 2007. **6**(1): p. 37.
229. Dev, S.B., D. Dhar, and W. Krassowska, *Electric field of a six-needle array electrode used in drug and DNA delivery in vivo: analytical versus numerical solution.* IEEE Trans Biomed Eng., 2003. **50**(11): p. 1296-300.
230. Aguilera, A.R., L.E.B. Cabrales, H.M.C. Ciria, Y.S. Pérez, E.R. Oria, S.A. Brooks, and T.R. González, *Distributions of the potential and electric field of an electrode elliptic array used in tumor electrotherapy: Analytical and numerical solutions.* Mathematics and Computers in Simulation, 2009. **79**(7): p. 2091-2105.
231. Ramo, S., J.R. Whinnery, and T.V. Duzer, *Fields and waves in communication electronics*. 1965: J. Wiley.
232. Corovic, S., A. Zupanic, and D. Miklavcic, *Numerical Modeling and Optimization of Electric Field Distribution in Subcutaneous Tumor Treated With Electrochemotherapy Using Needle Electrodes.* IEEE Trans Plasma Sci 2008. **36**(4): p. 1665-1672.

233. Kairouz, S., J. Hashash, W. Kabbara, W. McHayleh, and I.A. Tabbara, *Dendritic cell neoplasms: An overview.* Am J Hematol, 2007. **82**(10): p. 924-928.
234. Skorupski, K.A., C.A. Clifford, M.C. Paoloni, A. Lara-Garcia, L. Barber, M.S. Kent, A.K. LeBlanc, A. Sabhlok, E.A. Mauldin, F.S. Shofer, C.G. Couto, and K.U. Sorenmo, *CCNU for the treatment of dogs with histiocytic sarcoma.* J Vet Intern Med, 2007. **21**(1): p. 121-6.
235. Fulmer, A.K. and G.E. Mauldin, *Canine histiocytic neoplasia: an overview.* Can Vet J, 2007. **48**(10): p. 1041-3, 1046-50.
236. Davalos, R.V., B. Rubinsky, and L.M. Mir, *Theoretical analysis of the thermal effects during in vivo tissue electroporation.* Bioelectrochemistry, 2003. **61**: p. 99-107.
237. *ACS Detailed Guide: Brain/CNS Tumors in Adults*. 2011, American Cancer Society.
238. Prados, M.D. and V. Levin, *Biology and treatment of malignant glioma.* Semin Oncol., 2000. **27**(3 Suppl 6): p. 1-10.
239. Mirimanoff, R.O., T. Gorlia, W. Mason, M.J. Van den Bent, R.D. Kortmann, B. Fisher, M. Reni, A.A. Brandes, J. Curschmann, S. Villa, G. Cairncross, A. Allgeier, D. Lacombe, and R. Stupp, *Radiotherapy and temozolomide for newly diagnosed glioblastoma: recursive partitioning analysis of the EORTC 26981/22981-NCIC CE3 phase III randomized trial.* J Clin Oncol., 2006. **24**(16): p. 2563-9.
240. Hochberg, F.H. and A. Pruitt, *Assumptions in the radiotherapy of glioblastoma.* Neurology, 1980. **30**(9): p. 907-11.
241. Peignan, L., W. Garrido, R. Segura, R. Melo, D. Rojas, J.G. Carcamo, R. San Martin, and C. Quezada, *Combined use of anticancer drugs and an inhibitor of multiple drug resistance-associated protein-1 increases sensitivity and decreases survival of glioblastoma multiforme cells in vitro.* Neurochem Res., 2011. **36**(8): p. 1397-406. Epub 2011 May 5.
242. Garrido, W., M. Munoz, R. San Martin, and C. Quezada, *FK506 confers chemosensitivity to anticancer drugs in glioblastoma multiforme cells by decreasing the expression of the multiple resistance-associated protein-1.* Biochem Biophys Res Commun., 2011. **411**(1): p. 62-8. Epub 2011 Jun 17.
243. Thomson, K.R., W. Cheung, S.J. Ellis, D. Federman, H. Kavnoudias, D. Loader-Oliver, S. Roberts, P. Evans, C. Ball, and A. Haydon, *Investigation of the safety of irreversible electroporation in humans.* J Vasc Interv Radiol., 2011. **22**(5): p. 611-21. Epub 2011 Mar 25.
244. Linnert, M. and J. Gehl, *Bleomycin treatment of brain tumors: an evaluation.* Anticancer Drugs., 2009. **20**(3): p. 157-64.
245. Salford, L.G., B.R. Persson, A. Brun, C.P. Ceberg, P.C. Kongstad, and L.M. Mir, *A new brain tumour therapy combining bleomycin with in vivo electropermeabilization.* Biochem Biophys Res Commun., 1993. **194**(2): p. 938-43.
246. Ellis, T.L., P.A. Garcia, J.H. Rossmeisl, N. Henao-Guerrero, J. Robertson, and R.V. Davalos, *Nonthermal irreversible electroporation for intracranial surgical applications.* Journal of Neurosurgery, 2011. **114**(3): p. 681-688.

247. Gregor Serša, Maja Čemažar, Damijan Miklavčič, and Z. Rudolf, *Electrochemotherapy of tumours.* Radiol Oncol, 2006. **40**(3): p. 163-74.
248. Miklavcic, D., D. Semrov, H. Mekid, and L.M. Mir, *A validated model of in vivo electric field distribution in tissues for electrochemotherapy and for DNA electrotransfer for gene therapy.* Biochimica et Biophysica Acta, 2000. **1523**(1): p. 73-83.
249. Miklavcic, D., K. Beravs, D. Semrov, M. Cemazar, F. Demsar, and G. Sersa, *The importance of electric field distribution for effective in vivo electroporation of tissues.* Biophysical Journal, 1998. **74**(5): p. 2152-2158.
250. Gabriel, S., R.W. Lau, and C. Gabriel, *The dielectric properties of biological tissues: II. Measurements in the frequency range 10 Hz to 20 GHz.* Phys Med Biol., 1996. **41**(11): p. 2251-69.
251. Agerholm-Larsen, B., H.K. Iversen, P. Ibsen, J.M. Moller, F. Mahmood, K.S. Jensen, and J. Gehl, *Preclinical validation of electrochemotherapy as an effective treatment for brain tumors.* Cancer Res., 2011. **71**(11): p. 3753-62. Epub 2011 Apr 20.
252. Robert E Neal II, Paulo A Garcia, John L Robertson, and Rafael V Davalos, *Experimental Characterization and Numerical Modeling of Tissue Electrical Conductivity during Pulsed Electric Fields for Irreversible Electroporation Treatment Planning.* IEEE Trans Biomed Eng, 2011. **submitted**.
253. Edd, J., L. Horowitz, R. Davalos, L. Mir, and B. Rubinsky, *In vivo results of a new focal tissue ablation technique: irreversible electroporation.* IEEE Transactions on Biomedical Engineering, 2006. **53**(7): p. 1409-1415.
254. Sano, M.B., R.E. Neal, 2nd, P.A. Garcia, D. Gerber, J. Robertson, and R.V. Davalos, *Towards the creation of decellularized organ constructs using irreversible electroporation and active mechanical perfusion.* Biomed Eng Online, 2010. **9**(1): p. 83.